


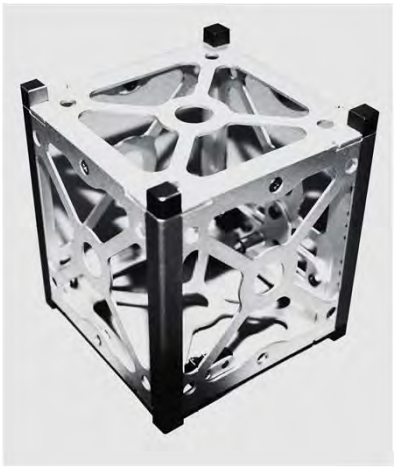

Aerospace and Defense • Additive Manufacturing • Unmanned Aerial Systems • Energy

The Center for Space Exploration and Technology Research at
The University of Texas at El Paso
Proudly Presents

Southwest Emerging Technology Symposium & Regional Small Business Summit 2019

Tuesday, March 26th – Wednesday, March 27th, 2019
El Paso Marriott
El Paso, TX

Welcome to the Southwest Emerging Technology Symposium and Regional Small Business Summit sponsored by Lockheed Martin, PRE-CAPP, National Nuclear Security Administration, U.S. Economic Development Administration, Horizon City Economic Development Corporation, The City of El Paso, El Paso Hispanic Chamber of Commerce, & Mike Loya Center for Innovation & Commerce. The goal of this symposium is to provide a formal setting for interactions among academic, government, industrial professionals, and regional small businesses.

The following individuals and organizations are acknowledged for their assistance with the symposium.

HOSTED BY

NASA MIRO Center for Space Exploration and Technology Research
W. M. KECK Center for 3D Innovation
Department of Mechanical Engineering
The University of Texas at El Paso

CONFERENCE CHAIRS

Ahsan Choudhuri Associate Vice President for Strategic Initiatives
The University of Texas at El Paso

Jack Chessa Chair, Mechanical Engineering
The University of Texas at El Paso

TECHNICAL CHAIRS

Yirong Lin Graduate Program Director | Associate Professor, Mechanical Engineering
The University of Texas at El Paso

LOGISTICS COMMITTEE

Luz Bugarin The University of Texas at El Paso
KiraLise Silva The University of Texas at El Paso
Gloria Salas The University of Texas at El Paso
Brenda Sanchez The University of Texas at El Paso

MODERATORS

Jason Adams The University of Texas at El Paso
Luz Bugarin The University of Texas at El Paso
Jack Chessa The University of Texas at El Paso
Ahsan Choudhuri The University of Texas at El Paso
Michael Hernandez Horizon City Economic Development Corp.
Joel Quintana The University of Texas at El Paso
Justin Vanhoose The University of Texas at El Paso

SESSION CHAIRS

Methaq S. Abed The University of Texas at El Paso
Jason Adams The University of Texas at El Paso
Omar Cedillos The University of Texas at El Paso
David Espalin The University of Texas at El Paso
Angel Flores-Abad The University of Texas at El Paso
Chance Garcia NASA - Marshall Space Flight Center
Arifur Khan The University of Texas at El Paso
Hossein Mallahzadeh The University of Texas at El Paso
Joel Quintana The University of Texas at El Paso
Mahamudur Rahman The University of Texas at El Paso
Cesar Terrazas The University of Texas at El Paso
Deepak Tosh The University of Texas at El Paso

INVITED SPEAKERS

Salvatore 'Tory' Bruno President & Chief Executive Officer
United Launch Alliance

Mark Davidson Small Business Innovation & Technology Partnerships
NASA Jet Propulsion Laboratory

Douglas Deason Chief Executive Officer
Deason Research LLC

Chance Garcia Liquid Propulsion Engineer
Engine Component Development & Technology Branch
NASA Marshall Space Flight Center

Nick Gonzales Director of Technical Operations, THAAD
Space Systems Company
Lockheed Martin Corporation

Michael Hernandez Executive Director
Horizon City Economic Development Corp.

Jessica Herrera Director of Economic and International Development
City of El Paso

Gregg Jones Branch Chief, Component Design and Technology Branch
NASA Marshall Space Flight Center

Michael Keidar A. James Clark Professor of Engineering
The George Washington University

Maria Reidpath Project Manager
National Energy Technology Laboratory (NETL)
U.S. Department of Energy

Ida Sanchez Chemical Engineer
Honeywell FM&T

Eduardo Seyffert Sr. Manager, Test Operations at the West Texas Launch Site
Blue Origin

Briggs White Crosscutting Technology Manager
National Energy Technology Laboratory (NETL)
U.S. Department of Energy

Regional Small Business Summit 2019

Tuesday, 26 March

LOCATION El Paso Marriott

7:00 AM - 7:45 AM

REGISTRATION Ballroom Foyer

BREAKFAST Junior Ballroom

7:45 AM - 8:15 AM Grand Ballroom

WELCOME

Ahsan Choudhuri Associate Vice President for Strategic Initiatives
The University of Texas at El Paso

Ricardo Samaniego County Judge
El Paso County

Donald "Dee" Margo Mayor (Invited)
City of El Paso

8:15 AM - 9:00 AM *Moderator: Ahsan Choudhuri* Grand Ballroom

KEYNOTE

THE FRONTIERS OF AEROSPACE & LM 6 STEPS FOR SBIR ENGAGEMENT

Nick Gonzales Director of Technical Operations, THAAD
Space Systems Company
Lockheed Martin Corporation

9:00 AM - 9:45 AM *Moderator: Michael Hernandez* Grand Ballroom

SMALL BUSINESS INNOVATION RESEARCH (SBIR) AND SMALL BUSINESS TECHNOLOGY TRANSFER (STTR) SESSION

Mark Davidson Small Business Innovation & Technology Partnerships
NASA Jet Propulsion Laboratory

THE SMALL BUSINESS INNOVATION RESEARCH & SMALL BUSINESS TECHNOLOGY TRANSFER PROGRAM AT THE U.S. DEPARTMENT OF ENERGY

Maria Reidpath Project Manager
National Energy Technology Laboratory (NETL)
U.S. Department of Energy

9:45 AM - 10:30 AM *Moderator: Luz Bugarin* Grand Ballroom

SMALL BUSINESS INNOVATION RESEARCH (SBIR) AND SMALL BUSINESS TECHNOLOGY TRANSFER (STTR) SESSION

WRITING COMPETITIVE SBIR PROPOSALS

Douglas Deason Chief Executive Officer
Deason Research LLC

10:30 AM - 11:30 AM *Moderator: Jack Chessa* Grand Ballroom

PANEL: REGIONAL ECONOMIC DEVELOPMENT

Jessica Herrera Director of Economic and International Development
City of El Paso

Michael Hernandez Executive Director
Horizon City Economic Development Corp.

11:30 AM - 12:00 PM *Moderator: Joel Quintana* Grand Ballroom

INVITED SPEAKER

PLASMA-BASED MICROPROPULSION FOR CUBESATS

Michael Keidar A. James Clark Professor of Engineering
The George Washington University

11:30 AM - 12:00PM — Executive Board Room

GUEST EXECUTIVE MEETING (INVITATION ONLY) — Briggs White & Roberto Osegueda

12:00 PM - 1:00 PM — Ballroom Foyer

SMALL BUSINESS SHOWCASE EVENT

12:00 PM - 1:00 PM — Junior Ballroom

LUNCH

1:00 PM - 5:15 PM — Transportation will be provided

UNIVERSITY OF TEXAS AT EL PASO - RESEARCH FACILITY TOURS (INVITATION ONLY)

Southwest Emerging Technology Symposium

Wednesday, 27 March

LOCATION El Paso Marriott

7:00 AM - 7:50 AM

REGISTRATION — Ballroom Foyer

BREAKFAST — Junior Ballroom

7:50 AM - 8:00 AM — Grand Ballroom

OPENING NOTES

Diana Natalicio President
The University of Texas at El Paso

8:00 AM - 9:00 AM — ***Moderator: Ahsan Choudhuri*** — Grand Ballroom

KEYNOTE

FOSSIL ENERGY TECHNOLOGIES – TRENDS AND EMERGING OPPORTUNITIES

Briggs White Crosscutting Technology Manager
National Energy Technology Laboratory (NETL)
U.S. Department of Energy

9:00 AM - 10:00 AM

PARALLEL TECHNICAL SESSIONS

ADDITIVE MANUFACTURING I	*Moderator: Cesar Terrazas, UTEP*	Bluebonnet
ADDITIVE MANUFACTURING II	*Moderator: David Espalin, UTEP*	Mockingbird
AEROSPACE & DEFENSE I - ITAR	*Moderator: Jason Adams, UTEP*	Southwest Boardroom
AEROSPACE & DEFENSE II	*Moderator: Chance Garcia, NASA MSFC*	Salon H
AEROSPACE & DEFENSE III	*Moderator: Arifur Khan, UTEP*	Salon I
ENERGY I	*Moderator: Angel Flores-Abad, UTEP*	Salon J

10:00 AM - 10:15 AM

BREAK

10:15 AM - 11:15 AM — ***Moderator: Ahsan Choudhuri*** — Grand Ballroom

KEYNOTE

IT IS A GREAT TIME TO BE A ROCKET ENGINEER

Gregg Jones Branch Chief, Component Design and Technology Branch
NASA Marshall Space Flight Center

11:15 AM - 12:00 PM

STUDENT SESSIONS

ENERGY STUDENT SESSION WITH BRIGGS WHITE — Mockingbird

Moderator: Jason Adams

AEROSPACE & DEFENSE STUDENT SESSION WITH NICK GONZALES — Bluebonnet

Moderator: Justin Vanhoose

12:00 PM - 1:00 PM — Junior Ballroom

LUNCH

1:00 PM - 2:00 PM — *Moderator: Ahsan Choudhuri* — Grand Ballroom

KEYNOTE

Salvatore 'Tory' Bruno President & Chief Executive Officer
United Launch Alliance

2:00 PM - 2:45 PM — *Moderator: Jason Adams* — Mockingbird

INVITED SPEAKER - NATIONAL NUCLEAR SECURITY ADMINISTRATION | KANSAS CITY NATIONAL SECURITY CAMPUS

LIFE AFTER UTEP

Ida Sanchez Chemical Engineer
Honeywell FM&T

2:00 PM - 2:45 PM — *Moderator: Justin Vanhoose* — Bluebonnet

INVITED SPEAKER - NASA MARSHALL SPACE FLIGHT CENTER

NASA MSFC ADDITIVE MANUFACTURED DEMONSTRATOR ENGINE (AMDE) THRUST CHAMBER ASSEMBLY HOTFIRE PROGRAM

Chance Garcia Liquid Propulsion Engineer
Engine Component Development & Technology Branch
NASA Marshall Space Flight Center

2:45 PM - 3:30 PM — *Moderator: Justin Vanhoose* — Bluebonnet

INVITED SPEAKER - BLUE ORIGIN

BLUE ORIGIN OVERVIEW

Eduardo Seyffert Sr. Manager, Test Operations at the West Texas Launch Site
Blue Origin

3:30 PM - 3:45 PM

BREAK

3:45 PM - 5:45 PM

PARALLEL TECHNICAL SESSIONS

ADDITIVE MANUFACTURING III	*Moderator: Omar Cedillos, UTEP*	Bluebonnet
AEROSPACE & DEFENSE IV	*Moderator: Deepak Tosh, UTEP*	Mockingbird
AEROSPACE & DEFENSE V	*Moderator: Joel Quintana, UTEP*	Southwest Boardroom
ENERGY II	*Moderator: Md Mahamudur Rahman, UTEP*	Salon H
ENERGY III	*Moderator: Methaq S. Abed, UTEP*	Salon I
ENERGY IV	*Moderator: Hossein Mallahzadeh, UTEP*	Salon J

5:45 PM - 7:00 PM — Junior Ballroom

DINNER & CLOSING REMARKS

Ahsan Choudhuri Associate Vice President for Strategic Initiatives
The University of Texas at El Paso

ABOUT THE SPEAKER

Salvatore T. "Tory" Bruno
President & Chief Executive Officer
United Launch Alliance

Salvatore T. "Tory" Bruno is the president and chief executive officer for United Launch Alliance (ULA). In this role, Bruno serves as the principal strategic leader of the organization and oversees all business management and operations.

Prior to joining ULA, he served as the vice president and general manager of Lockheed Martin Strategic and Missile Defense Systems. The business is a leading provider of ballistic missile and ballistic missile defense systems, supporting U.S. Department of Defense customers, as well as the U.K. Royal Navy and Ministry of Defense. Programs included the Navy's Trident II D5 Fleet Ballistic Missile (FBM), the Air Force's Intercontinental Ballistic Missile (ICBM) Reentry Systems, and the Missile Defense Agency's Terminal High Area Altitude Defense (THAAD), Targets and Countermeasures and Common Exoatmospheric Kill Vehicle (EKV) Concept Definition. He also managed the corporation's responsibilities in Atomic Weapons Establishment (AWE) Management Limited, a joint venture that produces and safely maintains the U.K.'s nuclear weapons. He is a former member of the board of directors of Lockheed Martin U.K. Ltd.

Bruno joined Lockheed Martin in 1984. He previously served as vice president and general manager of FBM and ICBM, as vice president of the THAAD Missile, as vice president of Engineering, as chief engineer for Strategic Missile Programs, as program manager for FBM Rocket Propulsion and in engineering positions involving design and analysis for control systems of rockets and hypersonic reentry vehicles. He holds several patents.

He holds a bachelor's degree in mechanical engineering from the California Polytechnic State University, in San Luis Obispo, California, and has completed graduate courses and management programs at Harvard University, Santa Clara University, the Wye River Institute, San Jose State University and the Defense Acquisition University.

Bruno is serving as a member of the National Space Council Users' Advisory Group chaired by Vice President Pence. In addition, he is an American Institute of Aeronautics and Astronautics (AIAA) Fellow, a companion of the Naval Order of the United States, a member of the Navy League and a former member of the Board of Directors of the Silicon Valley Leadership Group. He served on the National Blue Ribbon Panel for Bettering Engineering & Science Education and as Chairman of the Diversity Council of Lockheed Martin Space Systems.
He is the author of two books that explore the organization of the medieval Knights Templar from the perspective of modern business management: "Templar Organization: The Management of Warrior Monasticism" and "Templar Incorporated." He is a recipient of the Order of Merit of the Sovereign Military Order of the Temple of Jerusalem.

ABOUT THE SPEAKER

Nick Gonzales
Director Technical Operations, THAAD
Lockheed Martin, Space Systems Company

Nick Gonzales serves as Director of Technical Operations THAAD, at Lockheed Martin (LM) Space Systems Company (SSC). Prior to his role, he has served in various positions including the FBM Director of Programs and Director of Systems Engineering (SE) for Lockheed Martin Space Systems Company where he was chartered with pioneering the continued development of Lockheed Martin's world class SE organization.

Lockheed Martin has participated extensively in the development of our Nations Missile Defense endeavor and Mr. Gonzales most recently lead the design of Lockheed Martin's offering for the next generation interceptor kill vehicle. The purpose of this kill vehicle was to enhance homeland defense against missile attack. When the Government decided they would assemble the best industry had to offer into a cohesive design, Mr. Gonzales served as the LM representative to that industry team.

Prior to embarking on the design of Nations next generation kill vehicle for homeland defense, Mr. Gonzales dedicated a large portion of his career to developing and fielding the THAAD interceptor. He started this effort in the systems test group where he set up the launch control room for implementation of countdown go/no-go operations and managed the $90M development of the production test equipment used to ATP the missile rounds. He served as the manager of systems integration when the focus was on getting the interceptor qualified for flight. Mr. Gonzales transitioned to CSE during the flight test program, focusing on flight test mission success and on resolving issues discovered during flight operations. Finally, he served as the Director and CE of the THAAD interceptor, driving hard to obtain the approval of the United States Government to release the interceptor to the war fighters in order to defend our troops, friends, and allies in their theater of operation. Under his leadership, the THAAD missile team has provided the Missile Defense Agency (MDA) and the Nation with a missile system that has demonstrated groundbreaking capability and reliably achieving a perfect mission success record. Mr. Gonzales has actively participated in and led the development efforts associated with Missile Systems, Missile Software, Missile Structure/Propulsion Elements and all Test Equipment.

Mr. Gonzales has over 30 years of successful hands on engineering experience and has held leadership positions in Engineering and Program Management. He received his bachelors of science in mechanical engineering from San Jose State University with a minor in electronics. He is a recipient of the prestigious Lockheed Martin NOVA award and has received various other recognition awards from the corporation.

ABOUT THE SPEAKER

Gregg Jones
Branch Chief of Components Design and Technology
NASA Marshall Space Flight Center

Gregg Jones has over 30 years' experience designing, analyzing and building rocket engines. He has worked on the Space Shuttle Main Engine, the RL10, the J-2X, and many other engines and he has three patents for rocket combustion chambers. Mr. Jones currently leads NASA Marshall's Combustion Devices and Turbomachinery Branch where their focus is on developing new rocket manufacturing methods including 3-D printed copper chambers, blown powder regeneratively cooled nozzles, carbon-carbon nozzle extensions and 3-D printed turbomachinery and also on developing new lander and in–space engines to help return astronauts to the moon.

ABOUT THE SPEAKER

Briggs White
Crosscutting Technology Manager
National Energy Technology Laboratory (NETL)
U.S. Department of Energy

Dr. Briggs White is an experienced engineering management professional with a demonstrated history of working in the research industry.

Currently, Dr. White is serving as Crosscutting Technology Manager at NETL managing a portfolio of approximately 100 research projects and annual appropriations of $55 million. The program serves to accelerate R&D progress and develop concepts and technologies that enable improvements in fossil-based power generation. The program's scope includes sensors and controls, cybersecurity, modeling and simulation, high-performance materials, innovative combustion concepts, and water management. He has also served as the Chief of Staff for NETL's Science and Technology directorate – reporting directly to NETL's Chief Research Officer, as well as Chief of Staff for the Technology Development and Integration Center, NETL's project management organization.

He holds degrees in Materials Science & Engineering from Alfred University (BS), the University of Florida (MS, PhD), and the Univ. of Rome (PhD) with an emphasis on solid-state high-temperature electrochemical devices.

ABOUT THE SPEAKER

Mark Davidson
Small Business Innovation & Technology Partnerships
NASA Jet Propulsion Laboratory (JPL)

Mark Davidson is a member of the California Institute of Technology's Jet Propulsion Laboratory office of the Small Business Innovation and Technology Partnerships Office and NASA's Western Water Applications program office. Mark has held positions as the Corporate Treasurer and Head of Investor Relations at major aerospace parts distribution company and as the Corporate Director of Business Strategy at Northrop Grumman Corporation where he was responsible for evolving the company's portfolio strategy associated with all defense electronics including space, air, ground and maritime domains and naval systems including navigation, ship, weapons and engineering control. In this function he also participated in M&A, Joint Venture, divestitures and spin-off activities. He served as a Presidential appointee as the Deputy Assistant Secretary of the Navy for Reserve Affairs and is a retired Navy Captain. Mark holds an MBA from the U.S.C. Marshall School of Business, a Diploma from the U.S. Navy War College Command & Staff program, and a BA in Physical Geography from U.C.L.A.

ABOUT THE SPEAKER

Maria Reidpath
Project Manager
National Energy Technology Laboratory (NETL)
U.S. Department of Energy

Maria Reidpath is a Project Manager in the Enabling Technologies and Partnerships team at the U.S. Department of Energy's (DOE) National Energy Technology Laboratory (NETL). She also serves as the NETL Coordinator for the Small Business Innovation Research (SBIR) and Small Business Technology Transfer (STTR) Program. As Project Manager, Mrs. Reidpath manages extramural research projects in Crosscutting Technology areas such as Sensors and Controls, Advanced Manufacturing, Water Management, and High Performance Materials. As Coordinator for SBIR-STTR, Mrs. Reidpath serves as the point of contact with DOE's SBIR Office and the Office of Fossil Energy in the administration of all activities related to topic development, application and selection process, and the awarding of SBIR-STTR grants. Mrs. Reidpath holds a B.S. degree in Industrial Engineering from West Virginia University.

ABOUT THE SPEAKER

Douglas Deason
CEO
Deason Research LLC

Dr. Deason is CEO of Deason Research LLC, engaged in management of technology and innovation, particularly focusing on initiating and maturing research and development programs in the federal enterprise. He has a 40-year career in research and development. He has served as a senior manager/director in the Department of Defense overseeing small business, university and industrial research portfolios with a budget of over $140M annually. He is a frequently requested speaker at national and regional conferences in areas such as proposal writing, the SBIR/STTR program, working with prime contractors, and maturing technology through federal funding, as well as missile defense, nanotechnology, and advanced materials for challenging applications. He holds a Ph.D. in Materials Science and Engineering from the University of California, Berkeley.

ABOUT THE SPEAKER

Michael Keidar
A. James Clark Professor of Engineering
The George Washington University

Michael Keidar is A. James Clark Professor of Engineering. His research concerns advanced spacecraft propulsion, plasma-based nanotechnology, and plasma medicine. He has authored over 260 journal articles and author of textbook "Plasma Engineering: from Aerospace and Nano and Bio technology" (Elsevier, March 2013). He received 2017 Davidson award in plasma physics. In 2016 he received AIAA Engineer of the Year award for his work on micropropulsion resulted in successful launch of nanosatellite with thrusters developed by his laboratory. Physics of Plasmas selects 2001 paper on Hall thruster as one of its most cited papers in the 50 years of its publishing. He is one of pioneers of plasma medicine. His research led to development of the cold plasma scalpel, which is used to treat cancer. Many of his papers have been featured on the cover of high impact journals and his research has been covered by various media outlets. Prof. Keidar serves as an AIP Advances academic editor, Associate Editor of IEEE Transactions in Radiation and Plasma Medical Sciences and member of editorial board of half dozen of journals. He is Fellow of American Physical Society and Associate Fellow of American Institute of Astronautics and Aeronautics.

ABOUT THE SPEAKER

Eduardo Seyffert
Sr. Manager, Test Operations at the West Texas Launch Site
Blue Origin

Eduardo Seyffert is a Sr. Manager in Test Operations at Blue Origin's West Texas Launch Site. He currently manages the BE-4 liquid rocket engine test stand, and has been helping with BE-3 engine testing and New Shepard launch and landing operations since 2014.. He has an MS in aeronautical and astronautical engineering from Purdue University, and a BS in the same from MIT. Originally from El Paso, Eddie is excited to contribute to this year's symposium highlighting the region's burgeoning aerospace future.

ABOUT THE SPEAKER

Ida Sanchez
Chemical Engineer
Honeywell FM&T

Ida Sanchez received a Bachelor of Science in Metallurgical and Materials Engineering at the University of Texas at El Paso. She has experience in physical metallurgical engineering, focusing on carbon steels and stainless steels. Ida researched polymeric wear analysis, fracture surface characterization, electroless nanowire deposition, and polymer matrix composites at UTD and UTEP. She also evaluated process quality control at ArcelorMittal. In 2015, she transitioned to Honeywell FM&T and is currently focusing on research and development of metal powder for additive manufacturing.

ABOUT THE SPEAKER

Chance Garcia
Liquid Propulsion Engineer
Engine Component Development & Technology Branch
NASA Marshall Space Flight Center

Chance P. Garcia is an engineer at NASA Marshall Space Flight Center in the component technology design and development branch of the propulsion department. He hired into NASA in June 2013 after receiving his PhD from the University of Texas at El Paso. Currently he is working on additive manufactured rocket engine components as well support for the SLS core engines. Dr. Garcia has worked on several propulsion test programs, component development using new manufacturing techniques, and has experience with oxygen/hydrogen, oxygen/RP-1, oxygen/methane, methane, and hydrogen peroxide propulsion systems. He was also part of the first U.S. team to successfully hot fire a U.S. designed Oxygen Rich / RP-1 Staged Combustion system at Marshall Space Flight Center. Currently his focus is working to interconnect new additive manufacturing technologies into propulsion components such as injectors, thrust chambers, and nozzles.

Regional Small Business Summit 2019

Tuesday, 26 March

LOCATION El Paso Marriott

8:15 AM - 9:00 AM — *Moderator: Ahsan Choudhuri* — Grand Ballroom

KEYNOTE

THE FRONTIERS OF AEROSPACE & LM 6 STEPS FOR SBIR ENGAGEMENT

Nick Gonzales Director of Technical Operations, THAAD
Space Systems Company
Lockheed Martin Corporation

9:00 AM - 9:45 AM — *Moderator: Michael Hernandez* — Grand Ballroom

SMALL BUSINESS INNOVATION RESEARCH (SBIR) AND SMALL BUSINESS TECHNOLOGY TRANSFER (STTR) SESSION

Mark Davidson Small Business Innovation & Technology Partnerships
NASA Jet Propulsion Laboratory

THE SMALL BUSINESS INNOVATION RESEARCH & SMALL BUSINESS TECHNOLOGY TRANSFER PROGRAM AT THE U.S. DEPARTMENT OF ENERGY

Maria Reidpath Project Manager
National Energy Technology Laboratory (NETL)
U.S. Department of Energy

9:45 AM - 10:30 AM — *Moderator: Luz Bugarin* — Grand Ballroom

SMALL BUSINESS INNOVATION RESEARCH (SBIR) AND SMALL BUSINESS TECHNOLOGY TRANSFER (STTR) SESSION

WRITING COMPETITIVE SBIR PROPOSALS

Douglas Deason Chief Executive Officer
Deason Research LLC

10:30 AM - 11:30 AM — *Moderator: Jack Chessa* — Grand Ballroom

PANEL: REGIONAL ECONOMIC DEVELOPMENT

Jessica Herrera Director of Economic and International Development
City of El Paso

Michael Hernandez Executive Director
Horizon City Economic Development Corp.

11:30 AM - 12:00 PM — *Moderator: Joel Quintana* — Grand Ballroom

INVITED SPEAKER

PLASMA-BASED MICROPROPULSION FOR CUBESATS

Michael Keidar A. James Clark Professor of Engineering
The George Washington University

12:00 PM - 1:00 PM — Ballroom Foyer

SMALL BUSINESS SHOWCASE EVENT

12:00 PM - 1:00 PM — Junior Ballroom

LUNCH

1:00 PM - 5:15 PM — Transportation will be provided

UNIVERSITY OF TEXAS AT EL PASO - RESEARCH FACILITY TOURS (INVITATION ONLY)

Southwest Emerging Technology Symposium

Wednesday, 27 March

LOCATION El Paso Marriott

7:00 AM - 7:50 AM

REGISTRATION Ballroom Foyer

BREAKFAST Junior Ballroom

7:50 AM - 8:00 AM Grand Ballroom

OPENING NOTES

Diana Natalicio President
The University of Texas at El Paso

8:00 AM - 9:00 AM *Moderator: Ahsan Choudhuri* Grand Ballroom

KEYNOTE

FOSSIL ENERGY TECHNOLOGIES – TRENDS AND EMERGING OPPORTUNITIES

Briggs White Crosscutting Technology Manager
National Energy Technology Laboratory (NETL)
U.S. Department of Energy

9:00 AM - 10:00 AM

PARALLEL TECHNICAL SESSIONS

ADDITIVE MANUFACTURING I *Moderator: Cesar Terrazas, UTEP* Bluebonnet

9:00 AM - 9:20 AM Thermomechanical Properties of Large Area 3D Printed Parts
Presenter: Eduardo Meraz Trejo, UTEP

9:20 AM 9:40 AM Thermal Characterization of Abs/Carbon Fiber and Abs/Glass Fiber Composites Used in Large Area
Presenter: Fernando Rodriguez Lorenzana, UTEP

9:40 AM 10:00 AM In-situ Process Monitoring for Laser Powder Bed Fusion Additive Manufacturing
Presenter: Alfonso Fernandez, UTEP

ADDITIVE MANUFACTURING II *Moderator: David Espalin, UTEP* Mockingbird

9:00 AM - 9:20 AM Initial Investigation of Additive Manufacturing with TZM and Tungsten Powders for Aerospace
Presenter: Scott Wilkins & Nathaniel Jurado, UTEP

9:20 AM 9:40 AM Materials Designed and Optimized for Additive Manufacturing, Kicking Off the Next Generation of
Presenter: Hunter Taylor, UTEP

9:40 AM 10:00 AM Selective Nitriding of Titanium Substrates Using Open Source Laser Powder Bed Fusion Systems
Presenter: Andres Navarro, UTEP

AEROSPACE & DEFENSE I - ITAR *Moderator: Jason Adams, UTEP* Southwest Boardroom

9:00 AM - 9:20 AM Testing of Iridium Loaded Alumina Pellets for the Catalytic Decomposition of a Green
Presenter: Raul Cuevas, UTEP

9:20 AM 9:40 AM Orbital Factory X Design and Testing of a 1N Green Propellant Thruster
Presenter: Jonathan Valenzuela Brok, UTEP

9:40 AM 10:00 AM Spark Plasma Sintered Aluminum Oxide Filter for Hot Gas Applications
Presenter: Catalina Young, FIU

AEROSPACE & DEFENSE II *Moderator: Chance Garcia, NASA MSFC* Salon H

9:00 AM - 9:20 AM Design and Testing of a 500 lbf Liquid Oxygen/Liquid Methane Engine
Presenter: Adrian Welsh & Gerardo Ramirez Marquez, UTEP

9:20 AM 9:40 AM Software Development and Implementation of the tRIAC Data Acquisition and Control System
Presenter: Raymundo Rojo, UTEP

9:40 AM 10:00 AM Initialization and Troubleshooting of the MICIT System for LO2/LCH4 Engine Testing
Presenter: Corey Hansen, UTEP

AEROSPACE & DEFENSE III *Moderator: Arifur Khan, UTEP* Salon I

9:00 AM - 9:20 AM Centennial Small-Payload Launch Vehicle (CSpLV) - Concept
Presenter: Peniel Rodriguez & James Susen, UTEP

9:20 AM 9:40 AM Innovations in Pressure Fed Orbital Launch Vehicles
Presenter: Itzel Torres, UTEP

9:40 AM 10:00 AM A Bio-Inspired Guidance Method for a Soft Landing on Asteroid
Presenter: Rene Valenzuela, UTEP

ENERGY I *Moderator: Angel Flores-Abad, UTEP* Salon J

9:00 AM - 9:20 AM Thermal and Mechanical Energy Harvesting Using Piezoelectric Ceramics
Presenter: Luis A. Chavez, UTEP

9:20 AM 9:40 AM Model of Piezoelectric Sensor When Subject to Various Flows
Presenter: Alejandra Castellano, UTEP

9:40 AM 10:00 AM Experimental Setup for the Testing of Piezoelectric Mass Flow Sensor
Presenter: Eben Escobedo & Paul Perez, UTEP

10:00 AM - 10:15 AM

BREAK

10:15 AM - 11:15 AM *Moderator: Ahsan Choudhuri* Grand Ballroom

KEYNOTE

IT IS A GREAT TIME TO BE A ROCKET ENGINEER

Gregg Jones Branch Chief, Component Design and Technology Branch
NASA Marshall Space Flight Center

11:15 AM - 12:00 PM

STUDENT SESSIONS

ENERGY STUDENT SESSION WITH BRIGGS WHITE Mockingbird
Moderator: Jason Adams

AEROSPACE & DEFENSE STUDENT SESSION WITH NICK GONZALES Bluebonnet
Moderator: Justin Vanhoose

12:00 PM - 1:00 PM Junior Ballroom

LUNCH

1:00 PM - 2:00 PM *Moderator: Ahsan Choudhuri* Grand Ballroom

KEYNOTE

Salvatore 'Tory' Bruno President & Chief Executive Officer
United Launch Alliance

2:00 PM - 2:45 PM *Moderator: Jason Adams* Mockingbird

INVITED SPEAKER - NATIONAL NUCLEAR SECURITY ADMINISTRATION | KANSAS CITY NATIONAL SECURITY CAMPUS

LIFE AFTER UTEP

Ida Sanchez Chemical Engineer
Honeywell FM&T

2:00 PM - 2:45 PM *Moderator: Justin Vanhoose* Bluebonnet

INVITED SPEAKER - NASA MARSHALL SPACE FLIGHT CENTER

NASA MSFC ADDITIVE MANUFACTURED DEMONSTRATOR ENGINE (AMDE) THRUST CHAMBER ASSEMBLY HOTFIRE PROGRAM

Chance Garcia Liquid Propulsion Engineer
Engine Component Development & Technology Branch
NASA Marshall Space Flight Center

2:45 PM - 3:30 PM ***Moderator: Justin Vanhoose*** Bluebonnet

INVITED SPEAKER - BLUE ORIGIN

BLUE ORIGIN OVERVIEW

Eduardo Seyffert Sr. Manager, Test Operations at the West Texas Launch Site
Blue Origin

3:30 PM - 3:45 PM

BREAK

3:45 PM - 5:45 PM

PARALLEL TECHNICAL SESSIONS

ADDITIVE MANUFACTURING III		*Moderator: Omar Cedillos, UTEP*	Bluebonnet
3:45 PM - 4:05 PM	Development of a Wire Embedding Devices for Large Area Additive Manufacturing Systems *Presenter: Christopher J Minjares, UTEP*		
4:05 PM - 4:25 PM	Development of a Desktop Material Extrusion 3D Printer with Wire Embedding Capabilities *Presenter: Jose Motta, UTEP*		
4:25 PM - 4:45 PM	Additive Manufactured Ear Pinna for Sound Localization in Advanced Hearing Devices *Presenter: Carlos Acosta Carrasco, UTEP*		
4:45 PM - 5:05 PM	Multifunctional Sensing Using 3D Printed Nanocomposites *Presenter: Bethany Wilburn, UTEP*		
5:05 PM - 5:25 PM	Piezoelectric BaTiO3 Ceramics Fabricated Using Paste Extrusion 3D Printing Technique *Presenter: Anabel Renteria, UTEP*		
5:25 PM - 5:45 PM	Tuning of Mechanical and Electrical Properties of 3D Printing CNT-Photopolymer Nanocomposites *Presenter: Jaime Regis, UTEP*		
AEROSPACE & DEFENSE IV		*Moderator: Deepak Tosh, UTEP*	Mockingbird
3:45 PM - 4:05 PM	Simultaneous Localization and Mapping with an Autonomous Unmanned Aerial Vehicle *Presenter: Noah Lopez, UTEP*		
4:05 PM - 4:25 PM	Simultaneous Mapping and Localization of An Autonomous Drone *Presenter: Noshin Habib, UTEP*		
4:25 PM - 4:45 PM	Trajectory Generation from CAD for Aerial Inspection of Structural Components in GPS Denied *Presenter: Angel Ortega, UTEP*		
4:45 PM - 5:05 PM	A Cam-Based Trajectory Generation Method for UAV Inspection in GPS Denied Environment *Presenter: Mst Mousumi Rizia, UTEP*		
AEROSPACE & DEFENSE V		*Moderator: Joel Quintana, UTEP*	Southwest Boardroom
3:45 PM - 4:05 PM	Shock and Vibration Testing of the Orbital Factory II CubeSat *Presenter: Arthur Bruno, UTEP*		
4:05 PM - 4:25 PM	Orbital Factory II: 3D Printer *Presenter: Perla Perez, UTEP*		
4:25 PM - 4:45 PM	OFII Payload Control *Presenter: Eduardo Macias & Alan Caldelas, UTEP*		
4:45 PM - 5:05 PM	Orbital Factory II Integration and Orbital Analysis *Presenter: James Holt & Ashiqur Rahman, UTEP*		
ENERGY II		*Moderator: Md Mahamudur Rahman, UTEP*	Salon H
3:45 PM - 4:05 PM	High Pressure Experimental Boiling Test Facility Design to Increase CHF and HTC on External Tube *Presenter: Jaime Avendano, UTEP*		
4:05 PM - 4:25 PM	The Effect of Surface Roughness on LCH4 Convection Through Traditionally and Additively *Presenter: Raul Palacios, UTEP*		

ENERGY II (CONT.)	*Moderator: Md Mahamudur Rahman, UTEP*	Salon H
4:25 PM - 4:45 PM	Thermophysical Analysis of Material Extrusion 3D Printing Material *Presenter: Kazi Md Masum Billah, UTEP*	
4:45 PM - 5:05 PM	Application of Multiwavelength Pyrometer in Accurate Surface Temperature Measurement in Additive *Presenter: Md Moinuddin Shuvo, UTEP*	
5:05 PM - 5:25 PM	High-Temperature Environments for Thermoplastics Hybrid Manufacturing *Presenter: Leonardo I Gutierrez Sierra, UTEP*	
5:25 PM - 5:45 PM	Mechanically Activated Self-Propagating High Temperature Synthesis *Presenter: Luis Calvo, Victor Avalos, & Luis Gandara, UTEP*	
ENERGY III	*Moderator: Methaq S. Abed, UTEP*	Salon I
3:45 PM - 4:05 PM	An Alternative Method for Interpolating and Extrapolating Strain Predictions Using the Theta *Presenter: Jimmy Perez, UTEP*	
4:05 PM - 4:25 PM	Metamodeling of Minimum Creep Strain Rate Models with Temperature Dependence *Presenter: Ricardo Vega, UTEP*	
4:25 PM - 4:45 PM	Modified Wilshire Model for Long-Term Creep Deformation *Presenter: Jaime Cano, UTEP*	
4:45 PM - 5:05 PM	Probabilistic Evaluation of 304 Stainless Steel Using Sine Hyperbolic Creep-Damage Model *Presenter: Md Abir Hossain, UTEP*	
5:05 PM - 5:25 PM	Application of High Temperature Digital Image Correlation and Scanning Electron Microscopy to *Presenter: Jacob Pellicotte & Robert Mach, UTEP*	
5:25 PM - 5:45 PM	N-type Silicon Solar Cells Doped with Boron and Phosphorus *Presenter: Juan Jaramillo, UTEP*	
ENERGY IV	*Moderator: Hossein Mallahzadeh, UTEP*	Salon J
3:45 PM - 4:05 PM	Design of a Pressurized Oxy-Coal Combustor *Presenter: Mehrin Chowdhury, UTEP*	
4:05 PM - 4:25 PM	Characterization of a Pintle Injection for Gas-Slurry Combustion *Presenter: Ana Rios, UTEP*	
4:25 PM - 4:45 PM	Thermal and Structural Analysis of a Cylindrical High Pressure Oxy-Coal Combustor *Presenter: Md Mohieminul Islam Khan, UTEP*	
4:45 PM - 5:05 PM	Investigation of Flame Evolution of Turbulent Premixed Methane-Air Combustion at Different Flow- *Presenter: Md Amzad Hossain, UTEP*	
5:05 PM - 5:25 PM	Design and Experimental Demonstration of an Additively Manufactured Injector *Presenter: Md Nawshad Arslan Islam, UTEP*	
5:25 PM - 5:45 PM	Summary Energy Outreach Effort at UTEP for K-12 Students *Presenter: Daniela Morales, UTEP*	

5:45 PM - 7:00 PM — Junior Ballroom

DINNER & CLOSING REMARKS

Ahsan Choudhuri Associate Vice President for Strategic Initiatives
The University of Texas at El Paso

A BIO-INSPIRED GUIDANCE METHOD FOR A SOFT LANDING ON ASTEROIDS

R. Valenzuela Najera*1, A. Flores-Abad 1, L. Everett 1, A. G. Ortega 1, A. Choudhuri 1
1 University of Texas at El Paso
Mechanical Engineering Department, El Paso, TX 79968, USA;

Achieving a soft landing over the surface of small celestial bodies is an essential maneuver in space to advance the status of space exploration, sample collecting and in-situ resource utilization, among other on-orbit tasks. Landing on these bodies is challenging due to the reduced-gravity and airless environment. The correct planning of execution of the trajectory to land on the surface of the body is of cumbersome importance to prevent the vehicle from bouncing up and eventually reach escape velocity. In this paper, a bio-inspired trajectory planning method to land on the surface of a Near Earth Asteroid (NEA) with zero relative velocity is proposed. The method is based on Tau theory, which has been demonstrated to explain the way that humans and some other animals' approach to different target spots to perform tasks such as landing and grasping. We have selected the NEA Apophis asteroid as case study due to its accessibility, small rotational velocity and large period of rotation. Two landing scenarios are studied; one considers the case where the satellite is hovering at a low altitude; the other corresponds to a landing maneuver right after a deorbiting or breaking phase, which will cause residual velocity in the vehicle mainly in the vertical direction. The simulation results show that the introduced approach can achieve zero final relative velocity in both cases for different initial condition, which is a requirement for a soft landing; besides, different kinematic behaviors can be obtained by modifying the single variable, the Tau constant. The particular advantages of the method with respect to a commonly used approach are devised and analyzed as well.

1. Introduction

Small celestial bodies such as asteroids and comets are of growing attention because they can provide insights of the formation and evolution of the solar system. From the numerous small bodies in outer space, Near Earth Objects (NEO) are of particular interest due to their accessibility and Earth collision threat. Besides, NEO might poses material resources that can help to maintain space exploration sustainable. Landing on NEO to further obtain a sample is a challenging task mainly because of the airless and reduced-gravity environment, which may cause uncontrolled bounce if the trajectory is not properly planned. Many missions from the different space agencies have been launched to land in asteroids and comments, For example, NASA's Shoemaker [1], JAXA's Hayabusa [2-3] and Hayabusa2 [4], and ESA's Rosetta [5]. However, despite of the fact that Minerva and Philae [6], the corresponding lander modules of the missions, touched the surface of the celestial bodies, a firm and stable landing was not achieved due to different factors. More recently Hayabusa2 spacecraft has been sent to its journey to the Near Earth Asteroid Ryugu. Hayabusa2 also features a lander package termed MASCOT. It is planned that, upon arrival at asteroid Ryugu, MASCOT will be released in free fall from the main spacecraft. With the objective of successfully landing on a small celestial body, the trajectory to follow must be planned properly [7]. To advance towards the correct development of this challenging tasks, the community has introduced different methods to guide a spacecraft to achieve a soft landing. In [7-9], the authors proposed autonomous guidance methods where the landing process was transformed into the trajectory tracking of a curve given by a cubic polynomial. Some optimal trajectories have also been proposed to reduce fuel for example [10-11]. Advance closed-loop techniques such as sliding modes [12],[13], fuzzy logic [14] and predictive control [15] among others.

The guidance phase in most of the previous works is based on a splines defined by polynomials. However, polynomials have some drawbacks that may cause landing problems when used to guide of spacecraft for landing purposes. For example, a small deviation and/or uncertainty on the initial conditions of the maneuver will result in an erroneous calculation of the polynomial parameters and as a result the landing position may not be exactly reach or the desired final velocity can be also deviated.

In this work, we analyze the use of a bio-inspired method based on Tau-theory [16], which explains the way that humans and some animals guide their extremities to reach a specific spot. Because humans and animals have improved their capabilities through the natural selection process, this approach is worthy of being studied to devise its

applicability in the trajectory planning of a spacecraft landing on an asteroid. In Tau theory, it is explained that an animal or human naturally approach an object by closing gaps, these can be for example distance and orientation gaps. Since the gaps can all be close at the same time, the terminal conditions of the trajectory can be achieved, including zero or small relative velocity if desired. One advantage of the method is that with a single coupling constant, the kinematic properties of the trajectory can be modified to obtain different performances. To validate the approach, a simulation in 3D space will be created to recreate a landing trajectory on Apophis asteroid, which was selected due to its accessibility, diameter, large rotational period and small orbit condition code. It is expected that the simulation results will reveal the advantages of the method. The content of this work distributed as follows. Section 2 of this paper describes a rigid body kinematic analysis for the spacecraft that intends to perform a descent maneuver respect to the asteroid to obtain the motion equations. Section 3 shows the planning of the landing field using the cubic polynomial technique and the strategies of the Tau theory in the cases of orbiting and hovering. section 4 based on the results obtained in the previous section, shows us the results and simulation of trajectories using the strategies mentioned above. A comparative analysis between Cubic Polynomial and Tau theory trajectory generators is shown in order to observe advantages from one to the other.

2. Problem Statement

Consider a spacecraft in orbit or floating above an asteroid at some given initial moment. A descent maneuver is required and will be performed at a specific time, and the spacecraft begins to descend. In order to describe the kinematics and dynamics of the space vehicle, the reference frames depicted in Fig. 1 are defined. Assume that the origin of the coordinate system $O_l - X_l Y_l Z_l$ is at the selected landing site and that the $Z_l -$ axis matches the vector l with origin from the asteroid mass center to the landing point, $X_l -$ axis and $Y_l -$ axis perpendicular with $Z_l -$ axis satisfies a right-handed coordinate system. Furthermore, let the $O_a - X_a Y_a Z_a$ coordinate system origin be fixed with the asteroid mass center.

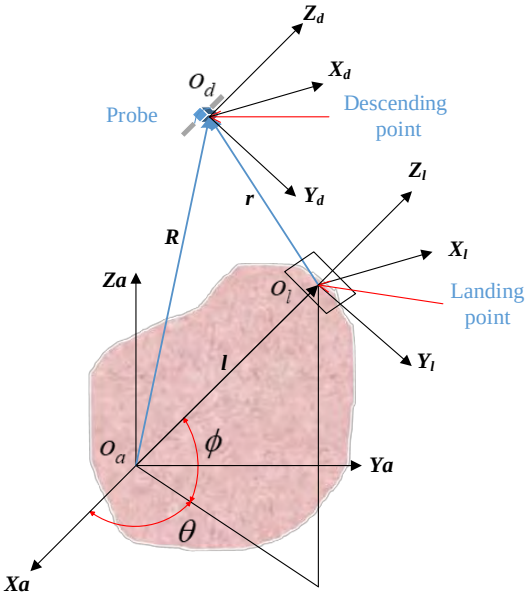

Fig. 1 Coordinate system definition in a reference frame.

2.1 Dynamic Model

A dynamic model [8] for the coordinate spacecraft can be represented by obtaining the landing dynamic equation in asteroid center inertial coordinate system, by:

$$\frac{d^2\mathbf{R}}{dt} = \mathbf{F} + \mathbf{U} + \boldsymbol{\delta} \tag{1}$$

where:

- **R** is the position vector from the target asteroid mass center to the spacecraft,

- **F** is control acceleration,
- **U** is the target asteroid gravity potential.
- **δ** is the disturbance caused by solar radiation

To obtain the dynamic equation with respect the landing site coordinate system, relative differentiation is required as:

$$\frac{d\mathbf{R}}{dt} = \dot{\mathbf{R}} + \boldsymbol{\omega} \times \mathbf{R} \tag{2}$$

$$\frac{d^2\mathbf{R}}{dt} = \ddot{\mathbf{R}} + 2\boldsymbol{\omega} \times \dot{\mathbf{R}} + \dot{\boldsymbol{\omega}} \times \mathbf{R} + \boldsymbol{\omega} \times (\boldsymbol{\omega} \times \boldsymbol{R}) \tag{3}$$

then:

$$\ddot{\mathbf{R}} = \mathbf{F} + \mathbf{U} + \boldsymbol{\delta} - 2\boldsymbol{\omega} \times \dot{\mathbf{R}} + \dot{\boldsymbol{\omega}} \times \mathbf{R} + \boldsymbol{\omega} \times (\boldsymbol{\omega} \times \mathbf{R}) \tag{4}$$

where $\boldsymbol{\omega}$ is the revolution angular velocity vector of the landing site coordinate system $O_l - X_l Y_l Z_l$ relative to the asteroid center inertial coordinate system.

If the spin axis of the target asteroid Z_l is coincident with the asteroid's maximum inertia axis l and the target asteroid rotates uniformly with the constant rate of revolution $\boldsymbol{\omega_a}$. we can simplify the equation letting,

$$\dot{\boldsymbol{\omega}} = 0 \tag{5}$$

the landing dynamic equation in vector format is obtained by:

$$\ddot{\mathbf{R}} = \mathbf{F} + \mathbf{U} + \boldsymbol{\delta} - 2\boldsymbol{\omega} \times \dot{\mathbf{R}} - \boldsymbol{\omega} \times (\boldsymbol{\omega} \times \mathbf{R}) \tag{6}$$

All vectors in Eq. (6) are projected to the three axes of landing site coordinate system (Σ^l), then, the scalar format of spacecraft motion equation in (Σ^l) can be obtained

$$\begin{bmatrix} \ddot{x} - 2\boldsymbol{\omega_a} \sin\phi\, \dot{y} - \boldsymbol{\omega}_a^2 \sin^2\phi\, x - \boldsymbol{\omega}_a^2 \sin\phi\, z \\ \ddot{y} + 2\boldsymbol{\omega_a} \sin\phi\, \dot{x} + 2\boldsymbol{\omega}_a \cos\phi\, \dot{z} - \boldsymbol{\omega}_a^2 y \\ \ddot{z} - 2\boldsymbol{\omega_a} \cos\phi\, \dot{y} - \boldsymbol{\omega}_a^2 \sin\phi \cos\phi\, x - \boldsymbol{\omega}_a^2 \cos^2\phi z \end{bmatrix} = \begin{bmatrix} U_x + F_x + \delta_x \\ U_y + F_y + \delta_y \\ U_z + F_z + \delta_z \end{bmatrix} \tag{7}$$

where:
- x, y, z are the three components of the spacecraft position vector
- U_x, U_y, U_z are the components of the gradient of gravitational potential and
- F_x, F_y, F_z are the components of the control accelerations.
- $\delta_x = \delta_y = \delta_z = \delta$ are the disturbances caused by solar radiation

Equation (7) can be simplified and expressed as follows:

$$\begin{bmatrix} \ddot{x} \\ \ddot{y} \\ \ddot{z} \end{bmatrix} = \begin{bmatrix} b_1\dot{y} + b_3 x + b_4 z + U_x + F_x + \delta \\ -b_1\dot{x} - b_2\dot{z} + \boldsymbol{\omega}_a^2 y + U_y + F_y + \delta \\ b_2\dot{y} + b_5 x + b_6 z + U_z + F_z + \delta \end{bmatrix} \tag{8}$$

where:

$$\begin{aligned} b_1 &= 2\boldsymbol{\omega_a} \sin\phi, \\ b_2 &= 2\boldsymbol{\omega}_a \cos\phi, \\ b_3 &= \boldsymbol{\omega}_a^2 \sin^2\phi, \\ b_4 &= \boldsymbol{\omega}_a^2 \sin\phi, \\ b_5 &= \boldsymbol{\omega}_a^2 \sin\phi \cos\phi, \end{aligned}$$

$$b_6 = \boldsymbol{\omega}_a^2 \cos^2 \phi \tag{9}$$

Equation (9) is linearized to a first order differential equations system to compute easier the solution, so it yields:

$$\begin{bmatrix} \dot{x}_1 \\ \dot{x}_2 \\ \dot{x}_3 \\ \dot{x}_4 \\ \dot{x}_5 \\ \dot{x}_6 \end{bmatrix} = \begin{bmatrix} x_4 \\ x_5 \\ x_6 \\ b_1 x_5 + b_3 x_1 + b_4 x_3 + U_x + F_x + \delta \\ -b_1 x_4 - b_2 x_6 + \omega_a^2 x_2 + U_y + F_y + \delta \\ b_2 x_5 + b_5 x_1 + b_6 x_3 + U_z + F_z + \delta \end{bmatrix} \tag{10}$$

3. Trajectory Planning

The trajectory to follow during landing must be planned to achieve a zero or small relative velocity between the spacecraft and the asteroid landing point. Although the main objective of this work is to present a trajectory based on the time-to-contact principle of the Tau theory, the descent planning in a cubic polynomial form is also shown with the purpose of verifying the advantages and / or disadvantages with respect to the Tau theory-based guidance

3.1 Cubic Polynomial-based Guidance

The planned landing trajectory is usually defined with a third order polynomial [7]; the cubic spline to satisfy the boundary condition is given by:

$$Z(t) = a_0 + a_1 t + a_2 t^2 + a_3 t^3 \tag{11}$$

$a_0,\ a_1,\ a_2, a_3$ are the cubic function coefficients.

The desired descent altitude and velocity is defined to satisfy the requirements of soft landing on the asteroid surface. Thus, multinomial coefficients are necessary to satisfy the initial and terminal constraints. The boundary condition is given by:

$$\begin{aligned} Z(0) &= Z_0 \\ \dot{Z}(0) &= \dot{Z}_0 \\ Z(\tau) &= Z_n \\ \dot{Z}(\tau) &= 0 \end{aligned} \tag{12}$$

where $Z(0)$ and $\dot{Z}(0)$ are the initial position and velocity at the time 0 in the descending plan trajectory, $Z(\tau)$ and $\dot{Z}(\tau)$ denotes the planned altitude and the altitude change rate at time τ

The planned descent trajectory position can be obtained by using Eq. (12):

$$Z(t) = Z_0 + \dot{Z}_0 t + \left(3Z_n - 3Z_0 - 2\dot{Z}_0\tau\right)\left({}^{t}/_{\tau}\right)^2 + \left(2Z_0 + \dot{Z}_0\tau - 3Z_n\right)\left({}^{t}/_{\tau}\right)^3 \tag{13}$$

the time derivative of Eq. (13) give us the descent velocity.

$$\dot{Z}(t) = \dot{Z}_0 + \left(6Z_n - 6Z_0 - 4\dot{Z}_0\tau\right){}^{t}/_{\tau^2} + \left(6Z_0 + 3\dot{Z}_0\tau - 6Z_n\right)\left({}^{t^2}/_{\tau^3}\right) \tag{14}$$

similarly, the acceleration descent equation can be obtained from Eq. (14)

$$\ddot{Z}(t) = \left(6Z_n - 6Z_0 - 4\dot{Z}_0\tau\right)/\tau^2 + (12Z_0 + 6\dot{Z}_0\tau - 12Z_n)\left({}^{t}/_{\tau^3}\right) \tag{15}$$

Now to plan the desired trajectory we assume an altitude position $Z_0 = 1450\text{m},\ Z_n = 0\ ,\ t = 0{:}1200\ \text{s},$ and $\tau = 1200$ s, we want to prove Eqns. $(13 - 14)$ at different velocity-values shown in Table 1.

Table 1 Velocity-values vz for descending trajectory

Velocity	vz1	vz2	vz3	vz4	vz5	vz6
Descending (m/s)	3	1	-1	-3	-4	-6

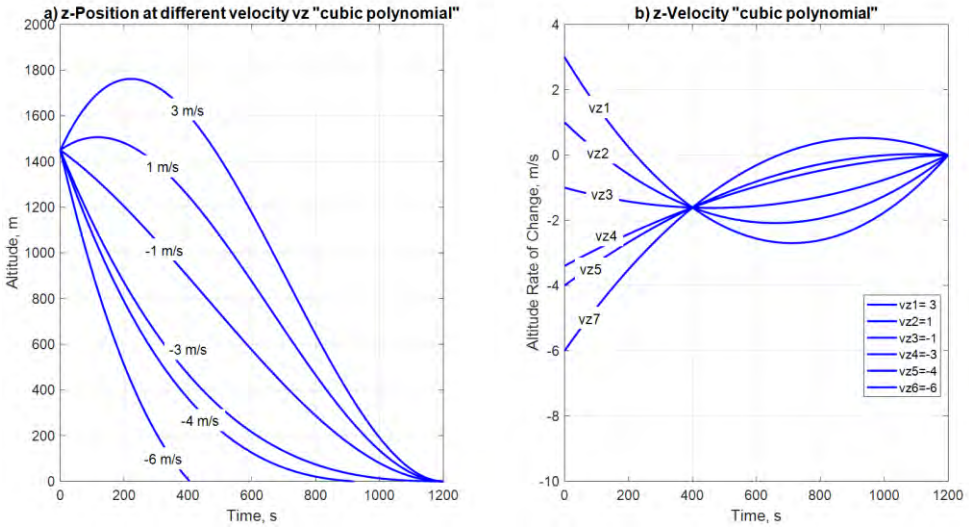

Fig. 2 Descending trajectories a) altitude and b) velocity time history at different vz values.

From Figure 2a and 2b it is clearly seen that the initial velocity of descent of the coordinate altitude *z* should be in accordance with the relation -1 <vz0 <8 to achieve a guided landing to the desired target, more specific -6<vz0<-3 for more precision.

3.2 Guidance Tau Theory-based

Tau theory generalized by Lee [16] was developed from the work on J.J. Gibson [17] and deals with the guidance of body movements of both, humans and animals. In the field of Biology and Psychology, the Tau theory explains how animals control their motion using visual feedback for different tasks including landing and perching. Tau theory is based on a concept called time-to-contact [18], which is the required time to reach an object if the current velocity is maintained. In 1998 Tau theory was extended by Lee introducing coupling-tau [19] which explain the movement synchronization closing gaps by means of the variable tau (τ). Some applications of the tau theory in motion control have been developed in control robots' motion [20] and for similar tasks such as perching, docking, braking, or landing in unmanned aircraft systems [21 – 24]. This work proposes the use of extended Tau theory to generate a trajectory for soft landing on an asteroid.

3.2.1 General Tau Theory

Since general Tau theory attempts to encompass perceptual and movements systems it is based on fundamental principles to guide movement [19].

1. The main task in guiding intentional motion is to control the closure of spatial and/or force gaps between effectors (or sensory organs) and their goals.
2. This requires sensing the closures of gaps in sensory inputs arrays, for example optical (vision), acoustic (echolocating bats), force (haptics), electrical (electrolocation fish), and electromagnetic (infrared detection by snakes)
3. The tau (τ) of each spatial and/or force gap (the time-to-closure of the gap at its current closure rate) basically what is sensed and controlled constantly to guide the movement".
4. A principal method of movement guidance is by coupling the taus of different action-gaps, that is keeping the taus in constant ratio during a movement.

The general requirement of our work to achieve the landing maneuver is to reach the target point O_l with zero velocity and zero acceleration in the contact from a specific approach O_d at a specific time t. To satisfy this requirement it is proposed to close three gaps that can be defined in the motion frame $O_d - X_d, Y_d, Z_d$ to the point $O_l - X_l, Y_l, Z_l$ as shown in Figure 1. The main movement should be performed in direction of *Z*, that is, we denote (τ_x, τ_y, τ_z) the taus corresponding to the gaps (Z_x, Z_y, Z_z), respectively.

The closure of action-gaps which is the separation between the animal's current motion and the goal state to be achieved by action. In this way, all movements are made to close an action gap. Tau (τ) of an action gap is the first order time to closure of the action gap at a specific rate and can be expressed as :

$$\tau(t) = \frac{z(t)}{\dot{z}(t)} \tag{16}$$

where $z(t)$ is the motion gap at time t and $\dot{z}(t)$ is the derivative of the motion gap respect the time.

It is important to note that our landing trajectory could be generated after having performed a hovering maneuver [25]. In the hovering a spacecraft kept its relative position with respect the asteroid through the frequent application of impulse force. Usually there are two types of hovering motion control: near-inertial hovering, where the spacecraft remains in a fixed location to the asteroid reference frame; and a body-fixed frame, where the spacecraft is rotating with the asteroid in the inertial space [26].

3.2.2 Case 1. Initial State: Right After Deorbiting (Non-zero initial velocity)

Assume that the spacecraft has reached a descent position after having been orbiting the asteroid and is ready to descend. In this case, it is possible to generate a descending trajectory starting from its position in the coordinate system *X, Y, Z* and its not zero initial velocity in the same coordinate axes and ending the target point with zero final velocity using Tau theory by controlling the closure of action gaps. Lee [23] explains that the theory applies to approach along any dimension and that the only information necessary for an animal to control a descent action is the tau time rate [16], which is given by the constant tau-dot:

$$\dot{\tau}(t) = k \tag{17}$$

where *k* is a constant used by tau to ensure the closing of gaps and achieve stop the motion descent without collision at the target point. The *k* values should remain within the range of $0 < k < 0.5$ Any other value outside this range causes that the landing point is not reached or that it reaches the objective point at an uncontrolled speed generating a collision on the target.

The constant tau-dot [18] guidance law states that braking with contact zero velocity can be controlled by monitoring the $\dot{\tau}(t)$ value and adjusting the deceleration so that $\dot{\tau}(t)$ remains constant, positive and less than 0.5. Another important tau-guidance law to consider is given by:

$$\tau(t) = kt + \tau_0 \tag{18}$$

where $t = 0$ and τ_0 correspond to the time and tau, respectively, when the tau-action is initiated, which in turn is defined by:

$$\tau_0 = \frac{z_0}{\dot{z}_0} \tag{19}$$

where, z_0 and $\dot{z}_0$ are the initial position and velocity of the spacecraft. Combining Eqns. (16), (18) and (19), we can solve it for $z(t), \dot{z}(t)$ and $\ddot{z}(t)$ to obtain the motion equations.

$$z(t) = z_0 \left(1 + kt \frac{\dot{z}_0}{z_0}\right)^{\frac{1}{k}} \tag{20}$$

$$\dot{z}(t) = \dot{z}_0 \left(1 + kt \frac{\dot{z}_0}{z_0}\right)^{\frac{1-k}{k}} \tag{21}$$

$$\ddot{z}(t) = \frac{\dot{z}_0^2}{z_0}(1-k)\left(1 + kt\frac{\dot{z}_0}{z_0}\right)^{\frac{1-2k}{k}} \tag{22}$$

From the above equations: *"Tau Action Gap"*, which describe the movement of an animal moving with an initial velocity until reaching a target with a zero speed in one direction and , $\dot{z}, and\ \ddot{z}$ will become zero at the same finite time. Considering $z_0 = 5{,}500$ m , $\dot{z}_0 = -5.6$ m/s and $t = 2500$ s, the position, velocity and acceleration of an action gap were calculated at different values of *k* using Eqns. $(20-22)$ are as shown in Figure 3 as well as shows the behavior of the a) position, b) speed and c) acceleration and time history at different values of k, from which it can be deduced that a suitable value for our trajectory planning is found at 0 < k < 0.5

Since our trajectory design needs to be performed with movement in the reference frame *X*, *Y*, *Z*, it is necessary to expand the closing of action gaps in the three coordinate axes. To achieve a three-dimensional trajectory, it is imperative to use the tau-coupling strategy, which establishes that multiple gaps such as controlling the direction and speed of approach need to be closed simultaneously synchronizing the closure of an angular space and a space of distance. A way to guide the movements and the closing of gaps is by tau-coupling $\tau_x, \tau_y,$ and τ_z using the tau-coupling during the movement, that is:

$$\tau_x = k_{x,z}\tau_z \tag{23}$$
$$\tau_y = k_{y,z}\tau_z \tag{24}$$

where k_{xz} and k_{yz} and are constants that regulates the kinematics of closure of gap x and y respectively. It can be shown if the values of k_{xz} and k_{yz} are selected between values from 0 to 0.5, then the variables $(x, \dot{x}, \ddot{x}), (y, \dot{y}, \ddot{y})$ and $(\mathrm{z}; \dot{z}, \ddot{z})$ becomes zero at the same time. This condition was presented by Lee [19] in which he mathematically tests the synchronization of the guided movements, that is:

$$x = Az^{1/k_{x,z}} \tag{25}$$

$$\dot{x} = \frac{A}{k_{x,z}} z^{\frac{1}{k_{x,z}}-1}\dot{z} \tag{26}$$

$$\ddot{x} = \frac{A}{k_{x,z}} z^{\frac{1}{k_{x,z}}-2}\left(\frac{1-k_{x,z}}{k_{x,z}}\dot{z}^2 + z\ddot{z}\right) \tag{27}$$

$$A = x_0/z_0^{1/k_{x,z}} \tag{28}$$

Because the main movements are of descent and these are given in the Z axis and we want to synchronize them with X and Y, similarly, the same criterion is applied to determine the position, speed and acceleration in the Y axis

$$y = Bz^{1/k_{y,z}} \tag{29}$$
$$\dot{y} = \frac{B}{k_{y,z}} z^{\frac{1}{k_{y,z}}-1}\dot{z} \tag{30}$$

$$\ddot{y} = \frac{B}{k_{y,z}} z^{\frac{1}{k_{y,z}}-2}\left(\frac{1-k_{y,z}}{k_{y,z}}\dot{z}^2 + z\ddot{z}\right) \tag{31}$$

$$B = z_0/y_0^{1/k_{y,z}} \tag{32}$$

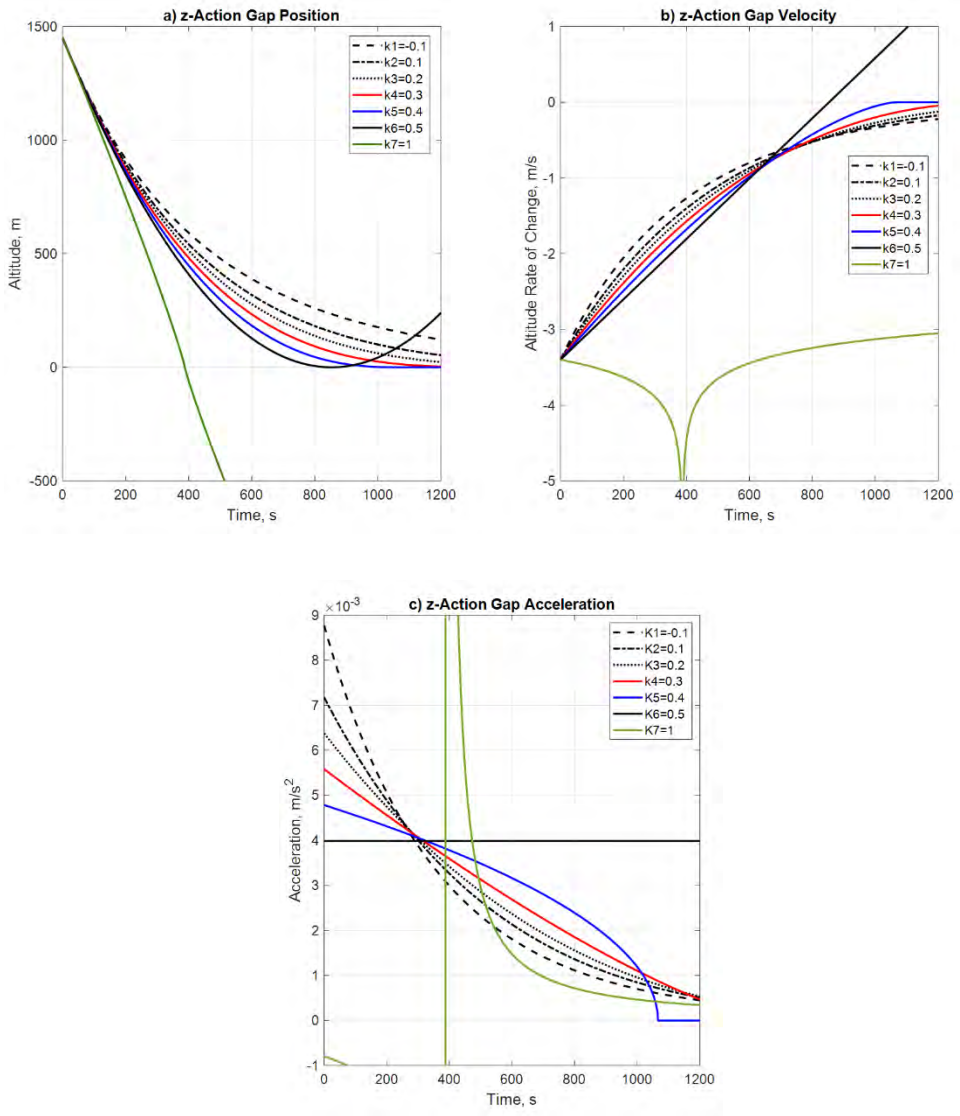

Fig. 3 Tau Action-Gap, a)Position, b)Velocity, c)Acceleration at different *k* values

3.2.3 Case 2. Initial State: Hovering

The Tau theory [19] states that there is more to guidance of movement than the extrinsic variables allow (Tau-Coupling). This becomes when we consider the problems of timing arrival at a goal and controlling the force and momentum at arrival. In the case of landing from near-inertial hovering position, the movement starts at rest, that is from zero initial velocity, accelerates and then slows down until the end of the movement reaching the position again at zero-speed and zero-acceleration. The movements are intrinsically guided by Tau coupling the gap $z(t)$ and the intrinsically guiding gaps are represented by:

$$\tau_z(t) = k_{z,g}\tau_g(t) \tag{33}$$

where $k_{z,g}$ is a positive constant value that determines the kinematics of the body in movement and $\tau_g(t)$ is a function of time that specifies the time of the gap to be closed under acceleration conditions, which can be derived from the dynamic's equation of free-fall motion under gravity acceleration g:

$$z_g(t) = \frac{1}{2} g t_g^2 - \frac{1}{2} g t^2 \tag{34}$$

$$\dot{z}_g(t) = -gt \tag{35}$$

Lee proposed the following $\tau_g(t)$ function [19]

$$\tau_g(t) = \frac{z_g(t)}{\dot{z}_g(t)} = \frac{1}{2}\left(t - \frac{t_g^2}{t}\right) \tag{36}$$

where t_g is the total duration time of the maneuver and t runs from 0 to t_g. The tau intrinsic guided law for closing gaps in a specified time t_g for a landing maneuver starting from a stationary state (i.e., $\dot{Z}(0) = 0$) is given by:

$$\tau_z(t) = k_{z,g} \frac{1}{2}\left(t - \frac{t_g^2}{t}\right) \tag{37}$$

By using Eqn. (37) and substituting in Eqns. (18) and (19) we obtain the first order differential equation:

$$\dot{z}(t) + \frac{-1}{k_{z,g} \frac{1}{2}\left(t - \frac{t_g^2}{t}\right)} z(t) = 0 \tag{38}$$

for which the solution is:

$$z(t) = \frac{z_0}{t_g^{2/k_{z,g}}} \left(t_g^2 - t^2\right)^{\frac{1}{k_{z,g}}} \tag{39}$$

$$\dot{z}(t) = \frac{-2 z_0 t}{k_{z,g} t_g^{2/k_{z,g}}} \left(t_g^2 - t^2\right)^{\frac{1}{k_{z,g}} - 1} \tag{40}$$

$$\ddot{z}(t) = \frac{2 z_0}{k_{z,g} t_g^{2/k_{z,g}}} \left(\frac{2t^2}{k_{z,g}} - t^2 - t_g^2\right) \left(t_g^2 - t^2\right)^{\frac{1}{k_{z,g}} - 2} \tag{41}$$

Equations $(39 - 41)$ represents the position, velocity and acceleration $(z, \dot{z}, \ddot{z})$ respectively for the guided motion closing intrinsic gap. Figure 4 shows $z(t), \dot{z}(t), \ddot{z}(t)$ time history at different k values

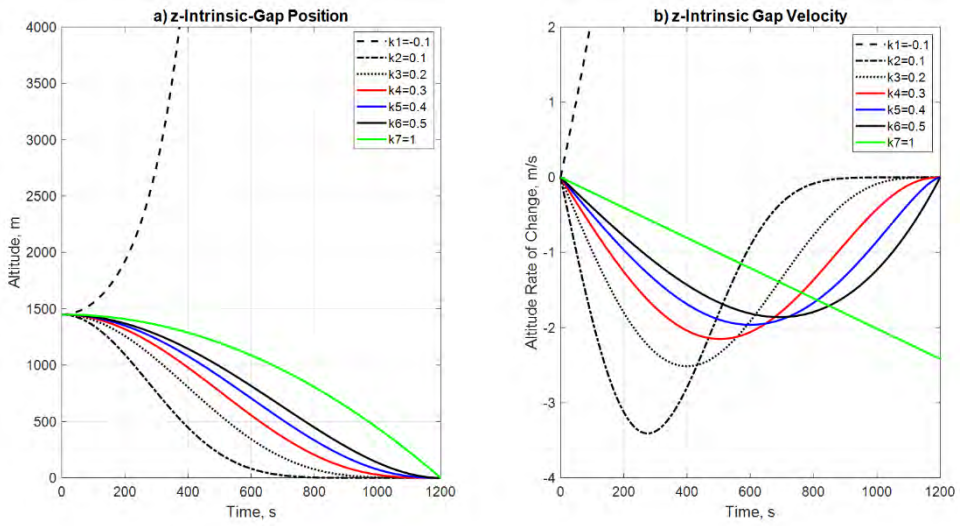

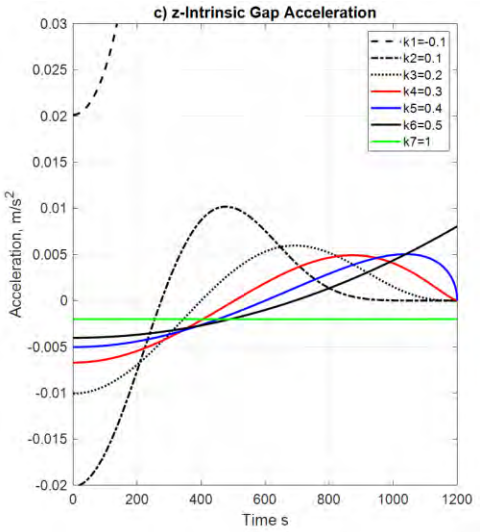

Fig. 4 Intrinsic Tau-Guidance a)Position, b)Velocity, c)Acceleration at different *k values*

For the intrinsic tau strategy, Figure 4 shows us again that the values for the constant k that satisfy the condition $x = 0, \dot{x} = 0, \ddot{x} = 0$ at the same time are included in the interval $0 < k < 0.5$.

More detail about the trend time history and final status after closing an action gap using different values of K in the equations of movement for the strategy tau action gap, tau coupling, and intrinsic tau are shown in the work done by Zhen Zhang [21].

4 Optimal k values.

The numerical values that the constant *k* can take for each of the cases of landing movement 1 and 2 can be extracted from Table 2, in which a list of data obtained from analysis of the consequences of the movement at different *k* values is shown for each of the movement strategies of the Tau theory [21].

Table 2 Motion final status for different *k*-values

Tau Action-Gap		***Coupling-Tau***		***Intrinsic-Tau***	
k value	***Final status***	***k value***	***Final status***	***k value***	***Final status***
$k < 0$	*Gap not close*	$k_{zx} < 0$	*Gap x not close*	$k_{zg} < 0$	*Gap not close*
$k = 0$	*Gap not close*	$k_{zx} = 0$	*Nonsense*	$k_{zg} = 0$	*Nonsense*
$0 < k < 0.5$	*Achieve goal*	$0 < k_{zx} \leq 0.5$	*Achieve goal*	$0 < k_{zg} < 0.5$	*Achieve goal*
$k = 0.5$	*Slight collision*	$0.5 < k_{zx} < 1$	*Collision*	$0.5 < k_{zg} < 1$	*Slight collision*
$0.5 < k < 1$	*Slight collision*	$k_{zx} = 1$	*Achieve gol*	$k_{zg} = 1$	*Achieve Goal*
$k = 1$	*Strong collision*	$k_{zx} > 1$	*Strong collision*	$k_{zg} > 1$	*Strong collision*
$k > 1$	*Strong collision*				

However, a more accurate approximation of the ideal value of the constant *k* can be obtained by optimal determination techniques under restrictions defined by the initial conditions of position and speed for the touchdown trajectory,

The optimal value of the constant *k* can be calculated by solving a nonlinear constrained optimization problem approach where an objective function and the inequality and equality constraints are required in the form of: $min\ f(x)\ such\ that\ c(x) \leq 0, ceq(x) = 0$ for which the problem can be solved by using the function `fmincon` of MATLAB

For case 1 (Initial velocity different zero), the Figure 3a shows that the shape of the curves described by the trajectories takes the form of a simple arc, for this reason the objective function is defined by the equation of arc length Eqn. (42):

$$L = \int_a^b \sqrt{1 + [f'(t)]^2}\, dt \tag{42}$$

and the non-linear equality constraints are defined by Eqn. (20), in such a way that the problem defined as:

$$min \quad f = 600 + (876.042 - 876.042 * (1 - 2.73103 * k_z)\text{^}(2/k_z) - 2392.5 * k_z)/((-2 + k_z) * (-0.366162 + k_z))$$

subject to:

$$ceq = 1450 * (1 + k_z * 1200 * (-3.3/622))\text{^}(1/k_z)$$

and

$$c = 0$$

The above problem solves the optimal value of the constant $k_z = 0.36616$. to initial condition given. The values for the constants k_x and k_y can be determined in the same way or select an ideal value from Table 2.

For the case 2 (initial velocity equal zero), the same methodology is applied but in this case the shape of the curves of Figure 4a have the form of an "S" so that the objective function is defined by the equation of the function "S" given by:

$$\mathrm{f(t)} = \frac{1}{1 + e^{-t}} \tag{43}$$

The search for the solution in the optimization problem is defined by:

$$\min \quad \mathrm{f} = 1/(1 + \exp(29 * 2\text{^}((-8 + k_{zg})/k_{zg}) * 25\text{^}((-2 + k_{zg})/k_{zg}) * (160000 - 1200\text{^}2/9)\text{^}(1/k_{zg})));$$

subject to:

$$ceq = ((1450/(1200\text{^}(2/k_{zg}))) * (1200\text{^}2 - 1200\text{^}2)\text{^}(1/xk_{zg}))$$

and

$$c = 0$$

The value obtained for k_z, was 0.2205 equal for k_x and k_y.

5. Trajectory Generation

5.1Simulation and Results

To confirm the validation of Eqns. $(13 - 15)$ for the cubic polynomial model, Eqns. $(20 - 22)$, $(25 - 28)$, and $(29 - 32)$ for coupling-tau strategy, and Eqns. $(39 - 41)$ for intrinsic-tau strategy, initial conditions shown in Table 2 were defined based on the experimental results shown in Figures $(2 - 4)$, these were obtained by using the MATLAB software.

Table 3 Initial Conditions for the Simulation Test

a) Initial condition for Cubic Polynomial landing strategy

Coordinates	*X*	*Y*	*Z*
Initial Position m	622	850	1450
Landing Position m	231.6	86.17	211.7
Velocity m/s	-0.9	-2.4	-3.3

b) Initial conditions for Coupling-Tau strategy

Coordinates	*X*	*Y*	*Z*
Initial Position m	622	850	1450
Landing Position m	231.6	86.17	211.7
Velocity m/s	-	-	-3.3
k values	1	1	0.3661

c) Initial conditions for Intrinsic-Tau strategy

Coordinates	*X*	*Y*	*Z*
Initial Position m	622	850	1450
Landing Position m	231.6	86.17	211.7
k values	0.35	0.2	0.3

As mentioned before, the landing strategy using the cubic polynomial technique, which is widely used in the design of trajectories for space and robot maneuvers is not the main objective of our work, however the analysis of position and velocity graphs give us a reference of how the landing-position and landing-velocity trajectories could behave using Coupling-Tau and Intrinsic-Tau Strategy. As can be seen in Figure 5 a), b), respectively, the path reaches zero position and zero velocity, however, the acceleration does not reach zero, instead it increases and reduces linearly its values in the reference axes *X*, *Y* and *Z* until reaching the time τ.

A three-dimensional representation of cubic spline is shown in Figure 5 c). in which we can see how the descent trajectory in the space would be. The position and speed in the axes *X*, *Y*, *Z* depend on the initial conditions given in the reference frame, note that any change in the initial conditions can generate a different trajectory than what is being shown. The trajectory looks like a curved profile on an inclined plane going back a little from the point of descent and then correcting the trajectory towards the target point. A three-dimensional elliptic figure has been included to simulate the celestial body.

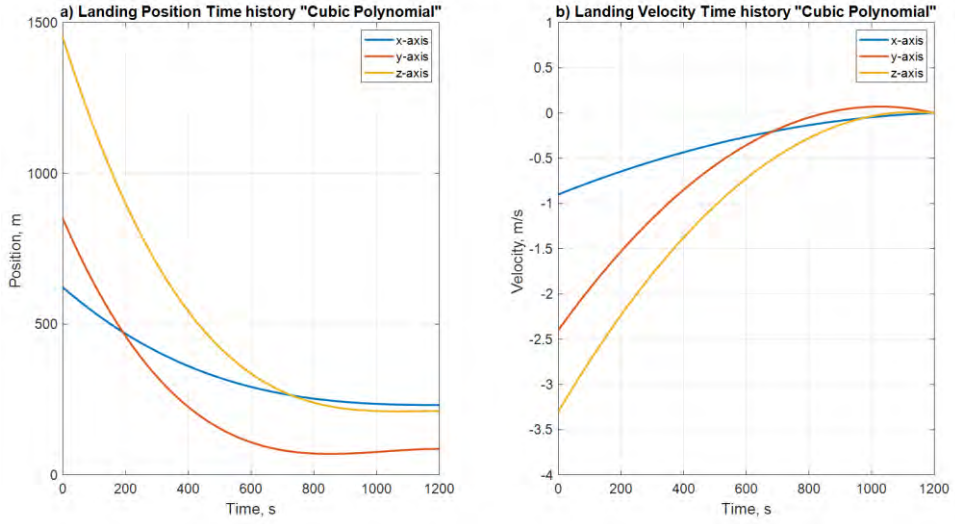

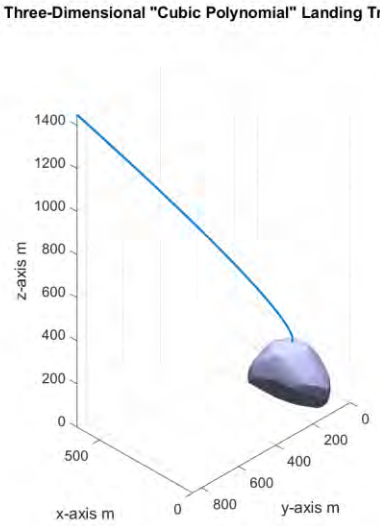

Fig. 5 Landing Time-History by using Cubic Polynomial, a)Position, b)Velocity, c)Three-Dimensional

Figure 6 show us the landing a) position, b)velocity and c) acceleration by using the coupling-tau strategy, we can see clearly how the motion of *Z*-axis is coupled with the motion of *X* and *Y*-axis to reach zero-position at zero velocity and acceleration. Different to the cubic polynomial technique the position, speed and acceleration in the *X* and *Y*- axes depend on the initial conditions of the *Z*-axis, any change in initial *Z*-position or initial *Z*-velocity or *k values* can be generated a different shape of trajectory curve. As we explain before tau-coupling landing strategy can be used in cases when the spacecraft is in a body-fixed frame position rotating with the asteroid (orbiting).

The three-dimensional representation for the landing trajectory using coupling-tau strategy is shown in Figure 6 d). In this case, notice how the edge of the trajectory curve follows a profile pattern of a plane from the initial position to the landing point. With the given *k values*, it can be seen how the coupling of the movement guided in the three axes *X*, *Y* and *Z* corrects its curvilinear movement to a straight line in vertical fall, this is due to the fact that it reached zero speed and zero acceleration since before Complete the duration time of the trajectory.

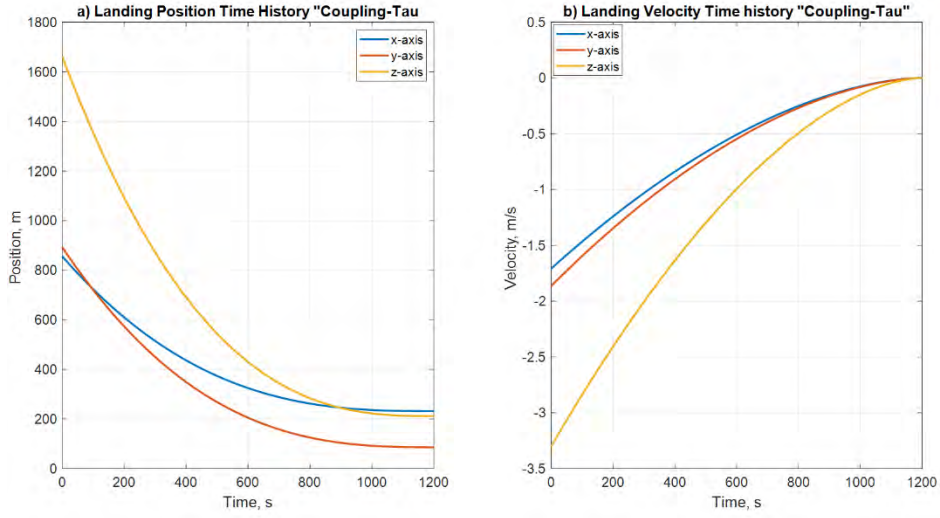

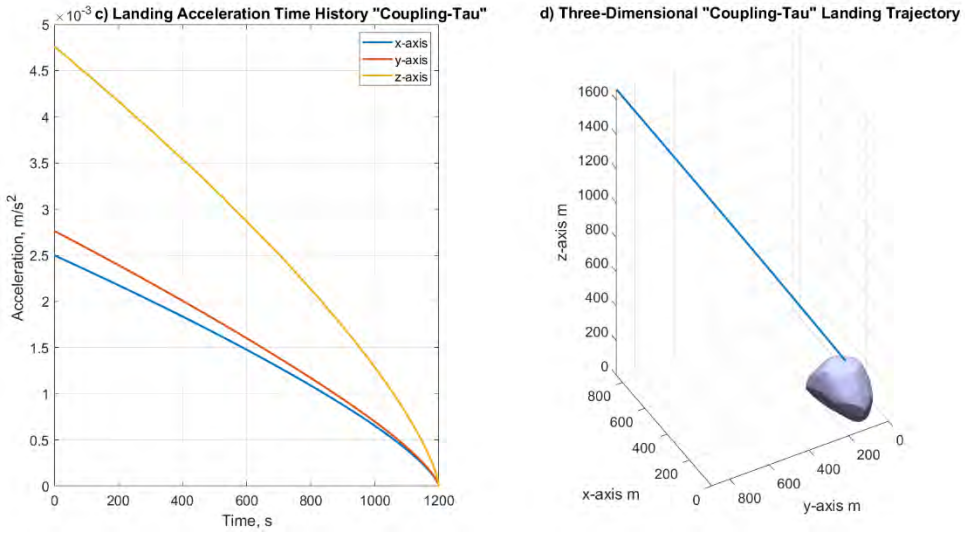

Fig. 6 Landing Time History by using Coupling - Tau, a)Position, b)Velocity, c)Acceleration, d)Three-Dimensional

In Figure 7, a trajectory design based on the intrinsic-tau strategy is shown. Unlike the coupling-tau strategy, the movements in the coordinate axes *X*, *Y* and *Z* are not coupled, remember that the intrinsic-tau strategy according to the laws of motion of the Tau theory is used in cases where the body moves from a fixed position with zero velocity towards the target point, which is the case in which our spacecraft is in near-inertial hovering position (hovering). As in the previous cases, the trajectory, a) position, b) velocity and c) acceleration time-history are shown, in which it can be observed that they reach the target point at zero-velocity and acceleration-zero at the maximum defined time.

Figure 7 d) shows the trajectory and landing in the three-dimensional space in which the curve shape can be observed as a very straight curve the point of descent towards the landing point, as in the coupling-tau strategy, the shape of the curve can be modified by adjusting the *k values* in the range from 0 to 0.5 to reduce the gaps in the guided movements, this can be very good in the sense of saving in consumption of fuel and / or energy

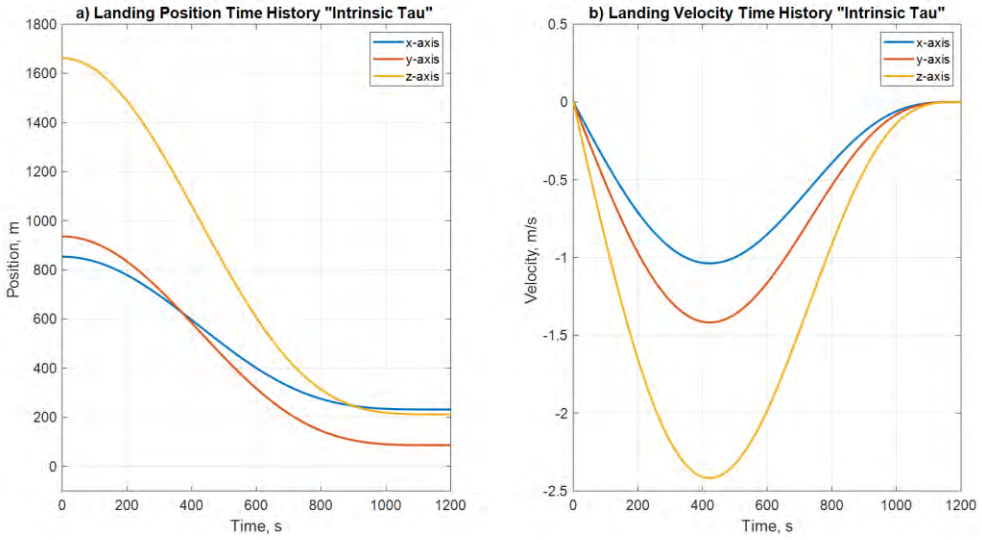

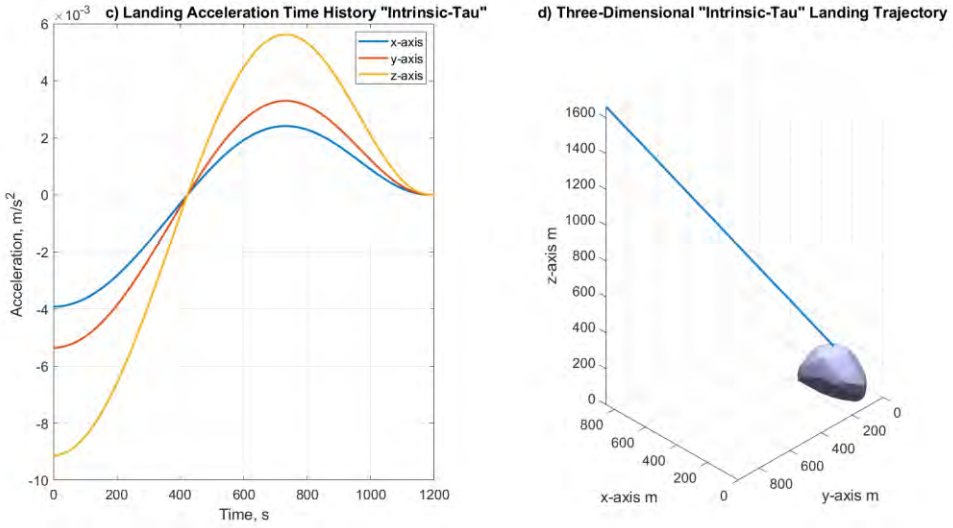

Fig. 7 Landing Time History by using Intrinsic - Tau, a)Position, b)Velocity, c)Acceleration, d)Three-Dimensional

A. Comparative Analysis.

In this section, Tau-guided trajectory is compared with a commonly-used technique such as the cubic polynomial. For this purpose, only the case of body-frame fixed position is analyzed since the way of determining differences can only be appreciated through changes in speed in the initial conditions. In the first place, taking as a reference the initial speed defined in Table 2 a), Figure 8 a) shows, that trajectory patterns at different initial velocities are shown to illustrate the effect that would cause an increment in the initial velocity, note that at speeds greater than - 8 m / s (the negative sign is only by convention for direction), the trajectory position time-history reaches the zero position from before reaching the established descent time, which would cause an imminent collision of the spacecraft against the asteroid. In Figure 8 b) it is confirmed that the trajectory reaches zero-velocity and then continues to accelerate.

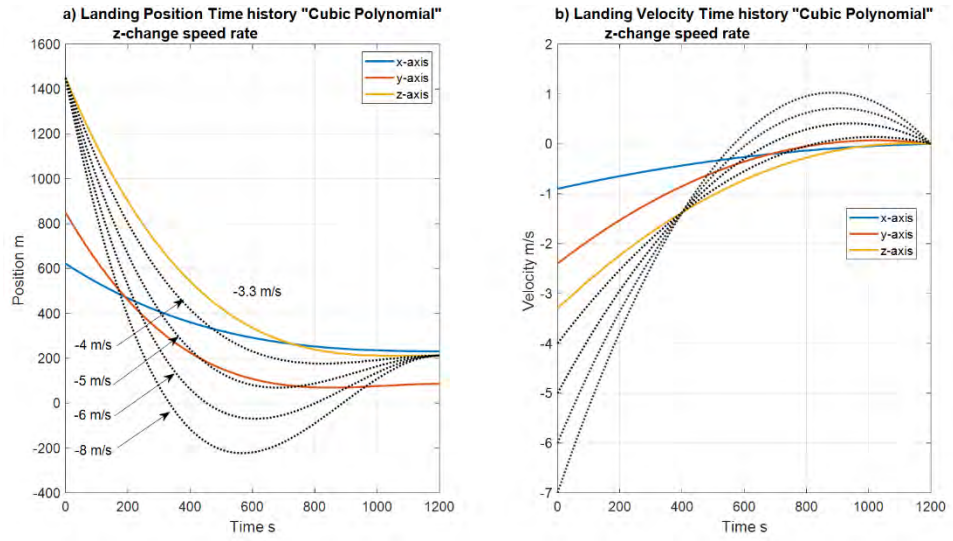

Fig. 8 Landing Position and Velocity "Cubic Polynomial" z-change speed rate

Now, the same concept of trajectory generation is applied in the *z* direction with the coupling-tau strategy. Figures 9 a) and 9 c) show that at any speed variation between -8 m / s and -10 m / s the descending trajectories in *X*, *Y* and *Z*

continue to reach zero-position at the same time. Figures 9 b) and 9 d) support the previous statement by achieving the zero-velocity synchronously, in both cases no changes or adjustments were made to the values of the constant *k*.

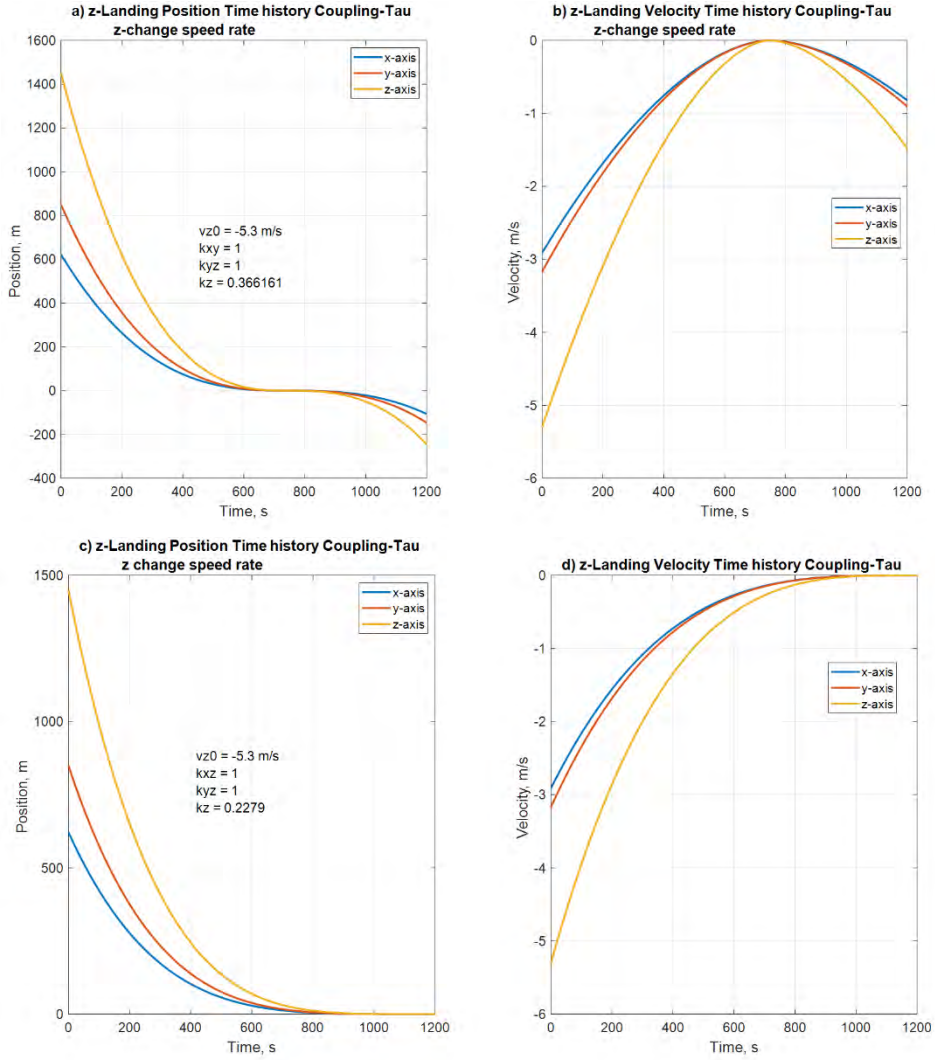

Fig. 9 Z-Landing Position and Velocity "Coupling-Tau" z-change speed rate a)position and b) velocity increase of speed from -3.3 m/s to -5.3 m/s at initial k-value, c)position and d)velocity at corrected k-value

If we continue to increase the initial velocities, we can observe that the basic principle of the Tau theory of achieving zero-position and zero-velocity at the same time is not fulfilled.

A three-dimensional representation represented in Figure 10 shows a change in the rate of speed to the initial conditions established and a), and how the trajectory can be corrected by simply modifying the value of the constant *k* b).

According to the comparison between the cubic polynomial technique and Coupling-tau for the design of the landing trajectory of a spaceship on an asteroid, we can affirm that the main advantage of the Tau-guided trajectory consists on the adaptation to different initial velocities. If the initial velocity changes, the cubic polynomial planned trajectory will lead in non-zero landing velocity, which means that a hard impact may occur and due to the reduced-gravity and airless environed, the spacecraft may bounce-up and reach scape velocity. While, the Tau-guided trajectory can achieve a soft landing even if the initial velocity changes.

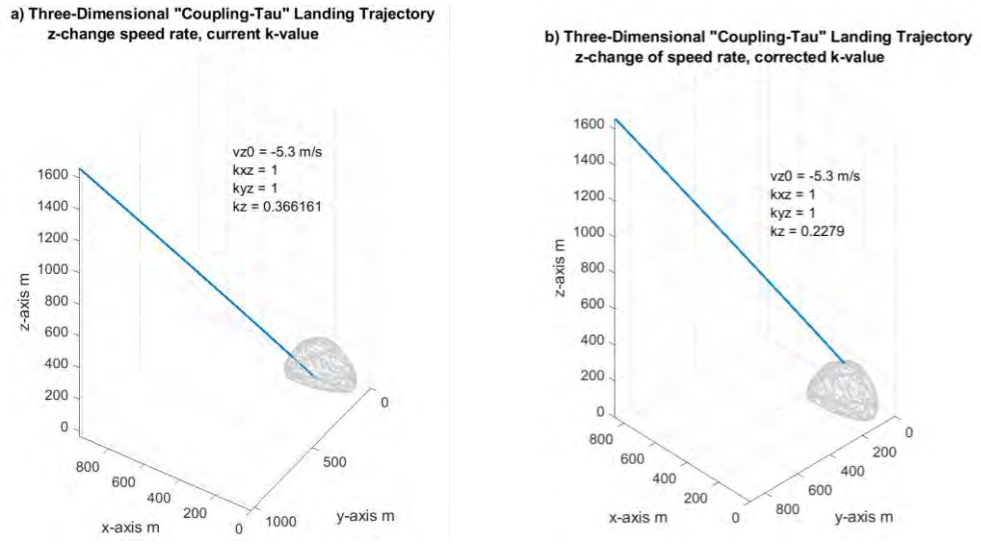

4. Conclusion

We have demonstrated the feasibility of using the Tau theory for the generation of landing maneuvers on an asteroid. Tau theory can be used to design a trajectory both from hovering and after deorbiting. It was shown that introduced approach adapts better to variations in initial velocities than the cubic polynomial case. In the near future, we will include the external disturbances causes for sun radiation and the gravitational potential.

References

[1] Veverka, J. "The landing of the NEAR-Shoemaker spacecraft on asteroid 433 Eros", *Nature*, Vol 413, [online journal], URL: https://www.nature.com/articles/35096507, [retrieved 27 September 2001].

[2] Yoshimitsu, T., Kubota, T. & Nakatani, I., "MINERVA rover which become a small artificial solar satellite", P*20th Annual AIAA/USU Conference on Small Satellites*, [online database] URL: https://digitalcommons.usu.edu/cgi/viewcontent.cgi?article=1554&context=smallsat

[3] Yano, H. "Touchdown of the Hayabusa spacecraft at the Muses Sea on Itokawa". *Science*, Vol. 312, [online journal], doi: 10.1126/science.1126164.

[4] Tsuda Y, Yoshikawa M, Saiki T, Nakazawa S, Watanabe SI. "Hayabusa2–Sample return and kinetic impact mission to near-earth asteroid Ryugu," *Acta Astronautica*. 2018.

[5] Accomazzo, A. "The final year of the Rosetta mission". *Acta Astronautica*, Vol. 136, 2017, pp. 354-359

[6] Biele, J. "The landing(s) of Philae and inferences about comet surface mechanical properties". *Science*, Vol 349, [online journal], URL: http://science.sciencemag.org/content/349/6247/aaa9816.full, [retrieved 31 Jul 2015].

[7] Huang, X., Cui, H., and Cui, P., "An Autonomous Optical Navigation and Guidance for Soft Landing on Asteroids," *Acta Astronautica*, Vol. 54, No. 10, 2004, pp. 763-771.

[8] Li, S., Cui, P., and Cui, H., "Autonomous Navigation and Guidance for Landing on Asteroids," *Aerospace Science and Technology*, Vol. 10, No. 3, 2006, pp. 239-247.

[9] Lan, Q., Li, S., Yang, J., and Guo, L., "Finite-Time Soft Landing on Asteroids Using Nonsingular Terminal Sliding Mode Control", *Transactions of the Institute of Measurement and Control*, Vol. 36, No. 2, 2014, pp. 216–223, published on line 2 August 2013.
doi: 10.1177/0142331213495040

[10] Lantoine, G., and Braun, R. D., "Optimal Trajectories for Soft Landing on Asteroids", Space Systems Design Lab., Georgia Inst. of Technology, AE8900 MS Special Problems Report, Atlanta, GA, published online December 2006.

[11] Yang, H., & Baoyin, H., "Fuel-Optimal Control for Soft Landing on an Irregular Asteroid*", IEEE Transactions on Aerospace and Electronic Systems*, Vol. 51, No 3, July 2015, pp. 1688-1697.
doi: 10.1109/TAES.2015.140295.

[12] Yang, H., Bai, X., and Baoyin, H., "Finite-Time Control for Asteroid Hovering and Landing via Terminal Sliding-Mode Guidance", *Acta Astronautica*, Vol. 132, 2017, pp. 78-89.

[13] Zhang Zezu, "Robust Sliding mode guidance and control for soft landing on small bodies", *Journal of the Franklin Institute*, Vol. 349, No. 2, 2012, pp. 493-509

[14] Li, Y., Wang, H., Zhao, B., & Liu, K., "Adaptive Fuzzy Sliding Mode Control for the Probe Soft Landing on the Asteroids with Weak Gravitational Field", *Mathematical Problems in Engineering*, Vol. 2015, [online database], URL:

https://www.hindawi.com/search/all/adaptive+fuzzy+sliding+mode+control+for+the+probe+soft+landing+on+the+asteroids+with+weak+gravitational+field/, [retrieved 7 May 2015]
[15] AlandiHallaj, M., & Assadian, N., "Soft Landing on an Irregular Shape Asteroid using Multiple-Horizon Multiple-Model Predictive Control", *Acta Astronautica*, Vol. 140, 2017, pp. 225-234
[16] Lee, D. N., "General Tau Theory: Evolution to date". *Perception*, Vol. 38, 2009, pp. 837-858
doi: 10.1068/ldmk-lee
[17] Gibson James, "The Ecological Approach to The Visual Perception of Pictures", *Pergamon Press Ltd*., Vol 11, 1978, pp. 227-235.
doi: 10.2307/1574154
[18] Lee David, "A Theory of Visual Control of Braking based on Information about Time-to-Collision, *Perception*, Vol. 5, 1976, pp. 437-459
doi: 10.1068/p050437
[19] Lee D. N.," Guiding Movement by Coupling Taus", *Ecological Psychology*, Vol 10(3-4), 1998, pp. 221-250,
doi: 10.1207/s15326969eco103&4_4
[20] Zhang H., Cheng B., Zhao J. "Extended Tau Theory for Robot Motion Control", 2017 IEEE International Conference on Robotics and Automation (ICRA), IEEE, Singapore, Singapore, 2017, pp. 5321-5326,
doi: 10.1109/ICRA.2017.7989626
[21] Zhang Z., Xie P., Ma O. "Bio-Inspired Trajectory Generation for UAV Perching Movement Based on Tau Theory", *International Journal of Advanced Robotic Systems*, Vol. 11, No. 141, 2014,
doi: 10.5772/58898
[22] Kendoul F., Ahmed B., "Bio-Inspired TauPilot for Automated Aerial 4D Docking and Landing of Unmanned Aircraft Systems", 2012 IEEE/RSJ International Conference on Intelligent Robots and Systems, IEEE, Vilamoura, Algarve, Portugal, pp. 480-487,
doi: 10.1109/IROS.2012.6385586
[23] Lee D., Davies M., Green P., Van Der Weel F., "Visual Control of Velocity of Approach by Pigeons when Landing", *Journal of Experimental Biology*, Vol. 180, 1993, pp. 85-104,
doi: 10.4324/9780203936672
[24] Kendoul F., "Four-Dimensional Guidance and Control of Movement Using Time-to-Contact: Application to Automated Docking and Landing of Unmanned Rotorcraft Systems", *The International Journal of Robotic Research*, Vol. 33(2), 2013, pp. 237-267,
doi: 10.1177/0278364913509496
[25] Wang Y., Xu Sh., "Body-Fixed Orbit-Attitude Hovering Control Over an Asteroid using Non-Canonical Hamiltonian Structure", *Acta Astronautica*, Vol 117, 2015, pp. 450-468
[26] Santos W., Prado A., Oliveira G., Santos L., "Analysis of Impulsive Maneuvers to Keep Around the Asteroid $2001SN_{263}$", *Astrophysics and Space Science Springer*, Vol. 363(14), [online journal], URL: https://link.springer.com/article/10.1007%2Fs10509-017-3234-5, [retrieved 18 December 2017]

A CAM-BASED TRAJECTORY GENERATION METHOD FOR UAV INSPECTION IN GPS DENIED ENVIRONMENT

M. M. Rizia[1*], A. Flores-Abad[1], M. McGee[1], A. Choudhuri[1]
[1] Mechanical Engineering, University of Texas at El Paso, El Paso, TX 79968, USA;
* Corresponding author (mrizia@miners.utep.edu)

Keywords*: UAV, Trajectory, GPS denied environment, CAM*

ABSTRACT

A wide range of inspection methods for large infrastructures including energy, transportation and defense sectors are available commercially. The use of unmanned aerial vehicles (UAV) for aerial inspection, is one such technology that is growing popular due to its inherent ability to inspect inaccessible and hazardous locations safely and also cost effectively, reducing the downtime of system being inspected compared to traditional methods. Computer Aided Manufacturing (CAM) and Additive Manufacturing (AM) are popular manufacturing technologies that have significantly progressed in recent years. These methods differ in principal, one being subtractive and the other, additive. However, the tools that operate to manufacture the parts, go through the same set of coordinates, layer by layer, following a programmed path. In this paper, a novel method is introduced that uses a similar method to generate UAV trajectory for inspection of large structural components such as a powerplant, in GPS denied environment from a Computer Aided Design (CAD) model that is readily attainable. This is an offline trajectory generation method that will enable UAV operation in areas of poor or no signal, for both internal and external inspection. Proximity sensors and anti-collision mechanism will be used as a fail-safe aid that may not be accounted for in an available CAD model.

1 Introduction

The Powerplants are essential part of the energy sector. Therefore, its correct operation is highly critical. These powerplants often encompass components and facilities that are difficult to access and/or hazardous to humans. Conventional maintenance and inspection of certain parts also cause significant downtime of the plant and incurs economic costs.

There have been a lot of measures and technologies developed so far for safe, efficient and economic inspection of powerplants. Due to the safety and accessibility issues, robotic technologies have also been developed and used to inspect them instead of manual maintenance. In United States, robot was used for remote monitoring of hazardous areas of powerplant [1]. Tokyo Electric Power in Japan used monorail-type compact inspection robots equipped for acoustic and thermal inspection of nuclear powerplant facilities [2]. Japan is also advancing in research and implementation of the use of humanoid robotic supervision of the power plant facilities [3]. However, such inspect systems are component specific.

The use of aerial robotic inspection has been gaining popularity with its progressive research and development in hardware system. In most cases the drone is usually RC controlled and

must be operated in the field of view of the operator. A significant number of these UAVs are heavily dependent on GPS for navigation. In the successful demonstration of a coal-fired power plant boiler inspection, Nikolic et al. [4] uses two external cameras and highly depends on the sensing capabilities of the hardware to avoid contact with the structure. Although this approach handles the particulate deposition problem well, but it limits the inspection payload. In another approach developed by Shan et al. [5], the UAV compares its image to Google Map database to navigate to anywhere on earth, but at the same time it faces limitation as there is lack of information in the third dimension and that there could be inconsistency in the map database.

CAM based trajectory methods have been proposed previously for other tasks eg robots in manufacturing etc. Cerit et al. [6] additively manufactured a small part using a CLS file to make a tool path for rapid prototyping. Zeng et al. [7] used coordinate from G code for grinding operation using KUKA robot path generator. Chen et al. [8] demonstrates the same for an automatic finishing operation of an offline path generation for an industrial robot based on data of cutter location. In this paper, a novel method is introduced that uses a similar technique to generate UAV trajectory for inspection of large installations in GPS denied environment. From Computer-Aided Design (CAD) of the model, CAD/AM toolpath is generated. The toolpath is converted to cartesian coordinates and then exported to MATLAB, where a time step is added for trajectory generation. The trajectory is validated Simulink via simulation. As it uses data-based navigation, thus payload decreases, resulting in better maneuverability and inspection precision. Systems with sensor and/or signal based navigation can also use this technique as there is no need of additional component installment.

2 Main Idea

Autonomous UAV systems have the great potential to reduce human participation in inspection and can also reduce system outage periods. A flying inspection system, although virtually universal, it faces several challenges such as strong GPS signal at all. But due the design of a powerplant, some areas may have poor or no GPS signal at all. This project presents an offline trajectory system for the UAV to fly in for inspection without using GPS. It is the first time in literature that a CAM system is used to generate UAV trajectory. Using a CAE software, the tool path data for the machining operation is obtained from the cutter nodal coordinates. The manufacturing path followed in CAM milling operation and a 3D printer (in AM) are essentially similar, one being subtractive, tool travelling in -Z axis (top to bottom) and the other being additive i.e. tool travels in +Z axis (bottom to top). Therefore, if the signs of the Z-coordinates in G code file for AM are reversed, it will yield a CAM operation path file. During both manufacturing operations, the tool moves layer by layer. These paths, with an appropriate offset, are similar to the flight path followed by an UAV, encompassing a structure to be inspected. Mentionable, this point cloud obtained caters for the camera field of view, to cover all inspection surfaces.

3 Methodology

3.1 CAD Model

Computer Aided Design (CAD) software is heavily used worldwide. Some CAD software also provide integrated Computer Aided Manufacturing (CAM) and Additive manufacturing features that directly sends manufacturing instructions to hardware such as CNC machines, 3D printers etc. Such fully integrated system is advantageous for its trouble-free, instantaneous design iterations without the need to reupload and or export files for each design modification. This apparently trivial gain makes improves productivity. In this project, Fusion 360 have been used that has incorporates the above-mentioned integrated features.

A critical part of this research is the CAD model of a power plant since the objective is to generate a trajectory from it to program a collision free UAV flight for effectively inspect. A CAD model of a powerplant was designed (Fig 01) for this project. The power plant model size is 218 x 130 x 170 (unit-mm, length x width x height). If the design of a facility or infrastructure of interest is already available, it can easily be imported to Fusion 360 in the "Model" environment.

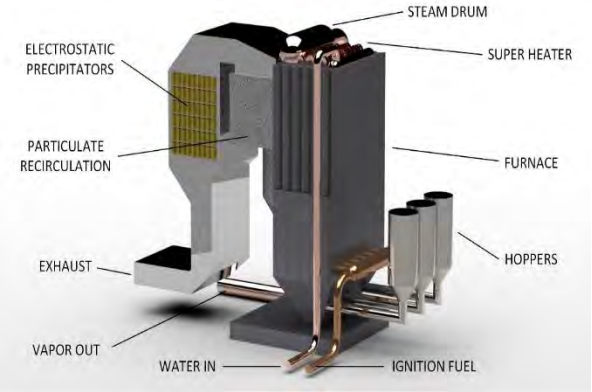

Fig.1. CAD model of coal-fired powerplant.

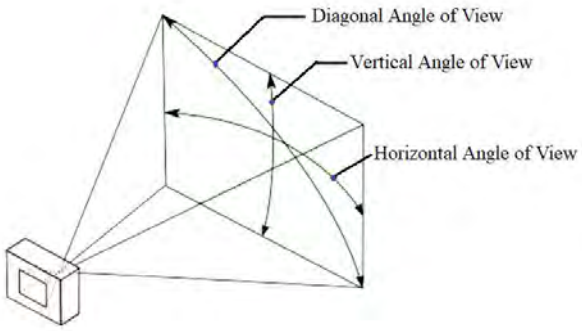

Fig.2. Camera field of view measured horizontally, vertically or diagonally.

3.2 Toolpath Generation in Manufacture Environment

In the "Manufacture" workspace of Fusion 360, the machining properties are setup i.e. setting up the appropriate operation type, defining work coordinate system, choosing apt stock offset, post processing setup etc. (Table 1). Boiler height commonly ranges between 12–30 m. For this study, a 17 m high boiler is chosen, which is scaled down to 170 mm due to the tool size limitation. Model scale,

$$S_L = \frac{l_p}{l_m} = 100{:}1 \quad (1)$$

Where, l_p = Length of prototype, l_m = Length of model. The angular field of view (α) is calculated from the chosen dimension (d), and effective focal length (f) as,

$$\alpha = 2\arctan\frac{d}{2f} \quad (2)$$

The angular field of view of a typical Intel(R) R200 model stereo and color camera is nominally 60 x 45 x 70 and 70 x 43 x 77 (horizontal (α_h) x vertical (α_v) x diagonal (α_d), degrees) respectively[9]. With 300 mm inspection offset distance (average camera focal length

30 mm) and considering a 30% overlap adjacent pictures (for a sharp and better image quality inspection profile), the real-life field of view is analytically calculated to be 170 x 250 mm^2 approximately (Fig. 2). Therefore, model scale yields field of view height 2.5 mm, hence this is the maximum step down/feed for CAM. No of parallel toolpath (slice) is 68.

Table 01: Machining parameters

Operation type	Milling operation (single axis) 2D Contour	Cutting tool	ϕ2.5 mm ball end mill
Maximum step down	2.5 mm	Feed/Revolution	0.0667 mm/rev
Machining Distance	71.03 m	Stock offset	2 mm~5 mm
Tolerance	0.01 (low)	Surface speed	39.27 m/min
Cutting feed rate	1000 mm/min	Machining time	1:10:14

In order to optimize the toolpath and thereby obtaining a proper drone flight trajectory, the toolpath needs to be uniformly distributed and well wrapped around the model (Fig 3). The endpoint of chosen tool machines out the part from the stock and a "toolpath" is obtained. Smooth transition and plunge in features were chosen to avoid sharp change in UAV heading. From the generated toolpath, a denser toolpath is observed near the circular, inclined and tapered areas. Also, additional noise is seen for the CNC tool safe retrievals/lead-ins/lead-outs. Mentionable, that the blue path lines describe machining on stock while the yellow path lines describe tool travel path.

3.3 Exporting Toolpath via Post Processor

In the "Post Process" option, a g-code (numerical control programming language) is processed and sent to a machine to drive it. Here, using a post process add-on, the cartesian coordinates of the tool endpoints are exported as .csv file. Thus, the Path Planning is obtained. There are 234,048 number of points in this power plant setup.

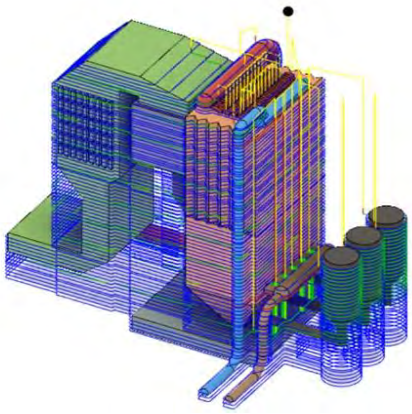

Fig.3. Tool path generated around the powerplant CAD model.

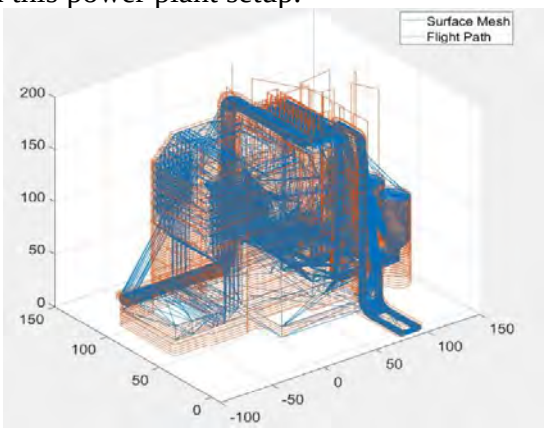

Fig.4. Flight path generated in MATLAB (blue lines- surface mesh, red lines- flight path).

3.4 Trajectory Generation, Simulation and Inspection

The set of coordinates in csv format represent the tool end points in 3D space. In MATLAB, the coordinates are given timesteps and processed to generate trajectory of the UAV for

powerplant inspection (Fig. 4). Time step can be varied in accordance with the inspection image requirement. The projected trajectory is virtually validated in SIMULINK environment. The final step is to take inspection photos with the on board (IR and EO) cameras and generate a 3D inspection profile. For this, a grid-based analysis of the pictures and re-stitching of the pictures with 30% overlap will be used as stated earlier. Mentionable, there may be some discrepancies between the CAD model and the real setup. To avoid such deviation and avoid collision, the UAV will be equipped with an anti-collision mechanism with necessary sensor that are already available with the UAV.

4 Discussion and Conclusions

This study developed a novel method to inspect powerplants with the use of CAD models and the system is completely free of the use of GPS. This approach saves a lot of time and reduces system downtime of the powerplant. One of the important aspects of this method is that it is software data based, therefore it does not need additional components to be installed in the UAV, thereby improves maneuverability and cost. UAV with GPS based flight methods can use this method without much cost, as a secondary method.

References

[1] H. T. Roman, "Robotic Applications in PSE&G's Nuclear and Fossil Power Plants," *Proceedings of the IEEE Transactions on Energy Conversion,* Vol. 8, No. 3, pp 584-592, 1993.

[2] S. Yamamoto, "Development of inspection robot for nuclear power plant," *Proceedings of the 1992 IEEE International Conference on Robotics and Automation*, Vol. 2, pp 1559-1566, Nice, France, 1992.

[3] N. Kawauchi, S. Shiotani, H. Kanazawa, T. Sasaki and H. Tsuji, "A plant maintenance humanoid robot system," *Proceedings of the 2003 IEEE International Conference on Robotics and Automation*, Vol. 3, pp 2973-2978, Taipei, Taiwan, 2003.

[4] J. Nikolic, M. Burri, J. Rehder, S. Leutenegger, C. Huerzeler and R. Siegwart, "A UAV system for inspection of industrial facilities," *Proceedings of the 2013 IEEE Aerospace Conference*, pp 1-8, Big Sky, MT, 2013.

[5] M. Shan, F. Wang, F. Lin, Z. Gao, Y. Z. Tang and B. M. Chen, "Google map aided visual navigation for UAVs in GPS-denied environment," *Proceedings of the 2015 IEEE International Conference on Robotics and Biomimetics (ROBIO)*, Vol 11, pp 27-33, Zhuhai, China, 2015.

[6] E. Cerit. & I. Lazoglu, "A CAM-based path generation method for rapid prototyping applications," *International Journal of Additive Manufacturing Technology*, Vol. 56, pp. 319-327, 2011.

[7] G. Zeng, C. Chen, D. Huang and Y. Zhu, "Robotic trajectory planning based on CL data," *Proceedings of the 2015 IEEE International Conference on Robotics and Biomimetics, ROBIO 2015*, Zhuhai, Vol. 11, pp 7-13, 2015.

[8] C. Chen, J. Li, Y. Zhu, L. Tu and W. Weng, "Automatic finishing system research for industrial robot." *Proceedings of the 2017 IEEE International Conference on Cybernetics and Intelligent Systems (CIS) and IEEE Conference on Robotics, Automation and Mechatronics (RAM)*, Ningbo, China, Vol. 11, pp 7-13, 2017.

[9] L. Keselman, J. I. Woodfill, A. Grunnet-Jepsen, and A. Bhowmik, "Intel (R) RealSense (TM) Stereoscopic Depth Cameras." *Proceedings of the IEEE Computer Vision and Pattern Recognition Workshops (CVPRW)*, pp. 1267–1276, 2017.

ADDITIVE MANUFACTURED EAR PINNA FOR SOUND LOCALIZATION IN ADVANCED HEARING DEVICES

C. F. Acosta Carrasco [1, 2*], A. Belmont[1, 3], V. Krull[4], A. Dittberner[4], R. B. Wicker[1, 2]

[1] *W.M. Keck Center for 3D Innovation, The University of Texas at El Paso, El Paso, TX 79968, USA;*
[2]*Department of Mechanical Engineering, UTEP, El Paso, TX 79968, USA;*
[3]*Department of Metallurgical, Materials & Biomedical Engineering, UTEP, El Paso, TX 79968, USA;*
[4]*G.N. Advanced Science, G.N. Hearing, Glenview, IL 60026, USA;*
* Corresponding author (cfacostacarrasco@miners.utep.edu)

Keywords*: additive manufacturing, ear pinna, fused deposition modeling, stereolithography.*

ABSTRACT

The fabrication of intricate features such as those found in the human ear can be accomplished by using additive manufacturing (3D printing) technology. Customizable and individualized advanced hearing devices can be fabricated by 3D printed as the process allows for preservation of the ear's geometry. The localization of sound can be captured by the outer human ear, also known as pinna. To study and fabricate an additive manufactured pinna, a pinna model from an anthropometric manikin for acoustic measurements was first attained. This pinna model was then 3D scanned to obtain a computer aided design (CAD) and the CAD file was fixed and converted into a Standard Tessellation Language (STL) file for 3D printing using material extrusion and vat polymerization technologies. Two fabrication processes were implemented to accommodate the 3D printed pinna onto the acoustic testing manikin. Dimensional accuracy measurements were compared between the manikin's pinna and the 3D printed replica. The additively manufactured pinnae will be subjected to further acoustic testing to analyze spatial cues preservation.

1 Introduction

The additive manufacturing (AM) process, also known as 3D printing, consists of layer-by-layer fabrication of an object with the usage of a computer aided design (CAD) file [1]. The CAD file is then transformed into a Standard Tessellation Language (STL) file for 3D printing. The selection of the 3D printing technology may be determined by many factors including mechanical performance, surface roughness, dimensional accuracy, among others. Although there are seven different AM technologies, two of the most well known polymers processes were used in this study; Fused Deposition Modeling (FDM) for material extrusion and Stereolithography (SL) for vat polymerization. Material extrusion is the process where material is dispensed selectively through an orifice [2]. FDM consists of depositing molten plastic filament in a layer by layer fashion through a nozzle onto a build platform [1]. With this technology, the dimensional accuracy of the part is dependent on the CAD model, the gantry system of the printer, and the layer thickness at which the nozzle can print [3]. Vat photopolymerization consists of a light activated polymerization selectively curing photosensitive resin in a vat [2]. SL by 3D systems (Rock Hill, SC, USA) was one of the first AM technologies available on the market [4], as well as the most known for the vat photopolymerization process. SL machines can output a resolution up to 50 micrometers [5]. These technologies were selected for the dimensional accuracy that can be achieved for

additive manufacturing the ear geometry, also known as pinna, to preserve the human spatial cues the human pinna possesses. Many customizable applications, such as frequency-controlled headphones, can be pursued by conserving sound location within AM ear pinnae, serving as an extension of the human body. This research work is being conducted via a collaboration between the W.M. Keck Center for 3D Innovation (Keck Center) and G.N. Advanced Science (G.N. Hearing, Glenview, IL, USA).

2 Pinna model CAD reconstruction

To fabricate the pinna, it is important to maintain the shape as accurately as possible to preserve the spatial cues the human pinna possesses. To validate the 3D printed pinna design, a KEMAR (G.R.A.S Sound & Vibration, Twinsburg, OH, USA) anthropometric manikin was used for acoustic research purposes. Specifically, the KEMAR small right pinna was used. An initial STL model was provided by G.N. Advanced Science, obtained through a 3D scan using a 3Shape HD600 (3Shape, Copenhagen, Denmark) which focused on capturing the ear geometry. This model was then adapted to fit the boundary of the KEMAR manikin system. The manikin head possesses a set of interfaces, allowing the pinna to properly fit in place as well as the addition of a microphone should the user desire to incorporate one for acoustic measurements. The KEMAR ear is made out of a soft and flexible silicone which allows for a tight fit to the KEMAR head. Measurements were taken using a caliper to obtain dimensions of the outer box of the pinna as well as matching of the interfaces. A CAD design was made using Fusion 360 (Autodesk, San Rafael, CA, USA) using the dimensions of the interfaces obtained from the KEMAR head. At the Keck Center, a 8-axis FARO ScanArm (FARO, Lake Mary, FL, USA) was used to 3D scan the outer perimeter of the KEMAR right pinna model to better match the interfaces on the CAD model with those of the KEMAR pinna. A STL model was achieved from the 3D scan after obtaining the scan cloud points with Geomagic Design X (3D systems, Rock Hill, SC, USA). The initial STL file was then brought into Fusion 360 for CAD modeling and reconstruction, along with the interfaces' CAD and the pinna box scan STL. Fit test interfaces samples were 3D printed using polycarbonate (PC) material on a Fortus FDM 400mc (Stratasys, Eden Prairie, MN, USA) to account for the correct pinna placement on the manikin system, shown in Fig.1.

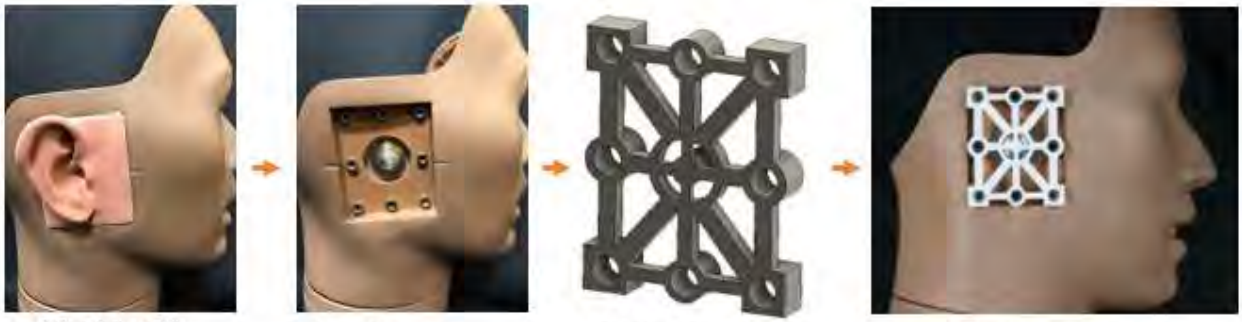

Fig.1. KEMAR system and CAD interfaces modeled

3 Design and fabrication process for 3D printed pinna

Once the interfaces matched the KEMAR manikin head, two designs were made to fit in and seal the 3D printed pinna onto the KEMAR system. A sealant was required for both designs for purposes of sound frequency testing so that the manikin microphone could work properly within the simulated auditory canal. The first design consisted of placing a 3D printed KEMAR pinna into a silicone casing. The silicone casing design was used to emulate the original small right KEMAR ear. The right pinna CAD was split into two components; the right pinna and casing. The right pinna was fabricated using polycarbonate (PC) on the Fortus 400mc with a layer thickness of 0.005 inches. The pinna model was also 3D printed using Somos NeXt (DSM, Heerlen, Netherlands) material on the Viper SLA (3D systems, Rock Hill, SC, USA) with a layer thickness of 0.003 inches. As for the casing, a three-part mold CAD was designed in Fusion 360 to accommodate for the silicone deposited and subsequently cured. The mold was 3D printed on the Fortus 400mc using PC material using a 0.005 layer thickness. The three parts were sprayed with a boron nitride mold release to avoid adhesion between the silicone and plastic. The platinum-based silicone TC-5045 A/B (BJB Enterprises Inc., Tustin, CA, USA) with a 45 Shore A was cured in the mold for 12 hours. Once the silicone part was cured and removed from the mold, the 3D printed pinna was fit into the casing. A fit test specimen was placed on the manikin to validate the concept, shown in Fig 2.

The second design consisted of a one-piece assembly where the KEMAR pinna CAD was 3D printed with the surrounding casing. For the pinna component to be sealed in the manikin an o-ring was placed on the back side of the pinna model. The o-ring approach only required CAD modifications on the back interface. Channels were designed to accommodate for the o-ring placement. The o-ring design was 3D printed using both Somos NeXt and PC materials. A silicone o-ring was attained and placed on the 3D printed pinnae by press fitting and using a

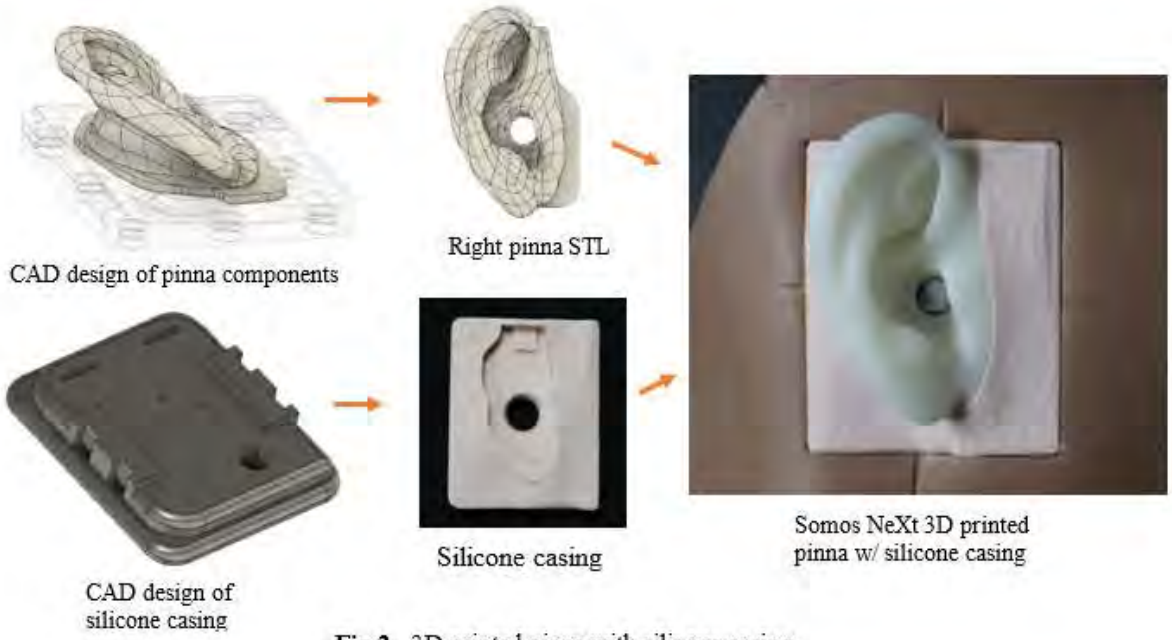

Fig.2. 3D printed pinna with silicone casing

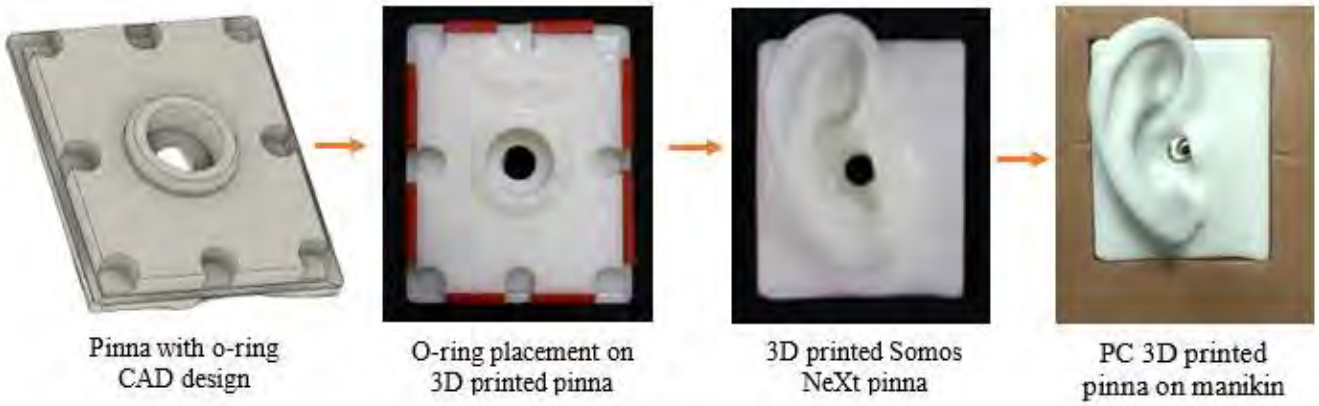

Fig.3. 3D printed pinna with o-ring

polyurethane adhesive. After the proper matching of the additive manufactured pinnae and the o-ring layout, the pinna was placed on the manikin system to fit test. Fig. 3 shows the fabrication process for the second design. Both designs matched the KEMAR head interfaces. The silicone casing pinna bonded smoothly into the manikin system due to the bounding box being fabricated out of silicone. The o-ring pinna had a stiffer placement into the manikin compared to the KEMAR pinna and the silicone casing pinna because of the 3D printed hard casing.

4 Dimensional accuracy measurements and future work

To assess the validity of the additive manufactured pinnae models, measurements of each model were taken following the pinna measurement methodology from Algazi et al. (2001) [6]. Each dimension shown in Fig. 4 was captured three times using caliper readings. The measurements shown in Table 1 were gathered from the KEMAR small right ear. These readings were obtained to serve as a validation baseline for the 3D printed specimens. The

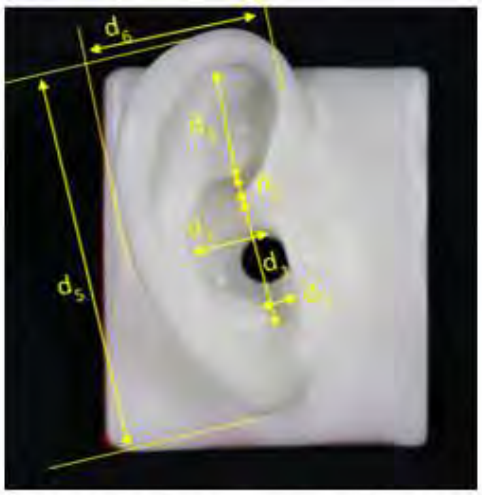

Fig.4. Dimensional measurements taken on pinna [5] [6]

Table 1. Measurements for right small KEMAR pinna in inches

Right small KEMAR pinna							
Measurements	d1'	d2'	d3'	d4'	d5'	d6'	d7'
1	0.6915	0.2575	0.5960	0.6185	2.2655	1.0315	0.2465
2	0.7300	0.2335	0.5780	0.6900	2.2670	1.0865	0.2130
3	0.7150	0.2525	0.5865	0.6605	2.2705	1.0380	0.2230
Mean	**0.7122**	**0.2478**	**0.5868**	**0.6563**	**2.2677**	**1.0520**	**0.2275**
SD	0.0274	0.0179	0.0127	0.0508	0.0036	0.0425	0.0243

Table 2. Measurements for right 3D printed Somos NeXt pinna in inches

Right 3D printed pinna Somos NeXt							
Measurement	d1'	d2'	d3'	d4'	d5'	d6'	d7'
1	0.7125	0.2460	0.5700	0.6585	2.2565	1.0750	0.2550
2	0.7010	0.2455	0.5640	0.6260	2.2505	1.0510	0.2220
3	0.7095	0.2560	0.5485	0.6685	2.2510	1.0415	0.2400
Mean	**0.7077**	**0.2492**	**0.5608**	**0.6510**	**2.2527**	**1.0558**	**0.2390**
SD	0.0084	0.0084	0.0157	0.0314	0.0047	0.0244	0.0234
KEMAR Mean	**0.7122**	**0.2478**	**0.5868**	**0.6563**	**2.2677**	**1.0520**	**0.2275**

Table 3. Measurements for right 3D printed PC pinna in inches

Right 3D printed PC pinna							
Measurement	d1'	d2'	d3'	d4'	d5'	d6'	d7'
1	0.7070	0.2350	0.5595	0.6490	2.2720	1.0710	0.2305
2	0.6975	0.2390	0.5815	0.6300	2.2765	1.0895	0.2360
3	0.7150	0.2520	0.5625	0.6340	2.2640	1.0580	0.2290
Mean	**0.7065**	**0.2420**	**0.5678**	**0.6377**	**2.2708**	**1.0728**	**0.2318**
SD	0.0124	0.0126	0.0169	0.0142	0.0090	0.0224	0.0052
KEMAR Mean	**0.7122**	**0.2478**	**0.5868**	**0.6563**	**2.2677**	**1.0520**	**0.2275**

Somos NeXt and PC pinnae measurements are shown in Tables 2 & 3, respectively. All three model dimensions were then recorded and plotted on scatter plot to further validate similarities and differences between each of the models, shown in Fig. 5. Results from dimensional analysis show that the 3D printed pinnae have been successfully replicated. The difference between the KEMAR right ear and both 3D printed materials lies on the thousandths of an inch spectrum. Which validates that the manufacturability of ear pinna is possible using AM. For further validation of the 3D printing process, the models fabricated were shipped to G.N. Advanced Science where acoustic testing will take place. Frequency recordings will be made to evaluate the 3D printed models and compare them to the original KEMAR pinnae. Both designs additively manufactured in FDM and SL technologies will then be analyzed for retention of

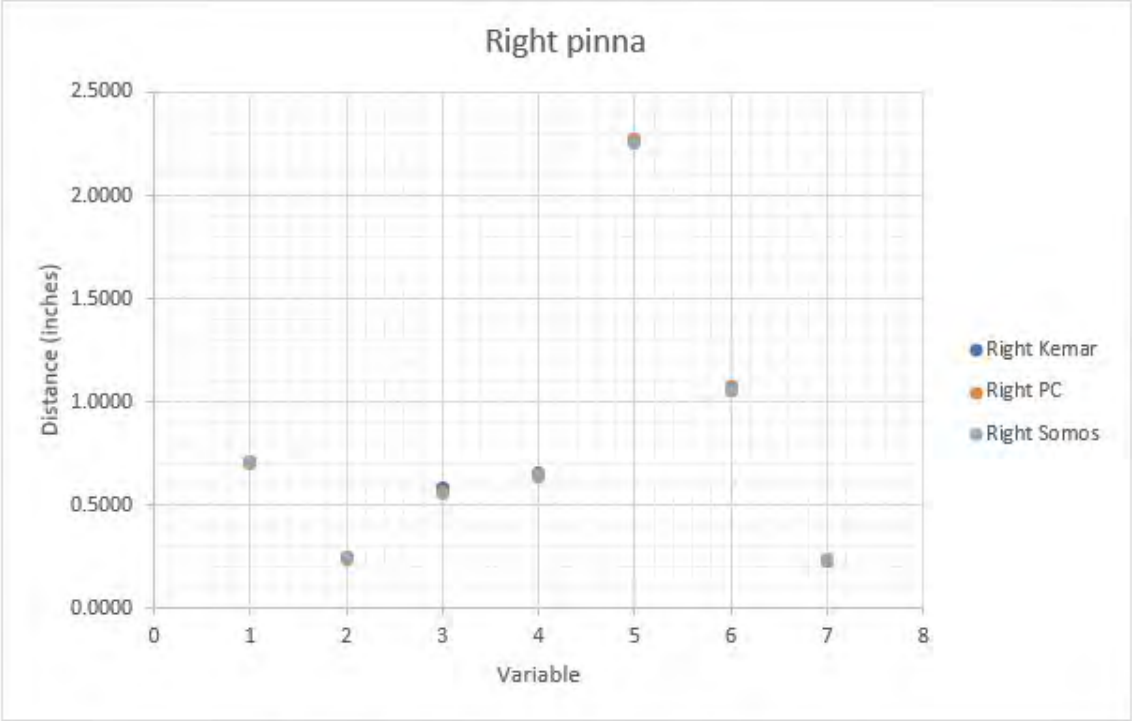

Fig. 5 Scatter plot of pinnae measurements comparison.

spatial cues. Future work also involves 3D scanning and CT scanning of ear specimens for improved dimensional accuracy, exploring different equipment for additive manufacturing of pinnae, as well as embedding a 3D printed pinna specimen into a headset for research into advanced hearing protection devices.

5 Conclusion

In conclusion, additive manufacturing is being used in many different applications including anatomical modeling. The main goal of this project is to preserve spatial cues on the pinna by preserving dimensional accuracies that can be achieved through 3D printing. Two technology processes were selected, FDM and SL, to achieve the necessary dimensions required to fabricate complex features such as the KEMAR pinna. CAD modeling was used succesfully to model the assembly of the 3D printed pinna and the KEMAR manikin. Dimensional accuracy measurements proved the additive manufactured pinna to be on the range of the KEMAR ear. Pending acoustic testing will determine whether the 3D printed geometry and material can preserve spatial cues for further capabilities regarding hearing protected devices.

References

[1] N. Guo, and M. C. Leu. "Additive manufacturing: technology, applications and research needs." *Frontiers of Mechanical Engineering* 8, no. 3, 215-243, 2013.

[2] ASTM International. “ASTM ISO/ASTM52900-15 Standard terminology for additive manufacturing – general principles – terminology.” West Conshohocken, PA; *ASTM International*, 2015. doi: https://doi.org/10.1520/ISOASTM52900-15

[3] B. N. Turner, R. Strong, and S. A. Gold. "A review of melt extrusion additive manufacturing processes: I. Process design and modeling." *Rapid Prototyping Journal* 20, no. 3 (2014): 192-204.
[4] K.V. Wong, and A. Hernandez. "A review of additive manufacturing." *ISRN Mechanical Engineering* 2012 (2012).
[5] J. Stampfl, S. Baudis, C. Heller, R. Liska, A. Neumeister, R. Kling, A. Ostendorf, and M. Spitzbart. "Photopolymers with tunable mechanical properties processed by laser-based high-resolution stereolithography." *Journal of Micromechanics and Microengineering 18*, no. 12 (2008): 125014.
[6] R. V. Algazi, R. O. Duda, D. M. Thompson, and C. Avendano. "The cipic hrtf database." In *Proceedings of the 2001 IEEE Workshop on the Applications of Signal Processing to Audio and Acoustics (Cat. No. 01TH8575)*, pp. 99-102. IEEE, 2001.

AN ALTERNATIVE METHOD FOR INTERPOLATING AND EXTRAPOLATING STRAIN PREDICTIONS USING THE THETA PROJECTION MODEL

J. Perez, C. Stewart
Mechanical Engineering, The University of Texas at El Paso, El Paso, TX 79968, USA;
Calvin Stewart (cmstewart@utep.edu)
Keywords: *Theta-projection, calibration, interpolation, extrapolation*

ABSTRACT

The theta projection constitutive model excels at fitting the shape creep deformation curves. The most widely used method for calibrating the model constants to the data curve is through the use of numerical optimization, where a least square non-linear scheme is used. The scheme optimizes the constants in relation to one another to generate a fit to the data with respect to an error function. This results in excellent fits, however because the constants are dependent on one another, the interpolated/extrapolated constants are not always consistent when plotted against stress. The scatter present with constants calibrated using this process of numerical optimization makes accurate predictions of interpolated or extrapolated strain difficult to obtain. For this reason, an analytical approach is used to calibrate the model constants. The analytical method allows the strain curve to be deconstructed and analyzed by regime, relating the constants to the shape of their respective regimes. The analytical approach ensures model constants have physical realism relative to the experimental data from which they're derived. This results in more consistent relationship between theta constants and stress. A trend is identified in the rupture times of test data as stress increases. To utilize this trend, an alternative interpolation/extrapolation function that relies on rupture time rather than temperature and stress is used to establish a relationship between the calibrated theta constants and rupture time. Simulations, interpolations and extrapolations are made using both the original interpolation function as well as the alternative prediction function and the results are compared qualitatively and quantitatively using the normalized mean square error (NMSE). It is found that the alternative function produces improved strain predictions.

1 Introduction

1.1 Theta model application

The process for application of the theta model proposed by R. W. Evans requires the constants to be calibrated to experimental data using a least square non-linear scheme and an error function [1-3]. These calibrated constants are related to temperature and stress via an interpolation/extrapolation function so that strain predictions can be made at any temperature-stress condition [1-3]. The theta projection model and interpolation function are as follows;

$$\varepsilon_{cr} = \theta_1(1-\exp(-\theta_2 t)) + \theta_3(\exp(\theta_4 t)-1) \tag{1}$$

$$\theta_i = \exp(a_i + b_i\sigma + c_i T + d_i \sigma T) \tag{2}$$

where θ_1, θ_2, θ_3 and θ_4 are material constants.

Scatter in numerically optimized theta constants results in somewhat unreliable predictions made using [Eq. (2)]. The nature of numerical optimization results in constants that may have no realistic trend which in turn results in scatter when related to temperature and stress. An analytical approach is used to calibrate theta constants to experimental data by separating the model by regime and relating the constants to the shape of each set of data used in calibration. This results in calibrated constants with a more consistent trend as the time till rupture changes with stress. The relationship of rupture time and each theta constant is used to make interpolated/extrapolated predictions of strain. This relationship is as follows;

$$\theta_i = A_i (t_r)^{-B_i} \tag{3}$$

where A and B are constants identified in calibration similar to the a, b, c, and d constants in [Eq. (2)]. This alternate method of calibration serves to further relate θ_1, θ_2, θ_3 and θ_4 to experimental data and establish a physically realistic trend in prediction. The rupture time used in [Eq. 3] is not the true rupture time of the experimental data, rather it is the last consistent time measurement recorded just before the material begins to fracture.

2 Calibration Process

2.1 Material and data information

The material used in this study is alloy P91. The test data used in calibration was recorded at 3 different stresses (10, 14 and 17 ksi) at a single isotherm of 1200ºF. Analyzing multiple stresses at a single isotherm simplifies analysis. Data used in post-audit validation is 4 tests at 9, 12, 15 and 19 ksi all at 1200ºF. All data used in this study was collected by Oak Ridge National Laboratory [4].

2.2 Calibration

Theta constants are calibrated to the experimental data using the analytical method. The calibrated fits are shown in Fig.1. Although the analytical fit underpredicts the full ductility of the experimental data, this conservative fit allows θ_1, θ_2, θ_3 and θ_4 to maintain a realistic trend as stress increases while fitting the data accurately.

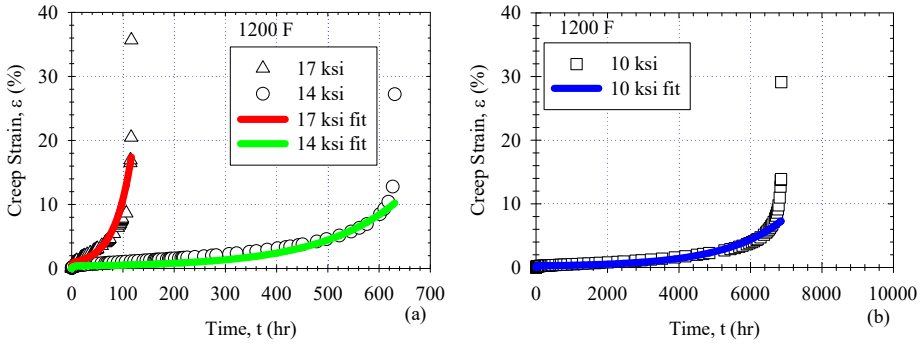

Fig.1. Calibration of the theta model to experimental data.

2.3 Calibrated theta constants using Eq.

The natural logarithm of calibrated theta values is plotted with respect to stress when applied to [Eq. 2] and are plotted with respect to rupture time when applied to [Eq. 3]. The plots are shown in Fig.2 and Fig.3. These plots serve to show the difference in prediction for interpolated and extrapolated values of theta. The impact of these two prediction functions becomes evident in section 3.

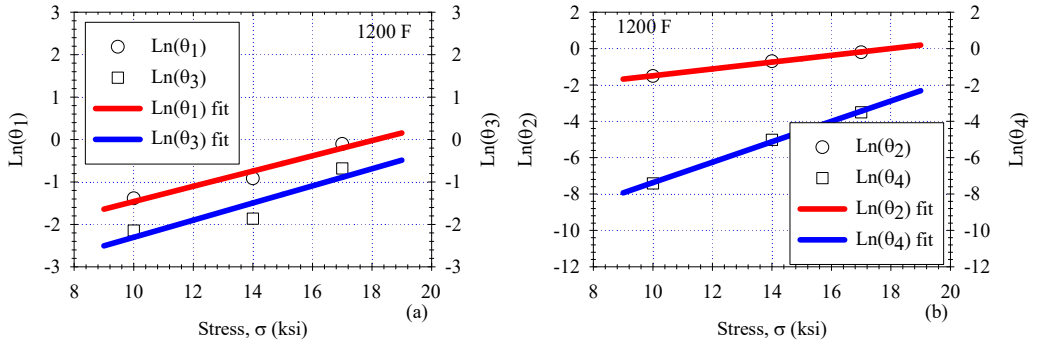

Fig.2. Calibrated theta values obtained using Eq. 2.

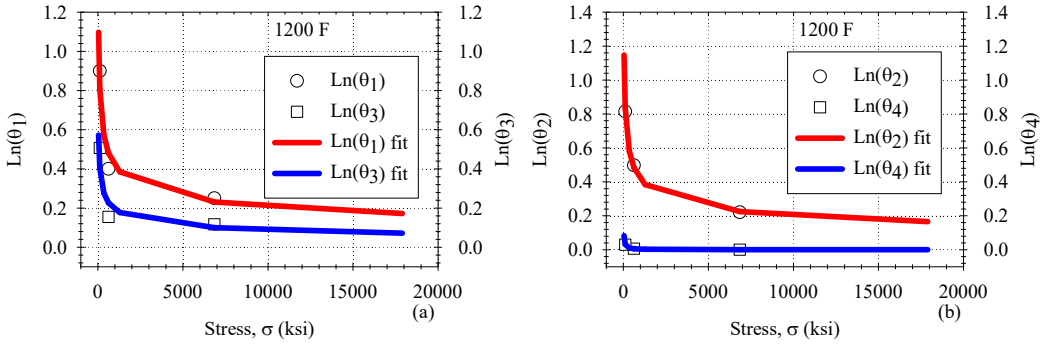

Fig.3. Calibrated theta values obtained using Eq. 3.

3 Results

3.1 Interpolations and Extrapolation

Interpolation and extrapolation performed using [Eq. 2] and [Eq. 3] are plotted together against validation data and is shown in Fig.4. It is evident that using [Eq. 2] produces fits that vary drastically qualitatively. Prediction at 19 ksi is the best representation of prediction using [Eq. 2], modelling the curve well and depicting ductility similar to the validation data. Prediction at 12 ksi using [Eq. 2] severely underpredicts the behaviour of creep deformation when compared to validation data and prediction at 9 ksi greatly overpredicts creep deformation. This shifting consistency is due to the nature of the prediction equation. Small variances in theta values predicted using [Eq. 2] result in a large shift in the way the creep curve will behave. The predictions made using [Eq. 3] maintain consistent behaviour in every instance. A comparison of the NMSE is shown in Table 1. From this table, the improvement

in prediction of [Eq. 3] over [Eq. 2] can be seen quantitatively. The NMSE equation is as follows;

$$NMSE = \frac{1}{n}\sum_{i=1}^{n}[(X_{sim,i} - X_{\exp,i}) / X_{\exp,i}]^2 \tag{3}$$

where n is the number of data points and X is the simulated or experimental data denoted by subscript.

Table 1 – Normalized mean square error comparison of interpolated/extrapolated predictions using Eq. 2 and Eq. 3 to validation data.

Stress	NMSE of predictions using $\theta_i = \exp(a_i + b_i\sigma + c_iT + d_i\sigma T)$	NMSE of predictions using $\theta_i = A_i(t_r)^{-B_i}$
19 ksi	0.232787	0.030612
15 ksi	0.078304	0.070085
12 ksi	0.372753	0.095080
9 ksi	7.428862	0.190037

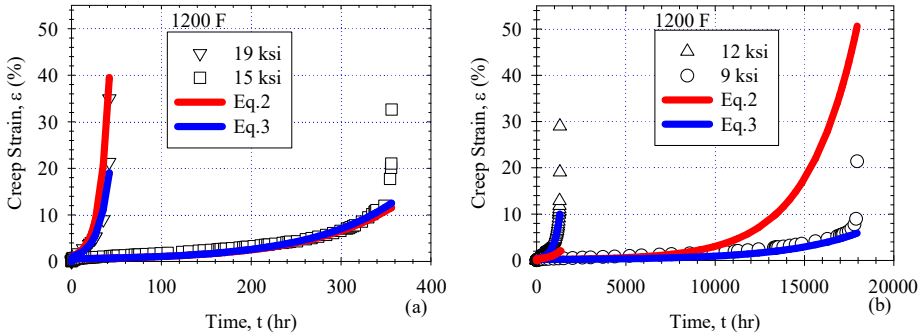

Fig.4. Interpolated and extrapolated strain predictions using Eq. 2 and Eq. 3.

4 Conclusions

It is evident from Table 1 that the predictions made using [Eq. 3] are quantitatively better in every instance. Analyzing the prediction plots in Fig.4 and the calibrated trends in Fig.3, the following conclusions can be drawn. The more data used in calibration, a more consistent trend in θ_1, θ_2, θ_3 and θ_4 can be derived using [Eq. 2]. When limited data is used in calibration, the trends established in θ_1, θ_2, θ_3 and θ_4 do not allow for accurate strain predictions for all stress conditions at a single isotherm. When using [Eq. 3], it is apparent that the relationship of theta constants to rupture time allows for more consistent and accurate predictions to be made, even when limited data is used in calibration. It should be noted that when using the analytical approach to calibration with [Eq. 3], the predictions do not depict the full ductility of the validation data. This results in conservative predictions of strain with time which may be useful in design.

5 Future Work

Due to [Eq. 3] relying on approximate rupture time rather than temperature and stress, it is necessary to predict the rupture time of a test specimen. The Wilshire model provides a means to predict the rupture time of a test [5]. Using the Wilshire model to predict rupture time with the alternative interpolation/extrapolation function used in this study and the analytical approach to calibration, a new method for applying the theta projection model may be developed.

References

[1] Evans, Russell W., and Brian Wilshire. Creep of metals and alloys. (1985).

[2] Brown, S. G. R., Evans, R. W., & Wilshire, B. (1986). Creep strain and creep life prediction for the cast nickel-based superalloy IN-100. *Materials Science and Engineering*, *84*, 147-156.

[3] Evans, M. (2002). Sensitivity of the theta projection technique to the functional form of the theta interpolation/extrapolation function. *Journal of materials science*, *37*(14), 2871-2884.

[4] Oak Ridge National Laboratories, "Materials Handbook for Generation IV Reactors." https://gen4www.ornl.gov/.

[5] Wilshire, B., & Battenbough, A. J. (2007). Creep and creep fracture of polycrystalline copper. *Materials science and engineering: a*, *443*(1-2), 156-166.

APPLICATION OF A MULTIWAVELENGTH PYROMETER IN ACCURATE SURFACE TEMPERATURE MEASUREMENT IN ADDITIVE MANUFACTURING

Md Moinuddin Shuvo*, Ryan B. Wicker
Department of Mechanical Engineering, The University of Texas at El Paso, TX 79968, USA;
W. M. Keck Center for 3D Innovation, El Paso, TX 79968, USA
* Corresponding author (mshuvo@miners.utep.edu)

Keywords*: Pyrometry, Multiwavelength Pyrometer, Temperature Measurement, Additive Manufacturing*

ABSTRACT

Accurate surface temperature measurement in additive manufacturing (AM) is preeminent as it enables process control, parameter development, measuring solidification rates, etc. Specifically in metal AM attaching a probe within the processing zone can compromise the purity and finish of the printed part. Hence, researchers are dependent on pyrometry – a non-contact temperature measurement method. This study focuses on the use of a multiwavelength (MW) pyrometer with 250 different wavelengths in the range of 850 to 1650 nm. The accuracy of the pyrometer was validated using a K-type thermocouple probe in a controlled environment at different elevated temperatures. The patented algorithm of the multiwavelength pyrometer along with its reported emissivity are both elucidated. Emissivity measurements of Cu and Ti-6Al-4V powders having different particle sizes and temperatures will be presented. The results show an increase in emissivity with the increasing temperature cycle and a constant emissivity during the cooling cycle. Behavior of the emissivity maps is discussed along with the issues encountered with the experimental setup for further improvement.

1 Introduction

Additive Manufacturing, popularly known as 3D printing is a manufacturing process where objects are built layer upon layer from a computer aided design, unlike traditional subtractive or formative manufacturing processes which deal with cutting, drilling, grinding, etc. [1]. The capability to produce complex work pieces which do not require tooling and mold modifications every time there is a change in the design, gives additive manufacturing superiority over traditional processes in the aerospace and automotive industries. While building an object in any AM technology, process control and parameter development is a crucial component. Specifically, in metal AM, obtaining accurate surface temperature measurements has always been a challenge to the researchers because of the instantaneous emissivity changes at different temperatures of the powder bed, phase changes due to high heating and cooling rates, the need to maintain pristine conditions of the processing zone, and complexity of in-situ measurement methods. Pyrometry- a noncontact based temperature measurement system, has been considered as the best possible solution for overcoming the challenges seen with other powder bed fusion temperature measurement techniques. Applications that have similarities with powder bed fusion process such as welding research with a high temperature gradient (1000K/cm) and small puddle physical size also makes

contact based temperature measurement impossible without affecting the temperature and velocity profile [2]. For this reason a noninvasive technique such as multiwavelength (MW) pyrometry can be the solution to this problem. Khan et al. studied a MW pyrometer algorithm for two different techniques- interpolation based pyrometry [2] and least squared based pyrometry [3].

The practical MW pyrometer used in this study, the SpectroPyrometer FMPI (FAR Associates, OH, US) was developed by R. Felice [4]. This pyrometer was used to measure the accurate surface temperature of powder bed while at elevated temperatures. The intensity of the radiation detected along with the reported emissivity of the measurement at different temperatures is also illustrated for two different grades of powder. The goal of this research is to incorporate accurate surface temperature measurements in additive manufacturing along with emissivity maps for different powders for in-situ monitoring with IR thermography. The MW pyrometer studied in this experiments not only provides opportunity for accurate surface temperature measurements but also produces emissivity maps as a function of temperature and wavelength, which is key in an IR thermography monitoring system.

2 Theory and Algorithm

The MW pyrometer used in this study uses the plank's radiation equation (1), which employs two distinct wavelengths for each calculation. After calculating the temperature, it uses the temperature value to measure emissivity substituting it back in the plank's equation (2) at a specific wavelength and corresponding intensity value.

$$T = \frac{\left(\frac{1}{\lambda_1} - \frac{1}{\lambda_2}\right)}{\ln R - 5\ln\left(\frac{\lambda_2}{\lambda_1}\right)} \tag{1}$$

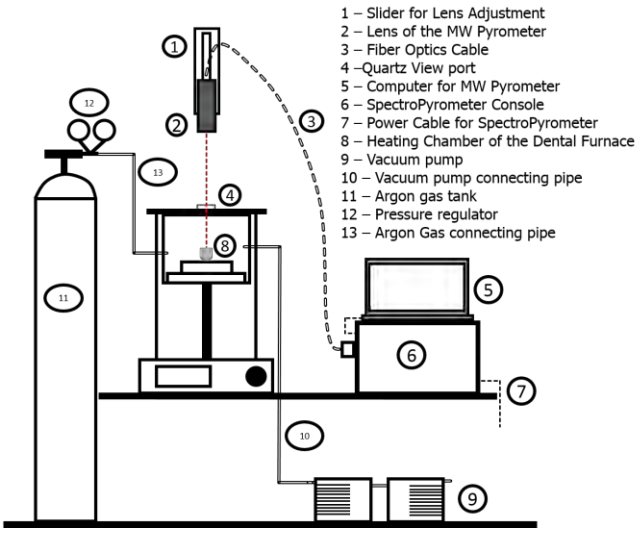

Fig. 1. Experimental setup

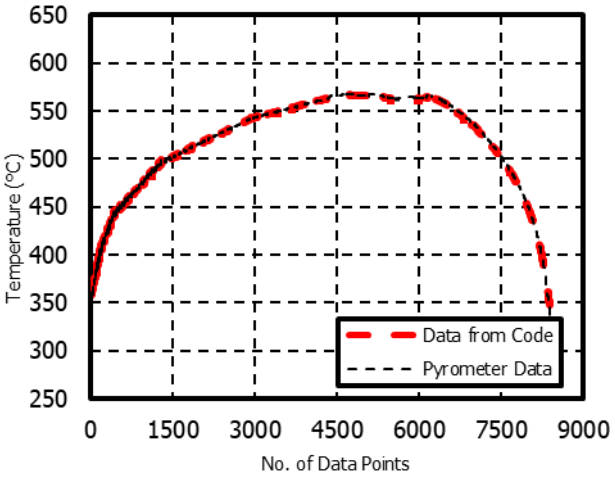

Fig. 2 Temperature results from the MW pyrometer with the temperature results from MATLAB code.

$$\varepsilon = \frac{H_\lambda \lambda^5 \left[e^{\frac{hc}{\lambda K_B T}} - 1 \right]}{2hc^2} \quad (2)$$

In equation (1) and (2), T is the individual two wavelength temperature, λ_1 and, λ_2 represent the specific two wavelengths selected, R is ratio of the generated spectral intensity $I_{\lambda_1}/I_{\lambda_2}$, λ is one of said distinct wavelengths at which radiation is quantified, H_λ is the radiation quantified at wavelength λ, h is Plank's constant, c is speed of light, K_B is Boltzman's constant.

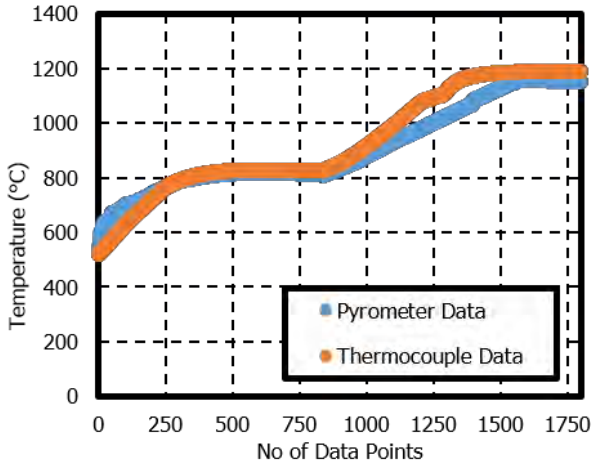

Fig. 3 Heating cycle temperature

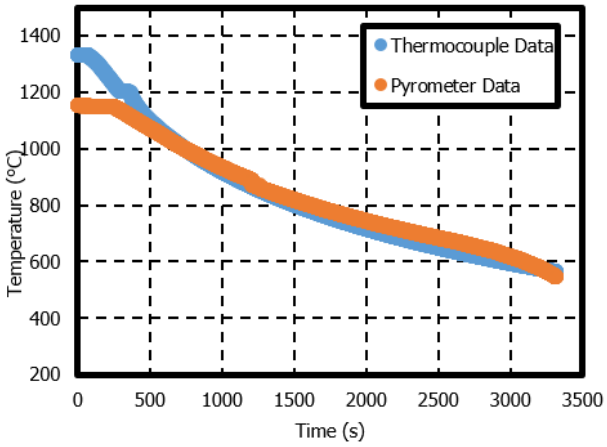

Fig. 4 Cooling cycle temperature

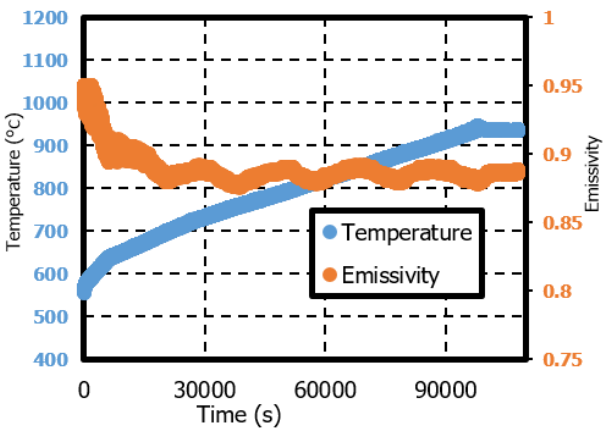

Fig. 5 Heating cycle temperature and emissivity vs. time curve for Cu powder

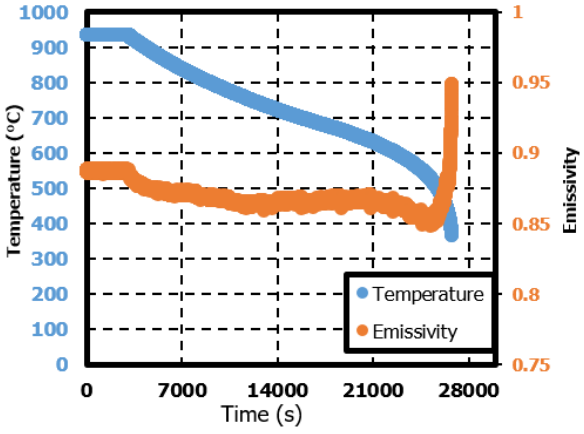

Fig. 6 Cooling cycle temperature and emissivity vs. time curve for Cu powder

3 Experimental Procedure

3.1 Experimental Setup

To simulate the environment inside a powder bed fusion chamber, a dental furnace was modified for optical access with controlled flow of argon inside the chamber. The setup consisted of a slider to adjust the optics focal length position, an argon tank with a pressure regulator, a vacuum pump, a quartz crucible (part # 319T050, Quartz Sci. Inc., OH, USA), a quartz view port at the top of furnace chamber, the SpectroPyrometer console, and a computer with the pyrometer program. Ultra-high purity (UHP) argon i.e. 99.9995% pure argon, was introduced into the furnace at a pressure of 3 psi. Fig. 1 shows the experimental setup used in this study. In addition, MATLAB code was developed to validate the measurements of the pyrometer, which are shown in Fig. 2. The code and the pyrometer measurements holds ±4°C accuracy.

3.2 Materials Studied

Two different powder materials were studied in this experiment, a Ti-6Al-4V titanium alloy and unalloyed copper (Cu). To determine the size distribution of the powder the Camsizer X2 (Retsch Technology GmbH, Retsch-Allee, Haan, Germany) particle size analyzer was used. For Cu powder the mean size distribution measured was 85.8 µm and for Ti-6Al-4V powder it was 53 µm. Both the powders were of electron beam powder bed fusion (EPBF) grade. To validate the measurement of the pyrometer, a K-type thermocouple probe developed by OMEGA Engineering (OMEGA Engineering Inc., Connecticut Ave., Norwalk, CT, USA) was introduced in very close proximity of the powder surface where the pyrometer lens was focused to take measurements. Samples of the Ti-6Al-4V and copper powders were collected and characterized using a variable pressure tabletop microscope from Hitachi (TM1000, Hitachi, Ltd., Tokyo, Japan).

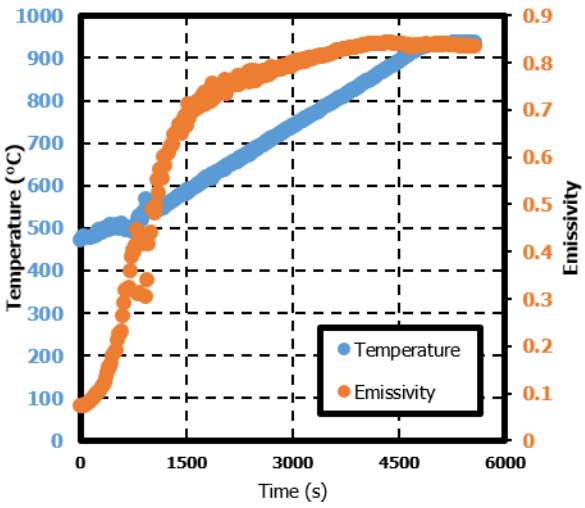

Fig. 7 Heating cycle temperature and emissivity vs. time curve for Ti-6Al-4V powder

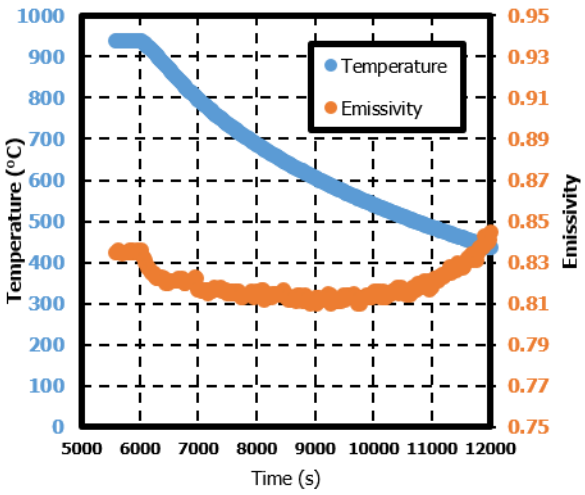

Fig. 8 Cooling cycle temperature and emissivity vs. time curve for Ti-6Al-4V powder

4 Results and Discussions

Fig. 3 and Fig. 4 show the heating and cooling cycle temperature measured by the thermocouple and the pyrometer. The furnace was raised to 800°C and 1200°C for two hold stages and subsequently cooled down. The measurements show a ±6°C average accuracy between the pyrometer and the thermocouple.

Fig. 5 shows the temperature and emissivity vs. time curves for Cu powders during the heating cycle. It can be seen that the emissivity of the Cu powder first decreases drastically from a value of 0.95 to 0.88 for a temperature rise from 600°C to 700°C and then continues to hold that value. The SEM images of the Cu powder studied in this experiment revealed high amounts of satellites and oxidation of the particles during the heating cycles. Oxidation and increased number of satellites which are an indication of high surface area, could both be the reasons behind higher emissivity values. Fig. 6 shows the temperature and emissivity vs. time curves for the same powder but for cooling cycle. In this scenario, the emissivity dropped slightly with the decreasing temperature and increases sharply to temperature below 550°C. This counterintuitive phenomenon could refer to physiochemical changes in Cu powder during the heating cycle and may have retained those changes as the powders cooled down to lower temperatures which dominates the intensity radiated over the temperature change. High emissivity at low temperatures were also reported by Sih et al. [5] who studied Iron powder with porosity of 0.56. In their experiment, the emissivity of the powder rose from 0.7 to 0.95 for a temperature rise from 400°C to 1000°C.

Fig 7. refers to the temperature and emissivity vs. time curves for Ti-6Al-4V powders during the heating cycle. There was a sharp increase of emissivity from 500°C to 600°C from a value of 0.1 to 0.7. This increase may be due to oxidation taking place during this heating process due to the moisture content trapped inside the furnace. Further increment in temperature increased the emissivity to 0.83 as the changes in emissivity slowed down to 900°C. Fig. 8 shows the cooling cycle for the same powder and much like with Cu powder, the emissivity dropped slightly to a lower value of 0.81, then increases rapidly as soon as the powder cooled down below 600°C.

5 Conclusions

This experiment provided an in-sight as to how accurate surface temperature measurements in powder bed fusion additive manufacturing technology can be achieved using multiwavelength pyrometer for process control and parameter development. The measured temperature from the MW pyrometer used in this study is comparable to steady state contact based temperature measurement techniques giving the obtained measurements further validity. In addition, the emissivity measured at different temperatures using Plank's law can be a vital tool as it works as an input parameter in IR thermography. The emissivity was measured at different temperatures for two different powder materials having different particle size. Increasing emissivity with the increment of temperature was seen, while it was almost constant during the cooling cycle. The sharp increase in emissivity values during the cooling cycle after 600°C can potentially be attributed to permanent physiochemical changes in powder particles. However, this hypothesis need further investigation. In addition, the moisture content present inside the

furnace may have caused the powder particles to oxidize creating a significant concern for the current experimental setup even when it was purged with argon gas. Further modifications may be required to produce emissivity maps of powders without oxidation.

References

[1] F42 Committee, "Standard Terminology for Additive Manufacturing Technologies," ASTM International.

[2] M. A. Khan, C. Allemand, and T. W. Eagar, "Noncontact temperature measurement. I. Interpolation based techniques," *Rev. Sci. Instrum.*, vol. 62, no. 2, pp. 392–402, Feb. 1991.

[3] M. A. Khan, C. Allemand, and T. W. Eagar, "Noncontact temperature measurement. II. Least squares based techniques," *Rev. Sci. Instrum.*, vol. 62, no. 2, pp. 403–409, Feb. 1991.

[4] R. A. Felice, "The Spectropyrometer—a Practical Multi- wavelength Pyrometer," *AIP Conf. Proc.*, vol. 684, no. 1, pp. 711–716, Sep. 2003.

[5] S. S. Sih and J. W. Barlow, "The Prediction of the Emissivity and Thermal Conductivity of Powder Beds," *Part. Sci. Technol.*, vol. 22, no. 4, pp. 427–440, Oct. 2004.

APPLICATION OF HIGH TEMPERATURE DIGITAL IMAGE CORRELATION AND SCANNING ELECTRON MICROSCOPY TO ACCELERATED CREEP TESTING

R. Mach[1], J. Pellicotte[1] and C. Stewart[1]*
[1] Department of Mechanical Engineering, University of Texas at El Paso, El Paso, TX 79968, USA;
* Calvin Stewart (cmstewart@utep.edu)

Keywords: *Accelerated Creep Testing (ACT), High Temperature Digital Image Correlation (HT DIC), Scanning Electron Microscopy (SEM), Stepped Isostress Method (SSM), Stress Relation Test (SRT)*

ABSTRACT

As new candidate materials for power generation are manufactured, scientists must subject these new alloys to physical experimentation to gather the necessary empirical evidence for material qualification of long-term creep. Conventional creep tests (CT) are traditional tests which produce full creep deformation curves; however, these tests may last up to 10^5 hours which is unrealistic when new alloys must be characterized. Due to the time dependency of CTs, Accelerated creep testing (ACT) are utilized. ACTs are a well-established method to reduce the time for material qualification; though, extensive research has only been conducted on carbon reinforced fibers.

In this study, ACTs, Stepped Isostress Method (SSM) and Stress Relaxation Test (SRT), are applied to nickel-based super alloy Inconel 718 (IN718) at 650°C to gather long-term creep behavior properties. Short-term conventional creep tests are conducted to validate the creep master curves generated from the ACTs. Digital Image Correlation (DIC) is used to observe the stresses and deformations from both the short-term CT and ACTs. Scanning Electron Microscopy (SEM) permits the comparison of material characterization between CTs and ACTs.

Material scientists will be able to rapidly experiment on new candidate materials. This allows for the potential to reduce the time to implement new creep resistant alloys from decades to months. In addition, this knowledge can be integrated into the design procedure for the next generation of Fossil Energy power generation.

1. STEPPED ISOSTRESS METHOD (SSM)

The development of new alloys requires accelerated methods to reduce the time to characterize material behavior. Most of these methods are based on the time-temperature-stress-superposition-principle (TTSSP) [1]. One such method, the time-stress superposition principle (TSSP) has been used to build creep master curves of viscoelastic materials [2]. In order to generate the creep master curves using TSSP, several specimens are tested at various stresses at a constant temperature. The data gathered from these experiments are then shifted based on a stress factor, ϕ_σ^T, and reference stress, σ_0, to form a creep master curve as shown in Fig. *1*. While the TSSP is able to produce creep master curves, the uncertainty of a materials creep behavior is not preserved.

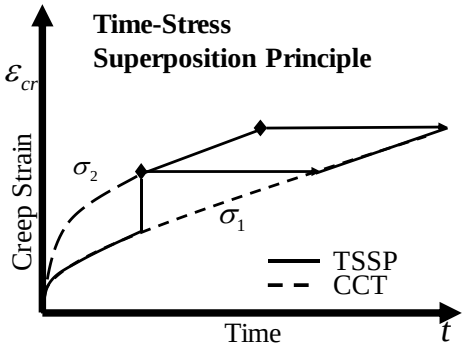

Fig. 1. Generation of master curve using TSSP

Based on the TSSP, a new accelerated creep test was developed. The stepped isostress method (SSM) takes a single specimen and subjects the specimen to several step-wise increases of stress while temperature is constant [4]. At each stress-step, a creep curve is obtained; these curves can then be adjusted to produce a master curve. In order to improve the current process for SSM, which is based on fitting different shifts to polynomials, a modified theta projection model is used to find the creep strain, ε_{cr}, as shown in Eq. (1):

$$\varepsilon_{cr} = \theta_1(1-e^{-\theta_2(t-t_0)}) + \theta_3(e^{\theta_4(t-t_0)}-1) \tag{1}$$

where θ_1 scales the primary regime, θ_2 controls the exponential decay of the primary regime, θ_3 scales the tertiary regime, θ_4 controls the exponential acceleration, t is the real time, and t_0 is the virtual start time at each stress-step [5]. Taking the derivative of the equation above results in the creep strain rate, $\dot{\varepsilon}_{cr}$, as shown in Eq. (2).

$$\dot{\varepsilon}_{cr} = \theta_1\theta_2 \exp(-\theta_2(t-t_0)) + \theta_3\theta_4 \exp(\theta_4(t-t_0)) \tag{2}$$

Fitting the data to the theta projection model allows for real physical properties to describe the material rather than just fitting data to fit a creep curve.

2. STRESS RELAXATION TEST (SRT)

The Stress Relaxation Test (SRT) is an ACT that can predict up 10^5 hours of creep-strain-rate data within a 20-hour experiment [7]. SRT can build multiple isotherms of data on a single specimen, determine activation energies, and generate a master minimum creep rate curve [9].

During SRT, the total strain is held constant, stress is recorded (over time) using a load cell, and temperature is held constant as observed in [Eq.(3)]

$$\varepsilon_{cr}(t) = \varepsilon_{tot} - \frac{\sigma(t)}{E} - \alpha\Delta T \tag{3}$$

where ε_{tot} is the total strain, $\sigma(t)$ is the stress data, E is Young's modulus, ε_{cr} is the creep strain, and $\alpha\Delta T$ accounts for the thermal expansion. While total strain and Young's modulus are constant, as time passes the creep strain rises to account for the relaxation of stress. Using strain

decomposition, the stress-time data is converted to stress versus creep-strain-rate through regression analysis. Regression is performed on stress data, $\sigma(t)$, to generate a function, $f(t)$, as shown below

$$\sigma(t) = f(t) \tag{4}$$

Creep-strain-rate is obtained by taking creep strain [Eq. (3)], replacing the stress data with the function [Eq. (4)], and differentiating with respect to time as follows

$$\begin{aligned} \dot{\varepsilon}_{cr} &= \frac{d\varepsilon_{cr}}{dt} = \frac{d}{dt}\left[\varepsilon_{tot} - \frac{f(t)}{E} - \alpha\Delta T \right] \\ &= -\frac{d}{dt}\left[\frac{f(t)}{E}\right] \end{aligned} \tag{5}$$

where an analytical solution exists.

3. HIGH TEMPERATURE DIGITAL IMAGE CORRELATION

Digital Image Correlation (DIC) can provide an accurate measurement of a specimen as it undergoes deformation. Accurate measurements can be taken at a point or an entire field containing strain gradients either at ambient temperature or elevated temperature. When conducting DIC at elevated temperature, however, precautions must be taken to ensure accurate measurements. The first is that heated air near the furnace window must be mixed with the surrounding area to ensure a constant index of refraction [6]. All glass in view of the DIC software must also be of high quality to ensure the images captured are not distorted [6].

It is important to use DIC when conducting accelerated creep testing in order to observe the strains and compare them with strains from conventional creep testing. The setup for this project consists of coating the specimen with a black and white random speckle pattern, a camera stand, a 2.0 Megapixel Digital Camera (1624 x 1224 @ 30 fps), a high temperature 450nm blue C-Mount lens filter, a 450nm blue Light-Emitting Diode (LED) focused light source, a 3D printed mount for the LED light, Correlated Solutions Vic Snap 8 software, and Correlated Solutions VIC-3D digital image correlation system as shown in Fig. *2*. Strain results in y-direction gathered from a Monotonic Tensile Test are observed in Fig. *3*.

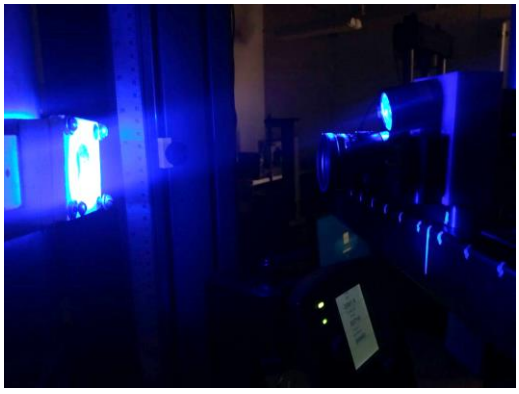

Fig. 2. High temperature DIC setup showing the 2.0 Megapixel Digital Camera and the blue light emitting diode, directly aligned with the specimen through the view port of the split tube furnace.

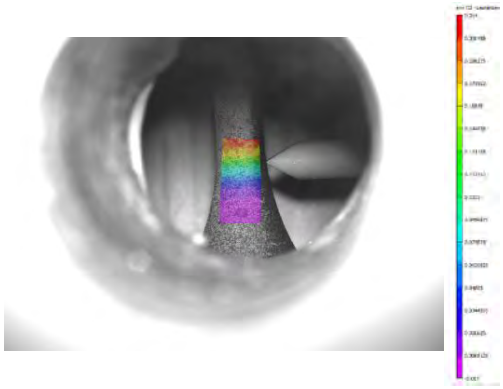

Fig. 3. Results for a Monotonic Tensile Test for IN718 at 650°C

4. SCANNING ELECTRON MICROSCOPY (SEM)

Scanning Electron Microscopy (SEM) is similar to light microscopy; however, SEM images are formed by detecting secondary and backscattered electrons that are emitted following collision with the specimen in a vacuum sealed chamber [11]. The vacuum chamber is required for SEM as it allows the electrons to travel from the source to the desired specimen while remaining unaffected. With a beam of electrons reflected from a specimen, images of high resolution are created as shown in Fig. *4* [12]. These images will allow the use of material characterization and failure analysis for the CTs, SSM, and SRT methods.

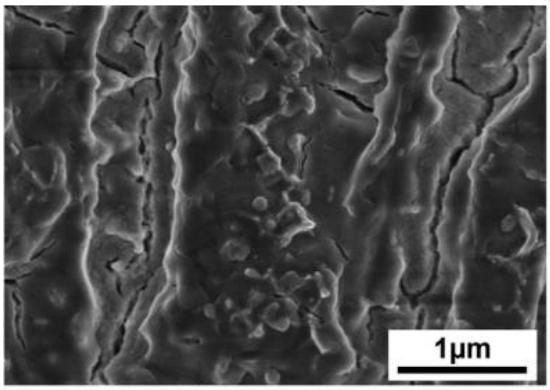

Fig. 4. High-Magnification SEM image showing IN718 microstructure

To begin SEM on a specimen there are steps to follow to ensure high quality and usable images [10]. First, you begin by obtaining a section of your specimen using a diamond cutting saw with optimal cooling to ensure no further damage on the specimen. Second, the specimen is mounted into a resin mold. Third, using different grit sandpapers the surface is prepared for polishing. Fourth, the resin is polished with solution to eliminate damage introduced by the previous steps. Lastly, if the microstructure is needing to be analyzed the material is etched in a chemical solution.

The process of SEM is categorized into five distinct steps: emission, attraction, direction, deflection, and detectors as shown in Fig. *5* [11]. First, electrons are generated and directly emitted towards the specimen placed on the stage. The electrons travel through an anode, a positively charged plate, that attracts the electrons to form a stable beam. Now that there is a stable beam of electrons a magnetic lens is utilized to direct the electrons towards the specimen into a scanning coil. The scanning coil uses a magnetic field to then deflect the beam of electrons about the

specimen to form the desired image. The electrons from the scanning coil reflect off the specimen and get drawn to the detectors, secondary and backscatter, to transfer information to the computer ultimately forming a readable image.

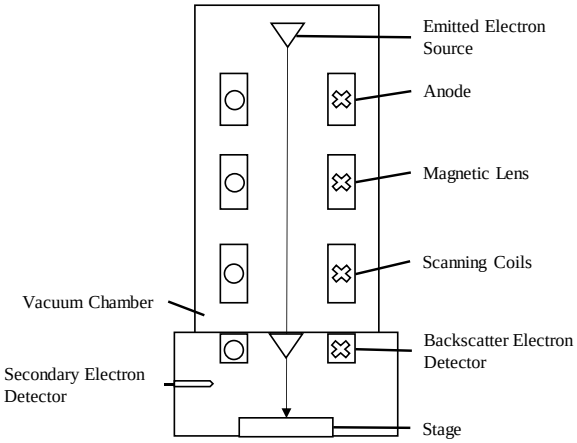

Fig. 5. Schematic of Scanning Electron Microscopy (SEM) machine components

5. CONSLUSION

As the demand for the implementation of new materials rise, ACTs are utilized. Digital Image Correlation (DIC) and Scanning Electron Microscopy (SEM) are methods that will increase efficiency and overall analysis of the Stepped Isostress Method (SSM) and Stress Relaxation Test (SRT).

6. REFERENCES

[1] Tanks, J., Rader, K., Sharp, S., & Sakai, T. "*Accelerated creep and creep-rupture testing of transverse unidirectional carbon/epoxy lamina based on the stepped isostress method"*. Composite Structures, 159, 455-462, 2017.

[*2*] Hadid, M., Guerira, B., Bahri, M., & Zouani, A. "*Assessment of the stepped isostress method in the prediction of long term creep of thermoplastics"*. Polymer Testing, 34, 113-119, 2014.

[*3*] Luo, W. B., Wang, C. H., & Zhao, R. G. "*Application of time-temperature-stress superposition principle to nonlinear creep of poly (methyl methacrylate) In Key engineering materials"*. Trans Tech Publications Vol. 340, pp. 1091-1096, 2008.

[*4*] Giannopoulos, I. P., & Burgoyne, C. J. "*Prediction of the long-term behaviour of high modulus fibres using the stepped isostress method (SSM)*". Journal of materials science, 46(24), 7660, 2011.

[*5*] Law, M., Payten, W., & Snowden, K. "*Finite element analysis of creep using Theta projection data"*. International journal of pressure vessels and piping, 75(5), 437-442, 1998.

[*6*] Lyons, J. S., Liu, J., & Sutton, M. A. "*High-temperature deformation measurements using digital-image correlation"*. Experimental mechanics, 36(1), 64-70, 1996.

[7] Woodford, D. A. "*Test methods for accelerated development, design and life assessment of high-temperature materials*". Materials & Design, 14(4), pp. 231-242, 1993.

[8] Osgerby, S. and Dyson, B. F. "*Constant Strain-Rate Testing: Prediction of Stress-Strain Curves From Constant-Load Creep Data*". Creep and Fracture of Engineering Materials and Structures, Eds. Wilshore, B. and Evans, R. W., The Institute of Metals, London, 53-61, 1993.

[9] Stewart, C. M., and Chessa, J. F. "*An Accelerated Creep Testing (ACT) Program for Advanced Creep Resistant Alloys for High Temperature Fossil Energy (FE) Applications*". University of Texas at El Paso, 2017.

[10] Akca, E and Trgo, E. "*Metallographic Procedures and Analysis – A Review*". Periodicals of Engineering and Natural Sciences, Vol. 3 No. 2, 2015.

[11] Nanakoudis, A. "*What is SEM? Scanning Electron Microscope Technology Explained*". ThermoFisher Scientific, 2018

[12] Jia. Q, Gu. D. "*Selective Laser Melting Additive Manufacturing of Inconel 718 Superalloy Parts: Densification, Microstructure and Properties*". Journal of Alloys and Compounds, 2013.

Centennial Small-payload Launch Vehicle (CSpLV) - Concept

James C Susen,[1] and Peniel Rodriguez[2]
University of Texas at El Paso, El Paso, Texas, 79902, United States

The Centennial Small-payload Launch Vehicle (CSpLV) project addresses the need for an orbital launch vehicle for the emerging Low Earth Orbit (LEO) small-satellite market. This report details the CSpLV as a viable operational Earth to orbit launch vehicle for the emerging small satellite market. The CSpLV will be a two and a half stage orbital launch vehicle with two Liquid Methane (LCH4)/ Liquid Oxygen (LOX) stages and four Solid Rocket Boosters (SRB). The CSpLV utilizes many state-of-the-art technologies including but not limited to carbon composites, LCH4/LOX propellants, additively manufactured components and a closed pressure fed engine cycle. The pressure fed engine cycle has the potential to be a game changing technology for the small-satellite space launch market by eliminating the need for expensive turbo machinery. The CSpLV project will provide the design of an affordable orbital launch vehicle capable of sending small payloads into orbit inexpensively, reliably, and often. Eliminating the need for pumps will significantly reduce the expense and complexity of small orbital launch vehicles.

I. Nomenclature

I_{sp}	=	specific impulse
ΔV	=	change in velocity
V_e	=	exhaust velocity
m_0	=	initial mass
m_f	=	final mass
F	=	thrust
f_{inert}	=	inert mass fraction
m_{pay}	=	payload mass

II. Introduction

The CSpLV is a multistage to orbit launch vehicle consisting of an upper stage, core stage, and 4 solid rocket boosters. The CSpLV is an effort by the University of Texas at El Paso (UTEP) and the NASA MIRO Center for Space Exploration and Technology (cSETR) to bring innovating technology to the orbital launch vehicle market. Driven by the mission of sending small-payloads to orbit inexpensively, reliably and often.

The space industry is expected to grow significantly over the next two decades. Currently the global space economy is $350 billion as reported by the Space Frontier Foundation. Goldman Sachs estimates the global space industry to reach $1 trillion by 2040 and Morgan Stanly estimates $1.1 trillion by 2040. That is relatively low compared to Bank of America Merrill Lynch report estimating the space industry to reach $2.7 trillion by 2040 [1]. The small-payload market is estimated to reach $69 Billion and an estimated 11,746 small-satellites by 2030 according to a forecast by Frost & Sullivan [2]. The number of large expensive Geostationary Earth Orbit, (GEO) satellite orders has been decreasing, while the number of LEO satellite orders have been increasing. The trend suggests that the future satellite growth is likely to be in the small satellite LEO market [3]. The need for competitive small-payload launch vehicles to meet this demand is critical for the United States to remain the leader in space technology and exploration.

The need for a small payload launch vehicles began with the retirement of the Solid Controlled Orbital Utility Test (SCOUT) rocket in 1994 [4] [5]. The scout launch vehicle was a four to five stage small payload orbital launch vehicle utilizing solid rocket motors for all stages. The SCOUT was used to launch small payloads into orbit starting in 1961 and had its final launch in 1994. The need is beginning to fill with new innovative companies like Rocket Lab offering small-sat launch capabilities [6].

---

[1] Team Lead for Lunch Vehicle, UTEP cSETR
[2] Research Assistant for Launch Vehicle, UTEP cSETR

In 2003 DARPA released a Phase 1 solicitation for a small launch vehicle concept. DARPA identified that a launch vehicle with a flyaway cost (including launch vehicle, range costs, consumables, payload integration and limited mission assurance activities) of $5 to $10 million could have a profound impact on small launch vehicles [7]. Although the Falcon 1 was retired the project can be considered a success with the Falcon 1 successor the Falcone 9 taking a large share of the orbital launch market [8]. However, with the retirement of the Falcone 1 rocket there is still a need for small payload orbital launch vehicles.

III. Concept Development

The research conducted by the Launch Vehicle team is intended to implement new technology and innovations to the orbital launch vehicle market. The CSpLV project is an effort to bring transformative technology to the space launch industry by bringing the orbital launch vehicle to the university level. Satellites previously the domain of governments and large corporations are now built and flown buy universities, individual crowd funders [9] and High Schools [10]. Thanks to recent technologic advances, such as additive manufacturing of super alloys, carbon composites materials compatible with cryogenics, and powerful miniaturized computers, launch vehicle technology has become more accessible on the university level. Just as the cube satellite technology has spurred enormous growth in the small satellite market, the CSpLV project hopes to become the spark that starts the same groundbreaking innovation in small payload launch vehicles.

Commented [j1]: Find a different adjective.

Commented [j2]:

Commented [j3]: Try to avoid repeating words and phrases in consecutive sentences. You used "Just as" to start your next sentence.

Commented [j4]: There is a reason I'm using game changing a lot ☺

Commented [j5R4]: It is repetitive. Find a different adjective.

Commented [j6]: Still like Revolution better

Commented [j7R6]: This is a technical paper, not a proposal or an advertisement campaign. Know your audience and tailor your noun and adjective structure to them, not your preferences.

IV. Pressure Fed Launch Vehicle

A. Mission

The mission is to place a 100 lbm payload into a 200-mile circular orbit with a flyaway cost of $1.5 million USD. The mission is derived from the NASA Technology Roadmaps TA 1: Launch Propulsion Systems [11]. The NASA Technology Roadmaps clearly define what technology NASA considers game changing. The CSpLV project is an attempt at creating this technology.

B. Requirements

The CSpLV project is designed to take advantage of key technology developed by the cSETR. The Center is currently working on LCH4/LOX combustion devices including spark igniters, 5 lbf reaction control and roll control thrusters, 500 lbf upper stage engine, and 2,000 lbf first stage engine. TMD Defense and Space LLC. has partnered with the cSETR, bringing with them thirty years of solid rocket motor experience. The combination of cSETR combustion research and technology and TMD Defense and Space solid rocket motor expertise brings the CSpLV concept into focus. The initial vehicle design will be a combination of solid rocket motors and LCH4/LOX engines, reaction control and roll control thrusters with electric spark igniters.

Commented [j8]: As a rule of thumb, spell out whole numbers less than ninety-nine, unless it is a part of a title.

Below is a list of vehicle requirements:

1. The use of Solid Rocket Boosters (SRB)
2. Upper stage utilizing the 500 lbf CROME LCH4/LOX engine
3. Boost stage utilizing a combination of 2,000 lbf CROME-X LCH4/LOX engines
4. Roll control and reaction control systems utilizing the 5 lbf LCH4/LOX thrusters
5. 2,000 lbf, 500 lbf engines and 5 lbf thrusters with electric spark ignition
6. 100 lbm payload to a 200-mile circular orbit

C. Assumptions

Several assumptions are made in the CSpLV concept feasibility study. A pressure fed Earth to orbit launch vehicle has not ever been successfully flown, therefore the launch vehicle team has conducted a feasibility study to determine if a pressure fed launch vehicle is possible. Several assumptions were made based on the requirements for the concept vehicle. Once the requirements were established a set of assumptions were established to simplify the problem enough to solve quickly and still get meaningful results. The Launch Vehicle team set up the assumptions to establish whether an Earth to orbit pressure fed launch vehicle is potentially possible.

$$\Delta v = v_e \ln \frac{m_0}{m_f}$$

The tool the Launch Vehicle team is using to validate the CSpLV concept is the ideal rocket equation. The ideal rocket equation is not a substitute for detailed models and simulations, but it is a powerful tool for determining if a mission is not possible with a few variables. The ideal rocket equation can be broken down into three main parts ΔV, V_e, and m_0/m_f. The ΔV represents the mission. In the case for the CSpLV the ΔV represents the velocity required to reach orbit. V_e represents the I_{sp} of the CSpLV engines and motors. The I_{sp} for the solid rocket motors is derived from other successful launch vehicles and the I_{sp} for the engines is given to the Launch Vehicle team by the CROME and CROME-X team. The m_0/m_f portion of the ideal rocket equation represents the inert mass fraction of the CSpLV, The inert mass fraction comprises the majority of the calculations for the CSpLV feasibility study.

Commented [j9]: Fact. Or make a comment for that matter. ☺ Jokes

The first assumption mad by the Launch Vehicle team is the ΔV required for orbit. The velocity required to stay in orbit is very well understood and predictable, however getting to orbit from the ground inherently has ΔV losses that are not as predictable. The losses include gravity, steering, drag and Earth rotational losses. Determining the ΔV losses without flying the rocket is difficult, so for this concept feasibility, the Launch Vehicle team is utilizing the ΔV loss from the Delta II rocket. The Delta II rocket has recently been retired and has a long history of successful launches [12]. The Delta II configuration is very close to what the Launch Vehicle team is proposing for the CSpLV. There are large contrasting differences between the two rockets. The size of the vehicles and payloads are different, the propellants and engine cycles are different, and the price per vehicle are different. However, the gravity, steering, drag, and Earth rotational losses will likely be very similar [13].

ΔV loss from the Delta II

- Gravity loss = 3773 ft/s
- Steering loss = 108 ft/s
- Drag loss = 446 ft/s
- Rotational loss = -1138 ft/s

Combining the losses together with the orbital velocity we get an estimated ΔV = 30,200 ft/s. The research team compared the estimated ΔV to historical known ΔV of various rockets including orbital velocity, gravity loss, drag loss, steering loss, and rotational loss. It can be seen that correlating the estimated ΔV for the CSpLV to other orbital rockets, the estimate is reasonable [14].

Below is a list of the various rockets being compared to CSpLV:

- Ariane A-44L =29,980 ft/s
- Atlas I =30,325 ft/s
- Delta 7925 =28,917 ft/s
- Space Shuttle =29,810 ft/s
- Saturn V =30,404 ft/s
- Titin IV/Centaur =30,207 ft/s

The exhaust velocity (V_e) is directly proportional to the I_{sp} of the engine. The CSpLV uses the CROME and CROME-X engines as defined by the launch vehicle design requirements along with solid rocket boosters for the zero stage. While solid rocket motors have been around for a long time and are well understood, LCH4/LOX rocket engines are new and at the time of this paper have never flown into space. However, the future of spaceflight is headed toward LCH4/LOX engines with Blue Origin building a factory for the LCH4/LOX BE-4 engine [15], Space-X developing the Raptor engine [16], and Aerojet Rocketdyne working on LCH4/LOX engines for commercial use and NASA [17].

The CROME and CROME-X engines are still in development and the I_{sp} for the engines can only be estimated. LCH4/LOX engines have not flown in space resulting in a lack of flight history as well. The I_{sp} used for the CSpLV concept are based on estimates given by the CROME and CROME-X engine teams and are considered conservative for the first-generation engines. As the engines develop and the LCH4/LOX combustion process is better understood, the I_{sp} will increase and the performance of the CSpLV will increase with it. The accepted I_{sp} for the CROME engine is 290 seconds vacuum and the I_{sp} for the CROME-X engine is 260 seconds. The CROME-X engines on the core stage of the CSpLV are going to launch from sea level and then rise through the atmosphere. The nozzle expansion ratio is

fixed and the I_{sp} and thrust of the engines will change as the rocket ascends. For this concept vehicle study, the team is assuming the thrust and I_{sp} of the engines are constant making the I_{sp} numbers averages for the length of the burn. Ideally, the change in thrust and I_{sp} would be taken into account, however for this concept feasibility, the team will address the issue by using the conservative numbers above for the I_{sp} and assume the thrust is a design decision.

The SRBs are ideally modeled with constant thrust and constant I_{sp} for simplicity. SRBs have been used from the beginning of the U.S. space program and are very well understood, several orbital rockets have used solid rocket motors. Solid rocket motors have been used as strap on boosters, entire stages, and in some cases, they are used for every stage. For the CSpLV the strap on SRB will have an I_{sp} of 240 seconds and an inert mass fraction of 0.13. The research team looked at solid rocket motors for launch vehicles that have successfully flown to verify that the team's numbers are reasonable [14]. On inspection the heritage SRB numbers look consistent with the Launch Vehicle team numbers.

SRBs used for comparison:

I_{sp}

- Shuttle RSRM = 268 s Vacuum
= 241 s Sea Level
- Shuttle ASRM = 269 s Vacuum
= 240 s Sea Level
- Titan Titan IV = 272 s Vacuum
= 235 s Sea Level
- Titan SRMU = 283 s Vacuum
= 242 s Sea Level
- Delta II Castor IVA = 267 s Vacuum
= 238 s Sea Level
- Delta II GEM = 274 s Vacuum
= 243 s Sea Level

f_{inert}

- Shuttle RSRM = 11.7%
- Shuttle ASRM = 10.5%
- Titan Titan IV = 18.5%
- Titan SRMU = 9.8%
- Delta II Castor IVA = 12.9%
- Delta II GEM = 9.06%

The f_{inert} for the upper and core stages cannot be estimated or compared to successful launch vehicles from the past, because there have not been any successful Earth to orbit launch vehicles utilizing a pressure fed system [18]. The challenge of a pressure fed system is the mass of pressurant (Helium) requited and the mass of the pressurant tanks and propellant tanks. Traditionally turbomachinery is used to pump low pressure propellant from the propellant tanks to the engine. This greatly reduces the weight of the tanks because they can be kept at a relatively low pressure (30-50psi). The CSpLV will utilize high pressure pressurant and propellant tanks. The tank walls need to be thick to accommodate the high pressure. The Launch vehicle team looked at three different materials appropriate for cryogenic use to determine the inert mass fraction of the CSpLV upper and core stages. The materials chosen were 316 stainless steel, 2090 Al-Li alloy, and IM7/977-2 Composites. An isentropic layup for the carbon composites was used for the analysis for simplification.

The mass of the liquid stages can only be estimated. The Launch Vehicle team is using the mass of the pressurant and propellant tanks and multiplying that number by a mass growth of 100%. That makes the inert mass of the rocket double the mass of the pressurant and propellant tanks including the helium. The tank pressure needed for the CROME and CROME-X engines is 400 psi. The tanks are given an ultimate load factor of 1.65 as a margin of safety. NASA uses an ultimate load factor of 2.0 for space flight pressure vessels, however an ultimate load factor of 1.5 is given for U.S. FAA regulations. The 1.65 used for the CSpLV tanks is less than NASA standard for a space flight tank but is higher than required by the U.S. FAA [19]. The Launch vehicle team is also using a factor of safety of 1.5 for the vehicle based off of the factor of safety used for the ARIS I and ARES V composites tanks.

D. Evaluation

Upper stage

The f_{inert} for the upper stage is calculated using 1,200 lbm of LCH4/LOX propellants at a 2.7 mixture ratio.

- IM7/977-2 carbon composites tanks f_{inert} = 17.0%
- 2090 aluminum lithium alloy tanks f_{inert} = 30.1%
- 316 Stainless steel tanks f_{inert} = 54.3%

Core Stage

The f_{inert} for the core stage is calculated using 10,200 lbm of LCH4/LOX propellants at a 2.7 mixture ratio.

- IM7/977-2 carbon composites tanks f_{inert} = 14.9%
- 2090 aluminum lithium alloy tanks f_{inert} = 26.8%
- 316 Stainless steel tanks f_{inert} = 50.6%

V. Down selection

After calculating the inert mass fractions for the upper and core stages it is clear that the liner less carbon composites tanks are the only viable option for a pressure fed launch vehicle. The aluminum alloy and stainless-steel tanks give a negative value for the rocket non-feasibility equation, which means a pressure fed rocket built out of either material would not produce the ΔV required for orbital insertion regardless of size. For juxtaposition, the ΔV for the three tank materials is given below.

- IM7/977-2 carbon composites tanks ΔV = 30,300 ft/s
- 2090 aluminum lithium alloy tanks ΔV = 22,800 ft/s
- 316 Stainless steel tanks ΔV = 13,600 ft/s

The liner less carbon composites tanks are the only tanks capable of providing the specific strength necessary for a pressure fed orbital launch vehicle. The f_{inert} of any of the other materials will result in a ΔV too low to reach orbit assuming a ΔV range of the Delta II being the lowest at 28,800 ft/s and the highest ΔV at 30,400 ft/s.

VI. Conclusion

A pressure fed LCH4/LOX orbital launch vehicle is possible utilizing the latest in liner less carbon composites cryogenic tanks. The research in this paper illustrates why pressure fed earth to orbit launch vehicles have been unsuccessful in the past and why a pressure fed vehicle may be feasible today. Carbone composites materials capable of maintaining strength without micro cracking at cryogenic temperatures have only been around for the last decade and this is a key technology necessary for making a pressure fed vehicle possible. This study also shows that producing a pressure fed orbital launch vehicle without the use of carbon composites would likely result in a launch vehicle either not reaching orbit due to the vehicle being too heavy to produce the required ΔV or exploding along the way due to compromised strength to save weight. Now that carbon composites capable of maintaining strength at cryogenic

temperatures are readily available, a pressure fed Earth to LEO launch vehicle is possible and likely to produce a vehicle that can be used to launch payloads into orbit inexpensively, reliably and often.

Acknowledgments

The Launch Vehicle tam would like to thank Dr. Choudhuri for lending us his vision for this project. Without Dr. Choudhuri's support this project would not be possible. The launch vehicle team would also like to thank Dr. Chessa for lending his knowledge to the team and forcing us to answer the hard questions. The Launch Vehicle team would also like to thank NASA MSFC's James Richard and Pat Lampton whose mentorship forms the foundation of the Launch vehicle team's knowledge.

References

[1] J. Foust, "A trillion-dollar space industry will require new markets," *Space News,* 5 July 2018.

[2] PR Newswire, "Small-satellite Launch Service Revenues to Pass $69 Billion by 2030," *small-satellite-grwth,* 07 January 2019.

[3] C. Henry, "GEO satellite orders continued to underwhelm in 2018," *Spacce News,* 4 February 2019.

[4] U. States, "MSTI-2," [Online]. Available: https://ilrs.cddis.eosdis.nasa.gov/missions/satellite_missions/past_missions/msti_general.html. [Accessed 23 01 2019].

[5] G. E. Reins and Alvis, J. F., "Advanced small launch vehicle study," United States, Dallas, TX, United States , May 1971 - Feb. 1972.

[6] K. Chang, "Rocket Lab's Modest Launch Is Giant Leap for Small Rocket Business," *The New York Times,* 10 Nov. 2018.

[7] D. J. Weeks, S. H. Walker, T. L. Thompson, R. L. Sackheim and J. R. London, "The DARPA / USAF Program Small Launch Vehicles," AIAA/USU, Logan, UT; United States, 2006.

[8] J. Bennett, "One Chart Shows How Much SpaceX Has Come to Dominate Rocket Launches," *Popular Mechanics,* 13 July 2017.

[9] "Crowd-sourced satellite heads into space," *Australian Broadcasting Corporation,* 05 08 2013.

[10] "High School Students Send Satellites into Space; Ingersoll Rand Foundation Sponsors STEM Project," *ENP Newswire,* 28 Feb 2018.

[11] National Aeronautics and Space Administration, "NASA Technology Roadmaps TA1: Launch Propulsion Systems," United States, 2015.

[12] A. Heiney, "ICEat-2," National Air and Space Administration, 15 September 2018. [Online]. Available: https://blogs.nasa.gov/icesat2/2018/09/15/icesat-2-successfully-launched-on-final-flight-of-delta-ii-rocket/. [Accessed 31 January 2019].

[13] United Launch Alliance, "Delta II Payload Planners Guide," United Launch Alliance, Littleton, Colorado, USA, 2006.

[14] R. W. Humble, G. H. Henry and W. J. Larson, Space Propulsion Analysis and Design, New York: McGraw-Hill Companies Inc., 1995.

[15] S. Clark, "World's largest methane-fueled rocket engine test-fired by Blue Origin," *Spaceflight Now,* 20 October 2017.

[16] Associated Press, "SpaceX to test methane rocket engine in Miss.," *The Washington Times,* 22 April 2014.

[17] Aerojet, "Aerojet to Test Advanced Liquid Oxygen Liquid Methane Rocket Engine for Lunar Ascent," Arojet, Sacramento, CA, USA, 2009.

[18] M. Woods, "Rocket Failure Brings Favorable Fame," *The Blade,* p. 44, 23 September 1981.

[19] S. M. Arnold, B. A. Bednarcyk, C. S. Collier and P. W. Yarrington, "Spherical Cryogenic Hydrogen Tank PreliminaryDesign Trade Studies," in *48th Structures, Structural Dynamics, and Materials Conference*, Waikiki, HI; United States, 2007.

CHARACTERIZATION OF A PINTLE INJECTOR FOR GAS-SLURRY COMBUSTION

A. Rios[1], M. Chowdhury[1], A. Choudhuri[1] *
[1] Mechanical Engineering, Center for Space Exploration and Technology, El Paso, TX 79968, USA;
* Corresponding author (ahsan@utep.edu)

Keywords*: high pressure, combustion, oxy-fuel, pintle injector*

ABSTRACT

The production of nitrides oxides from the power generation industry are one of the major contributors to the depletion of the ozone layer. Therefore, the energy industry has a great interest in methods that can combine both clean and high energy release, such as pressurized oxy-combustion. This study presents the fluid injection profile of a pintle injection for a pressurized oxy-coal combustor. The injection and spray angles have been recorded through shadowgraph images. Two tips of different orifice sizes have been tested and compared in order to select a tip that provides a small spray angle and high atomization. A mixture of borosilicate glass beads and water at different concentrations by weight are included in the test matrix. It was found in this work that the spray angle decreases as the Total Momentum Ratio decreases. The 2 mm tip presents a low angle with high atomization.

1 Introduction

Oxy-fuel combustion refers to burning a fuel with oxygen resulting in the products carbon dioxide and water vapor [1-3], an approach to cleaner energy generation if applied to coal combustion. In addition, oxy-combustion provides similar or higher efficiencies of air fired systems despite additional parasitic loads of the air separation and carbon capture units [4]. The injector for this method has to properly deliver the oxidizer and fuel, while maintain a constant mixture. Additionally, the injector contributes to the combustion stability. The pintle injector has presented very effective atomization and ensured mixing propellants in rocket engines, associated with high performance in range of $96 - 99\%$ [5]. Thus, this paper presents the fluid flow characterization of a pintle injector with enhanced performance capable of introducing a coal slurry up to 10 bar.

2 Design Methodology

2.1 Injector

A key feature of the pintle injector design is its modularity. Figure 1 presents the schematic of pintle injector design developed in this work. It consists of total 5 components: main body, pintle post, pintle tip, distribution plate, and closing plate. The main body and the pintle post are welded at the top of the main body; the distribution plate is supported by the closing plate and fits into the pintle post. The closing plate threads into the main body. The design allows for the pintle tip and closing plate to be interchangeable. This means that they can be changed for others of different sizing to create a range of sprays, without having to manufacture a new body.

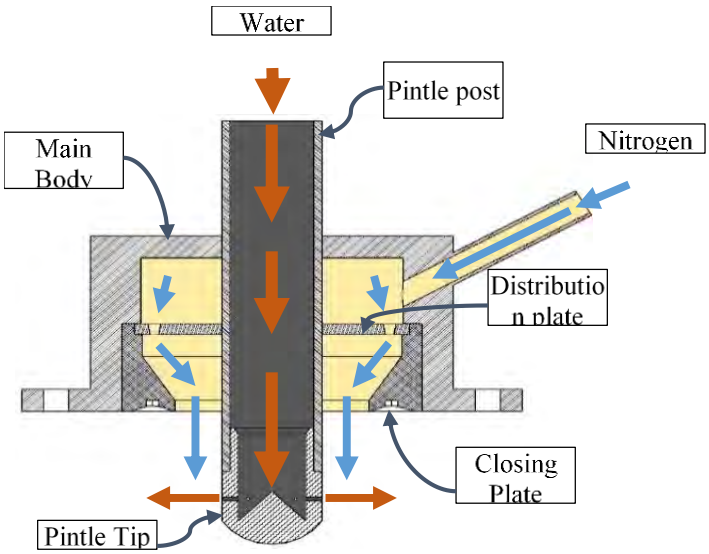

Figure 1 Pintle Injector Cross Section

After defining the properties and mass flowrates for the nitrogen and slurry, and using Eqns (1)- (4) [6], from the design phase, Total Momentum Ratio and the angle of the spray can be mathematically obtained. Starting from an orifice diameter and number of orifices, the total area of the slurry is calculated from Eqn (1)

$$A_{sl} = N\frac{\pi}{4}D_o^2 \tag{1}$$

From the area and the mass flowrate, the velocity of the slurry is calculated, as shown in Eqn (6).

$$v_{sl} = \frac{\dot{m_{sl}}}{A_{sl}\,\rho_{sl}} \tag{2}$$

From the mass flowrates of oxygen and oxygen area, the oxygen velocity can be calculated from Eqn (3)

$$v_o = \frac{\dot{m_o}}{A_o\,\rho_0} \tag{3}$$

The total momentum ratio between the oxygen and the slurry estimated by Eqn (4).

$$TMR = \tan\alpha = \frac{\dot{m_{sl}}v_{sl}}{\dot{m}_o v_o} \tag{4}$$

4 Experimental Results

The glass bead test was first conducted by starting the slurry mixture with high concentration in water content, going from 25% Glass Beads to 75% Water up to 65% Glass Beads to 35% Water. The test matrix was designed to collect data of the performance of the pintle and the system different concentrations of the mixture. This determined the addition of pintle tips with increased orifice size to adjust for the Total Momentum Ratio. Tips with orifices of 1mm, 2mm, 3mm and 5mm were tested for this work. To date, this test has been completed and some results are presented in the next section. The second stage of cold-water test is with the powder coal to determine the exact conditions the fire test will be operated at to achieve the desired results.

The results presented in this paper are for the 40 % Glass Beads: 60% Water mixture. The image presented in **Error! Reference source not found.** (for 2 mm orifice size tip) show the spray of the injector with a constant mass flow of the slurry and different mass flow for the nitrogen, creating a range of spray angles. The detailed test matrix for this work is presented in Table 1.

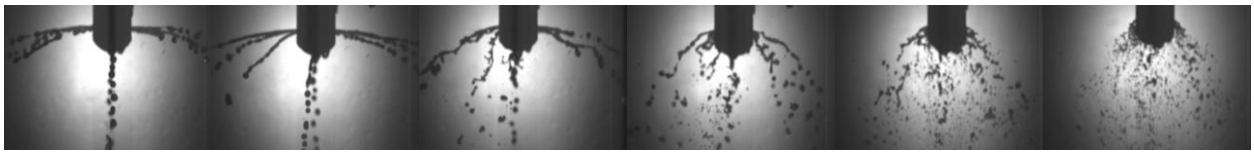

Figure 2 The 2 mm Tip Injection

Table 1: Test Matrix

Tip (mm)	Water Mass Flow (kg/s)	Nitrogen Mass Flow (kg/s)	TMR	Theoretical Angle	Experimental Angle
2	0.04322	0	n/a	90	90
2	0.04322	0.0034	25.10	83	85
2	0.04322	0.0061	15.07	81	77
2	0.04322	0.0071	14.21	79	70
2	0.04322	0.0091	11.95	76	52
2	0.04322	0.0013	7.43	63	45

The experimental results are presented in Fig. 2, where the injection angle as a function of TMR for 2 mm tip. It is evident from the results that with a lower TMR, a lower spray angle can be achieved. Figure 3 also presents the comparison between the experimental and theoretical values for spray angle as a function of TMR. The discrepancy between the

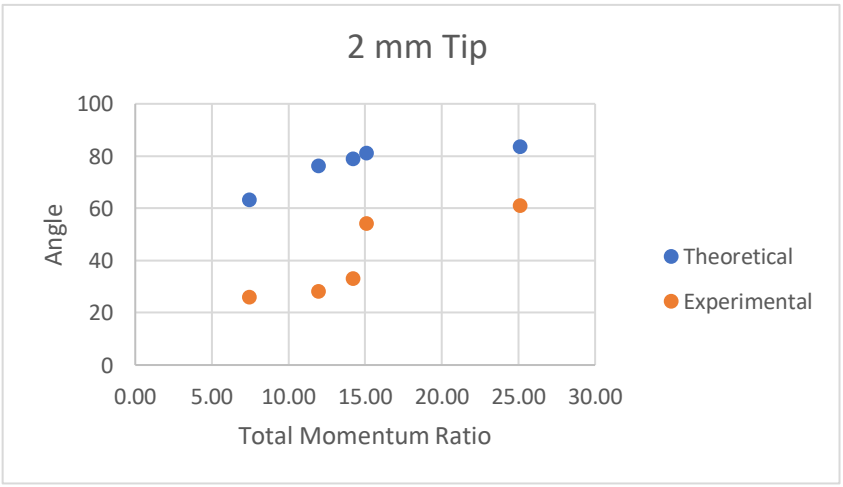

Figure 3 Spray Angle vs TMR for 2 mm tip

theoretical angle and the one measured through experimentation can be observed in both figures.
It is believed that this is due to the fact that the theoretical angle only accounts for same-like phase reactants interacting with each other. The results of the spray angle are an important factor in order to recreate the injection without any impingement inside the combustor when the hot fire test start.

5 Conclusion and Future Work

In summary, this paper presents the slurry flow characterization of a pintle injection with enhanced performance. Pintle injector has been traditionally used for rockets and propellants in the same phase. This study characterizes the injection of a slurry of solid glass beads and liquid water, with gaseous nitrogen acting as the secondary reactant. The result of the tip of 2-in orifice size has been tested and reported. Through shadowgraph, the angle has been measured and compared to the TMR of different sprays to observe the lowest angle where atomization occurs. Future works includes cold water test with coal powder for injector characterization.

Acknowledgement

This research is supported by the US Department of Energy, under award DoE Award Number: DE-FE-0029113 (Program Manager: Mark Freeman). However, any opinions, findings, conclusions, or recommendations expressed herein are those of the authors and do not necessarily reflect the view of the Department of Energy and Air Liquide.

References

[1]Glarborg, P., & Bentzen, L. L., "Chemical effects of a high CO_2 concentration in oxy-fuel combustion of methane," *Energy & Fuels,* Vol. 22, No. 1, 2008, pp. 291-296.

[2]Zhang, N., & Lior, N., "Two novel oxy-fuel power cycles integrated with natural gas reforming and CO_2 capture," *Energy,* Vol. 33, No. 2, 2008, pp. 340-351.

[3]Buhre, B. J. P., Elliott, L., Sheng, C. D., Gupta, R. P., & Wall, T. F., "Oxy-fuel combustion technology for coal-fired power generation," *Progress in energy and combustion science,* Vol. 31, No. 4, 2005, pp. 283-307.

[4]Matuszewski, M., "Advancing oxycombustion technology for bituminous coal power plants: an R&D guide," *US Department of Energy Final Report*, 2010/1405, April 2012.

[5]I. Introduction, "Experiments with Pintle Injector Design and Development," pp. 1–11, 2015.

[6]Anderson W.E., Long M.R. and Heister S.D., "Liquid Bipropellant Injectors", *Liquid Rocket Thrust Chambers: Aspects of Modeling, Analysis and Design*; *AIAA*, PP. 141-165, 2004.

Design and Testing of a 500 lbf Liquid Oxygen/Liquid Methane Engine

Manuel J. Herrera[1], Zachary Welsh[1], Gerardo Marquez[1], Jason Adams[2], Jack Chessa[2], and Ahsan Choudhuri[2]
The University of Texas at El Paso, El Paso, TX, 79968, United States

I. Abstract

The purpose of this paper is to present an overview of the design and preparation for testing of a 500 lbf liquid oxygen/liquid methane rocket engine. The Centennial Restartable Oxygen Methane Engine (CROME) is a steady state engine with a throttleable thrust range of 500 to 125 lbf. The engine will be tested on a horizontal test stand located in Fabens, TX to validate operating conditions, characterize engine performance (i.e. thrust, c*, and ISP) at different thrust levels, and identify/understand the limitations of the engine. The design of said test facility and procedures will also be discussed within this paper.

II. Nomenclature

CROME = Centennial Restartable Oxygen Methane Engine
cSETR = Center for Space Exploration and Technology Research
EDM = Electron Discharge Machining
FFC = Fuel Film Cooling
IRSU = In-situ resource utilization
LCH4 = Liquid Methane
LOX = Liquid Oxygen
PT = Pressure Transducer
RCS = Reaction Control System
TC = Thermocouple

III. Introduction

THE development of liquid oxygen/liquid methane (LOX/LCH4) propulsion systems has recently become a topic of interest ever since this particular propellant combination was determined to be a suitable candidate for use in space exploration. One of the main objectives for the center is to design and develop the first methane-fueled propulsion system fired in space. Daedalus, a suborbital demonstrator vehicle, aims to achieve this through utilizing CROME as its main propulsion system and an oxygen/methane reaction control system (RCS), both of which will be tested at the D1 horizontal test stand located in Fabens, TX. This test stand was designed and developed specifically to hot-fire test CROME, but has the capability to test engines that produce up to 5000 lbf.

The D1 test stand is comprised of two trailers, which allow for the test stand to be towed out to the designated test site when testing and back to the hangar after testing for safe storage or maintenance. One trailer, commonly referred to as the propellant trailer, has two 100-gallon spherical run tanks, the pressurant bottles (i.e. 6 GN2 manifolded bottles per tank), and the fuel and oxidizer tanks for CROME's ignition system. The second trailer or the engine trailer has the thrust stand to which the engine module is mounted on that contains the engine and all its manifolding. Flex hoses are used to connect the run lines, bleed lines, and igniter propellant lines between the two trailers.

The engine will be developed in three stages: D1, D2, and D3. CROME is currently in the first stage of its development phase, D1, whose intent is to demonstrate successful and repeatable operation, validate operating conditions, and characterize engine performance (i.e. specific impulse and c* efficiency) through the hot-fire testing of CROME at the D1 test stand located at UTEP's tRIAc test facility. During the D2 phase, CROME will be redesigned using the data and insight from prior testing and is intended to be a more flight-like configuration of the engine. D3, will be the flight-ready engine.

---

[1] Graduate Research Assistant, UTEP Mechanical Engineering
[2] Insert Job Title, Department Name, and AIAA Member Grade (if any) for third author.

IV. Mission

The mission of this project is to advance LOX/LCH4 propulsion technology. This propulsion system will be tested and developed as a sea-level engine but will be reconfigured for space flight. When flown in space, focal points of interest will be the evaluation of engine performance, system interaction, and the ability to restart in microgravity conditions. Obtaining this data will provide the aerospace community with a better understanding of how well a LOX/LCH4 propulsion system operates in space and give insight on where improvements can be made for future exploration missions.

CROME also serves as a platform for students to gain knowledge, experience, and insight in the process of designing, developing, and soon testing of a LOX/LCH4 rocket engine. More specifically, engine preliminary design analysis, material selection, mechanical and thermal analysis of components, drafting blue prints for manufacturing hardware, test stand design and engine testing.

V. Engine Overview

CROME, a pressure-fed bi-propellant engine, will operate as a steady state engine with a thrust range of 125 to 500 lbf. The engine features a fixed area pintle injector, a unique in house developed oxygen/methane torch igniter as the ignition source, and utilizes liquid methane film cooling. It also uses temperature and pressure sensors to verify hardware integrity and operating conditions. There are 27 thermocouples (TC) mounted radially and axially on the combustion chamber; these temperature measurements will be used to monitor the hot-wall temperature, assess the effectiveness of the fuel film cooling, and will be used as a cut-off to mitigate melting the chamber.

Figure 5.1 depicts the main component engine assembly.

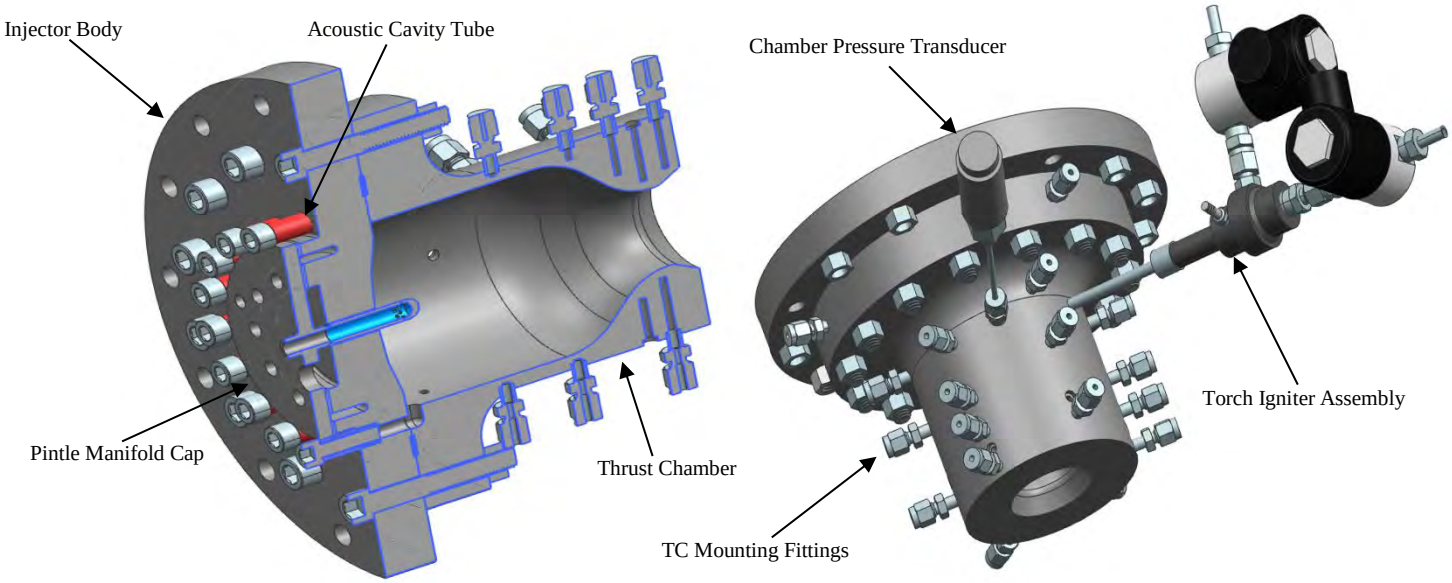

Figure 5.1 a) CROME component assembly cross section. b) Isometric view of CROME component assembly.

Figure 5.2 depicts the engine module assembly, which as stated before, contains the engine assembly and all the manifolds leading to the engine, which are the propellant run-lines, the bleed lines, the engine purge line and all of its sensors/components in line.

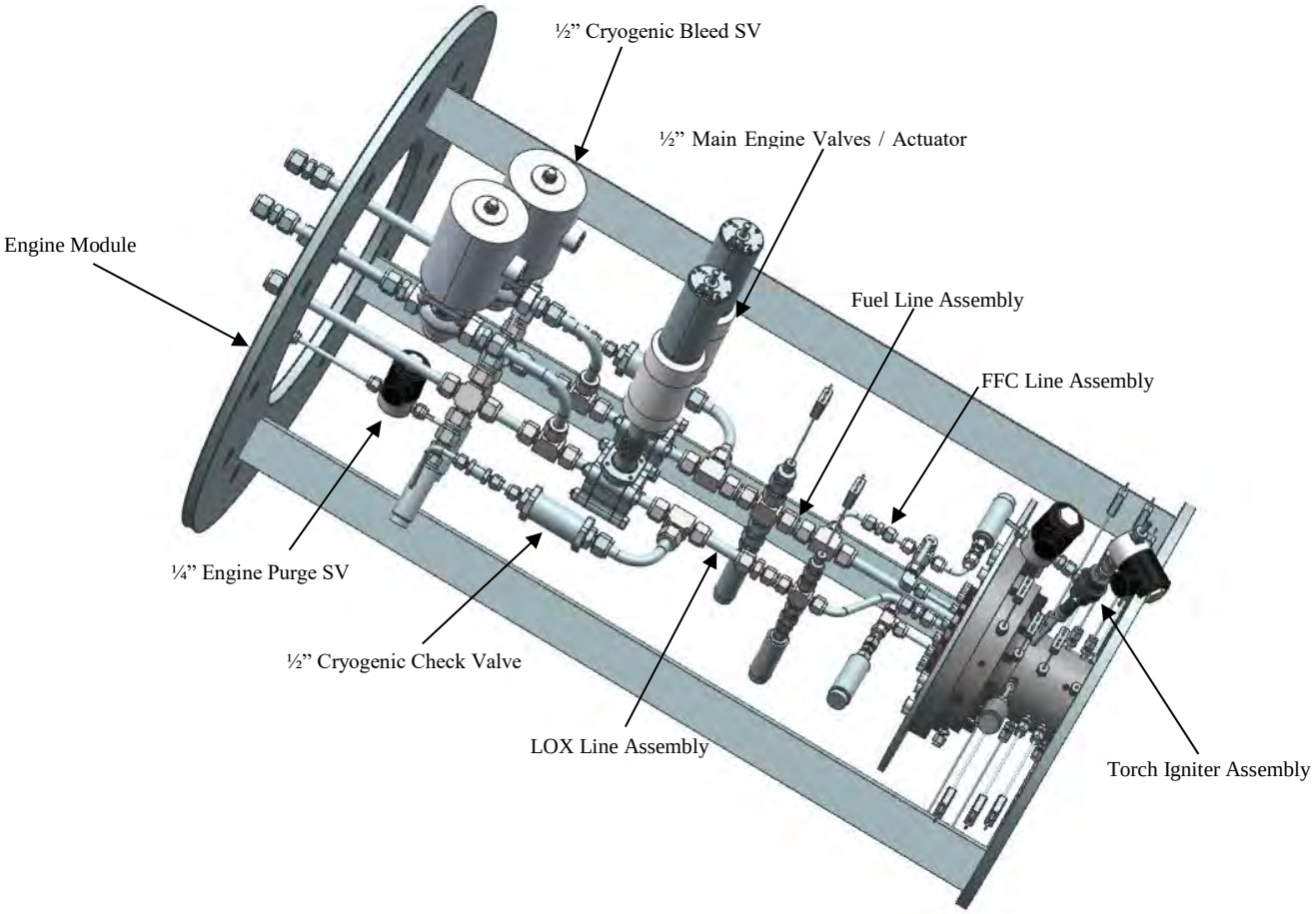

Figure 5.2 Engine module assembly.

Figure 5.3 is an image of the D1 test facility taken within the tRIAc hangar.

Figure 1. D1 horizontal test facility assembly. a) Isometric image of both trailers in its testing position. b) Image of the propellant trailer which show the run tanks, the pressurant k-bottles and the oxygen run line.

VI.Engine Testing

When hot-firing an engine, it is essential to operate safely and effectively. The easiest way of achieving that is by testing with approved procedures. The procedures currently being written/revised is the assembly and disassembly procedure, engine and facility leak check procedure, the cryoshock procedure, the cold flow procedure, the igniter check procedure, and the hot-fire test procedure.

The assembly and disassembly procedure ensure that sub-systems are assembled correctly after any maintenance; for example, changing out the face seals in the engine or assembling all the lines on the oxygen system when they return from being oxygen cleaned. It also specifies all interface requirements like bolt sizes, quantities and required preloads.

It is important to leak check the propellant delivery system and the engine before commencing any testing to ensure that there aren't any inappropriate flow communications or leaks out to ambient. This is achieved by pressurizing the system of interest up to a safe shop pressure (e.g. 50 psig) with a fluid, in this case gaseous nitrogen (GN2) and visually inspecting for leaks with snoop. After amending any leaks, a pressure decay test is conducted at the expected operating pressure. The engine throat will be plugged during these tests and will be leak checked independently from the facility. After successfully leak checking the facility and engine the appropriate lines will be insulated.

Conducting a cryoshock procedure was recommended by engineers at NASA's Johnson Space Center and by engineers from Blue Origin. A cryoshock test essentially qualifies the propellant delivery system to operate with cryogens by flowing a cryogen, in this case liquid nitrogen, through the system and allowing for all components to cool down and then being cycled. This ensures that all solenoid valves and hand valves operate at cryogenic temperatures and establishes confidence in the test facility before testing with the actual propellant: liquid oxygen and liquid methane.

Cold flows also known as propellant blowdowns are typically conducted when changing mainstage conditions (i.e. a different thrust level) to validate mass flow rates and in doing so ensuring the required mixture ratio is achieved. Each propellant is flowed through the propellant delivery system and through the engine into atmosphere. This test also allows for the flow resistance to be measured from the tank to the main engine valves with its respective fluid, which is useful for selecting the appropriate tank pressure.

The last procedure is the hot-fire test procedure. This procedure encompasses operations like purging the system and engine, filling the run tanks with its corresponding propellants, pressurizing the tanks, conditioning the run lines, setting the appropriate cut-offs/redlines, setting the appropriate auto sequence settings, operating the hot-fire test, specifying shutdown sequences, and establishing criteria to continue testing. An igniter check will be performed before hot-fire testing each test day to ensure successful and reliable ignition. Table 1 shows the initial simplified test matrix.

Table 6.1 CROME Simplified Test Matrix

Mainstage Test	Power Level (%)	Film Cooling (%)	Duration (s)	Pc (psi)	m_f (lbm/s)	m_o (lbm/s)
1	25	30	3	70	0.18	0.48
2	50	30	3	125	0.32	0.86
3	75	30	3	180	0.45	1.23
4	100	30	3	235	0.59	1.6

VII.Future Work

The D1 test stand is partially assembled. The oxygen side of the system is being dissasmbled and packed for shipping to Astro Pak for oxygen cleaning, which is when the methane side will be assembled. Once oxygen cleaning is completed and returned, all lines will be re-assembled in a clean room and transitioned to tRIAC where they will carefully be connected so as to not contaminate the system. Upon reassembly of all facility lines and being leak checked the the run lines and propellant tanks will be insulated with cryogel and insulation tape. Test procedures are being written, revised, and approved. An internall test readiness review (TRR) will be held early March and testing will commence mid March where leakchecks, a facility cryoshock, cold flows, an igniter check and hot-fire testing will take place. Following the completion of CROME's initial test campaign, the test data will be used to design a more flight like engine.

VIII.Acknowledgments

The development of the CROME engine is funded by the National Aeronautics and Space Administration (NASA's) Minority University Research and Education Project. (MUREP) (Grant NNX158Q04A). NASA MUREP Institutional Research Opportunity (MIRO) is "established to strengthen and develop the STEM research capacity and infrastructure of Minority Serving Institutions, MSIs." (NASA Education, 2018).
The authors would like to express their thanks to the following cSETR student researchers: Steven Torres, Corey Hanson, Mariana Chaidez, Luz Bugarin, Linda Hernandez, Raul Ponce, Raymundo Rojo, Rachel Pilgrim, Jesus E. Trillo, Jonathan Candelaria, Pedro Nunez, Javier Chaparro, Dylan Ott, Abner Moreno Tarango, Jahir Fernandez for their help with the design, development, and analysis. As well as the County of El Paso for their support with the development of the Technology Research Innovation Acceleration Park (tRIAc) in Fabens.

C. Young, C, Zhang, A. Loganathan, B. Boesl, and A. Agarwal

Densification and Oxidation Behavior of Spark plasma sintered Hafnium Diboride-Hafnium Carbide Composite

Abstract

The current study reports on Hafnium Diboride (HfB_2) and Hafnium Carbide (HfC) based ultra-high temperature ceramics and their oxidation behaviors. Pure Hafnium Diboride, Hafnium Carbide, and HfB_2-50 vol.% HfC were consolidated using spark plasma sintering (SPS) without the use of sintering aids. HfB_2-HfC composite displayed a high sintered density of 98% as compared to 87% density of pure HfB_2. The increased density of the HfB_2-HfC composite is attributed to the bimodal powder distribution which allowed for the smaller HfC particle to occupy the voids between the larger HfB_2 particles resulting in improved packing efficiency and particle surface energy attributed to the smaller HfC particle being a large driving force in the sintering process. This improved density and particle packing efficiency of the HfB_2HfC compact also allowed Oxidation studies of each material were carried out by exposing them to a high-speed plasma jet in a temperature exceeding 2700°C and by thermogravimetric analysis (TGA) up to 1400°C. Results of these studies show an improved oxidation resistance of HfB_2-50vol% HfC in comparison to HfB_2 and HfC, resulting in a thinner oxide scale and a slowed rate of mass gain than HfB_2 and HfC during testing via plasma jet and TGA, respectively. This increase in oxidative is attributed to the increased density of the composite.

Keywords:

Hafnium Diboride, Hafnium Carbide, Spark Plasma Sintering, Oxidation, Surface Energy

Introduction

Ultra-high temperature ceramics (UHTCs) including carbides, nitrides and diborides of early transition metals have been of increasing interest due to their extremely high melting point, high hardness, and elastic moduli. These materials are of particular interest for applications such as the nose and leading wing edge of hypersonic vehicle applications. [1] Most UHTCs cannot be used solely densified without using sintering aids, forming composites, or solid solutions. [2,3,4,5,6,7]The prime reasons for this situation is the low sinterability of the UHTCs due to the strong covalent bonds.

Hafnium diboride (HfB_2), among all the UHTCs, is recognized as one of the best oxidation resistant ultrahigh temperature ceramics. [8,9] Upon oxidation, it forms porous HfO_2 which serves as scaffold filled with low melting point B_2O_3.[12] Such combination results in dense oxidation layers that protect the underlying materials from further oxidation. However, B_2O_3 starts to evaporate around 1100°C, which leaves the underlying materials vulnerable to oxidation. [4] Additionally, the sinterability of HfB_2 is considerably poor; the sintered samples are usually porous which provides extra pathway for oxygen penetration and lead to further oxidation. Silicon carbide (SiC) is added as sintering aid as well as reinforcement for oxidation resistance in HfB_2.[12] Although the role of SiC in aiding sintering is yet to be fully understood, it is believed that silicon based melts enable the liquid phase sintering which leads to higher densification in the final product. As for the oxidation resistance enhancement, the Si addition stabilizes the B_2O_3 by forming

amorphous borosilicate phase. [8-9] The latter phase is stable up to 1600 °C before it starts evaporating. [11] The drawbacks of the SiC addition are also glaring: the most studied HfB_2-SiC composition is HfB_2-20 vol. % SiC. Such large amount of SiC will not only alter the properties of the HfB_2, but also introduce unnecessary complex secondary phases to the composites. Although SiC is able to stabilize the B_2O_3 during oxidation up to 1600 °C, this temperature is still relative low considering the application temperature for ultrahigh temperature ceramics is usually greater than 2700°C. [8,11] Thus HfB_2-SiC is still not the ideal UHTC composites.

Hafnium carbide (HfC) is another ultrahigh temperature ceramic that has superior oxidation resistance. Unlike HfB_2 which forms liquid phase oxide to seal the pores in the oxide scales, HfC forms a dense, crack-free oxycarbide layer when exposed to the oxygen that prevents further oxidation. [3,5,12,13] The oxycarbide layer is a metastable phase obtained from the oxygen absorption into HfC and substitute carbon atoms. HfC can absorb up to 30% of oxygen without transforming into HfO_2. Zhang et al. sintered pure HfC without any sintering aid addition by spark plasma sintering (SPS) and achieved 98% dense pellet. In this study, it was seen pure HfC, during oxidation testing by plasma jet, quickly oxidized and formed HfO_2 due to the sonic speed of the oxygen entering the sample being tested, and the oxycarbide layer formed was merely microns thick. Thus, leading to a thick oxide scale formation, of roughly 165 μm, on the surface of the sample. [5,6,7]

Experimental Method

Material

Powder Processing

Spark Plasma Sintering

Characterization

Oxidation Testing

Post-oxidation Characterization

Results & Discussion

Effect of Ball Milling

For the fabrication of the binary HfB_2-50 vol.% HfC composite for this study, seen in figure 1, ball milling in tungsten carbide milling media was used to break down the agglomerations and homogenously mix HfB_2 and HfC for the HfB_2-50 vol% HfC powder to be consolidated. From XRD done previous to and post ball milling period, it was seen there was no contamination of the tungsten carbide milling media

Densification during SPS

The binary HfB_2-50vol% HfC composite, without the use of a sintering aid, fabricated achieved a final density of 98% of the theoretical value calculated by the rule of mixtures from the densities of HfB_2 and HfC. The addition of HfC aids in refinement of microstructure and the removal of surface oxides from HfB_2 particles, thus aiding in the consolidation of HfB_2. [9,10,13] However, in most of these studies, the addition of HfC is used as a sintering aid.

The increased particle surface and planar surface energy within HfC leading, HfC to have an increased affinity for consolidation at a lower sintering temperature. Thus, HfC begins to consolidate before and around HfB_2 particles within the composite. This can be seen in the back scattered FIB image of the cross section of HfB_2HfC, where micropores can be seen at the grain boundaries and within the larger HfC grains seen in figure 5. This pointing to the diffusion of HfC particle into one another to lower their surface energies and forming these larger grains, thus also furthering the consolidation of the composite.

Oxidation Behaviors

Oxidation testing was conducted via plasma gun, in standard atmospheric conditions, and thermogravimetric analysis. Testing conducted via plasma on each sample at a distance of 75mm from the sample to the gun face, allowing for ample airflow in front of the sample surface during testing. Testing conducted via thermogravimetric analysis was done on small portions of the sintered samples in standard atmospheric conditions at 5°C per minute up to 1400°C.After oxidation testing by plasma gun analysis of each compact revealed the mixed HfB_2HfC composite shows an improved oxidation character in comparison to HfB_2 and HfC samples produced, as can been seen in figure 7. This is believed to be due to the increased densification of the final composite, as well as the oxidation mechanisms of both HfB_2 and HfC working in tandem to produce a semi-protective oxide layer on the surface of the HfB_2HfC composite, as seen in figure 7. Thermogravimetric analysis conducted of each sample further supports the proposed mechanism of oxidation of HfB_2HfC.

Conclusion

References

1. Fahrenholtz WG, Wuchina EJ, Lee WE, Zhou Y, editors. Ultra-high temperature ceramics: materials for extreme environment applications. John Wiley & Sons; 2014 Oct 10.
2. Monteverde F. Hot pressing of hafnium diboride aided by different sinter additives. Journal of materials science. 2008 Feb 1;43(3):1002-7.
3. Sciti D, Silvestroni L, Bellosi A. Fabrication and properties of HfB 2–MoSi 2 composites produced by hot pressing and spark plasma sintering. Journal of materials research. 2006 Jun;21(6):1460-6.
4. DeGregoria AJ. Creep and Oxidation of Hafnium Diboride Based Ultra High Temperature Ceramics at 1500C. Air Force Institute of Technology WPAFB United States; 2015 Dec 1.
5. Zhang C, Gupta A, Seal S, Boesl B, Agarwal A. Solid solution synthesis of tantalum carbide-hafnium carbide by spark plasma sintering. Journal of the American Ceramic Society. 2017 May 1;100(5):1853-62.
6. Zhang C, Loganathan A, Boesl B, Agarwal A. Thermal Analysis of Tantalum Carbide-Hafnium Carbide Solid Solutions from Room Temperature to 1400° C. Coatings. 2017 Jul 28;7(8):111.
7. Zhang C, Boesl B, Agarwal A. Oxidation resistance of tantalum carbide-hafnium carbide solid solutions under the extreme conditions of a plasma jet. Ceramics International. 2017 Dec 1;43(17):14798-806.
8. Justin JF, Jankowiak A. Ultra High Temperature Ceramics: Densification, Properties and Thermal Stability. AerospaceLab. 2011 Nov 1(3):p-1.
9. Gasch M, Ellerby D, Irby E, Beckman S, Gusman M, Johnson S. Processing, properties and arc jet oxidation of hafnium diboride/silicon carbide ultra high temperature ceramics. Journal of Materials Science. 2004 Oct 1;39(19):5925-37.
10. Gasch M, Johnson S. Physical characterization and arcjet oxidation of hafnium-based ultra high temperature ceramics fabricated by hot pressing and field-assisted sintering. Journal of the European Ceramic Society. 2010 Aug 1;30(11):2337-44.
11. Justin JF. Sintering and properties of Ultra High Temperature Ceramics for aerospace applications. InODAS 2013 2013 May 27.
12. Licheri R, Orrù R, Musa C, Locci AM, Cao G. Consolidation via spark plasma sintering of HfB2/SiC and HfB2/HfC/SiC composite powders obtained by self-propagating high-temperature synthesis. Journal of Alloys and Compounds. 2009 Jun 10;478(1-2):572-8.

13. Ni DW, Liu JX, Zhang GJ. Microstructure refinement and mechanical properties improvement of HfB2–SiC composites with the incorporation of HfC. Journal of the European Ceramic Society. 2012 Aug 1;32(10):2557-63.
14. Ghosh D, Subhash G, Orlovskaya N. Slip-line spacing in ZrB2-based ultrahigh-temperature ceramics. Scripta Materialia. 2010 Jun 1;62(11):839-42.
15. Diouf S, Menapace C, Molinari A. Study of effect of particle size on densification of copper during spark plasma sintering. Powder Metallurgy. 2012 Jul 1;55(3):228-34.
16. German RM. Prediction of sintered density for bimodal powder mixtures. Metallurgical Transactions A. 1992 May 1;23(5):1455-65.
17. Busby JT, Hash MC, Was GS. The relationship between hardness and yield stress in irradiated austenitic and ferritic steels. Journal of Nuclear Materials. 2005 Feb 1;336(2-3):267-78.
18. Savino R, Fumo MD, Silvestroni L, Sciti D. Arc-jet testing on HfB2 and HfC-based ultra-high temperature ceramic materials. Journal of the European Ceramic Society. 2008 Jan 1;28(9):1899-907.
19. Khalil NZ, Vajpai SK, Ota M, Ameyama K. Effect of Particle Size Distribution on SiC Ceramic Sinterability. Materials Transactions. 2015 Nov 1;56(11):1827-33.
20. Wonisch A, Kraft T, Moseler M, Riedel H. Effect of Different Particle Size Distributions on Solid-State Sintering: A Microscopic Simulation Approach. Journal of the American Ceramic Society. 2009 Jul;92(7):1428-34.

DESIGN AND EXPERIMENTAL DEMONSTRATION OF AN ADDITIVE MANUFACTURED INJECTOR

Md Nawshad Arslan Islam[1], Md. Amzad Hossain[1], and Ahsan Choudhuri*
[1] Mechanical Engineering, Center for Space Exploration and Technology, El Paso, TX 79968, USA;
* Corresponding author (ahsan@utep.edu)

Keywords*: Additive manufacturing, Powder bed fusion, High-pressure combustion*

ABSTRACT

The article presents an exploration of design and prototyping of oxy-fuel injectors with integrated temperature sensing capabilities using powder bed fusion additive manufacturing (AM) technologies. A primary focus of this work was to design and fabricate a complex oxy-methane injector with integrated temperature measuring capacity. The injector was then test fired in high-pressure conditions at different firing inputs (55- 275 kW). A combustion pressure of 16.4 bar was achieved for 275 kW firing input. Integrated thermocouples provided thermal soak back measurement of the injector. The maximum temperature reported was 198°C at 275 kW firing input. Visual inspection and leak checks yielded in no defects observed. There were no significant difference in operation characteristics between AM and conventional machined injector.

1 Introduction

Additive manufacturing (AM) is a new paradigm in manufacturing industry that provides fabrication of complex geometries impossible by conventional process. Over the past few years, AM has proven itself as a viable method to fabricate custom-designed metallic components rapidly. AM process is particularly attractive for manufacturing complex energy system due to lack of assembly requirement and unlimited geometrical flexibility. Powder bed fusion additive manufacturing processes have received considerable attention due to its high energy density and energy efficiency that allows full density metal components of comparable or even better quality than those produced by traditional methods[1,2]. Thus, the AM process is especially attractive for fabricating complex components such as fuel injectors for gas turbine combustors which require operation under extreme environments.

The unique layer-by-layer fabrication technique allows the embedding of sensors within complex components without post-production component modifications[3,4]. Sensors can be embedded in powder bed fusion AM fabricated components through two distinct processes: *Stop and Go* of the fabrication process or Post-integration of sensors. *Stop and Go* of the fabrication process allows sensor placement within a cavity during fabrication where the process is allowed to continue upon sensor placement. This process requires an extremely accurate re-alignment of the powder-bed during the restart process. In addition, metallization and shorting of sensors due to a considerably high temperature of the process creates significant fabrication challenges and limit the types of sensors that can be embedded. Post-integration process provide embedding sensors in customized compartments selectively built within the part at the end of fabrication process. This is a practical alternative of *Stop and Go* process without requiring post-production component modifications.

The proposed effort was aimed at exploration of design and prototyping of a Low-NOx fuel injector with integrated temperature sensing capabilities using powder bed fusion techniques (EBM and SLM). Fuel injectors commonly used in turbine combustors have complex internal cavities and passages to ensure tailored mixing of air and fuel to achieve high performance. Since the current design methodology of these injectors is based on conventional fabrication techniques (e.g., multi-step machining and welding processes), a new paradigm of design methodology needs to be developed for their adaptation in the EBM fabrication process[5,6]. Following the fabrication the injector was tested at high pressure combustion conditions to check for operational

2 Technical Methodology

2.1 Injector

A co-axial shear fuel injector was designed and fabricated for this work. The design of the fuel injector is provided in fig. 1(a). The fuel injector assembly has four injection ports, one in the center (primary injector) and the other three (secondary injectors) in a circular circumference around the primary injector. The injector was designed to provide a total firing input of 500 kW during full injector operation. The total firing input was divided among the primary and secondary injectors; 55% to primary injector and 15% to each of the secondary injector. Several challenges were encountered for manufacturing the injector. The first challenge was fabrication of the nozzle shape to incorporate pressure drop and prevent flashback. Another challenge was to construct the airfoil-shaped support for the fuel lines. The airfoil shape is located inside the oxidizer line as shown in fig. 1(b). This design is impossible to produce by the conventional manufacturing process. Other challenges were the inclusion and removal of internal supports for the 90° angle of the auxiliary oxidizer lines. In addition, several external supports were required for fabrication. These supports were modified for easy removal.

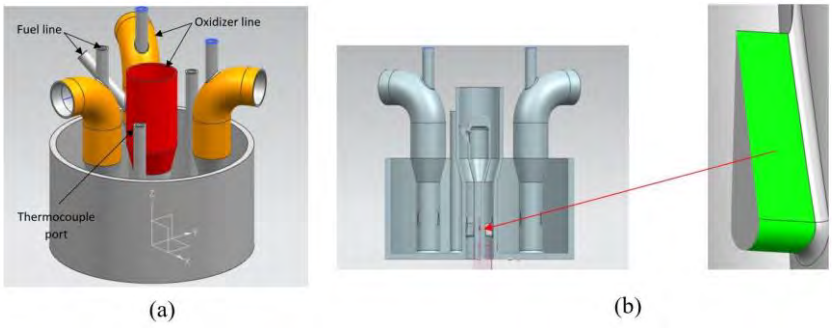

Figure 1. (a) Design of the AM manufactured injector (b) Air foil shaped support for fuel line inside the oxidizer line

The injector was fabricated in the SLM 125HL machine using Inconel 718. Build preparation was done in Materialise Magics software. The design was modified for inclusion of a lattice (mesh) structure to support the fabrication of the angled fuel inlets (in the inlet orifice). Difficulties were encountered during removal of support material from internal channels. The high stiffness support required to overcome thermal stress during fabrication created challenge for removal. A sparse lattice was generated and merged into the injector STL design file using Magics Structures module. Easy removal external supports were included, and the design was

ready for printing. The injector was cut off the starting plate, and the supports were removed at the end of fabrication. There were two types of deformation on the angled oxidizer lines after the fabrication. Lack of enough support near the orifice of the oxidizer line allowed the feature to warp during fabrication. Uneven powder layers implemented another deformation at the inlets. Dimensional measurements of the orifices were taken to quantify the deformation. A minimum error of 1.47% and a maximum error of 3.67% were measured.

Figure 2. The fabricated injector before HIP process with test fit components (left), complete injector ready for test after HIP process and heat treatments (right)

Table 1. Burner parameters

Parameters	Primary Injector	Secondary Injector
Power Input (kW)	40 - 275	15 - 75
CH_4 mass flow rate (kg/s)	0.0008 - 0.004	0.0003 – 0.0015
O_2 mass flow rate (kg/s)	0.0032 – 0.016	0.0012 - 0.006
CH_4 velocity (m/s)	3.5 - 18	3.5 – 17
O_2 velocity (m/s)	0.75 - 3.5	0.75 – 3.5
Momentum flux ratio	≈12	≈12

Following the fabrication in SLM, compression fittings and thermocouples were test fit on the injector in preparation for testing fig. 2 (left). SLM machine had a smaller build plate which required separate fabrication of the flange. Flange and extension fittings were then welded on the injector and the oxidizer lines respectively. Compression fittings were placed on fuel and oxidizer inlets and thermocouple ports. Afterward, hot isostatic pressing (HIP) treatment was done on the injector. The HIP process closes small defects and pores commonly found in 3D printed parts. IN718, are hot isostatic pressed at 1140 ± 15°C and 100 MPa for 3 hours. An oxide film formation was observed due to excessive amount of moisture present during the process. Then the injector underwent a heat treatment cycle of 1065 ± 15 °C for 90 min. subsequently, the parts were solution treated and aged following AMS2774. This resulted in formation of proper microstructure to provide the high-temperature strength of Inconel 718. Additionally the process relieved residual stresses from the welding process. After the treatment K type thermocouples were integrated into the sensor ports and the injector was ready for testing. Figure 2 (right) shows the complete injector. The burner parameters are presented in table 1.

2.2 High Pressure Combustion set up

The primary injector was tested at high-pressure conditions to observe the fuel injector behavior during oxy-methane combustion. Figure 3 shows the high-pressure combustor system utilized for the test campaign. The detailed descriptions and design of the combustor can be

found in the work of Chowdhury et al.[7]. The major parts of the high-pressure combustor are main burner (fuel injector), metal window covers, igniter manifolds, end cap attachments, and optical access port. The end cap attachments at the exhaust end of the combustor choke the exhaust flow resulting in increased chamber pressure. Igniters were used to create a pilot flame to ignite to main burner flow. The igniter operates for a total of 3 seconds, which result in 2 seconds overlap with the main flow. Once the main burner flow is ignited, the igniter shuts OFF. The main burner stays in operation for 15 seconds. Upon completion of main burner operation, A high pressure nitrogen purge is introduced in to combustor to get rid of any unburned fuel mixture. A 15 seconds delay is maintained between main burner operation and nitrogen purge to avoid NOX formation. The test matrix for the tests are presented in table 2.

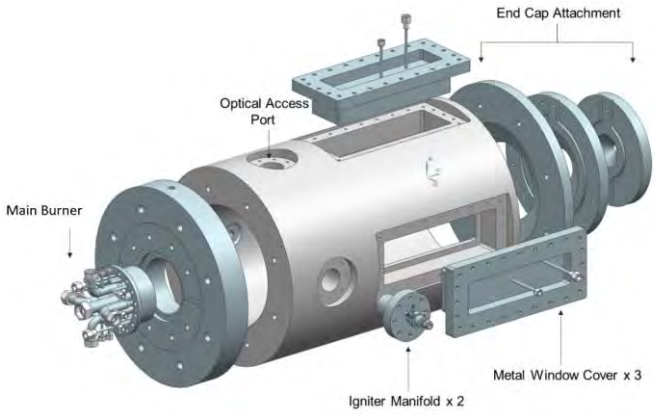

Figure 3. High-pressure combustor

Table 2. Test matrix for primary injector hot fire test

Case	Central Injector Firing Input (kW)	Tank pressure (psig)		Mass flow rate (g/s)	
		Oxygen	Methane	Oxygen	Methane
1	55.0	56.0	64.0	4.40	1.10
2	82.5	84.0	96.0	6.60	1.65
3	110.0	111.0	128.0	8.80	2.20
4	137.5	139.0	160.0	11.0	2.75
5	165.0	167.0	192.0	13.2	3.30
6	192.5	195.0	224.0	15.4	3.85
7	220.0	223.0	257.0	17.6	4.40
8	248.5	251.0	289.0	19.8	4.95
9	275.0	279.0	321.0	22.0	5.50

A high capacity feed system is used to deliver the fuel and the oxidizer to the test setup. The feed system consists of several control valves (electrically actuated and mechanically actuated) and monitoring systems (flow meters, pressure transducers, thermocouples, etc.). The high-pressure combustion system is operated through a remotely accessible control system. National Instrument CDAQ and CRIO system are incorporated in the control system to remotely control all the devices to achieve proper fuel-oxidizer mixture in the combustion chamber.

3 Experimental Results

The primary injector was test fired following the test matrix provided in table 2. Figure 4(a) shows image of high pressure combustion test at 249 kW firing input. The operational stability of the injector was checked by comparing the experimentally obtained and analytical firing

input. Figure 4(b) is a plot displaying evaluations of operational characteristics of the primary injector firing input vs. tank pressure. A maximum of 12% difference was observed between the firing inputs. The maximum difference occurred for the second data point on the test matrix. It was also noticed that the injector was able to performed better at higher firing input.

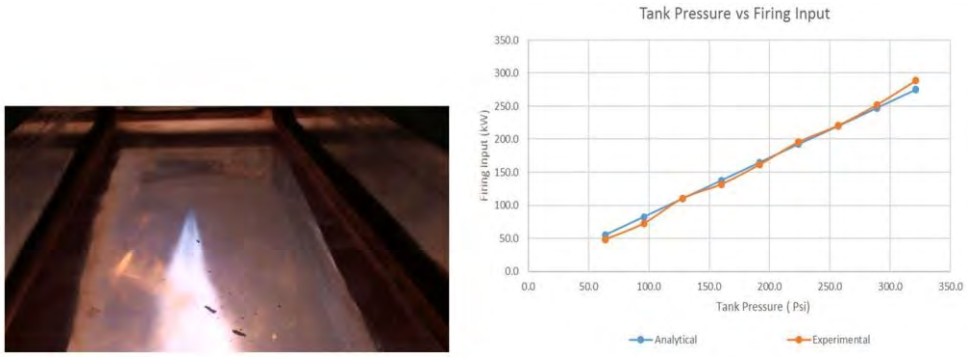

Figure 4. (a) High pressure combustion at 249 kW firing input (b) comparison of analytical and experimental obtained firing input

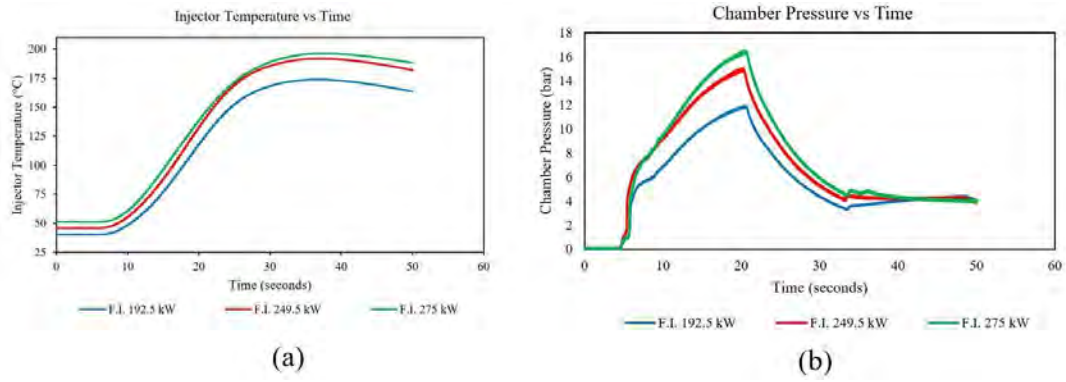

Figure 5. (a) Temperature measurement of injector (b) chamber pressure at different firing input

During the experiment, the pressure inside the chamber build up rapidly following the combustion. The choked exhaust path complemented the pressure increase and resulted in swift increase in temperature inside the chamber. The swirling motions and vortex formation inside the chamber exposed the injector to the exhaust gas, resulting in a temperature rise of the injector. The thermocouples embedded on the injector provided real time temperature of the injector during tests. A maximum temperature of 195 °C was noticed at 275 kW firing input. Figure 5(a) presents the temperature plots for different firing inputs. From the plot it is seen that the temperature increment continued even after the flame was extinguished. This was due to the hot gas contact and conduction from combustor wall. Once the purge sequence was activated the temperature decreased due to cold nitrogen exposure. This implies for more extended test periods to be possible, cooling capabilities need to be further researched. The maximum chamber pressure attained was 16.4 bar for 275 kW firing input. A continuous flame was observed during the tests, and the experiment was successful in demonstrating these parameters. Successive tests were conducted to check for repeatability for both pressurized and

atmospheric conditions. Figure 5(b) presents chamber pressure at different firing inputs. Visual inspection was performed on the injector after the pressurized test. No cracks or leaks were observed. A leak check was performed using nitrogen however resulted in no leaks found.

5 Conclusion

The current study reports a metal additive manufacturing process of complex injectors integrated with embedded temperature sensor. The fabricated injector was successfully tested at high-pressure combustion conditions. The maximum combustion pressure achieved was 16.4 bar at 275 kW firing input. Thermal soak back measurements during the test were obtained by the integrated thermocouples in the injector. The injector temperature rapidly increased to 198°C within the 15 seconds of ignition at a firing input of 275 kW.

6 Future Work

The corresponding injector will be fired for extended testing period. In addition, CO_2 dilution can be investigated to check for the high-pressure combustion characteristics. Cooling systems can be looked in to for extensive testing.

Acknowledgement

This research is supported by the US Department of Energy, under award DoE Award Number: DE-FE0026330 (Federal Project Manager Maria Reidpath). However, any opinions, findings, conclusions, or recommendations expressed herein are those of the authors and do not necessarily reflect the view of the Department of Energy.

References

[1] Puebla, K., Murr, L. E., Gaytan, S. M., Martinez, E., Medina, F., and Wicker, R. B., "Effect of melt scan rate on microstructure and macrostructure for electron beam melting of Ti-6Al-4V," *Materials Sciences and Applications,* Vol. 3, No. 5, 2012, pp. 259.

[2] Murr, L.E., Gaytan, S.M., Ceylan, A., Martinez, E., Martinez, J.L., Hernandez, D.H., Machado, B.I., Ramirez, D.A., Medina, F., Collins, S. and Wicker, R.B., "Characterization of titanium aluminide alloy components fabricated by additive manufacturing using electron beam melting," *Acta materialia,* Vol. 58, No. 5, 2010, pp. 1887-1994.

[3] Kairm, H., Delfin, D., Shuvo, M.A.I., Chavez, L.A., Garcia, C.R., Barton, J.H., Gaytan, S.M., Cadena, M.A., Rumpf, R.C., Wicker, R.B. and Lin, Y., "Concept and model of a metamaterial-based passive wireless temperature sensor for harsh environment applications," *IEEE Sensor Journal,* Vol. 15, No. 3, 2015, pp. 1445-1452.

[4] Hossain, M.S., Gonzalez, J.A., Hernandez, R.M., Shuvo, M.A.I., Mireles, J., Choudhuri, A., Lin, Y. and Wicker, R.B., "Fabrication of smart parts using powder bed fusion additive manufacturing technology," *Additive Manufacturing,* Vol. 10, 2016, pp. 58-66.

[5] Ponche, R., Kerbrat, O., Mognol, P. and Hascoet, J.Y., "A novel methodology of design for Additive Manufacturing applied to Additive Laser Manufacturing process," *Robotics and Computer-Integrated Manufacturing,* Vol. 30, No. 4, 2014, pp. 389-398.

[6] Vayre, B., Vignat, F. and Villeneuve, F., "Designing for additive manufacturing," *CIrP,* Vol. 3, 2012, pp. 632-637.

[7] Chowdhury, A.A., Cruz, J., Aboud, J., Rios, A., Choudhuri, A.R., Love, N.D., Kim, H., Dungel, B. and Tsiava, R, "Design and Experimental Demonastration of a High Pressure Oxy-Methane Combustor," *2018 AIAA Aerospace Sciences Meeting, AIAA SciTech Forum, Kissimmee, Florida,* January 8-12, 2018 pp AIAA 2018 -1476

DESIGN OF A PRESSURIZED OXY-COAL COMBUSTOR

M. Chowdhury[1], A. Rios[1] , M. Khan[1] and A. Choudhuri[1]*
[1] Mechanical Engineering, Center for Space Exploration and Technology
El Paso, TX 79968, USA;
* Corresponding author (ahsan@utep.edu)

Keywords: *high pressure, combustion, oxy-fuel, combustor*

ABSTRACT

A combustor design is presented in this paper to operate up to 20bar pressure for an oxy-coal combustion cycle. The combustor is designed to accommodate different components necessary for the delivery for an oxy-coal combustion cycle. The combustor is made of stainless steel 410. The design has options for optical access for visual inspection and for laser diagnostics and also has provision for sensory ports to measure different parameters. The combustor design provides a general layout for the design of combustors to be used for similar combustion process with different design criteria.

1 Introduction

Energy Production from coal combustion has been used from the onset of civilization. However, the emissions from coal combustion pose a major threat to environment. The quest for cleaner energy has led to the introduction of many different alternatives including oxy-fuel combustion. Oxy-fuel combustion uses oxygen to burn with fuel. If the fuel is a hydrocarbon, the products are primarily carbon dioxide and water vapor. The water can be condensed from the product stream and the carbon dioxide can subsequently be sequestered. The process provides opportunities to capture as much as 100% carbon dioxide[1] and has potential to increase the efficiency of the entire cycle[2]. Pressurizing an oxy-combustion cycle may further enhance cycle efficiencies[3]. For pressurized oxy-coal combustion different configurations are proposed in literature[3-7]. A major layout for oxy-coal pressurized cycle is ENEL. This cycle operates at an elevated pressure of 10bar. One of the major challenges of testing this cycle is to have technology to support the cycles. There are limited guidelines or literature available about the construction of the combustion chamber for such combustion process. The key criteria for the design are to be able to deliver the coal slurry, ignite the coal towards the center of the combustor, have optical access as well as to operate at elevated pressure. Thus, this paper presents a design for a combustor to operate at up to 20bar pressure for oxy-coal combustion.

2 Design Methodology

The combustor and its different parts are made of Stainless Steel 410. The material was choosen for its yeild strength at high temperature. The combustor has been designed to be modular, composed of different sections joined by stainless steel flanges. Metal gaskets are put in

between the flanges to ensure a seal during combustion. The combustor is mounted vertically on a test stand using eye bolts. The combustor assembly is presented in Fig. 1.

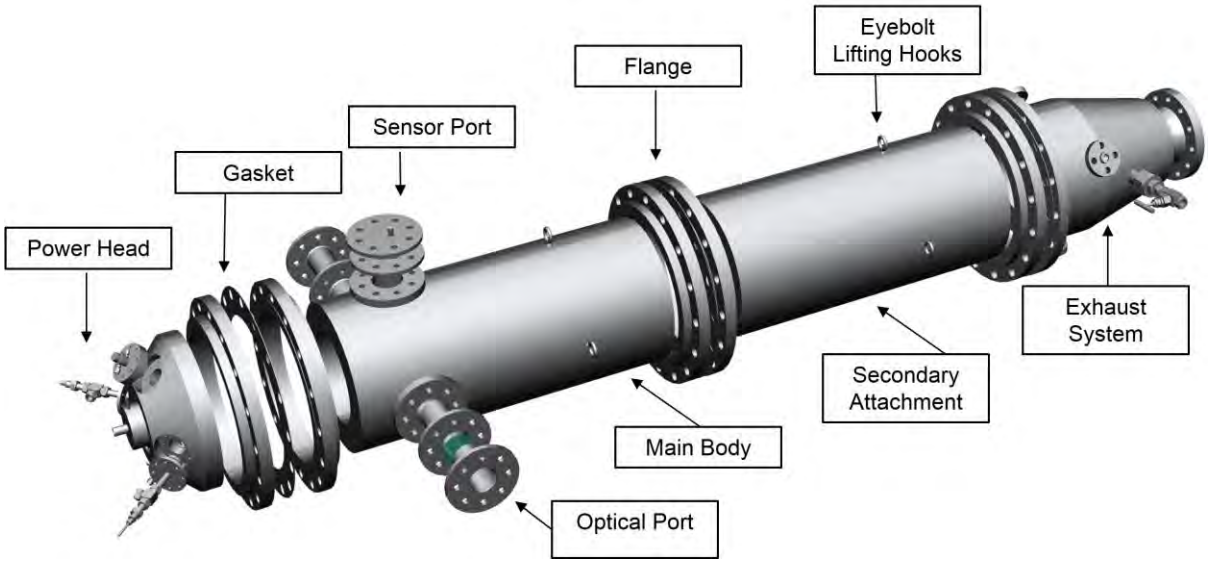

Fig. 1. Exploded view of combustor assembly

2.1 Powerhead

The powerhead is designed to deliver the input materials for the combustion process. It is designed as a tapered cap at an angle of 45° . It houses a pintle injector, two pilot burners and two igniters. The pintle injector delivers the coal slurry and the oxidizer. It is placed centrally in the powerhead. The methane operated pilot burners are ignited by the igniters. All four of these components are placed equidistantly on the outer circumference of the powerhead as

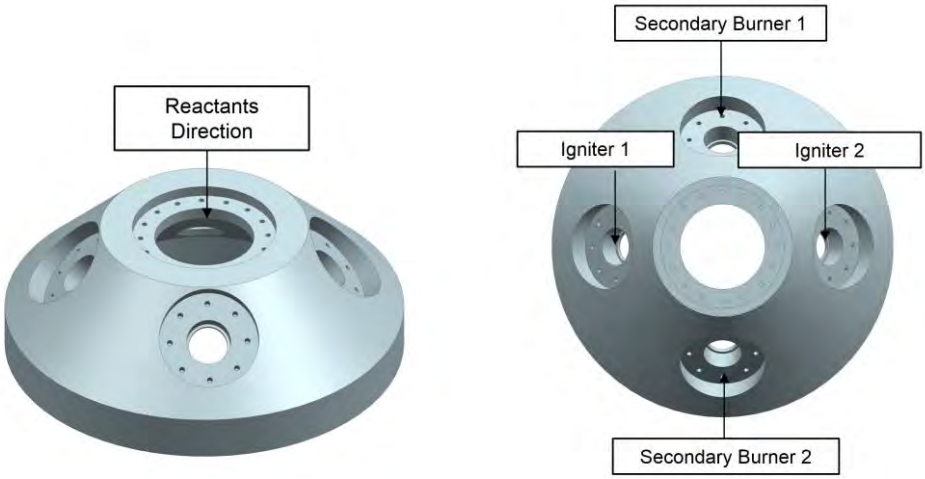

Fig. 2. Powerhead

shown in Fig. 2. The components of the powerhead are each placed in windows of 2-inch diameter. The powerhead is tapered to move the collision point of the flames of the pilot burners towards the end of the powerhead. This would give clearance for the coal slurry to be heated and form the flame in the center of the combustor. This will also help in avoiding the pilot flames to directly impinge on the combustor wall.

2.2 Main body

The main body of the combustor consist of two cylindrical sections. Each of the 39.4inch long sections have an outer diameter of 18 inches and inner diameter of 11inches. The first part of the combustion chamber has three windows. The windows are placed at 0, 90 and 180 degrees to accommodate laser diagnostic tools, as shown in Fig. 3.

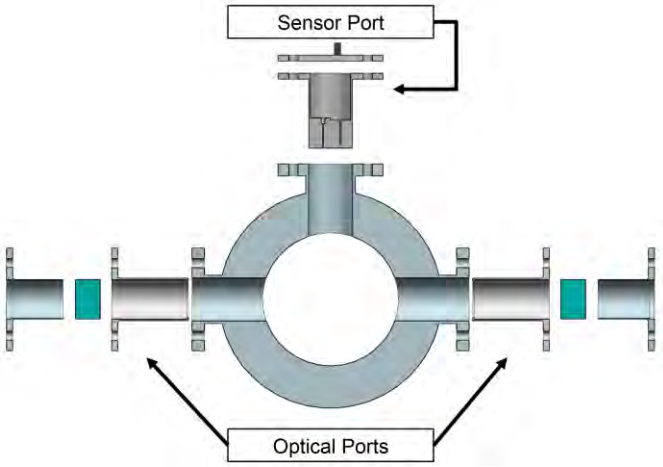

Fig. 3. Exploded view of the sensory and optical ports on the combustor

Each window is a 2 inch bore through the chamber of the combustor wall and houses a quarts optical port, these port are used for imaging and visual investigations. When imaging is not required, sensory ports as shown in figure can be fitted into the port. Thermocouples and pressure transducers are attached in the sensory ports, as shown in Fig. 4, to measure the temperature and the pressure.

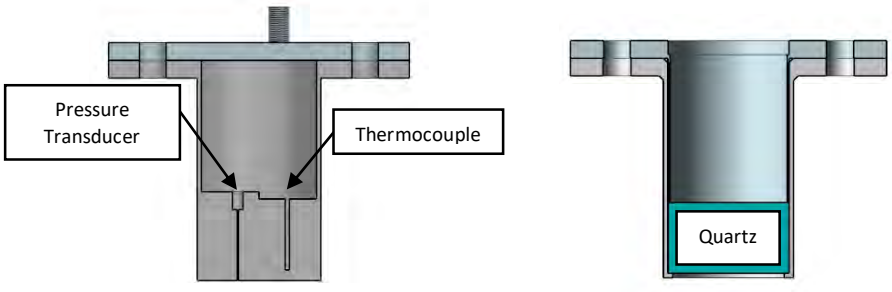

Fig. 4. Sensory and Optical ports

The second section of the combustor will be identical in size to the first one. However, windows will not be present, as the operation of the combustor would cause the windows to be covered in soot.

2.3 Exhaust System

For coal combustion, slagging and fouling is a significant issue. The partially unburnt coal and ash accumulation in the combustor is called fouling. The key factors that affect ash deposition are particle trajectory and ash viscosity[8]. The exhaust system is conical in shape. The shape aids in concentrating the exhaust products to a narrow stream and to travel in a straight path. As the combustor is mounted vertically, gravity plays a part in directing the solid particles towards the exhaust. This section has pressurized water sprinklers attached to it. The water sprays cool the exhaust gases and help the ashes to settle down as slurry. The end part of the exhaust is a detachable cylinder. This part collects the ash and water. The ash cake is collected from this part in regular intervals. A needle valve is attached with a line in the exhaust section after the sprinklers. By choking the flow, pressure is built up in the system. The exhaust gases are collected through this line. Post processing is performed to separate carbon diode from the flue gas. The exhaust design with the cross-sectional view is presented in Fig. 5.

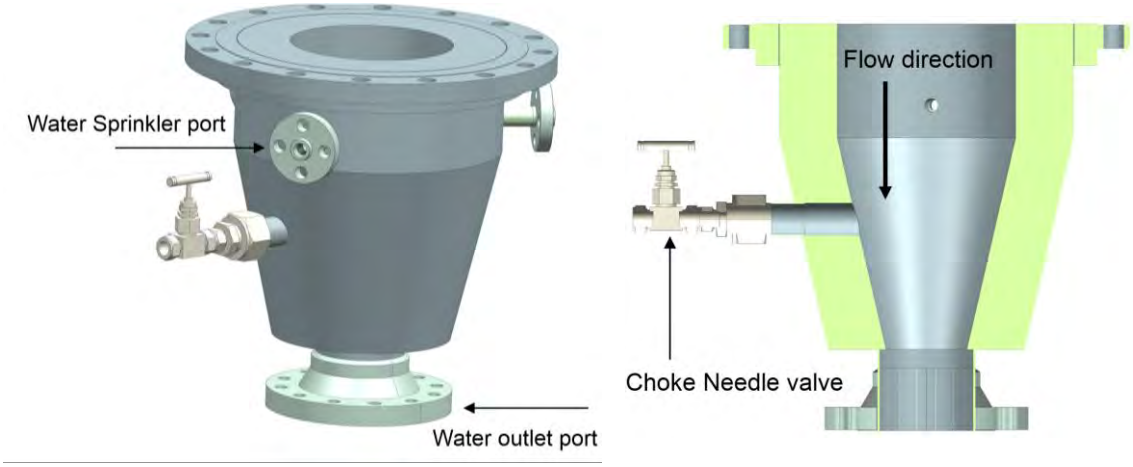

Fig. 5. Exhaust system with cross-sectional view

3 Conclusion

The design of an oxy-coal combustor is presented in this paper. The design is based on the specific requirements of the cycle. This study aims to provide a guideline for future designs with modifications to suit to specific coal and firing inputs. Future works include implementation of cooling system in the design and building and testing the combustor.

Acknowledgement

This research is supported by the US Department of Energy, under award DoE Award Number: DE-FE-0029113 (Program Manager: Mark Freeman). However, any opinions, findings,

conclusions, or recommendations expressed herein are those of the authors and do not necessarily reflect the view of the Department of Energy or Air Liquide.

References

[1] US Energy Information Administration*, Electric Power Monthly*, February 2017, Preliminary data for 2016.

[2] Zebian, Hussam, Marco Gazzino, and Alexander Mitsos. "Multi-variable optimization of pressurized oxy-coal combustion." *Energy* 38.1 (2012): 37-57.

[3] Houghton JT, Ding Y, Griggs DJ, Noguer M, van der Linden PJ, Dai X, et al., editors. *Climate change 2001: the scientific basis*. Cambridge University Press; 2001.

[4] A. Gopan, B.M. Kumfer, J. Phillips, D. Thimsen, R. Smith and R.L. Axelbaum. "Process design and performance analysis of a Staged, Pressurized Oxy-Combustion (SPOC) power plant for carbon capture". *Applied Energy*, *125*, pp.179-188, 2014.

[5] Dennis, R., "US DOE FE Advanced Turbine Program: Suggested Next Steps for UTSR" , Purdue Univ., 2014.

[6] B.J.P. Buhre, L.K. Elliott, C.D. Sheng, R.P. Gupta, T.F. Wall, "Oxy-fuel combustion technology for coal-fired power generation", *Progress in Energy and Combustion Science*, pp. 283–307, 2005.

[7] J. Hong, G. Chaudhry, J.G. Brisson, R. Field, M. Gazzino and A.F. Ghoniem. "Analysis of oxy-fuel combustion power cycle utilizing a pressurized coal combustor". *Energy*, *34*(9), pp.1332-1340, 2009.

[8] N. Berguerand, and A. Lyngfelt. "Design and operation of a 10 kWth chemical-looping combustor for solid fuels–Testing with South African coal". *Fuel*, *87*(12), pp.2713-2726, 2008.

DEVELOPMENT OF A WIRE EMBEDDING DEVICE FOR LARGE AREA ADDITIVE MANUFACTURING SYSTEM

Christopher J. Minjares[1,2*], David Espalin[1,2], Ryan Wicker[1,2]
[1] Department of Mechanical Engineering, The University of Texas at El Paso, El Paso, USA
[1] W.M Keck Center for 3D Innovation, El Paso, USA
* Corresponding author (cjminjares@miners.utep.edu)

ABSTRACT

Additive Manufacturing (AM), commonly known as 3D Printing, has greatly contributed to the existing methods of manufacturing and prototyping as AM allows the designer to produce parts of high complexity in shorter lead times when compared to traditional manufacturing methods. Additionally, the implementation of multi-functionality on AM produced parts has been identified as an area of interest by the AM community. Previous AM systems have implemented methods to produce conductive traces, typically of solid copper wire or conductive inks, to generate circuitry within the AM fabricated parts. Furthermore, the integration of circuitry also increases the tensile strength of the printed part by creating a composite with a plastic matrix and a copper wire fiber. The goal of this study is to generate multi-functional parts using a modified Big Area Additive Manufacturing (BAAM) system to take advantage of its high material deposition rates and large printing volume when compared to medium size material extrusion AM systems. The BAAM system will include a multi-axis wire embedding tool which will create solid wire interconnections while at the same time providing structural reinforcement. A discussion of the design requirements, the mechanical design of the arm, and the development of the wire embedder tool were analyzed in this study.

1 Introduction

AM processes have many advantages over traditional manufacturing methods as it allows for the creation of parts with high complexity. For example, to allow for fast heat dissipation on a part, the designer can manipulate the internal features with different composite plastic materials (blends) to cool the part at a faster rate without compromising the mechanical strength. Medical, automobile, and aerospace fields are interested on the capacities of AM [1]. The integration of multi-functionality allows for the implementation of extra features that well expand the capabilities of a AM fabricated part aside from simply structural.

This study was oriented to the use of conductive material to create electrical interconnections within the plastic part. The selected material is copper wire due its low resistivity when compared to conductive inks. In addition, conductive inks can be very expensive compared to copper wire. The heating method for embedding was chosen to be arc welding since other types of heating will consume large amounts of energy. In addition, arc heating is a method that uses a non-consumable tungsten electrode which is subjected to electrical current to heat up the wire while providing a shielding gas to avoid contamination and to produce plasma [2].

The BAAM system was developed in 2015 by Oak Ridge National Laboratory (ORNL) in collaboration with Cincinnati Incorporated. The BAAM system can generate large parts with faster production rates when compared to medium thermoplastic material extrusion printers.

The printing volume of medium size 3D printers is in the range of $0.03m^3$ to $0.5m^3$ and allows for deposition rates of 0.015 kg/hr to 0.082 kg/hr. Additionally, the cost per kg of filament material ranges from $100 to $200. On the other hand, the BAAM system has a printing volume of $8m^3$ with material deposition rates up to 40 kg/hr. The cost the BAAM material ranges from $2 to $10 per kilogram [3]. The cost of the material and the fast deposition rate makes the BAAM system very attractable to implement different tooling for multifunctionality. In addition, Cincinnati Incorporated is offering support on the development of the wire embedding tool. This hybrid processes will be the first of its kind to be mounted on a large area AM system. The main objective of this paper is to show the mechanical design of the tool along with several design requirements taken to develop this technology.

2 Process and Project Requirements

To physically integrate the wire embedder to the Big Area additive manufacturing system (BAAM), a robotic arm was needed for embedding solid wire on the XZ and YZ planes. This implies that the robotic arm had be design with pivot axis A and B. Additionally, the arm was design to pivot about the same two axes. The robotic arm had be able to support the weight of the tool while maintaining precision, therefore DC motors with gearboxes and encoders where chosen . In addition, the length of the wire embedding tool had to be considered due to the possibility of a collision between the tool and both the substrate and the extruder. Figure 1 shows a preliminary idea of steps that the wire embedding tool followed when embedding copper wire using the BAAM system. The process is as follows:

- The machine pauses the print at a layer where embedding will occur, defined by the user.
- The tool is positioned automatically to its homed location.
- The wire embedder is positioned bellow the extruder to avoid any collision with the substrate (Figure 4A).
- The wire embedding tool approaches the plastic surface until contact (Figure 4B).
- The motor and the welding torch are both activated to drive the copper wire and heat the wire for embedding (Figure 4C).
- The roller pushes the wire against the substrate as the tool travels across the substrate (Figure 4D).
- When the tool reaches its travel destination the arc and the motor will turn off (Figure 4E).
- The copper wire was cut using a high amperage weld (Figure 4F)
- Finally, the tool will translate up to avoid any collision between the wire embedder and the substrate (Figure 4G)

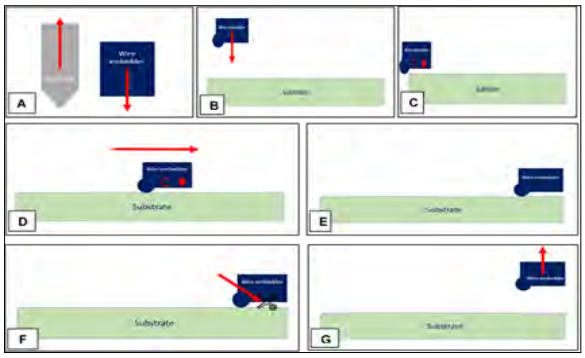

Figure 1: Embedding process of BAAM wire embedder. A) Bring the wire embedder down. B) Move the wire embedder tool close to the substrate. C) Turn on the motor and the arc torch. D) Start the wire embedding Process. E) Turn Off the motor and the arc torch. F) Cut the Wire at the end of the process. G) Move the wire

3 Wire embedding tool

The wire embedding tool required different mechanisms and components to completely automate the wire embedding process. The main plate consisted of an aluminum plate which has a 45-degree angle to avoid collision between the substrate and the tool. This aluminum plate contains the components necessary to make the tool functional. The first mechanism is a spool holder. The spool holder had a spool of 14-gauge copper wire. The main part needed to make this mechanism was an L-aluminum bracket, 3in x 3in (L x H), to allow for free rotations without touching any surface. A double end threaded shaft attaches the L-bracket to the aluminum main plate where the spool is going to be mounted. The spool rotates along a shaft 3½ in length with a thread size of 5/16"-18. Also, to avoid any movement other than rotation, a wing nut with the same thread as the threaded shaft was implemented. The second main mechanism is a V-grooved bearing that attached to the main plate to guide the wire to the straightener. A 80mm double threaded shaft was placed on the main plate and attached using M12 x 1.75 Nuts. The third mechanism is the wire straightener designed to maintain the copper wire straight until reaching the end of the tool. Three V-groove bearings were placed to straighten and pull the copper wire.

A wire driving mechanism was implemented using a DC motor with an encoder that pinches the wire with the help of one of the V-groove bearings. The driving roller has grooves that, with the help of one of the V-grooved bearing, pinch the wire allowing different gauges of wire. An arc welder electrode was placed directly after the wire straightener. The arc is needed to create enough heat on the wire to deform the plastic and embed on the substrate and mechanically locking the wire. The roller mechanism is a tool what was attached to the wire embedding tool to press the copper wire against the plastic substrate to melt the polymer surrounding the wire, hence mechanically bonding the wire and the substrate once cooled. Springs attached to the roller helped maintain the roller's surface parallel when having an uneven surface. A two inch diameter and 0.25 in wide roller was used to allow for embedding on rough and uneven surfaces. Figure 2 shows the assembled mechanisms of the wire embedding tool.

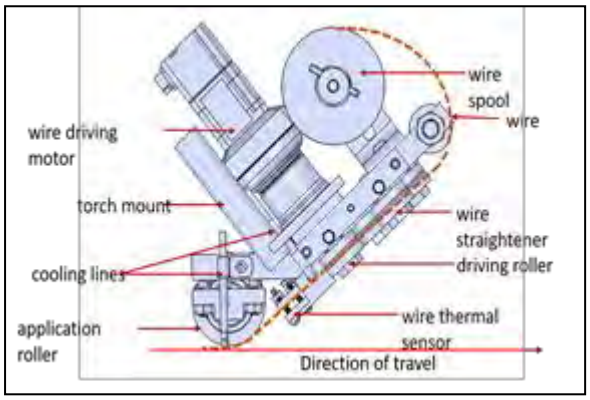

Figure 2: Components of the wire embedder tool assembled together

To help with the finding of repeatable parameters for embedding, a pyrometer was included. In addition, a proximity sensor was also implemented to have the same offset between the tool and the substrate. On right end of the wire embedder a pyrometer sensor has been placed to read the temperature of the substrate before initiating with the embedding process as shown in Figure 3. The pyrometer was also held by a mount attached to the aluminum plate. Both pyrometer and a proximity sensor was placed on the left-end as shown in Figure 3. Additionally, a mount was attached on the right-end of the aluminum plate carrying a pyrometer (Figure 3).

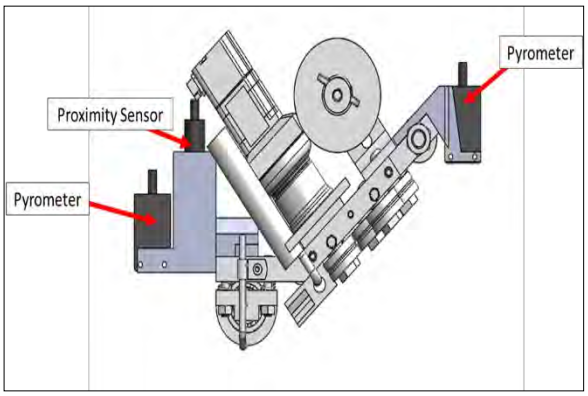

Figure 3: Pyrometer and Proximity sensor mounted on the Wire embedder

4 Robotic Arm

A method to control the wire embedder around different planes inside the BAAM system was the main contributor of the robotic arm design. The robotic arm was mounted in front of the extruder to maintain the large printing volume of the BAAM system. In addition, an actuator translates the robotic arm up and down. Once the substrate is printed, the actuator is translated down well below the extruder and allow for space to embed and avoid possible collision with the extruder. Also, the tool had to embed in different directions, hence the addition of a motor that allows the tool to rotate about the Z axis. In addition, the tool needs to be able to embed at 90 degrees. This means that the tool had to be capable of placing the wire on the walls of the substrate. Therefore, a Rotary motor was implemented to rotate the tool about C-axis.

The implementation of a separate PLC controller was used to control the wire embedder, actuations, and motors. The parker PAC controller was identified due to previous experience with using this controller. The preliminary design of the wire embedding tool includes four motors that move the tool in the Z-axis (up/down), rotation about A-axis, motion

of C-axis, rotation about C-axis, and a motor for driving wire. In addition, a slip ring was implemented to allow free rotations along the A-axis without the entanglement of the power and air lines of the embedding tool. The original connectors for the Parker motors will be used with additional slack to have the tool rotate along the C-axis. The tool rotating along the C-axis will have a set limit of rotations that the tool can achieve. Figure 4 shows the components needed to achieve the rotations around the A, B and C axis using yaskawa motors along with the slip ring and the actuator. The A-axis rotary motor required pulley system off-set the motor and help with wire routing from the slip ring. The wires and the air lines had to pass through the slip ring to achieve free rotations. The pulley system was connected to the motor using a flange. The motor flange was connected to a shaft using a coupler. At the bottom of the motor shaft there are two taper bearings that help with the rotations by making them smoother. Below the slip ring a 2 in diameter shaft using a flange and that mechanism was applied to translate the rotation along A-axis.

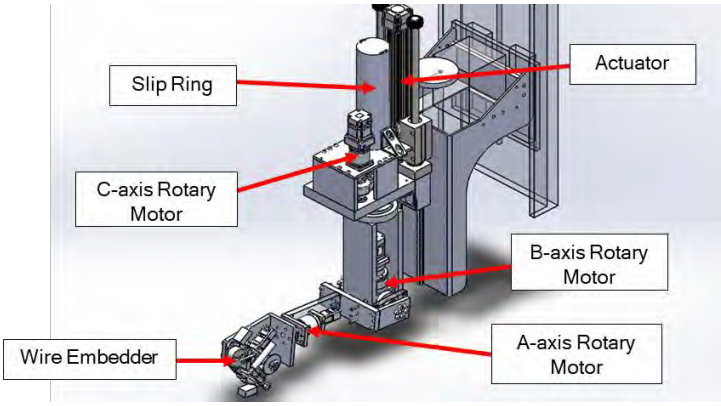

Figure 4: Components of the Arm

Figure 5 shows the final design for the arm with the integration of wire embedder tool.

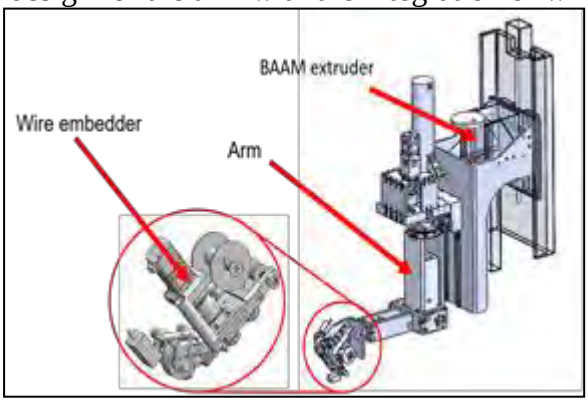

Figure 5: Design of the arm and the wire embedder attached to the BAAM extruder

5 Results

To have evidence the tool being able to embed, a CNC router was used. The wire embedder tool was mounted with a provisional mount on a CNC router to control the tool along the X, Y and Z-axis. The parameters used in the arc welding torch were 40 Amps and 20 Volts. This experiment proved that the concept for the wire embedder is functional with the use of arc

welding (Figure 4), however, a heat transfer model of wire embedding with arc welding is under development.

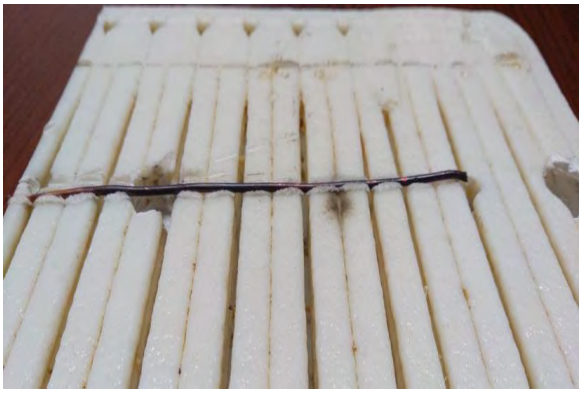

Figure 4: Copper Wire Embedded in the substrate

After analyzing the needs of the tool, the manufacturing side took place to have the physical version of the design. The complete assembly of the tool had to be shipped to Cincinnati Incorporated where they are be testing every single component of the completed tool. Once the company is ready to ship back the tool, the company is going to make final adjustments in the BAAM system at the University of Texas at El Paso to mount the wire embedding tool and testing of the motors and actuation with a printed substrate will take place. This automated process will allow for the creation of large area multi-functional 3D printed parts.

Figure 3: Wire Embedder and the Arm assembled together

6 Conclusion

In conclusion, the addition of a wire embedding tool will allow the BAAM to be the first large scale wire embedder to produce multi-functional parts. This will help with the rapid production of large parts in remote areas where traditional fabrication of parts is not possible. These technologies together still have a lot of improvements that can be made. For instance, determining the temperature of the copper wire before and after embedding will provide a better understanding of what is happening while the embedding process happens. Also, the implementation of sensors will help with parameterizing the embedding process. Finally, the tool will be mounted to the BAAM system to begin testing the components in the real environment without human interaction to improve the design as necessary.

7 Acknowledgment

This research was performed through the National Center for Defense Manufacturing and Machining under the America Makes Program entitled “Multi-Functional BAAM: Big Area Additive Manufacturing w/ Multi-Purpose Wire Embedding” and is based on research sponsored by Air Force Research Laboratory under agreement number FA8650-12-2-7230. The U.S. Government is authorized to reproduce and distribute reprints for Government purposes notwithstanding any copyright notation thereon. This research was conducted at The University of Texas at El Paso (UTEP) within the W.M. Keck Center for 3D Innovation (Keck Center) with support, in part, provided through the Mr. and Mrs. MacIntosh Murchison Chair I Endowment at UTEP (RBW).

References

[1] Ian Campbell, David Bourell, Ian Gibson, (2012) "Additive manufacturing: rapid prototyping comes of age", Rapid Prototyping Journal, Vol. 18 Issue: 4, pp.255-258, https://doi.org/10.1108/13552541211231563

[2] Espalin, David, *"High Feed Rate Wire Heating and Embedding for Large Area Additive Manufacturing of Parts Containing Embedded Electronic Functionality"* (2017). ETD Collection for University of Texas, El Paso. AAI10825126. https://digitalcommons.utep.edu/dissertations/AAI10825126

[3] Love, L. J., & Duty, C. (2015). Cincinnati Big Area Additive Manufacturing (BAAM). *info. ornl. gov. http://info. ornl. gov/sites/publications/files/Pub54708. pdf*.

EXPERIMENTAL SETUP FOR THE TESTING OF PIEZOELECTRIC MASS FLOW RATE SENSOR

P. Perez[1], L. Guitierrez[1], E. Escobedo[1], J. Aboud[1], and N. Love[1]*
[1] Department of Mechanical Engineering, Affiliation, El Paso, TX 79968, USA;
* ndlove@utep.edu

ABSTRACT

The implementation of a quick response piezoelectric sensor in a compressor to predict surge and stall is desired. A piezoelectric sensor generates a voltage response due to stress acting on it. This response will be calibrated in a 2D analysis set-up to represent changes in pressure, and mass flow rate depending on the application. To effectively calibrate our test article, a 2-D set-up system will be created. A key concern about the implementation of this sensor is secure mounting, since detachment can lead to severe damage inside the compressor.

Keywords: Flow sensor, Micro-cantilever, Air Velocity, PZT.

1.Introduction

Nowadays, piezoelectric materials have opened so much interest in the area of research. In modern power systems, extreme fluctuations of parameters such as mass flow, pressure, or temperature can create surge and stall events that end up damaging critical system components. Many previous studies have demonstrated the successful application of MEMS techniques to the fabrication of a variety of flow sensors [1-4]. According to a previous study Yu-Hsiang et al. [1] has developed a MEMS-based air flow sensor featuring a free-standing micro-cantilever structure. In the sensing operation, the air flow velocity is detected by measuring the change in resistance of a piezoelectric layer deposited on a cantilever beam as the beam deforms under the effect of the passing air flow. Young et al. [2] proposed a self-resonant flow sensor based on a resonant frequency shift due to turbulence-induced vibrations. The response of the cantilever beam was modulated with its own resonant frequency. The flow drag force induced a mechanical strain on the cantilever beam, and then, the modulated frequency shifted. Huicong et al. [3] proposed a piezoelectric PZT microcantilever characterized in terms of flow sensing and energy harvesting capability. A self-sustained flow-sensing autonomous microsystem for applications in outdoor environment is possible by employing one PZT microcantilever for flow sensing and integrating an array of PZT microcantilevers for energy harvesting from wind-driven vibrations. Weinstein. [4]. Proposed a cantilevered piezoelectric beam in a heating, ventilation and air conditioning (HVAC) flow. The geometry consists of a fixed cylinder and a bilayer cantilever with one end clamped on the cylinder and the other end free. The fixed cylinder is used to generate vortex street. The positioning of small weights along the fin enables tuning of the energy harvester to operate at resonance for flow velocities from 2 to 5 m/s, which are characteristic of HVAC ducts. Power generation of 200 μW for a flow speed of 2.5 m/s and power generation of 3 mW for a flow speed of 5 m/s was achieved. These power outputs are sufficient to power a wireless sensor node for HVAC monitoring systems or other sensors for smart building technology.

In this study, we suggest a simple method for the implementation of a high response piezoelectric sensor into the Hybrid Performance Project built by NETL to characterize and mitigate the probability of compressor surge and stall. Surge and stall occur when the flow separates from the blades and causes the compressor to stop rotating, creating a no increment in pressure. Hence, this situation leads to failure of the entire cycle that can be expensive and sometimes impossible to fix and making the industries to invest high amounts of money on this. A solution is to implement a high piezoelectric sensor to identify when surge and stall will occur and stop the process before a catastrophic situation happens. For this problem, the team suggested to create a 2D flow set up on which the piezoelectric sensor will generate a current when exposed to a temperature or pressure change. The current generated by the sensor will be calibrated to represent pressure change, this pressure change is obtained as a signal from the piezo that allows to monitor minimal changes and prevent surge and stall in the system.

2. Modeling and Experimental Setup

This set-up testing will be carried out in the Lockheed Martin Laboratory at The University of Texas at El Paso. The experimental set-up involves two flow inlets and one outlet open to the atmosphere. Two fans will be used as the source of the flow, each inlet will be connected to one DC axial fans capable to give 9500 RPMs. The flow produced by these sources will cause stress and bending on the piezoelectric sensor, and this will make the sensor to produce a voltage. The voltage readings and air flow velocity will be then calibrated to try to avoid surge and stall. Two reductions coupling that goes from 10.16 cm to 5.08 cm are attached to the axial fans, this is done in order to meet our velocity requirements due to the increase in velocity after the reduction coupling. The reduction couplings are connected to acrylic pipes with a cross-section of 5.08 cm. These acrylic pipes will lead to an acrylic box with dimensions of 10cmx10cmx10cm, where the test article will take place. Two ‘flow straightener’ placed in both inlets decreased turbulence in the approaching air flow.

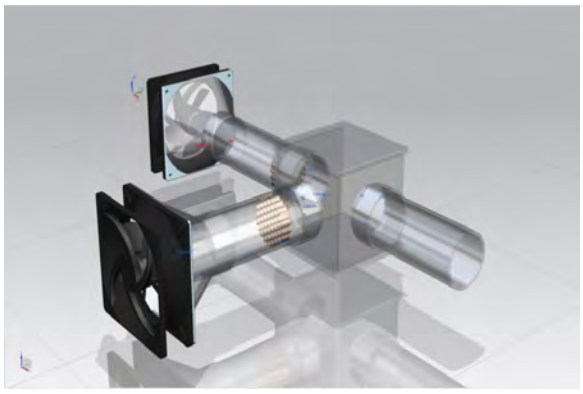

Fig. 1. Experimental setup assembly

Table. 1. Fan requirements. Calculations before and after the reduction. Velocity increase due to the diameter reduction.

Fan		
	Before Reduction	*After Reduction*
Velocity Max (m/s)	*17.02*	*68.09*
Volumetric flow rate (m^3/s)	*0.138*	*0.138*
Diameter (m)	*0.102*	*0.051*
Area (m^2)	*0.008*	*0.002*

Table. 2. Properties and calculation through the inlet pipe. Minimal pressure drop is obtained through the pipe line.

Properties	
Air Density (kg/m^3)	*1.184*
*Air Viscosity (kg/m*s)*	*2E-05*
Gravity (m/s^2)	*9.81*
KL (Loss coefficient)	*0.04*
Friction factor	*0.018*
Reynolds Number	*2E+05*
Head loss minor (m)	*0.591*
ΔPL (minor) (Pa)	*6.861*
ΔPL (major) (Pa)	*1048*
ΔPL (Total) Pa	*1055*
ΔPL (Total) psi	*0.173*

Even though, the fan is capable of producing a maximum velocity of 68.09 m/s, the fan will be set to a maximum of 40 m/s. Chang et al. [1] utilized a piezoceramic sensor for the testing set up and a maximum velocity of 40 m/s for the flow was simulated since at a higher velocity, the sensor could suffer damage. The sensor utilized for this testing process, has similarities with our desired design since it is a piezoceramic sensor. On that way, we can assume the same principle for the velocity of the flow and not exceed 40 m/s since this could cause damage to the testing part. Therefore, a maximum velocity limit will be set for the testing purposes.

The access and installation of the test article is easier having a removable top. Once, lowered the top 8 pins are created in order to hold and keep it in place. Lowering the top creates a direct pressure applied to the piezoelectric.

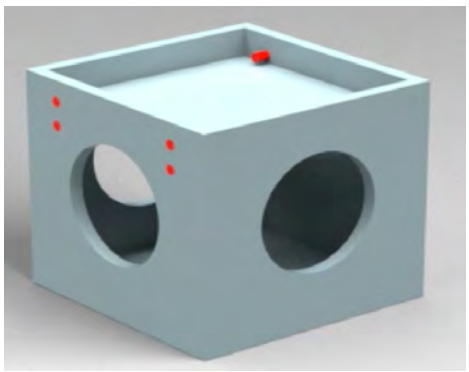

Fig. 2. Drop-down top with supports.

Also, a top cover with 3 different predetermined positions to place the piezoelectric mount with the use of screws was designed. It will allow testing at different distances from the inlet to observe changes within the wind velocity.

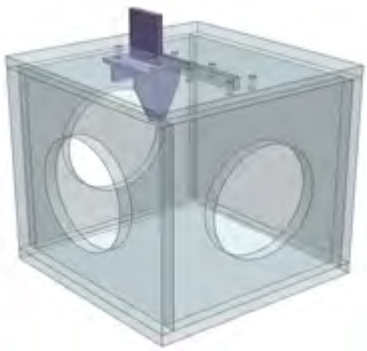

Fig. 3. CAD model of top section with multiple positions for the piezoelectric.

The mount of the piezoelectric sensor was designed to adjust in any of the three predetermined positions in the top of the acrylic box. Whenever the position of the mount is going to be changed, first the top of the box must be removed and then the mount can be separated from the top and then place it in another position. This will also be helpful in case the design of the sensor needs to be changed, as long as the top part of the mount remains the same, the shape and dimensions of the sensor can be change and the same setup can still be used. The mount will be made out of aluminum and there will be a layer behind the piezoelectric material to prevent it from failing.

When air flows over the cantilever structure, the beam is deflected in the downward direction causing a change in the cross-sectional area, and hence the PZT colored by the grey area. The fluid flow induces a mechanical oscillation of the cantilever beam creating periodic vortex streets generated behind the structure. Therefore, the vibration frequency of the structure is related to the stress generated on the piezoelectric creating voltage readings what will end up being used to measure the velocity flow.

Fig. 4. CAD model of piezoelectric sensor mount.

Finally, a fan control system will be used to controlled fans speed by increasing or decreasing the RPMs. The fan control needs a power supply to operate and it will be connected to the fan by using a four pin Molex connector.

Summary

Surge and stall are common problems in turbomachinery that affects the efficiency and effectiveness. With the objective of preventing these phenomena to happen, an experimental setup where a piezoelectric sensor can be implemented and tested is to be designed. The setup consists of a cubic box with two inlets, where the incoming air will be propelled by fans, and one outlet open to the atmosphere. The velocity of the wind will be manipulated with a fan controller. The purpose of having two inlets is to simulate a 2-dimensional flow to make a more realistic testing. The sensor will be placed on the top of the box, which will be removable and will have three different predetermined positions to place the sensor. When the sensor is subjected to stress, due to its properties, it will generate a voltage reading which will be used to determine the amount of stress caused by the wind. The magnitude of the stress will be helpful to know when surge or stall may occur. The purpose of changing the position of the sensor and the velocity of the flow is to test the accuracy of the sensor when subjected to different stresses.

References

[1]- Wang, Yu-Hsiang, et al. *"A MEMS-Based Air Flow Sensor with a Free-Standing Micro-Cantilever Structure."* Sensors, vol. 7, no. 10, 2007, pp. 2389–2401., doi:10.3390/s7102389.

[2]- Seo, Young Ho, and Byeong Hee Kim. *"A Self-Resonant Micro Flow Velocity Sensor Based on a Resonant Frequency Shift by Flow-Induced Vibration."* Journal of Micromechanics and Microengineering, vol. 20, no. 7, 2010, p. 075024., doi:10.1088/0960-1317/20/7/075024.

[3] - Liu, Huicong, et al. *"Development of Piezoelectric Microcantilever Flow Sensor with Wind-Driven Energy Harvesting Capability."* Applied Physics Letters, vol. 100, no. 22, 2012, p. 223905., doi:10.1063/1.4723846.

[4] - Liu, Huicong, et al. *"Development of Piezoelectric Microcantilever Flow Sensor with Wind-Driven Energy Harvesting Capability."* Applied Physics Letters, vol. 100, no. 22, 2012, p. 223905., doi:10.1063/1.4723846.

High Pressure Experimental Boiling Test Facility Design to Increase CHF and HTC on External Tube Surfaces using Micro/Nano-Scale Engineered Structures

Jaime Avendano[1], Mahadi Hasan[2], and Md Mahamudur Rahman[3]

NASA Micro Center for Space Exploration Technology Research (cSETR)
Department of Mechanical Engineering
University of Texas at El Paso, El Paso, Texas, 79902, United States

ABSTRACT

This articles focuses on the design of a high pressure pool boiling experimental test facility for engineered external tube surfaces. Several different tube materials including copper, stainless steel, Inconel, and titanium alloys have been selected as the reference heaters. Various micro, nano, and hierarchical structures have been selected as the engineered structures for increasing pool boiling heat transfer on external tubes using de-ionized water as the working fluid. A stainless steel pressure vessel has been designed consisting of tube heater array, viewports, internal condenser, thermocouples for liquid and gas temperature measurements, differential pressure transducer, pressure relief gage, and bath immersion heaters. This research aims to develop a high pressure (up to 10 bars) pool boiling test facility that will be used to characterize the critical heat flux and heat transfer coefficient of engineered structures. Thus, this novel work will allow to have a database as well as demonstrate the increasing heat transfer performance of engineered structures on external tubes and tube arrays, as well as provide the design compatibility of commercial heat exchanger using engineered micro- and nano-scale structures.

INTRODUCTION

Developing efficient heat dissipation technologies is of critical importance towards the development and the commercialization of next-generation compact and high-performance electronic devices, cooling systems, power generation systems and chemical processing units, as well as retrofitting the existing thermal management schemes. As such, phase change heat transfer systems more specifically boiling heat transfer systems have attracted significant attention due to their ability to extract a large amount of latent energy stored within the fluid.

Pool boiling is an efficient mode of phase change heat transfer process accompanied by bubble nucleation, growth, and departure from the heated surface in a stagnant liquid. Noticeably, boiling becomes vigorous and more effective at higher heat fluxes as vapor production increases with the increase in active bubble nucleation sites and so does the efficiency of heat transfer processes, also termed as heat transfer coefficient (HTC), by maintain low wall-superheat at the heat transfer surface. However, if the applied heat flux exceeds the upper governing limit of a heat transfer surface, which is also termed as the critical heat flux (CHF) limit, the insulating effect of stable vapor blanket covering the surface starts dominating the bubble agitation and thus, inhibits the effective heat transfer as well as results in a rapid inflation of surface temperature, often leading to burnout. It is therefore essential to design and develop advanced thermal management schemes to further increase the boiling efficiency through HTC as well as, most importantly, the CHF limits of heat transfer surfaces.

[1]Undergraduate Research Assistant, NASA Micro Center for Space Exploration Technology Research, Department of Mechanical Engineering
[2]Graduate Research Assistant, NASA Micro Center for Space Exploration Technology Research, Department of Mechanical Engineering
[3]Assistant Professor, NASA Micro Center for Space Exploration Technology Research, Department of Mechanical Engineering

Motivated by these goals, numerous researches have been conducted in the past several decades to enhance the limits of boiling heat transfer. Specifically, in the last one decade, with the advancement in fabrication technologies significant improvements have been reported through integrating the micro- and nano-scale features to the boiling surfaces. Several engineered surfaces have been considered including additive features as well as subtractive features such as hydrophilic porous layers [1], nanowires [2-4], nanorods [5, 6], oxide nanostructures [7], micropillars [7-9], hoodoos [10], micro-ridges [11, 12], and hierarchical structures [7, 13-15]. As of today, these surfaces have been shown to increase the pool boiling CHF ranging from +30% to +240% as compared to the reference heaters. A representative pool boiling heat transfer enhancement using surface engineering has been shown in Fig. 1, reported by Rahman et al. [16]. Four different nanostructures and five different microchannel structures were incorporated on flat copper surfaces, and significant CHF and HTC enhancement has been demonstrated.

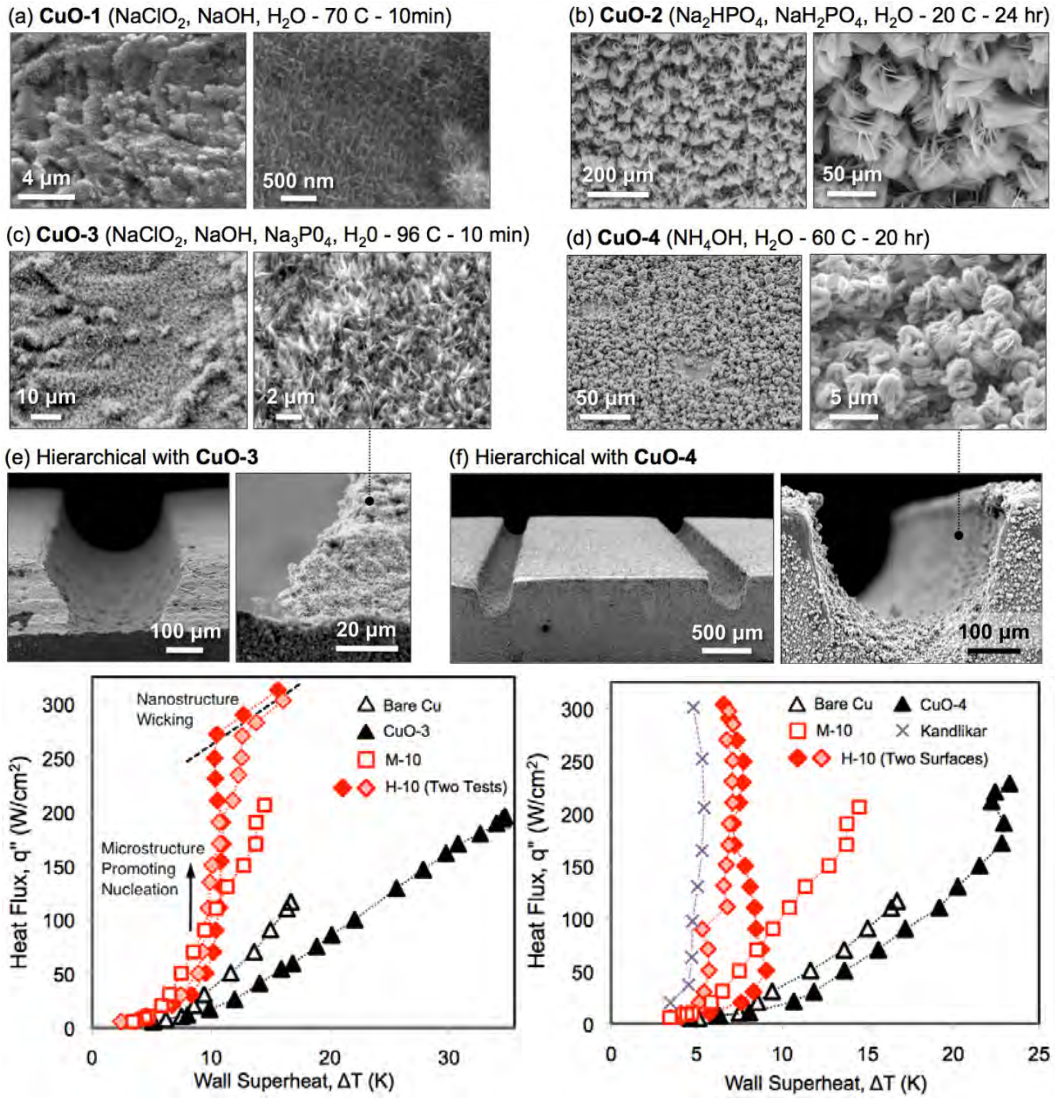

Figure 1: Pool boiling heat transfer enhancement using engineered micro/nano hierarchical channel surfaces: (a) – (d): fabricated four different nanostructures, (e) – (f): nanostructures on micro-channel surfaces [16].

Although significant heat transfer enhancement has been reported using engineered micro- and nano-scale structures, the results are limited to flat surfaces. Whereas, a vast majority of the industrial boiling heat transfer applications are associated with tube surfaces. For example, external tube boiling is very important to reduce energy consumption in the industrial, commercial and residential applications including air condition, power plant heat exchangers, desalination plants [17]. Air conditioning equipment represents close to a $100 billion, 100 million-unit per year global market, and accounts for 4.5 exajoules site energy consumption per year, comprising just over 4% of global building site-energy consumption [18]. The International Energy Agency projects that air conditioning energy consumption by 2050 will increase 4.5 times over 2010 levels for non-Organization of Economic Coordination and Development [18]. Thus it has become significantly important to characterize and demonstrate the heat transfer enhancement on complex geometries such as external tubes using engineered structures, more specifically on tube bundles.

The aim of this work is to design a pool boiling heat transfer test facility capable of measuring the critical heat flux and the heat transfer coefficient on engineered external tube surfaces up to 10 bar pressure. Motivated by a previous pressurized boiling facility designed to test boiling performance of FK-649 at high pressure, a pressurized pool boiling test facility will be constructed to test saturated water up to 10 bar pressure conditions [19, 20]. This work will give a new perspective on understating of critical heat flux for tube bundle at high pressure conditions, as well as provide a guideline for designing the future generation engineered boiling heat exchanger surfaces.

ENGINEERED SURFACES

Several different commercial heat exchanger materials including copper, stainless steel, additively manufactured Inconel, and Titanium alloys will be considered to characterize the heat transfer performance of engineered external tubes during pool boiling up to 10 bar pressure. Among a wide variety of engineered structures such as nano-structures, micro-pillars, micro-channels, and micro/nano hierarchical structures, this work has identified several potential structures based on the material compatibility as well as the reported enhancement in both CHF and HTC. Figure 2 shows the selected structures those will be fabricated on the external tube surfaces and tested in the pool boiling test facility reported in this article.

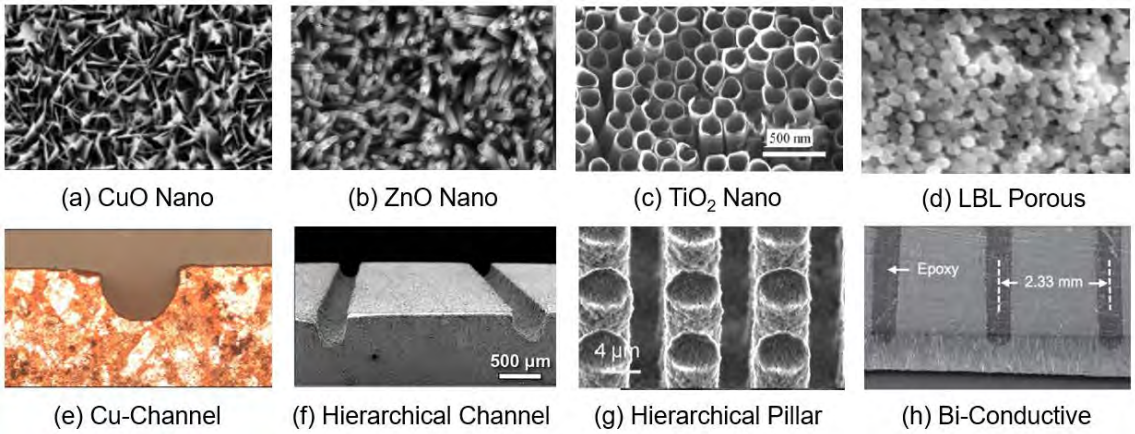

Figure 2: Selected engineered structures for the high pressure external tube pool boiling: (a) CuO nanostructures [13], (b) ZnO nanowires [21], (c) TiO_2 nanotubes [22], (d) porous layer-by-layer SiO_2 surface [1], (e) channel geometries [23], (f) nanostructures on micro-channels [16], (g) nanostructures on micro-pillars [7], (h) mixed conductivity design [23].

SURFACE CHARACTERIZATION

Prior to boiling, the fabricated engineered structures will be characterized using scanning electron microscopy (SEM). The surface roughness will be measured using atomic force microscopy (AFM). The surface wettability will be characterized using the sessile droplet contact angle measurement technique as shown in the Fig. 3(a). The surface wickability will be characterized using a custom-built capillary tube technique where the liquid volume flux will be determined based on volumetric flowrate of liquid within the structures, and the wetted area, as shown in Fig. 3(b).

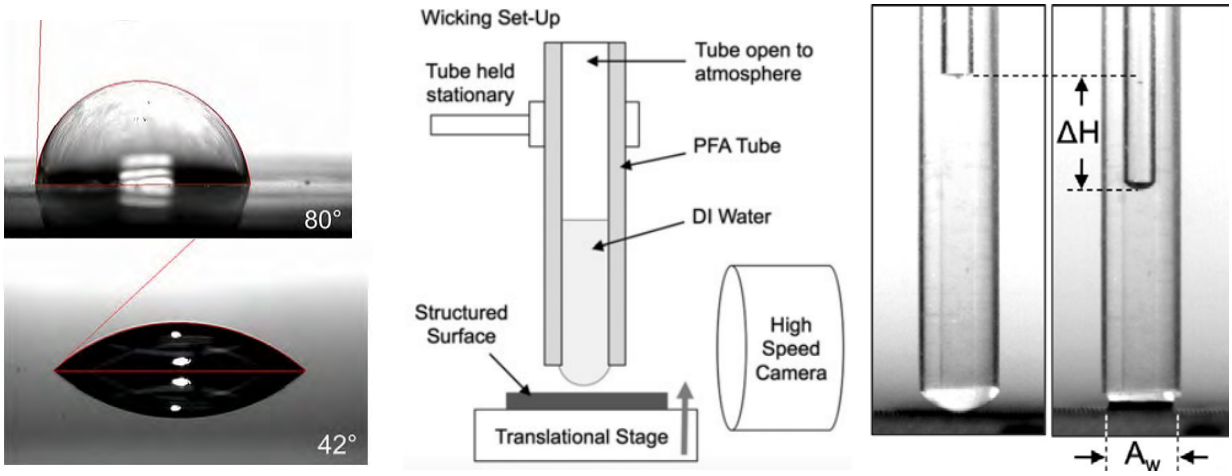

(a) (b)

Figure 3: Surface wettability and wickability characterization: (a) surface contact angle measurement [4], (b) surface capillary wicking test setup schematic [25], and (c) capillary tube based wicked volume flux measurement [13].

EXPERIMENTAL DESIGN

The pressurized boiling facility has been designed to characterize the heat transfer performance of engineered external tube and tube bundles up to 10 bar pressure using water as the working fluid. The tubes will be tested up to the CHF limit. Both boiling on single tube and a 5×5 tube array will be performed in this research. Metal tubes of various materials including copper, stainless steel, Inconel, Titanium alloys of 10-20 mm outer diameter and 10 mm long will be used in this work. The tubes will be resistively heated using insulated electric wire heaters inserted inside the tubes. Thermocouples will be inserted in various locations inside the tube to determine the surface temperature of at the tube outer surface. Ceramic insulation tubes will be place at the ends of the tubes to minimize heat loss as well as define the heater area of the tubes. Various engineered structures including nano-scale, micro-scale, and micro/nano hierarchical structures will be fabricated on the tubes using advanced micro- and nano-manufacturing technologies, as well as micro-machining techniques. A schematic of the designed both single external tube, as well as tube bundle is presented in Fig. 4.

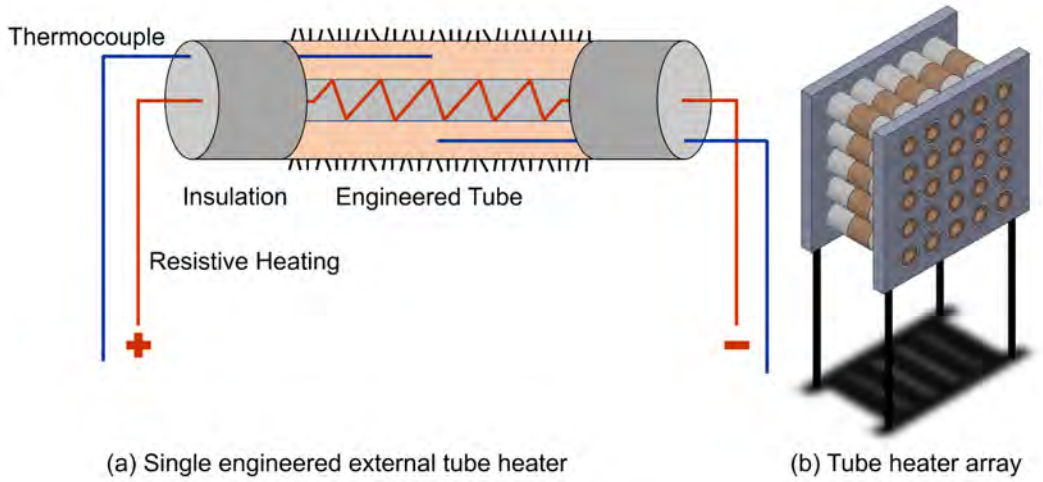

Figure 4: Schematic of engineered external tube boiling surface design: (a) resistive heating of single engineered external tube, and (b) schematic of 5×5 boiling tube array.

The pool boiling test rig has been designed to withstand high temperature and high pressure up to 20 bar. Stainless steel chamber has been selected to be the pool boiling chamber and pressure vessel. It consists two glass viewing windows, a differential pressure transducer, a pressure relief valve, condenser coil, one thermocouple for liquid temperature, one thermocouple for vapor temperature measurement, a degassing vent, a drain valve, and several bath heaters. A schematic of the boiling chamber with selected components is shown in Fig. 5.

The support of the facility will be achieved with 4 high-strength steel threaded rods of 3/4"-10 thread size, 2 feet long 316 stainless steel head screws. The height at which the facility is standing was designed taking into consideration a free space to remove the tube array bundle and change the specimen being tested in an efficient way. The facility will be attached to an optical table to avoid vibration and have a flat surface level in order to have accurate readings.

The boiling facility is being designed by optimizing space in order to minimize the heating power of water bath to reach saturation temperature, especially at high pressures. The liquid bath will be heated by several immersion heaters placed along the bottom part of the facility. A DC power supply will be used to provide power to the immersion heaters. This facility requires components to regulate the pressure. A differential pressure transducer will be used to maintain the chamber pressure at

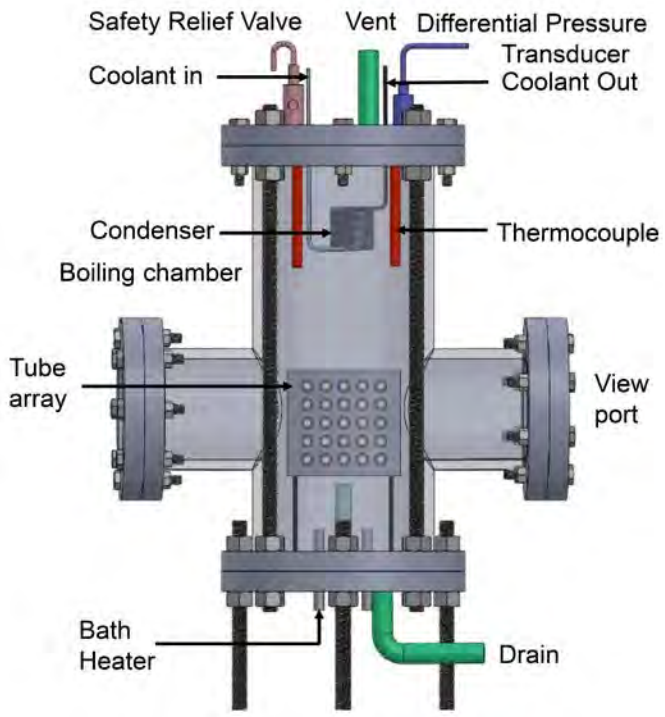

Figure 5: Schematic of high pressure external tube pool boiling test facility

the saturation condition. A copper coil will be used as an internal condenser, which will be placed on the top of the facility. The coil will have two ends in order for the coolant to have an inlet and an outlet. A chiller will be used to circulate refrigerant through the condenser, and a valve will be used to control the refrigerant flow rate in order to maintain the saturation pressure with increasing given heat flux. Two type E thermocouples will be placed inside the pressurized facility to measure the fluid and the gas temperatures, this type of thermocouples was selected for this experiment because of its accuracy and strong signal than type k and type j thermocouples, as well as it can be used on temperatures up to 1000 °F. On the top of the facility there will be a top vent in order to degas the working fluid. At the bottom of the facility there will be a release mechanism in order to drain all the fluid after the experiments. The experiments will be conducted maintaining the water pressure up to 10 bar. The boiling phenomena will be visualized through viewports using a high speed camera.

CONCLUSIONS

The aim of this research is to design a high pressure (up to 10 bar) pool boiling test facility capable of measuring both critical heat flux and heat transfer coefficient on external tube surfaces. Several engineered micro- and nano-scale engineered structures have been selected for external tube boiling on various reference tubes incldinf copper, stainless steel, Inconel, and Titanium alloys. The pool boiling tube and tube bundle have been designed as well as the boiling vessel has been designed. The measurement equipment and materials have been selected in order to manufacture and test this boiling facility. Thus this work provides a platform in designing the high pressure pool test facility required for characterizing the heat transfer performance on engineered external tube surfaces for commercial heat exchangers.

FUTURE WORK

In order to determine the critical heat flux on tube boiling, the designed pressurized boiling facility will be manufactured. There is little understanding on tube boiling as heating mechanism and inexistent knowledge on high pressure conditions, by conducting this experiment new data will bring a different way to enhance critical heat flux.

REFERENCES

[1] Tetreault-Friend, M., Azizian, R., Bucci, M., McKrell, T., Buongiorno, J., Rubner, M., and Cohen, R., 2016, "Critical heat flux maxima resulting from the controlled morphology of nanoporous hydrophilic surface layers," Applied Physics Letters, 108(24), p. 243102.
[2] Chen, R., Lu, M.-C., Srinivasan, V., Wang, Z., Cho, H. H., and Majumdar, A., 2009, "Nanowires for Enhanced Boiling Heat Transfer," Nano Letters, 9(2), pp. 548-553.
[3] Lu, M.-C., Chen, R., Srinivasan, V., Carey, V. P., and Majumdar, A., 2011, "Critical heat flux of pool boiling on Si nanowire array-coated surfaces," Int. J. Heat Mass Transfer, 54(25–26), pp. 5359-5367.
[4] Yao, Z., Lu, Y. W., and Kandlikar, S. G., 2011, "Effects of nanowire height on pool boiling performance of water on silicon chips," International Journal of Thermal Sciences, 50(11), pp. 2084-2090.
[5] Li, C., Wang, Z., Wang, P.-I., Peles, Y., Koratkar, N., and Peterson, G. P., 2008, "Nanostructured Copper Interfaces for Enhanced Boiling," Small, 4(8), pp. 1084-1088.
[6] Rahman, M. M., Ölçeroğlu, E., and McCarthy, M., 2014, "Scalable Nanomanufacturing of Virus-templated Coatings for Enhanced Boiling," Advanced Materials Interfaces, pp. n/a-n/a.

[7] Chu, K.-H., Joung, Y. S., Enright, R., Buie, C. R., and Wang, E. N., 2013, "Hierarchically structured surfaces for boiling critical heat flux enhancement," Applied Physics Letters, 102(15), pp. 151602-151604.
[8] Chu, K.-H., Enright, R., and Wang, E. N., 2012, "Structured surfaces for enhanced pool boiling heat transfer," Applied Physics Letters, 100(24), pp. 241603-241604.
[9] Honda, H., Takamastu, H., and Wei, J. J., 2001, "Enhanced Boiling of FC-72 on Silicon Chips With Micro-Pin-Fins and Submicron-Scale Roughness," Journal of Heat Transfer, 124(2), pp. 383-390.
[10] Bon, B., Klausner, J. F., and McKenna, E., 2013, "The Hoodoo: A New Surface Structure for Enhanced Boiling Heat Transfer," Journal of Thermal Science and Engineering Applications, 5(1), pp. 011003-011003.
[11] Zou, A., and Maroo, S. C., 2013, "Critical height of micro/nano structures for pool boiling heat transfer enhancement," Appl. Phys. Lett., 103(22).
[12] Zou, A., Singh, D. P., and Maroo, S. C., 2016, "Early Evaporation of Microlayer for Boiling Heat Transfer Enhancement," Langmuir, 32(42), pp. 10808-10814.
[13] Rahman, M. M., Ölçeroğlu, E., and McCarthy, M., 2014, "Role of Wickability on the Critical Heat Flux of Structured Superhydrophilic Surfaces," Langmuir, 30(37), pp. 11225-11234.
[14] Ahn, H. S., Lee, C., Kim, J., and Kim, M. H., 2012, "The effect of capillary wicking action of micro/nano structures on pool boiling critical heat flux," International Journal of Heat and Mass Transfer, 55(1–3), pp. 89-92.
[15] Ahn, H. S., Lee, C., Kim, H., Jo, H., Kang, S., Kim, J., Shin, J., and Kim, M. H., 2010, "Pool boiling CHF enhancement by micro/nanoscale modification of zircaloy-4 surface," Nuclear Engineering and Design, 240(10), pp. 3350-3360.
[16] Rahman, M. M., and McCarthy, M., 2017, " Effect of Length Scales on the Boiling Enhancement of Structured Copper Surfaces," ASME. J. Heat Transfer, 139(11), pp. 111508-111508-9.
[17] Emery, T. S., Jaikumar, A., Raghupathi, P., Joshi, I., and Kandlikar, S. G., M., 2018, " Dual enhancement in HTC and CHF for external tubular pool boiling – A mechanistic perspective and future directions," International Journal of Heat and Mass Transfer, 122 (0), pp. 1053-1073.
[18] 'The Future of Air Conditioning for Buildings Report Department of Energy" http://www.energy.gov/eere/buildings/downloads/future-air-conditioning-buildings-report> (Accessed: 27-feb-2019).
[19] Forrest , E. C., Hu, L. W., Buongiorno, J., and McKrell, T. J., "Pool Boiling Heat Transfer Performance of a Dielectric Fluid With Low Global Warming Potential", Heat Transfer Engineering, 34 (15), pp. 1262-1277.
[20] Rahman, M., M., Wang, C., Saccone, G., Bucci, M., Buongiorno, J., "Mechanistic prediction of wickability and CHF enhancement in micro- and nano-engineered surface", Proceedings of the 17th International Topical Meeting on Nuclear Reactor Thermal Hydraulics (NURETH-17), Xi'an, China, September 3 - 8, 2017.
[21] Wemp, C. K., and Carey, V. P., 2017, "Water Wicking and Droplet Spreading on Randomly Structured Thin Nanoporous Layers," Langmuir, 33, 14513−14525.
[22] Yue, C., DongChuan, M., HongBin, Z., Nan, D., and ShuShen, L., 2009, "Pool boiling on the superhydrophilic surface with TiO2 nanotube arrays," Science in China Series E: Technological Sciences, 52(6), pp. 1596-1600.
[23] Rahman, M., M., Pollack, J., and McCarthy, M., 2015, "Increasing Heat Transfer Using Low Conductivity Materials", Scientific Reports, 5, 13145.

HIGH-TEMPERATURE ENVIRONMENTS FOR THERMOPLASTIC HYBRID MANUFACTURING

L.I. Gutierrez Sierra[1, 2], J.L. Coronel[1,2], R. B. Wicker[1, 2], D. Espalin[1, 2]

[1] *W.M. Keck Center for 3D Innovation, The University of Texas at El Paso, El Paso, TX 79968, USA;*
[2]*Department of Mechanical Engineering, UTEP, El Paso, TX 79968, USA;*
* Corresponding author (ligutierrezsierra@miners.utep.edu)

Keywords*: hybrid manufacturing, fused deposition modeling, high temperature environment, thermal contraction*

ABSTRACT

Hybrid manufacturing is an emerging field within additive manufacturing (AM) that combined complementary technologies with AM to fabricate geometrically complex parts that perform multiple functions. One example of a hybrid manufacturing system is the Foundry Multi3D system, which is the focus of this work. Since the Foundry Multi3D system consists of transporting a partially printed part through varying temperature regions, warping was an effect caused by temperature gradients. As a proposed solution, designs for a mobile and stationary high temperature environment (HTE) chamber were made whereby the mobile chamber served to shield the part from heat transfer losses when taken out of the printer. The stationary chamber decreased heat losses when the 3D printer platform was on the CNC router bed, which executes a complementary machining operation. The constant ambient temperature for the built part throughout the entire process minimized thermal contractions and warping.

1 Introduction

Additive manufacturing (AM) is the process in which an object is built layer-by-layer with the help of a Computer Aided Design (CAD) [1]. Hybrid manufacturing is the combination of two or more manufacturing processes (e.g. AM and machining)[2]. The Foundry Multi3D System is an example of a hybrid manufacturing system. This system combines AM, using two Stratasys' Fused Deposition Modeling (FDM) Fortus 400mc industrial printers, with several other manufacturing post-processes by utilizing a Computer Numerical Control (CNC) router and a six-axis robotic arm (Yaskawa Motoman MH-50) for part transportation between stations. Current efforts are being made to mitigate the effects of thermal gradients (between printer oven and ambient) while transporting build with the robot, while post-processing is being carried out in the CNC router, and for part removal.

The Multi^{3D} System faces challenges that directly deform the build's geometry. As the recently printed part exits the printer's oven, it is immediately exposed to a large temperature gradient due to the low ambient temperature. This temperature gradient creates thermal stresses within

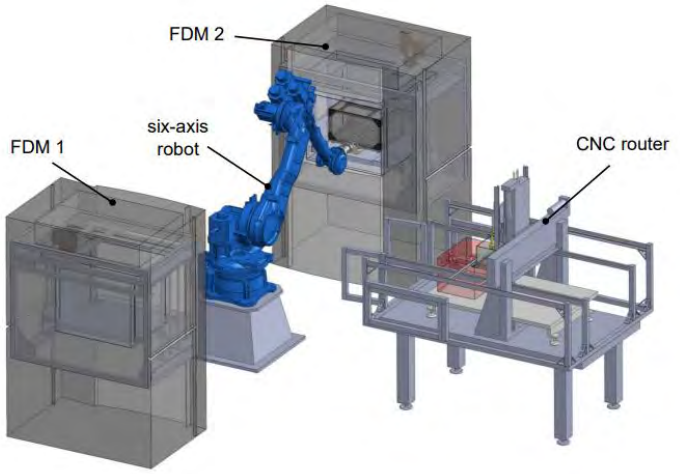

Fig 1. Multi^{3D} system CAD concept [3]

the part. Alongside with thermal stresses, there are thermal displacements, which can shrink, enlarge, or warp the built part. These defects can lead to a malfunctioning part by changing its mechanical properties such as the tensile strength. In the case of the thermoplastic polyether ether ketone (PEEK) 150P, cooling rates affect its mechanical properties. A higher cooling rate produces a lower crystallinity which also leads to a lower tensile strength; and a slow cooling rate produces a higher crystallinity which leads to a higher tensile strength [4]. To have a repeatable set of experiments, a consistent set up must always be used to have the same conditions throughout the entire test.

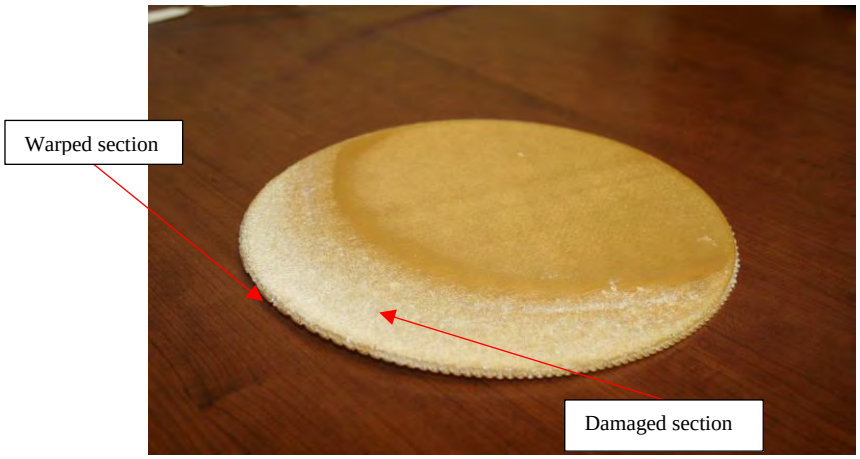

Fig 2. Warped ULTEM 1010 sample

2 Proposed Solution

To counteract the warping effects, two high temperature environments were designed. The first high temperature environment is a mobile unit that serves to shield the printed part from large temperature gradients while the build is being transported within the Multi^{3D} System. This

unit's heating system consists of two 400W AC ceramic finned heaters and a centrifugal fan to generate a flow through both heaters. This hot air will be circulating within the heated environment and maintain a constant temperature controlled with a PID controller with a thermocouple monitoring the envelope temperature. The second environment is adapted to the CNC router used for manufacturing post-processing. This environment consists of two 1250W AC ceramic finned heaters (installed in the back portion) with two AC fans pushing air through each heater towards the front section of the router (where the post-processing will be carried out). Previous literature review has shown how thermal and residual stresses begin to accumulate when the part's temperature drops below the material's glass transition temperature (Tg) [5][6]. Therefore, both high temperature environments are to be maintained at the printer's oven temperature, which is close to the material's Tg.

3 Validation

To validate the mitigation of warping effects, a 3D scanner (FARO Design ScanArm) will be used to scan a benchmark part with no high temperature environments used for part removal and then compare the obtained point cloud or standard tessellation (.STL) file with the part's CAD file. After the benchmark comparison is made, the same parts will be manufactured with the use of both high temperature environments for part removal. The parts will undergo different cooling rates to characterize an optimal cooling rate for each FDM material available. These parts will then be 3D scanned and compared to the original part's CAD file.

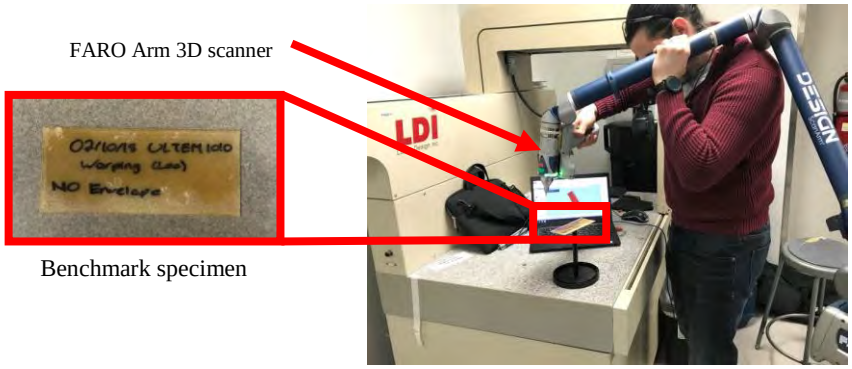

Fig 3. 3D Scanning of ULTEM 1010 Benchmark specimen

4 Results

The mobile high temperature environment was tested to reach a temperature of ~220ºC. This target temperature was chosen due to ULTEM 1010's high glass transition temperature (~210ºC). The mobile environment did not reach the target temperature; however, efforts are being made to insulate the bottom portion of the environment to avoid heat losses towards the steel optical table it was sitting on. Two benchmark specimens were manufactured out of polycarbonate (PC) and ULTEM 1010. PC was selected due to its continuous use in projects and ULTEM 1010 was chosen due to its high printing temperature, which will exemplify the worst-case scenario. 3D scanning was done for both specimens. The first scans showed noise from the laser scanner due to the material's reflectiveness; therefore, the specimens were

coated with powder to get an opaquer surface and eliminate the noise. The scan files obtained will need to be processed for comparison with the original CAD files.

5 Future Work

The scan data will be processed using Geomagic Design X to obtain a point-cloud and a final .STL file that will be compared to the original specimen's .STL file. The use of the 3D scanner allows the scanning of complex geometries; however, to further validate this data, the coordinate measuring system (CMM) will obtain precise geometric measurements of the specimen's features and defects. A comparison between the part's original .STL file and the 3D scanned .STL file will be carried out using GOM Inspect software. Finally, an optimal cooling rate will be obtained that will be used for part removal once the final work piece is finalized. These cooling rates will work for the mitigation of the part's warping due to the final exposure to ambient temperature

References

[1] Berman, B. "3-D printing: The new industrial revolution". *Business Horizons*, Vol. 55, pp 155-162, 2012.

[2] Zhu, Zicheng, et al. "A review of hybrid manufacturing processes–state of the art and future perspectives." *International Journal of Computer Integrated Manufacturing* 26.7 (2013): 596-615.

[3] Ambriz, Steven Daniel. *Design and development of the portable build platform and heated travel envelope for the Multi 3D manufacturing system*. The University of Texas at El Paso, 2015.

[4] Lee, Woo I., et al. "Effects of cooling rate on the crystallinity and mechanical properties of thermoplastic composites." *Journal of Reinforced Plastics and Composites* 6.1 (1987): 2-12.

[5] Kim, Kwang-Soo, H. Thomas Hahn, and Robert B. Croman. "The effect of cooling rate on residual stress in a thermoplastic composite." *Journal of Composites, Technology and Research* 11.2 (1989): 47-52.

[6] Wang, Tian-Ming, Jun-Tong Xi, and Ye Jin. "A model research for prototype warp deformation in the FDM process." *The International Journal of Advanced Manufacturing Technology* 33.11-12 (2007): 1087-1096.

Initial Investigations in Additively Manufacturing with TZM and Tungsten powders for Aerospace Applications

Scott T. Wilkins,[1] Nathaniel Jurado,[2] Justin H. Vanhoose,[3] and Emily Herzog[4]
The University of Texas at El Paso, El Paso, Texas, 79925, The United States of America

I. Abstract

Additive manufacturing (AM), or 3D printing, is becoming crucial for creating inexpensive, effective components for aerospace applications. AM allows for the creation of effective designs that cannot be fabricated using contemporary manufacturing. This process not only allows for more creative approaches, but also decreases manufacturing time and cost. Printed components need to withstand the harsh environments common in aerospace and rocket propulsion. Two metal powders currently being researched for AM of rocket propulsion components are Titanium Zirconium Molybdenum (TZM) and Tungsten. Both materials possess mechanical properties that can withstand the environments undergone in rocket propulsion. However, these properties are altered if the material is additively manufactured. In order to use 3D printed TZM and Tungsten components for rocket propulsion, an understanding of the altered mechanical properties needs to be attained. To accomplish this, multiple printed specimen will be manufactured to test material structure, tensile strength, thermal capabilities, and other variables. This paper covers the mechanical background of TZM and Tungsten used in AM and aerospace, as well as the necessary requirements for conducting preliminary experiments.

II. Nomenclature

AM = Additive Manufacturing
PBF = Powder Bed Fusion
TZM = Titanium Zirconium Molybdenum
SLM = Selective Laser Melting
EBM = Electron Beam Melting

III. Introduction

The advancement of additive manufacturing technology has massively benefitted the aerospace industry. Since the early 2000s, new innovations in the fields of engineering and computer science have changed the capabilities of aerospace systems, such as the inclusion of carbon fiber, neural network computing, and advanced metal alloys. These innovations as well as a growing space market are an ideal scenario for continuing to grow the presence of mankind existing in space.

AM is a process in which layers of material are selectively positioned and laminated together to form 3-dimensional objects. This technology is beneficial for aerospace engineering because it allows for components to be designed and fabricated that wouldn't normally be possible from conventional manufacturing. According to NASA's presentation, "*Additive Manufacturing of Aerospace Propulsion Components,"* their rocket propulsion systems, utilizing AM, had greater cycle time, more complexion in design, and a significant reduction in fabrication time [1]. Systems designed for the NASA-Air Force-Aerojet Collaborative Effort had lead times estimated to be one year

[1] Graduate Research Associate, The Center for Space Exploration and Technology Research
[2] Undergraduate Research Associate, The Center for Space Exploration and Technology Research
[3] Research Engineer/Scientist Associate, The Center for Space Exploration and Technology Research
[4] Graduate Research Associate, The Center for Space Exploration and Technology Research

decrease to only taking four months while implementing an AM process. Greater design complexity and reduced fabrication time are also made possible from shape-optimization software used by most AM industries.

The Space Industry is rapidly becoming commercialized through privatized companies. According to a study conducted by SmarTech Publishing, AM will be a "cornerstone" in a developing $330 billion-dollar space market within the next ten years [2]. One of the greatest hurdles in space travel is the high cost per kilogram of getting vehicles and payloads into orbit. An interesting aspect AM has is that it naturally optimizes reduction of mass and has shorter development times [2]. This is possible because the process of AM is fundamentally layering material to build components instead of subtracting from a larger block. This has shown to be more cost effective, and less wasteful [2].

For printing metals, a process called Powder Bed Fusion (PBF) is commonly used. PBF takes particles of powdered metal (roughly 10 – 50 microns in diameter) and selectively sinters them together, via a plasma laser or electron beam [3]. (Fig. 1) [4]. This allows for designs to be fabricated without a large sum of steps for post-processing.

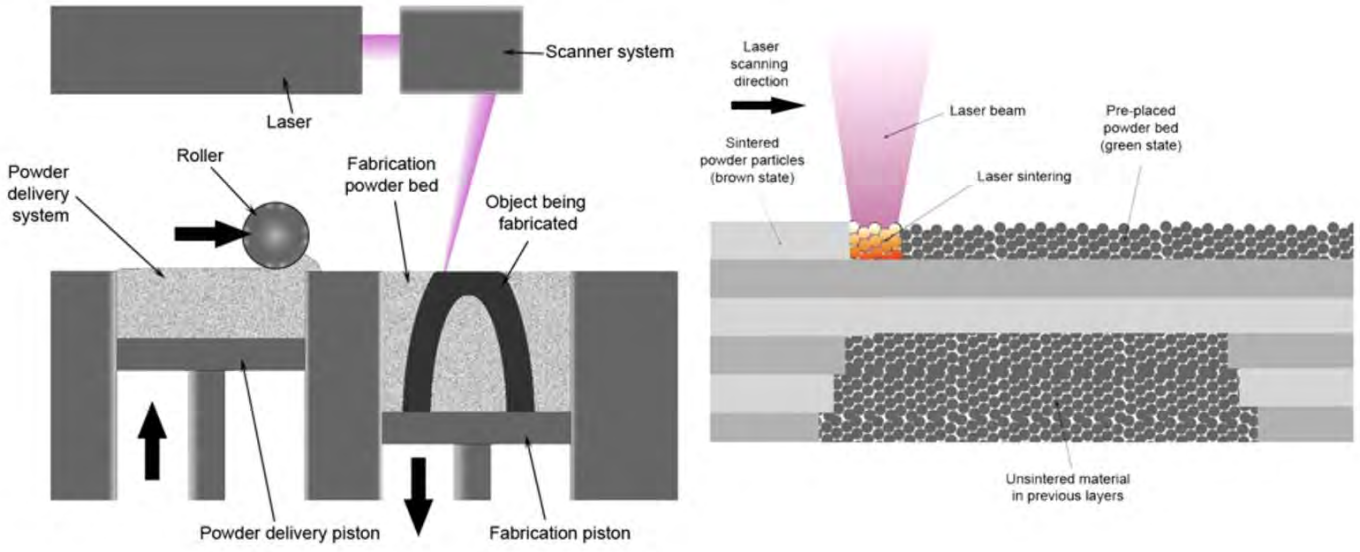

Figure 1: Image showing the general process of PBF AM

There are two main categories of PBF, Selective Laser Melting (SLM), and Electron Beam Melting (EBM) [3]. EBM fuses together metal particles or wire with an electron beam in an inert environment. Typically, EBM is a faster process than SLM, however the tradeoff is an increase in surface roughness seen in the printed parts. SLM uses a high-density laser to fuse/melt metal particles in the print bed together. This application is better suited for more complex geometries having thinner walls/channels. Although it has a slower build rate than EBM, due to the flexibility with geometry complexity and finer surface finishes typically seen, it will be the method of choice in this research.

Tungsten and TZM have melting temperatures that are suitable for the high temperature exhaust gases that a thruster will be subjected to. The thermal properties of TZM and Tungsten are maintained after being additively manufactured. However, the AM process does effect the mechanical structure of the piece. Due the lamination process in PBF, porous regions occur between the layers of material. These regions could lead to decreased tensile strength in a part [4].

To test these mechanical changes, multiple tensile specimen will be printed as a part of this research. The tensile strength of a specimen changes along different axes depending on how the layers were laminated together [5]. In order to investigate this further, tensile specimen will be printed and tested in different orientations. The combinations of initial literarute investiagtions as well as this preliminary printing/material strength testing will

ultimately result in the processes to develop small thrusters, injectors, CubeSat propellant tanks, and other aerospace components.

IV. Additively Manufacturing Refractory Metals TZM and Tungsten

TZM is a molybdenum alloy that contains trace amounts of titanium (0.5%), zirconium (0.08%), and carbon (0.02%). When compared to pure molybdenum, TZM has higher melting point and tensile strength. Stated in Ping Hu's paper, TZM exhibits molybdenum characteristics, such as high melting point, elastic modulus, thermal and electrical conductivity, and temperature stability, along with low thermal expansion coefficient [5]. Due to solution and precipitation strengthening achieved by additive elements, TZM alloy has high hardness and creep resistance at extreme temperatures. TZM alloys have become desirable in astronautics, metallurgy, electronics and military applications [6].

Powdered TZM molybdenum is offered by most vendors in purity ranging from 99.0% to 99.999% purity. The differing purity has potential to affect the mechanical properties of prints, but not drastically. For this effort, powder will be selected with a purity ranging from 99.0% to 99.95%. Following is a table displaying the physical and mechanical properties of TZM.

TZM Chemical Composition:

Element	Content (%)
Molybdenum, Mo	99.40
Titanium, Ti	0.5
Zirconium, Zr	0.08
Carbon, C	0.02

TZM Physical Properties:

Density	Lb/in^3	0.37
	Gm/cm^3	10.22
Melting Point	°F	4753
	°C	2623
Thermal Conductivity	$Cal/cm^2/cm°C/sec$	0.48
Specific Heat	Cal/gm/°C	0.073
Coefficient of Linear Thermal Expansion	Micro-in/°F x 10^{-6}	2.50
	Micro-in/°C x 10^{-6}	5.20
Electrical Resistivity	Micro-ohm-cm	6.85

TZM Mechanical Properties:

Yield Strength	PSI	87,000
Ultimate Tensile	PSI	100,000
Hardness	DPH	220

Figure 2: Properties of TZM

Tungsten has the highest melting point of all known refractory metals, 3420 degrees Celsius [6]. Tungsten has a low thermal expansion, and can be made in ideal spherical powder sizes for PBF, ranging from twelve – twenty-two microns [6]. Printing conducted by Chaolin Tan and his team showed that it was even possible to achieve densities very close to the density of solid Tungsten (19.01 g/cm^3 compared to 19.6 g/cm^3) when using a laser linear energy of 0.667 J/mm [6].

Tungsten powder can be challenging to work with in AM, primarily because of its high melting point, thermal conductivity, and oxidation [7]. Typically, Tungsten require SLM style PBF printing methods coupled with spherical type powders. Another problem that can be encountered is that Tungsten has a tendency to crack. Formation of oxides contributes to cracking [8]. There has been work conducted focused on alloying Tungsten with Tantalum. This has shown promising results in that in some cases it has reduced cracking by up to eighty percent [8].

Tungsten is also prone to a phenomenon known in AM as "balling." Balling occurs when large agglomerations or droplets solidify before they are completely melted [9]. This is the main cause for the high amount

of surface roughness that is characteristic to printing with Tungsten. Another factor for surface roughness is the oxidation of Tungsten. It has been found that using a second laser, (usually a femtosecond laser) can re-melt the agglomerations and provide a smoother finish [9].

Before attempts are made to print any major components, preliminary specimens will be printed using both powders. These will be used to hone in the print process. The specimens will be 0.5-inch cubes and tensile specimens sized to ASTM E8 standards. According to Dr. D. Faidel in his paper "*Investigation of the Selective Laser Melting Process with Molybdenum Powder*," cube specimens are used to prime the printer, test print surface roughness, read print density, and understand specific print parameters. These parameters include maximum spot diameter, spot velocity, and laser power. For the tensile specimen, the ASTM E8 standards are being used because it has relative dimensions compared to components that will be printed in the future and because of ASTM's extensive theory testing on similar designs.

V. Future Work for Additive Manufacturing Projects

This section is to convey some of the future work that will be done using TZM and Tungsten powders. The overall scope of the work being done is to additively manufacture components that will be used in aerospace research. For the TZM research, currently it is desired to do some preliminary printing of tensile cubes and cylinders. These specimens will be subjected to various tests to encapsulate the properties of the printed TZM as well as perfect the printing process. Ultimately it is desired to print two thruster housings that will be pressure tested. Further study will be required before any print plans are made for using Tungsten. Following is a depiction of the preliminary test specimen.

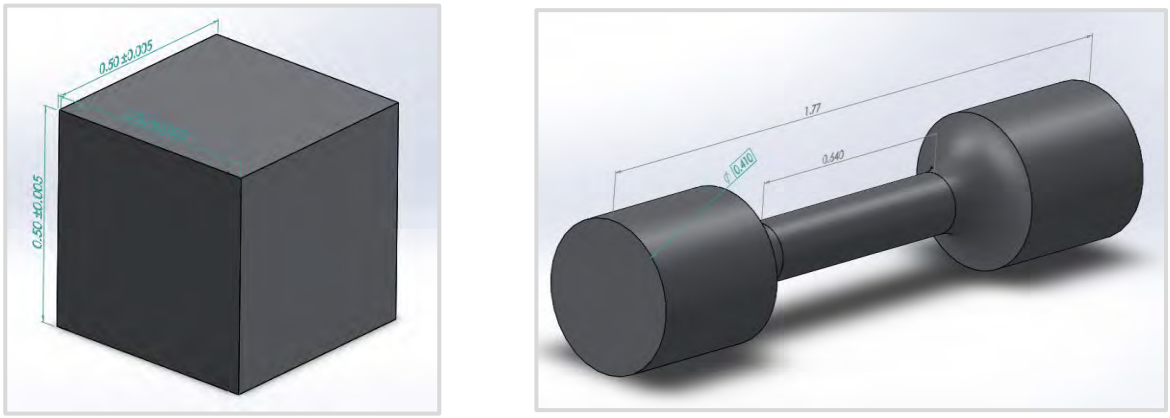

Figure 3: Tensile Specimen

After several preliminary prints have been conducted, and the process of using these metals is further understood, it is desired by cSETR to continue using AM to create a variety of aerospace components. These components include several small thrusters, propellant tanks for SmallSat Propulsion module, smart propellant injectors, and more. Following are depictions of the components that have been AM within the center or by collaborators before, or desired to be in the future.

Figure 4: 5N Monopropellant Thrusters Printed with IN 718

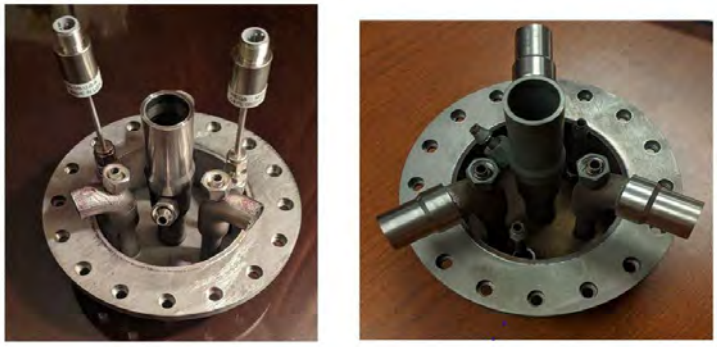

Figure 5: Smart Propellant Injector Printed with IN 718

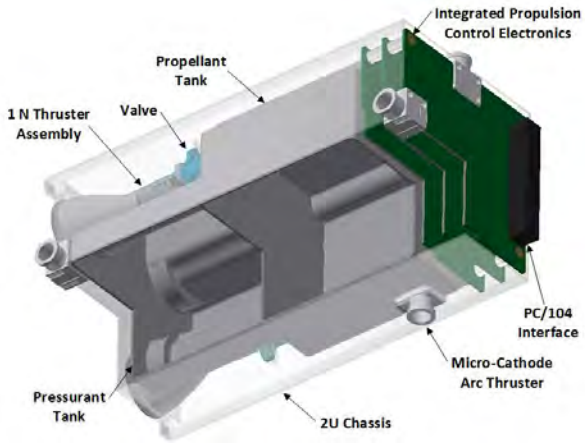

Figure 6: Depiction of SmallSat Propulsion Module

VI. Conclusions

With the continual growth of the space industry coupled with developments of new technologies, the need for AM components in aerospace is higher than ever. AM offers interesting solutions to creating components that have complex geometries and need to be made out of materials that can withstand harsh environments. cSETR has a strong desire to begin research in using two metal powders for printing aerospace components, Tungsten and TZM. TZM is a molybdenum-based powder that has the high melting point of molybdenum, but almost twice the tensile strength. Not much research has been conducted on using TZM, but there is beginning to be a demand to start using it in the industry, Tungsten has the highest melting point of all known refractory metals. However, complications with cracking, balling, and rough surface finishes requires there to be more in-depth research before using it in AM. This

paper depicts the literature review that has been conducted on using these powders for a PBF type of printing, specifically for SLM. It is a strong desire for the center to now begin printing tensile specimen to experiment both with the printing parameters and after print testing. Future work will cumulate the results form this preliminary printing/testing to ultimately yield cost effective, functioning aerospace components integrated into other efforts of research.

References

[1] Ajay Misra, Joe Grady, Robert Carter *"Additive Manufacturing of Aerospace Propulsion Components."* NASA Glenn Research Center, presented at Additve Manufacturing Conference, Pittsburgh, PA, October 01, 2015

[2] *"Additive Manufacturing for Space Industry Applications."* Published by SmartTech Analysis, July 13, 2017

[3] Muniz-Lerma Ja, Nommeots-Nomm A, Waters KE, Brochu M "*A Comprehensive Approach to Powder Feedstock Characterization for Powder Bed Fusion Additive Manufacturing: A Case Study on AlSi7Mg."* November 27, 2018

[4] Mahmud Ashraf, Ian Gibson, M.G. Rashed, *"Challenges and Prospects of 3D Printing in Structural Engineering."* January 2018

[5] Nan Kang, Yunlong Li, Xin Lin, Enhao Feng, Weidong Huang, *"Microstructure and Tensile Properties of Ti-Mo alloys Manufactured via using Laser Powder Bed Fusion."* Published in Journal of Alloys and Compounds, August 30, 2018

[6] Hu, Ping & Yang, Fan & Song, Rui & Wang, Kuai-She & Hu, Bo-Liang & Cao, Wei-Cheng & Liu, Dong-Xin & Kang, Xuan-Qi & Volinsky, Alex. (2016). Pt-plating effect on La-TZM alloy high temperature oxidation behavior. Journal of Alloys and Compounds. 686. 10.1016/j.jallcom.2016.06.183.

[7] Dianzheng Wang, Chenfan Yu, Xin Zhou, Jing Ma, Wei Liu, Zhijian Shen, *"Dens Pure Tungsten Fabricated be Selective Laser Melting."* February 21, 2017.

[8] Wang, Dianzheng & Wang, Zhimin & Li, Kailun & Ma, Jing & Liu, Wei & Shen, Z. (2018). Cracking in laser additively manufactured W: Initiation mechanism and a suppression approach by alloying. Materials & Design. 162. 10.1016/j.matdes.2018.12.010.

[9] Xin Zhou, Xihe Liu, Dandan Zhang, Zhijian Shen, Wei Liu *"Balling Phenomena in Selective Laser Melted Tungsten."* Journals of Materials Processing Tech. 0924-0136, February 2015

Initialization and Troubleshooting of the MICIT System for LO_2/LCH_4 Engine Testing

Corey Hansen[1], Raymundo Rojo[2], Jack Chessa[3], and Ahsan Choudhuri[4]
NASA MIRO Center for Space Exploration and Technology Research (cSETR)
University of Texas at El Paso, El Paso, Texas, 79968-0521, USA

This article presents the design, buildup, and pre-test troubleshooting of the Mobile Instrumentation and Control Interface Trailer (MICIT) for LO_2/LCH_4 rocket engine testing. This system is designed to be a modular system control and data acquisition hub for any of the various LO_2/LCH_4 engine testing activities taking place at TRIAc park in Fabens, TX. It is a cRIO/cDAQ based system which interfaces with a command center computer running LabView. This connection is completed via a fiberoptic connection, enabling the MICIT to be relocated anywhere onsite without moving the command center computer. The MICIT features support for with capacity for expansion in the future.

Terms

cSETR – The Center for Space Exploration and Technology Research

TRIAc park – Technology Research Innovation Acceleration park

MICIT – Mobile Instrumentation and Control Interface Trailer

PT – Pressure Transducer

TC - Thermocouple

SV – Solenoid Valve

FM – Flow Meter

TFM – Turbine Flow Meter

VFM – Venturi Flow Meter

Cryo – Cryogenic

500lb – Colloquial reference to the 500lbf engine currently (as of 2019) in development

Introduction

The use of liquid oxygen (LO_2) and liquid methane (LCH_4) in rocket engines are becoming more appealing in the space industry. The benefits of using LO_2/LCH_4 as a propellant combination in rocket engines include the fact that the fuel and oxidizer are considered a less toxic propellant combination compared to other propellant combinations, they allow for in-situ resource utilization (ISRU) capabilities, and that LCH_4 has a relatively high energy density compared to other fuels such as LH_2. In support of advancements in this field, the Center for

[1]Graduate Research Assistant, cSETR, The University of Texas at El Paso, 79968, Student Member, AIAA
[2] Graduate Research Assistant, cSETR, The University of Texas at El Paso, 79968, Student Member, AIAA
[3] Associate Director, cSETR, Associate Professor, Mechanical Engineering, The University of Texas at El Paso, 79968
[4] Director, cSETR, Professor, Mechanical Engineering, The University of Texas at El Paso, 79968, Associate Fellow, AIAA

Space Exploration and Technology Research (cSETR) at The University of Texas at El Paso has been in development of several LO_2/LCH_4 engines and the associated propellant feed systems, test stands, and control/data acquisition systems. The MICIT is the cSETR LO_2/LCH_4 team's instrumentation and control interface trailer, which designed to support all planned an ongoing LO_2/LCH_4 engine system testing. The MICIT features support for 4 igniters, 64 solenoid valves, 12 amplified cryogenic pressure transducers, 8 turbine flow meters, 4 venturi flow meters, 5 banks of load cells, 4 differential pressure transducers, 22 standard pressure transducers, 4 dynamic pressure transducers, 3 accelerometers, 32 K-type thermocouples, and 32 E-type thermocouples, with capacity for future expansion on both the instrumentation and control interface fronts.

MICIT Subsystems

The MICIT is broken into several closely related subsystems for ease of documentation. These subsystems are all housed in one of two server racks, designated MICIT-L and MICIT-R. Each subsystem's designation is derived from the rack in which it resides followed by a number representing its location on the front switchboard panel. For example, the front panel of the subsystem which supports data acquisition from the venturi flow meters is located on the 3rd panel of the right-side server rack and is designated MICIT-R3, or R3 for short. Designations for individual components are further derived from the subsystem name. For example, the 24th E-type TC connector on the front panel is designated MICIT-R7_24, or R7_24 for short. By following this naming convention, test directors for multiple LO_2/LCH_4 testbeds can call for connections to be made specifically for the test they manage, without causing confusion for any other team which may use the MICIT. Some panels, such as MICIT-L1, were designed with a certain test article in mind and as such will probably not be applicable to any other test articles.

MICIT-L1 – Motor Valves

The L1 panel supports the stepper motors which actuate the main valves on the 500lb test article. Each connector cluster is composed of 2 banana plugs and a Dsub-9 connector. The banana plugs provide power to the motor and the Dsub-9 provides a connection for a combination of digital and analogue inputs and outputs to the servo controller.

Figure 1: MICIT-L2 Schematic

MICIT-L2 – Igniters

The L2 panel supports the igniter subsystem. Each connector cluster is composed of 2 banana plugs and a BNC connector. The banana plugs provide power to the igniter and the BNC connector provides a connection to the signal generator that controls the igniter spark timing.

MICIT-L3 – 120V AC SV

The L3 panel supports part of the solenoid valve subsystem. Each connector cluster is composed of 2 banana plugs. Each of the 16 sets of banana plugs provides 120V AC power to a solenoid valve. The positive (red) side is switched by a relay in the first relay board.

MICIT-L4 – 12V DC SV

The L4 panel supports part of the solenoid valve subsystem. Each connector cluster is composed of 2 banana plugs. Each of the 16 sets of banana plugs provides 12V DC power to a solenoid valve. The positive (red) side is switched by a relay in the first relay board.

MICIT-L5 – 12V DC SV contd.

The L5 panel supports part of the solenoid valve subsystem. Each connector cluster is composed of 2 banana plugs. Each of the 16 sets of banana plugs provides 12V DC power to a solenoid valve. The positive (red) side is switched by a relay in the first relay board.

MICIT-L6 – 24V DC SV

The L6 panel supports part of the solenoid valve subsystem. Each connector cluster is composed of 2 banana plugs. Each of the 16 sets of banana plugs provides 24V DC power to a solenoid valve. The positive (red) side is switched by a relay in the first relay board.

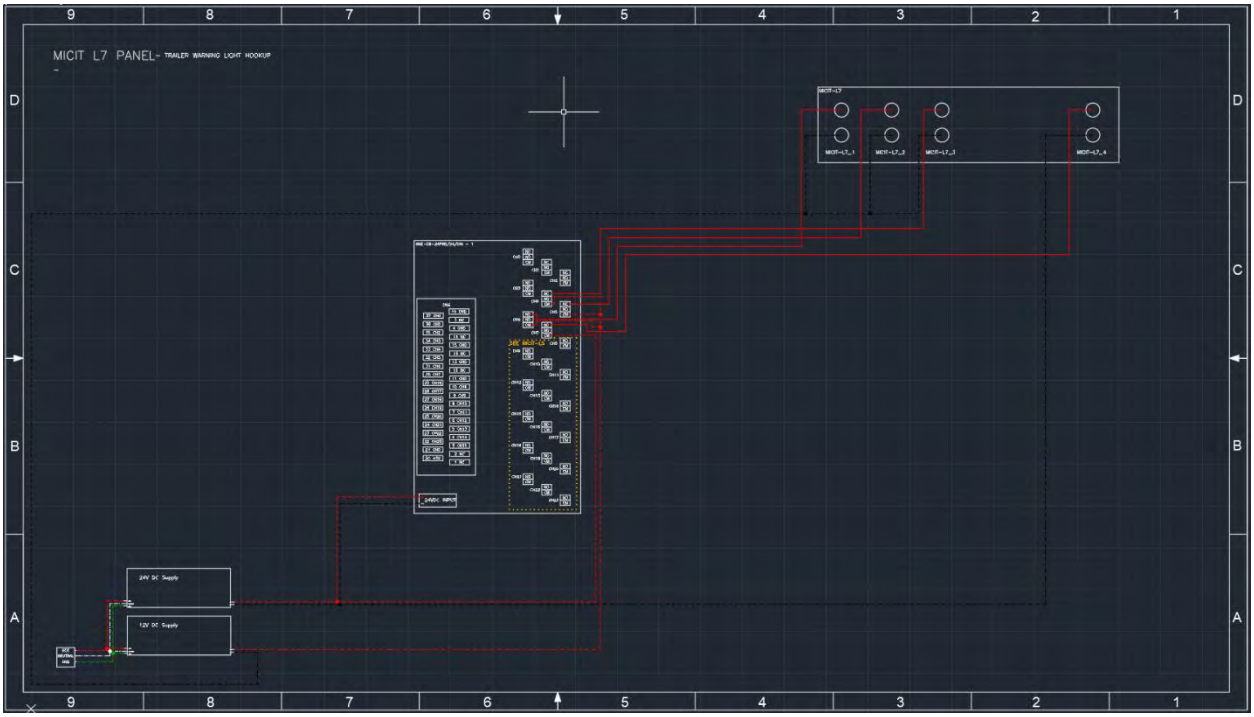

Figure 2:MICIT-L7 Schematic

MICIT-L7 – Warning Lights

The L7 panel supports the test warning lights on the top of the trailer. These lights are controlled by relays in the third relay board and serve to inform on-site personnel about the state of testing operations. The MICIT will be near the test site for all testing activities and serves as

an easily identifiable landmark for test operation status. The schematic of L7 is shown in Figure 7.

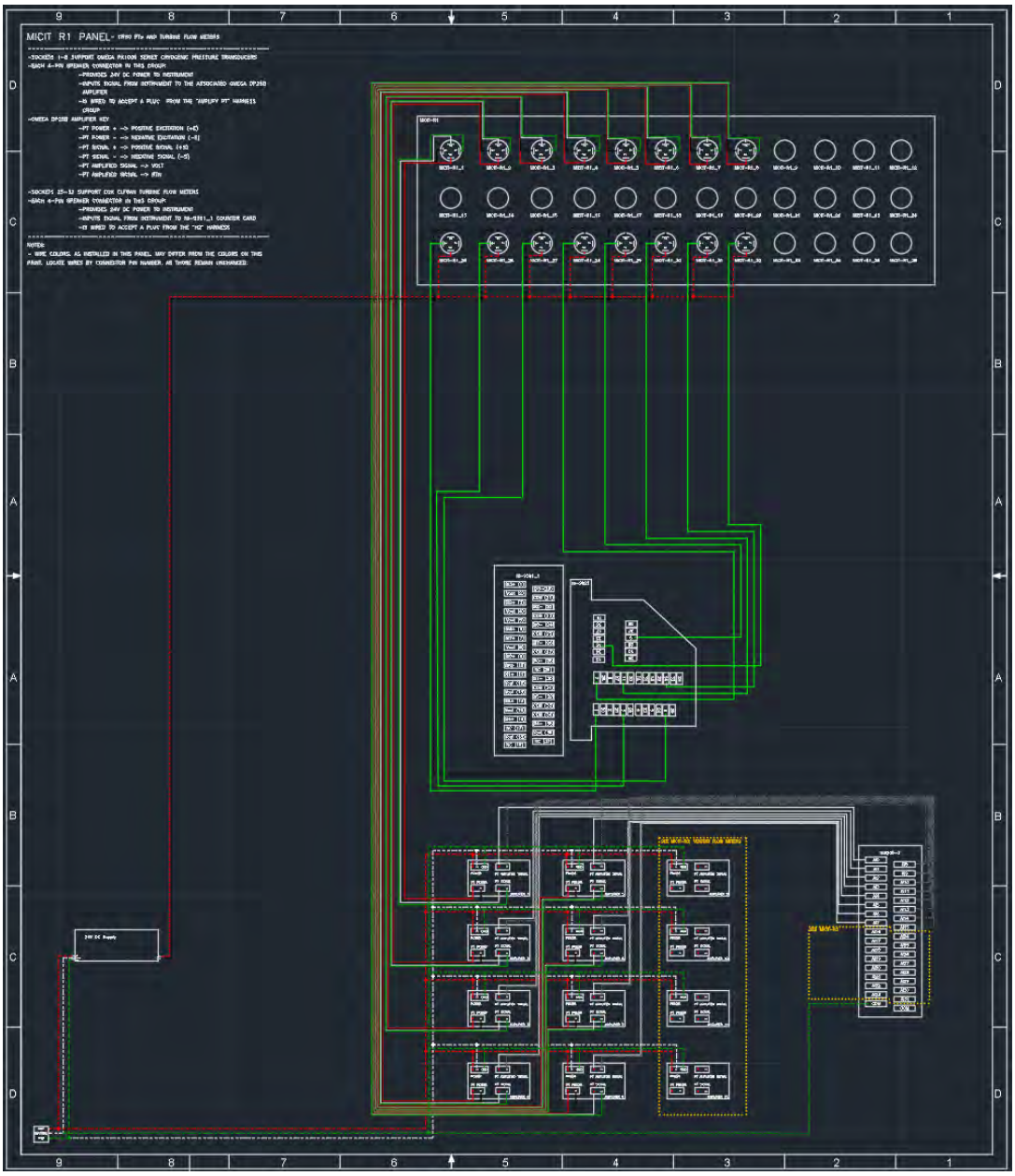

Figure 3:MICIT-R1 Schematic

MICIT-R1 – Cryo PTs and Turbine FMs

The R1 panel supports the Cryo PT and TFM subsystems. Each connector cluster in the Cryo PT subsystem consists of a single 4-pin speaker connector. The Cryo PT subsystem is set up to support any Omega PX1005 series cryo PT and uses Omega DP25B series amplifiers. The amplifiers are set up to provide 10V across +E and -E, read a 0-100mV differential signal between +S and -S, and output a 0-5V signal, proportional to the signal outputted by the PT,

across the Signal and RTN leads. The output from each amplifier is inputted to NI-9205_3 where the signal is measured. The pinout is shown in Table 1. The configured amplifier settings are shown in Table 2. The schematic of R1 is shown in Figure 8.

Table 1:Cryo PT Pinout

Pin	**Label**	**Description (Color)**
1+	+S	Positive leg of the signal provided by the PT.
1-	-S	Negative leg of the signal provided by the PT.
2+	+E	Positive excitation voltage provided to PT.
2-	-E	Negative excitation voltage provided to PT.

Table 2: Cryo PT Amplifier Settings

Category	**Subcategory**	**Setting**	**Description**
INPT	N/A	100m	100mV input
decp	N/A	FFFF	Decimal place set to 1000
RDsO	N/A	N/A	Reading point settings
RDsO	In1	0138	Signal from the PT @ambient pressure
RDsO	RD1	0014	Displayed pressure at In1 signal
RDsO	In2	3320	Signal from PT @PT 500psi
RDsO	RD2	500	Displayed pressure @ In2 signal
RDcF	R.1	N	
RDcF	R.2	4	
RDcF	R.3	F	
OTcF	N/A	N/A	Output configuration settings
OTcF	0.1	E	
OTcF	0.2	V	
OTsO	N/A	N/A	Output point settings
OTsO	RD1	0000	Displayed pressure
OTsO	OUT1	0000	Output voltage @RD1
OTsO	RD2	500	Displayed pressure max
OTsO	OUT2	10	Output voltage @RD2
LKcF	N/A	N/A	Lockout Configuration
LKcF	RS	E	Reset button enable/disable

The RDsO, RDcF,OTcF, and OTsO settings groups control the linear interpolation points which the amplifiers use to display the input they receive from the sensor. The settings shown in Table 2 are an example configuration for a 0-500psi Omega PX1005 PT, calibrated using calculated loads. Another calibration method is to use known loads instead of calculated ones.

This requires the operator to apply a pressure to the sensor, and use the amplifier to measure that output in place of the calculated values in “IN1” and “IN2” in the RDsO menu. See the DP25B product manual for more information on scaling with known loads.

The TFM subsystem is set up to support COX LoFlo turbine flow meters. Each TFM connector provides 24V power and a signal input lead. The pinout is shown in Table 3.

Table 3:TFM Pinout

Pin	**Label**	**Description (Color)**
1+	-E	Negative leg of the excitation voltage supplied to TFM.
1-	N/A	Not Used
2+	+E	Positive excitation voltage supplied to TFM.
2-	S	Signal returned from TFM

Each TFM outputs a square wave signal, with a frequency corresponding to the flow rate it is measuring. This signal is inputted to NI-9361_1 where the frequency is measured. Instument calibration is handles in LabView.

MICIT-R2 – Load Cells

The R2 panel supports the load cell subsystem. Each connector in this subsystem contains one Dsub-9 connector. This subsystem is set up to support either individual load cells or load cell summation boxes, which take the outputs from up to 4 individual load cells and sum their inputs, allowing them to be used in conjunction as a scale for larger components or thrust levels. The schematic is shown in Figure 9.

Table 4:Load Cell Pinout

Pin	**Label**	**Description (Color)**
1	+E	Positive leg of the excitation voltage supplied to load cell.
2	+S	Positive leg of the signal returned from the load cell
3	-S	Negative leg of the signal returned from the load cell
4	-E	Negative leg of the excitation voltage supplied to load cell

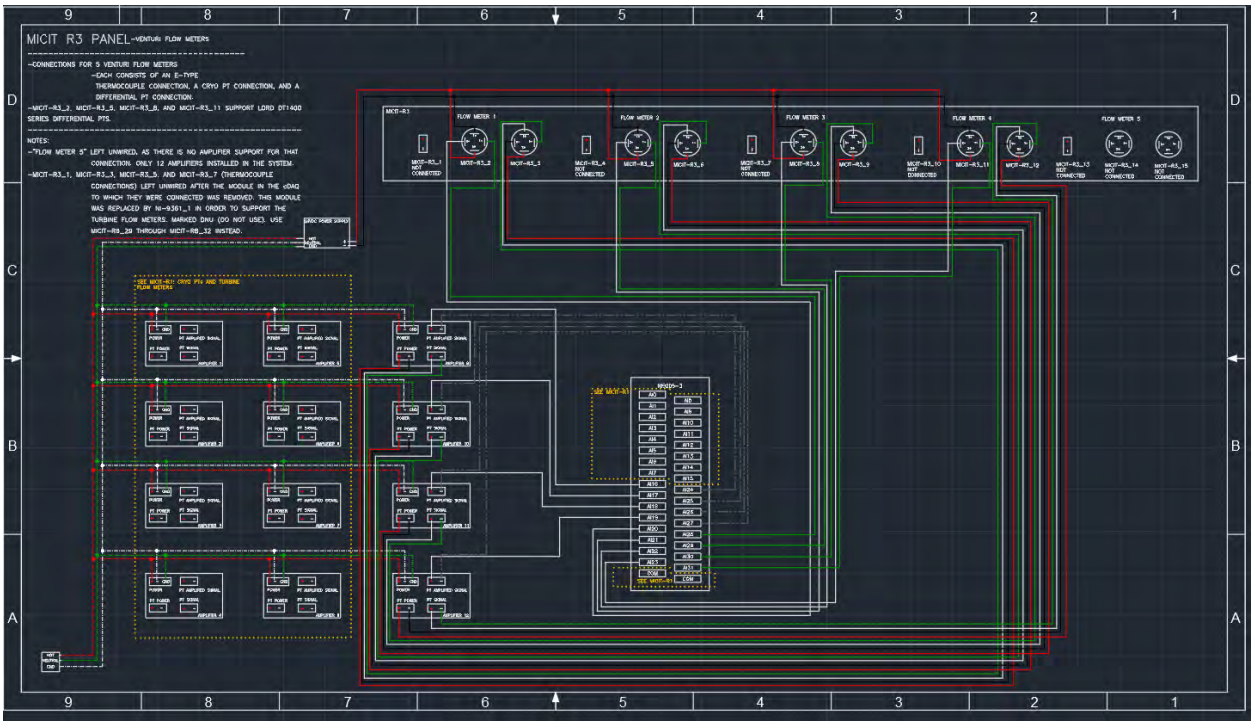

Figure 4:MICIT-R3 Schematic

MICIT-R3 – Venturi Flow Meters

The R3 panel supports the venturi flow meter subsystem. Each connector cluster consists of an E-Type TC connector and two 4-wire speaker connectors. The E-Type connector is unused at this time, as the slot in the cDAQ to which they were connected has been reallocated to the TFM counter card. These connectors can be brought back into service at any time with the addition of a second cDAQ chassis, or an ethercat chassis connected to cDAQ-1. The firstspeaker connector in each cluster supports a differential PT and provides 24V DC power and two signal leads. The second speaker connector in each cluster provides support for a Cryo PT, with 10V DC power and two signal leads leading back to an amplifier in the same configuration as described in R1.

MICIT-R4 – Single ended PT

The R4 panel supports the single ended PT subsystem. Speaker plug connectors provide 24V power to the instrument, and a single signal return to cDAQ-1.

Table 5 Single Ended PT Pinout

Pin	**Label**	**Description (Color)**
+1	-	Negative leg of the excitation voltage supplied to the PT.
-1	N/A	N/A
+2	+	Positive leg of the excitation voltage supplied to the PT
-2	S	Signal Returned from the PT.

MICIT-R5 and R6

The R5 and R6 panels support high speed instrumentation such as dynamic PT's and accelerometers. This subsystem uses BNC connectors to provide shielded connections to avoid noise in the signal returned from the instrument.

MICIT R7 and R8

The R7 and R8 panels support K and E-Type thermocouples, respectively. There are 32 connectors for each TC type, allowing for 64 independent temperature measurements to be taken with this subsystem. Schematics are shown in figures 5 and 6.

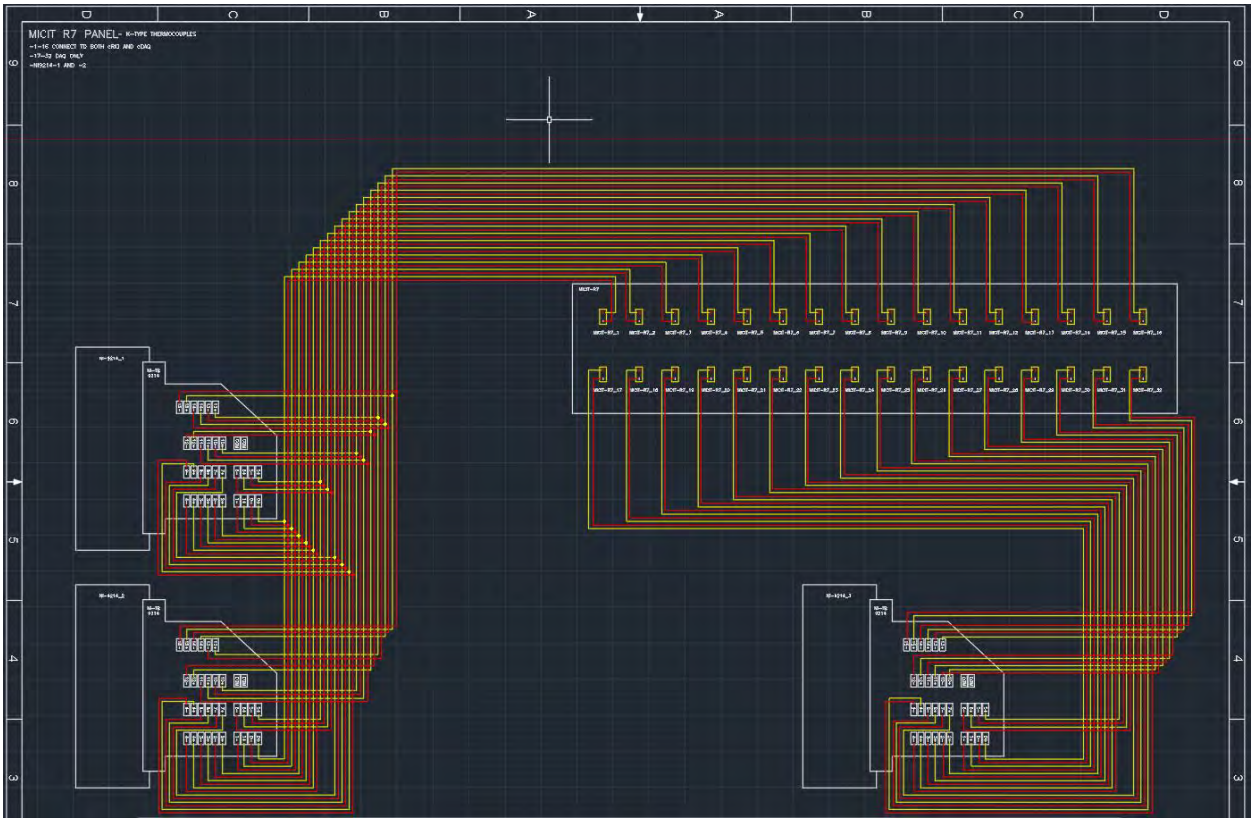

Figure 5: K-Type TC Schematic

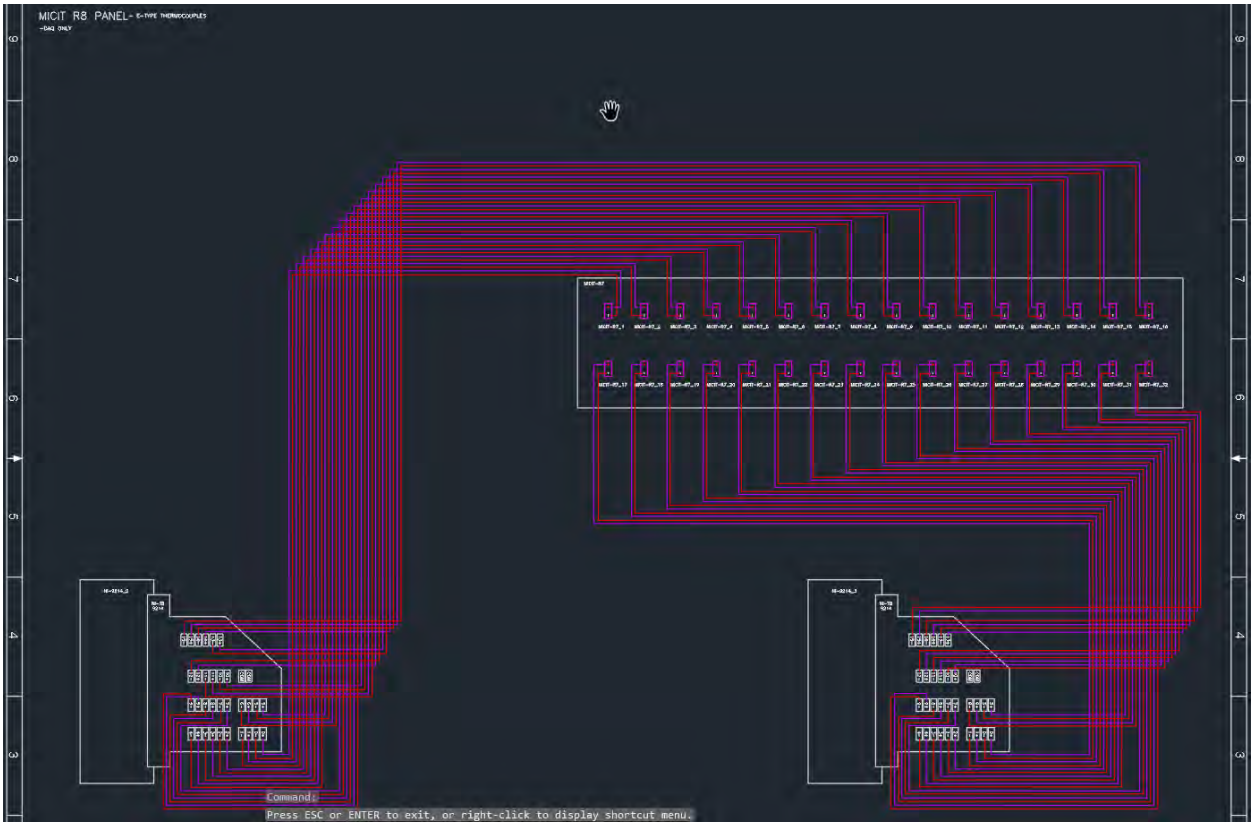

Figure 6: E Type TC Schematic

Bibliography

Omega Engineering, Inc. DB25B-S:Strain Gage Panel Meter User Guide. Norwalk, CT

Innovations in Pressure Fed Orbital Launch Vehicles

Lucero Buendia[1], *Itzel A. Torres*[2], *Armando A. Ochoa*[3]
University of Texas at El Paso, TX, 79968

A launch vehicle can be used to transport objects into an orbital outside or within Earth's atmosphere. This class of vehicles consists of engines, a core stage tank, an inner stage, an upper stage, a payload fairing among electrical and other fitting components. The Launch Vehicle Team at the Center for Space Exploration and Technology Research (cSETR) has a goal to design a launch vehicle that will take a 100 lb payload, to Low Earth Orbit (LEO). The project will consist of carbon composite components to reduce weight while maintaining efficiency. This can provide a more affordable cost per launch of approximately 1.5 million dollars. The purpose of this document is to outline the challenges of designing a pressure fed system and list innovations like common bulkhead tanks, LOX methane engines, and carbon composite materials.

I. Nomenclature

ISP = Specific Impulse
L/D = Length/Diameter

II. Introduction

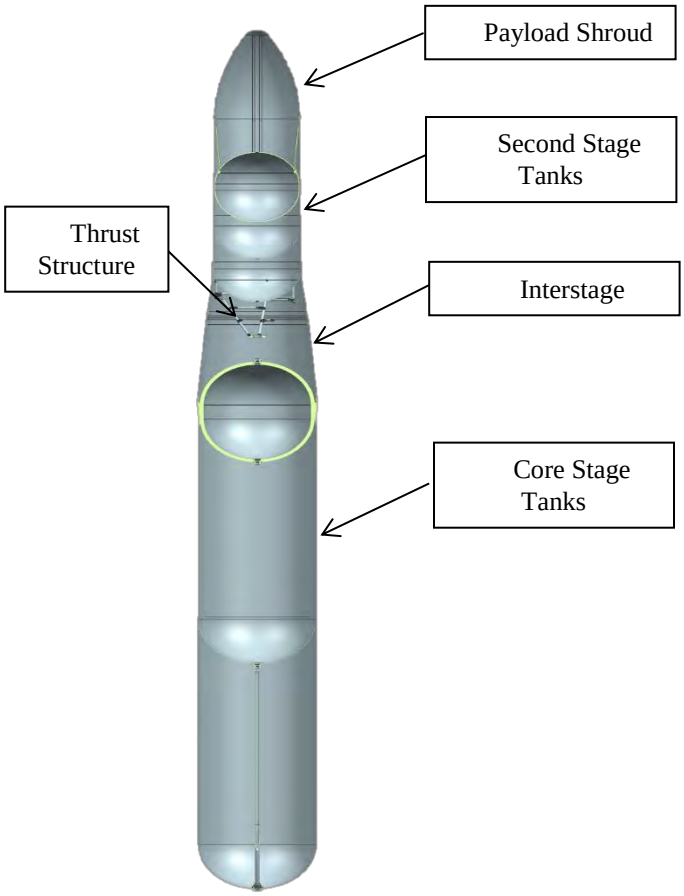

Figure 1: Assembly of Launch Vehicle

The Center for Space Exploration and Technology Research team at University of Texas at El Paso has been working on different ways to innovate an orbital launch vehicle with additive manufacturing materials. Using such materials will drastically reduce the weight of the overall structure as well make the launch more affordable. When designing the launch vehicle, the team needed to take into consideration ISP in order to determine the size of the tanks. Designing the tanks have been a challenge because certain design criteria's such as weight and dimensions have really limited how big the tank can be. With the sizing of the tanks also followed the sizing of theshroud and interstage design. Each time the tanks were redesigned, the shroud and interstage were redesigned as well to compensate for the new dimensions of the tanks.

Currently, the overall length of the vehicle is approximately sixty-eight feet with different diameters for the second and core stage with the interstage connecting the two. Figure 1 shows the full assembly of the vehicle with updated parts and components. The following sections of this paper describe in detail aspects of each part such as the modeling, analysis, and assembly.

III. Second Stage

In order to minimize aspects of failure in the design, the vehicle will use a pressure fed system. Pressure fed systems tend to increase the weight of the tanks due to the extra weight of pressurized gas. In order to compensate, the tanks will be carbon composite common-bulkhead tanks. This will result in the combination of helium, methane, and oxygen tanks into one body where they will share a common wall. Carbon composite, although not 3D printed, is a form of additive manufacturing, in which the carbon fiber is wrapped around a lining surface layer by layer.

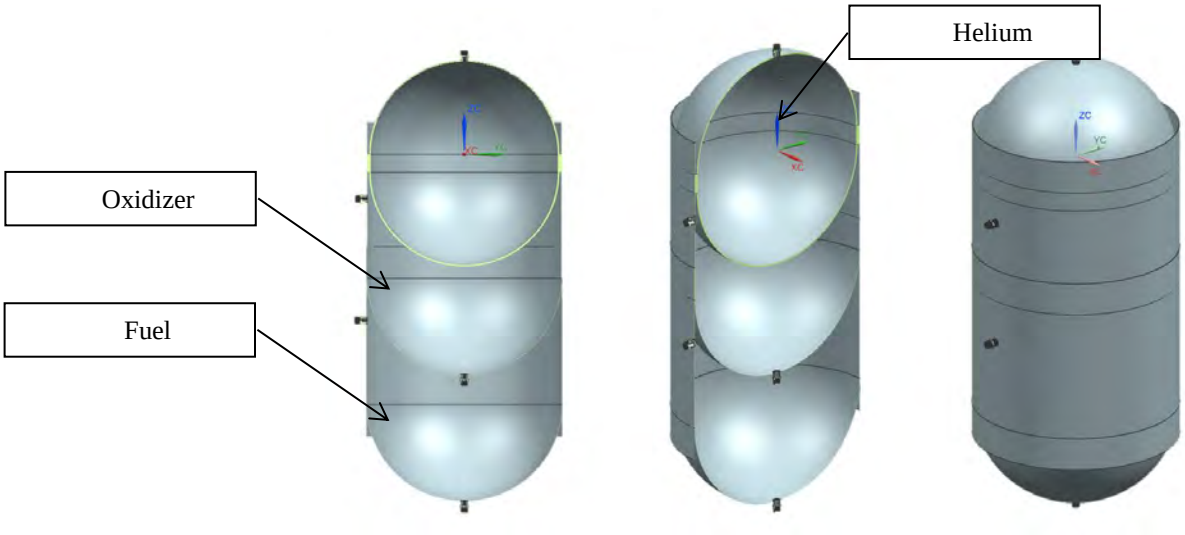

Figure 4:
Second Stage Tanks

To begin, the size of the second stage tank is calculated based on its inert mass fraction. This was based off the Isp for the propellant, LOX-Methane, and distance for the desired orbit LEO. Once the amount of fuel and oxidizer needed were found, the tank volumes were determined. Each tank volume was increased when considering extra space needed for ullage, boiling, and trapped propellant. To find the volume of the helium tank the amount of helium needed to feed both fuel and oxidizer tanks was calculated.

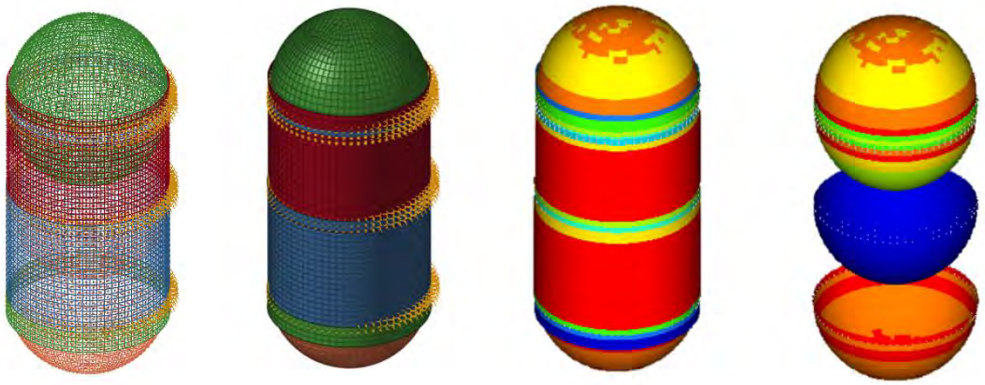

Figure 5:
Tank Analysis

The model, as shown in figure 4, was designed in three different sections to resemble the assembly process of the tanks. The helium tank is almost perfectly spherical except for a small cylindrical section for the oxidizer tank to slide into. The oxidizer and fuel tanks are very similar; the only difference is slight changes in length and diameter which allows these parts to slide into each other and have about a six-inch overlap where they will be attached to each other. The oxidizer tank will have an extra six inches extruding from the top to act as a shoulder to where the fairing will be attached. The bottom shoulder will be a ring attached separately and will slide in to connect to the bottom of the fuel tank. The carbon composite material the tanks will be made of is manufactured by wrapping the threads around the tank lining while it cures. Drilling holes into the threads will weaken the material and in order to avoid this, flanges will be included in the manufacturing so a hole can be manufactured then threaded.

Modal and stress analysis on the tanks (figure 5) were performed using Altair Hypermesh. Each component was meshed individually then connected with rigids. The pressures and loads were then added, and the analysis was run for stresses. Using a design safety factor of 1.5, each individual component was optimized to a minimum thickness. Because of the way carbon composite is manufactured it was preferred to keep cylindrical parts at least two times thicker than the spherical components. For the helium spheres, although material could still be removed from the bottom half, they remained the same thickness because it would make manufacturing easier. The common-bulkhead for the oxidizer tank experiences the same pressure on top and bottom and was made half its cylindrical section. For this reason, not all components are completely optimized, although more material could be removed it would complicate the manufacturing.

IV. Interstage

The interstage is a vital component of any launch vehicle during launch and stage separation. The basic idea for an interstage is to connect two important components together, in this case the second stage and the core stage tanks. The structure must be able to hold a specific amount of weight from the stages above without any moment, static, axial or buckling failures. The entire interstage for the Centennial Small Payload Launch Vehicle will be composed of carbon composite materials which will help economically as well as in overall weight.

One major design criterion that was followed during this design was the NASA SP-8007 “Buckling of Thin-Walled Circular Cylinders,” which states that any thin walled circular cylinder must have a breakdown factor of 0.65 applied to the design. A major factor of safety that this interstage design must follow is, under general NASA guidelines, 1.25. Other design criteria that was followed while designing the interstage was applying static load of one thousand four hundred (1,400) lbs multiplied by six (6) G’s of force from flight and the total weight of the interstage needed to be under 40 lbs.

During the design stage, there was a total of three different iterations of the interstage which included different materials and strucutral layouts. This gave the team options to decide which design was the most effective based on

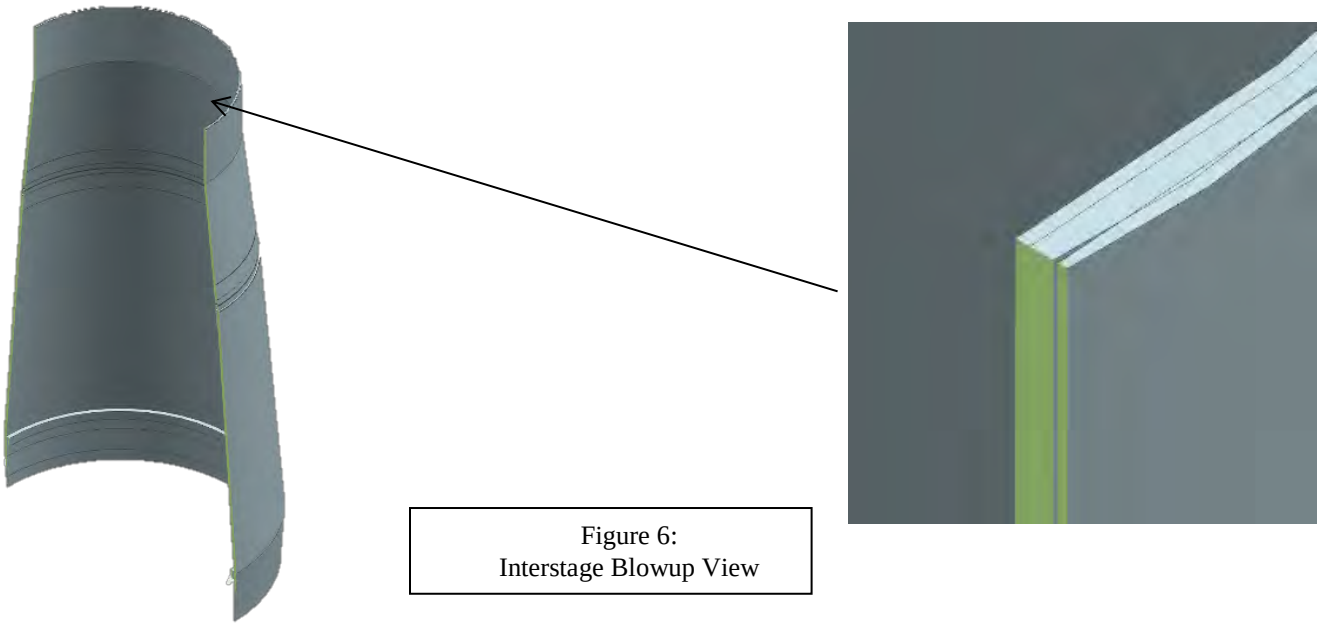

Figure 6:
Interstage Blowup View

each analysis. One iteration included a simple carbon composite shell with flanges on either end to connect to the other parts of the launch vehicle. The second iteration included an exterior carbon composite shell along with an interior carbon composite iso-grid structure design. The final iteration that was accepted and followed through with was a honeycomb sandwich design. This design included a carbon composite exterior shell, aluminum honeycomb core as well as a carbon composite interior shell as shown in figure 6. The honeycomb core will have increased rigidity versus an iso-grid design and address buckling/moment failures. The team modeled their interstage based off the Atlas V rocket interstage design which includes an aluminum exterior shell and an aluminum honeycomb core. The main difference between current commercial or private company designs and this design is the use of additive manufacturing materials for the entire structure.

Figure 7 on the right shows how the analysis of each iteration was approached. The overall static load of twelve thousand nine hundred and twenty-three pounds (12,923 lbs), which comes from multiplying the original static load of one thousand four hundred (1,400) lbs and six (6) G's of force from flight divided by the buckling factor of 0.65;

$$overall\ static\ load = \frac{1{,}400\ lbs * 6\ G's}{0.65} = 12{,}923\ lbs$$

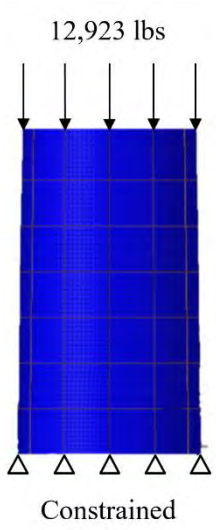

Figure 7:
Interstage Hypermesh Analysis

was applied to the top of each iteration and constrained at the bottom to simulate no movement in any direction. After the analysis in Hypermesh Software was complete, it was determined that the honeycomb design would be, as predicted, the strongest. However, it weighed approximately 52 lbs, which is over the desired weight limit. The main item the team took into consideration was that it would be ideal to have a strong and slightly overweight interstage design than a weaker, lighter one.

When the interstage is completely manufactured, all the components will be glued together by means of epoxy and the interstage itself will be epoxied to both the core and second stage tanks. During the design phase it was planned to use bolted and rivet connections for the top and bottom pieces of the interstage however after doing research on materials and how they react with one another, it was determined that the interstage would just be epoxied rather than bolted or riveted since steel does not react well with carbon composite. Also using epoxy makes the overall component weigh less which helps us reach the goal of using a system that is structurally strong and light weight.

V. Core Stage

Similarly, to the second stage tank, the core stage tank will be an assembly of three tanks. One designated for Helium, LOX, and methane, respectively. The core stage tank will be the biggest tank on this launch vehicle since it will require more propellant and fuel for takeoff. Boosters will be attached to this tank which will be separated after burning out. After this, the first stage engine will take over. The total amount of propellant that is required is 10120 lbs. Both the oxidizer and the fuel tanks must withstand pressures of 400 psi each. The helium tank, on the other hand, needs to be pressurized to 6000 psi. According to the literature review from NASA, a margin of safety of 1.63 and a safety factor of 1.5 is acceptable. These factors were also chosen mainly to meet the goal. If the rocket is too heavy overall, it clearly will not launch. In this case, the core tank assembly including fittings, tubing and electrical equipment cannot exceed (1,800 pounds). The oxygen to fuel ratio required for the mission is 2.7. Volume estimated for the helium tank is 30.69 cubic feet and 104 cubic feet for both the fuel and oxidizer tank.

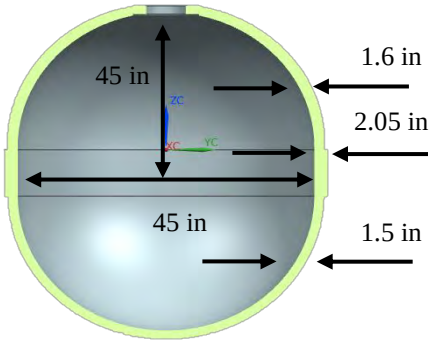

Figure 8:
Helium Tank

Tank assembly components will not be spherical. It will be an assembly of a cylinder with half spheres on both ends of the cylinder. To reduce the stress in the helium tank, the cylinder will be as short as possible. As

mentioned before, the assembly will consist of sliding each tank (helium, oxidizer, fuel) inside each other in that order and will then be secured with epoxy.

The Helium tank (figure 8) is the only component that is composed by a cylinder and two semi-spheres on both ends. The cylinder has an inner diameter of 45 inches and an outer diameter of 49.1 inches. The upper semi-sphere has an inner diameter of 45 inches and an outer diameter of 48.2 inches while the lower semi-sphere has an outer diameter of 48 inches. The image below shows how the helium tank will look.

Unlike the Helium tank, the oxidizer tank (figure 9) is only composed of one cylindrical component with a semi-sphere attached at the bottom. The oxidizer tank has a length of 145.24 inches including the bulkhead and an inner diameter of 49.1 inches with a thickness of 0.19 inches. The common bulkhead radius is 24.55 and it has a thickness of 0.19. The oxidizer tank will have one inlet and one outlet. The inlet will connect to the helium tank and the outlet will connect to the engine.

The interstage will be sitting on top of a 1-inch shoulder. The fuel tank has an inner diameter of 49.48 inches and a thickness of 0.19 inches. The common bulk head has a radius of 24.74 and a thickness of 0.23 inches. The fuel

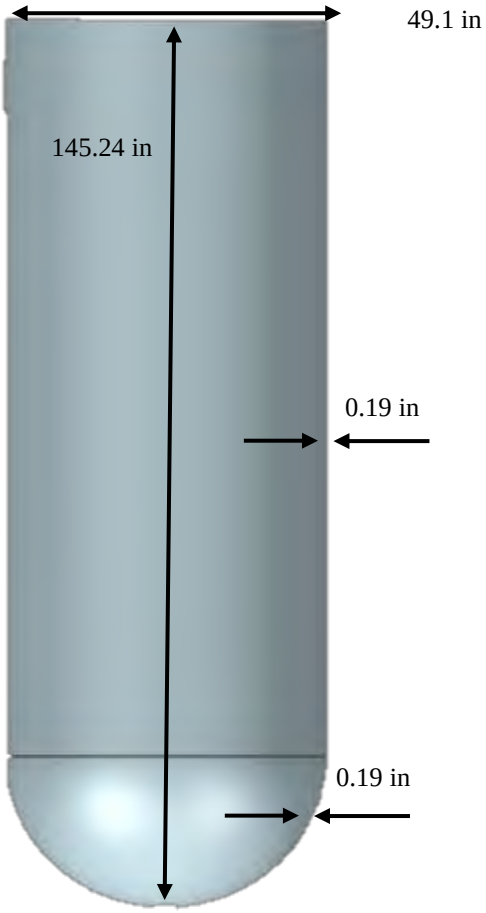

Figure 9:
Oxidizer Tank

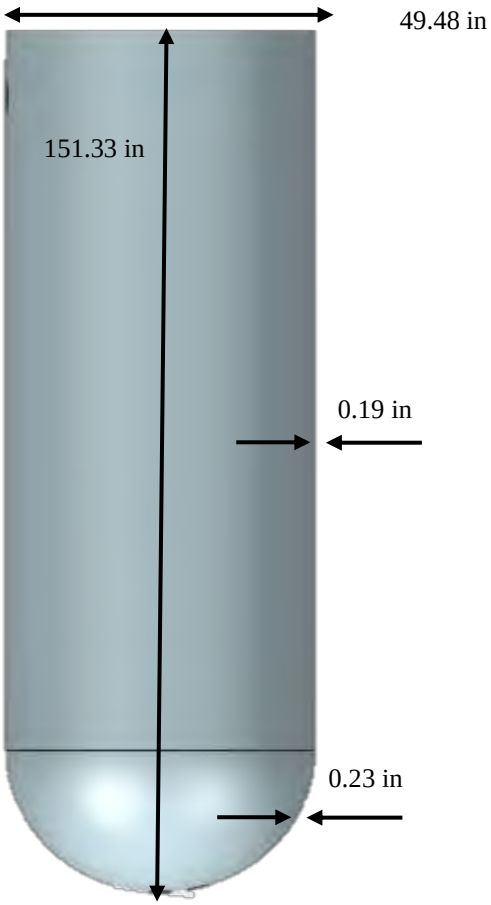

Figure 10:
Fuel Tank

tank, as shown on figure 10, will have three openings for flanges: one inlet and two outlets. The inlet will be attached to the helium tank while one of the outlets will be from the fuel to the engine while the other one will be from a line going through the inside of the fuel tank that will be attached to the outlet from the oxidizer tank. This line must be secured before the oxidizer and fuel tanks are secured. Once the tank has been glued it will be difficult to reach the inside of the tanks. For stability and due to the tank's height, stringers will be added to both the oxidizer and fuel tank. These hoops will be 1 inch thick and 1 inch wide.

The tank was analyzed without the fittings, only the main components where considered. Each part of the core tank was meshed individually so that the thickness could be changed accordingly. In this case, the thickness had

to be altered such as that the tank could withstand 1800-pound force at 6gs while maintaining a factor of safety of 1.5 and margin of safety of 1.63. The analysis clearly showed us that the tanks are optimized to its full potential with given dimensions from previous figures. Next step is to manufacture the tanks, fittings and lines.

VI. Conclusion

After much design and consideration, an iteration was chosen for each part and component in this report based on the analysis results with each iteration fitting with one another. With the carbon composite design which gives us a light weight, ridged structure, the design proves to be revolutionary. Further tests need to be completed before such a launch is even attempted however with the proper steps taken, the launch vehicle may prove that such additive manufacturing and economic goals can be achieved.

VII. Acknowledgments

The Launch Vehicle team would like to thank Dr. Choudhuri for lending us his vision for this project. Without Dr. Choudhuri's support this project would not be possible. The Launch Vehicle team would also like to thank Dr. Chessa for lending his knowledge to the team and forcing us to answer the hard questions. The Launch Vehicle team would also like to thank NASA MSFC's James Richard and Pat Lampton whose mentorship forms the foundation of the Launch Vehicle team's knowledge.

VIII. References

[1] Peterson, J.P. Seide, P. Weingarten, V.I. "Buckling of thin-walled circular cylinders," Tech. Report, NASA Langley Research Center, VA. August 1968.

[2] Henson, G. Jone, Clyde S. III "Chapter 7: Materials for Launch Vehicle Structures," Tech. Report, NASA Marshall Space Flight Center, AL. August 2018.

[3] G. E. Reins and Alvis, J. F., "Advanced small launch vehicle study," United States, Dallas, TX, United States , May 1971 - Feb. 1972

[4] United Launch Alliance, "Atlas V," United Launch Alliance, Littleton, Colorado, USA.

[5] Space X, "Falcon 9," Space X, Hawthorne, California, USA.

[6] R. W. Humble, G. H. Henry and W. J. Larson, Space Propulsion Analysis and Design, New York: McGrawHill Companies Inc., 1995.

IN-SITU PROCESS MONITORING FOR LASER POWDER BED FUSION ADDITIVE MANUFACTURING

A. Fernandez[1], H. C. Taylor. White[1], R. B. Wicker[1]*
[1] Mechanical Engineering, W.M. Keck Center for 3D Innovation, El Paso, TX 79968, USA;
* Alfonso Fernandez (afernandez16@miners.utep.edu)

Keywords*: in-situ Monitoring, Metal Additive Manufacturing*

ABSTRACT

Laser powder bed fusion (LPBF) Additive Manufacturing (AM) has been recently gaining relevance in various industries for the production of metal parts. Even though LPBF technology has dramatically improved in recent years, the process is not yet fully understood, and it lacks process control. . Several OEMs of LPBF equipment have implemented different methods for monitoring the fabrication process to help researchers and industry increase their understanding and control of the process. In this work, the monitoring techniques for two commercially available LPBF systems were evaluated to determine the advantages and disadvantages of each system. The first monitoring system evaluated was the software suite of an EOS M290 machine consisting of the EOSTATE Meltpool Monitoring and EOSTATE OT applications. The second system evaluated was the in-line pyrometry and CMOS camera monitoring capabilities of an Aconity3D AconityONE LPBF system. The monitoring capabilities of the EOS M290 describes the melt pool with intensities, showing either hot or cold spot defects in the process. The monitoring capabilities on the AconityONE system show the intensity of the scanning spot, in addition with a video of the scanning from where solidification rates can be obtained. Both monitoring systems can be correlated with failure and success of the builds; however, they will not show all the defects that may occur in the print.

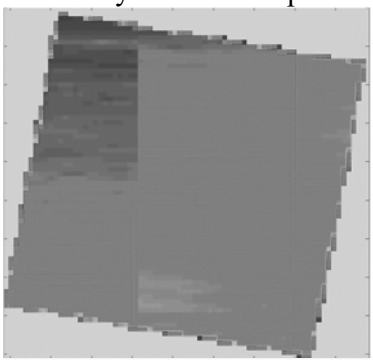

Fig. 1. Image created by EOSTATE Meltpool monitoring software

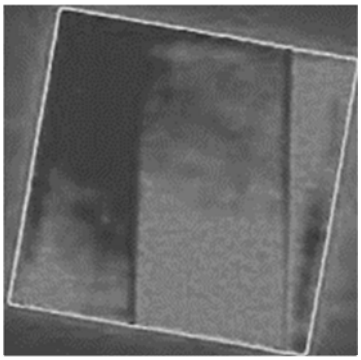

Fig. 3. Image created by EOSTATE OT monitoring software

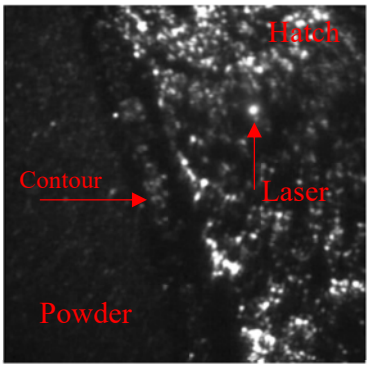

Fig. 4. Aconity's inline sCMOS camera image

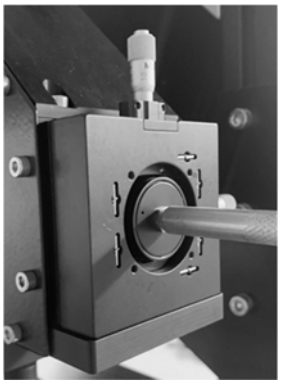

Fig. 2. Repositioning system for in-line pyrometry on the AconityONE machine

1 Introduction

Laser powder bed fusion (LPBF) is an additive manufacturing process that relies upon melting powdered material to form a part in a layer-by-layer basis. Although several companies have used LPBF technology to produce metal parts, the process is not yet fully controlled, as there have been a lack of methods to identify errors or defects in situ, and correct these in the process. The anomalies that are found in the building process are due to a number of variables that are innate to the powder and the process. When a thin, 30-50 µm, layer of powder is

distributed along the platform, it is not consistent from layer to layer. The powder is packed to different densities, thus particle distribution is never even across the reservoir. Cooling and heating rates also influence the occurrence of anomalies during the build process. The scan vector lengths change with the melt area geometry and in turn, alter the heating and cooling rates of individual features destabilizing the process and producing defects.

In-situ process monitoring efforts have been pursued by researchers and industry to increase the confidence in LPBF technology in obtaining quality end use products [1]. In-situ monitoring methods will help in the identification of anomalies as they occur during the build and provide the user with adequate data to make a decision to continue, correct, or stop the build [2,3]. Several commercially available machines have already implemented monitoring methods to identify possible defects found throughout the build process. These include thermal radiation measurements at specific near infrared (NIR) wavelength ranges for intensity measurements, as well as coaxial high-speed cameras to watch the solidification of the metal.

2 Methods

To analyze the monitoring capabilities that companies are implementing, two machines were selected with different monitoring strategies. The first was an EOS M290 (EOS GmbH, Munich, Germany) machine with EOSTATE meltpool and optical tomography (OT) monitoring. The second machine analyzed was the AconityONE (Aconity3D GmbH, Aachen, Germany) with full monitoring capabilities consisting of two inline single wavelength pyrometers and an inline sCMOS camera with a frame rate of up to 8000hz.

The EOSTATE Meltpool monitoring system consists of two photodiodes that record the intensity of light emitted at the range of 400-9000nm wavelengths when the system is scanning with the laser. One photodiode is located in-line with the laser scanner and the other one is located on the top of the chamber. The in-line photodiode is directed specifically to the point where scanning is taking place while the off-line photodiode is static at a specific location above the build chamber for reference measurements. The Meltpool monitoring system records both intensities and stores them with position values taken from the scanner, creating an intensity map with an image, as shown in Fig. 5.

The EOSTATE OT monitoring system uses a sCMOS camera located over the build chamber and focused on the build platform. As the camera works recording intensity values and placing them in a grayscale image, the system records the intensity and uses the data to create a picture with intensity values in an RGB map [4]. The sCMOS camera is continually capturing images throughout the building process with exposure times of about 0.1 seconds. These images are then integrated into a single image to provide an intensity map that will show different characteristics of the layer such as cold or hot spots. Images of each layer are provided by the OT monitoring system, an example is shown in Fig. 6.

Both EOSTATE monitoring systems, Meltpool monitoring and OT, analyze the layers to identify anomalies throughout the build and they are exported at the end of the build for an engineer to analyze and discern what anomalies are critical and produced defects, as well as which of these are non-detrimental.

The AconityONE's monitoring system relies upon two in-line pyrometers and an in-line sCMOS camera. Each pyrometer can be repositioned to obtain data at different positions relative to the laser spot while the powder is scanned and melted. Repositioning the pyrometers can be utilized to acquire the radiation intensity of different locations such as the melt pool, the

cooling rate after laser melting, or to the side of the scanning vector to look at thermal conductivity and heat dissipation of the melting track.
The sCMOS camera that is attached in-line on the scanning head takes video at >5000 fps to visually monitor the solidification of the metal. A still frame taken by the sCMOS camera is shown in Fig. 7.

3 Results and Discussion

Both machines have very different methods of monitoring and provide different types of data while in use during a build. The EOSTATE OT monitoring system shows anomalies throughout the build that may become detrimental defects. It will show an intensity map in a picture created by integrating all of the pictures taken during a single layer. This image shows the intensity recorded over the layer and detects spots where the intensity is higher or lower than the average intensity of the whole build. This process of identifying anomalies is repeated automatically throughout all of the layers and a report is output showing these anomalies. With this report, it is possible to understand the quality of the part without having to do any additional non-destructive testing on the part.

The EOSTATE Meltpool analysis system records the intensity from both the in-line and the off-line photodiodes creating an image with intensity values by introducing these at specified coordinates based on the position of the mirrors inside the laser scanner. The software that the machine uses to analyze the data allows for the detection of anomalies by analyzing the signals themselves and comparing them to the other signals at the same layer. This monitoring system is commonly used for research as the parameters are more flexible compared to those of the EOSTATE OT system.

The AconityONE's monitoring system can record intensities with its dual pyrometer system which is in-line with the scanning head. Both pyrometers can be positioned as desired using the milimetric screws attached on the sides of the pyrometer inlet (Fig. 8), creating opportunity to measure intensities at different locations relative to the laser spot. With the data that this monitoring system outputs, it is possible to make an intensity map such as the one created by the EOSTATE Meltpool software. The system outputs a file with x-y locations and intensity values corresponding to each location, allowing the creation of this map.

The sCMOS camera attached in-line with the scanning head allows the Aconity's monitoring system to show a visual of the solidification of the melt pool. With the visual aid that the video provides, it is possible to calculate solidification rates by considering the framerate selected for the monitoring.

Although the AconityONE's software is not as advanced as the EOSTATE Meltpool software, the possibility that Aconity provides of creating different setups with the pyrometer positions makes it a great system for research and development. Both monitoring systems offered by EOS act in a similar manner, yielding a similar output, as the purpose of both systems is to find anomalies during the build. In comparison with the monitoring capabilities offered by Aconity, it appears that the Aconity's monitoring system is more versatile but less refined than that from EOS. The monitoring system that the EOSTATE offers is more advanced and oriented to production manufacturing than the one provided by Aconity. However, the Aconity's monitoring system may be best suited for research purposes as it allows for more modifications and research based monitoring than the EOSTATE monitoring system.

4 Conclusion

In conclusion, both systems have advanced monitoring capabilities that can be used for different purposes. Each of them was created specifically for the individual machines. The AconityONE machine was created for research purposes as almost all parameters can be modified and it has an open architecture, which allows for even greater modifications. As such, Aconity's monitoring system is more inclined toward research activities. On the other hand, the EOS machine is for production as most or all of the parameters are restricted to what the manufacturer has provided. For this reason, the nature of the monitoring system is more oriented to production and correlating anomalies to defects.

References

[1] C. Zhao, K. Fezzaa, R. W. Cunningham, H. Wen, F. De Carlo, L. Chen, A. D. Rollett, T. Sun. "Real-time monitoring of laser powder bed fusion process using high-speed X-ray imaging and diffraction". *Scientific Reports*, Vol. 7, No. 3602, 2017.

[2] M. J.Matthews, G. Guss, S. A. Khairallah, A. M. Rubenchik, P. J. Depond, W. E. King. "Denudation of metal powder layers in laser powder bed fusion processes". *Acta Materialia*, Vol. 114, No. 1, pp 33-42, 2016.

[3] P. Bidare, I. Bitharas, R. M. Ward, M. M. Attallah, A. J. Moore. "Fluid and particle dynamics in laser powder bed fusion". *Acta Materialia*, Vol. 142, No. 1, pp 107-120, 2018.

[4] G. Zenzinger, J. Bamberg, A. Ladewig, T. Hess, B. Henkel, W. Satzger. "Process monitoring of additive manufacturing by using optical tomography". AIP Conference Proceedings, Vol. 1650, No. 1, pp 164-170, 2015.

INVESTIGATION OF FLAME EVOLUTION OF TURBULENT PREMIXED METHANE-AIR COMBUSTION AT DIFFERENT FLOW-MIXTURE RATES USING THE PLIF CH-CX

Md. Amzad Hossain[1*], Md. Nawshad Arslan Islam[1] and Ahsan Choudhuri[1]
[1]NASA MIRO Center for Space Exploration and Technology Research, The University of Texas at El Paso, El Paso, TX 79968, USA;
* Corresponding author (mhossain8@miners.utep.edu)

Keywords: PLIF CH-CX, Methane-air mixture, Premixed combustion, Higher order turbulence

ABSTRACT

This study reports the investigation of flame evolution of a highly turbulent flow over a backward facing step, inside a windowed combustor. A CH-CX planar laser-induced fluorescence (PLIF) is used to investigate the effect of high turbulence on the flame dynamics and flame evolution. Reynolds number, Re = 15000 and equivalence ratio of 0.7 and 1.0 are considered for this study. It is found that the flame grows very fast at these turbulent conditions. The effect of different equivalence ratios does not influence the flame evolution since Re is the same. It was also observed that the width of the flame profiles increases as the flame progress downstream. A MATLAB based tool was developed and used to minimize the challenges encountered in experiments and post image processing. Finally a correlation is developed between the flow turbulence and the flame evolution at Re = 15000.

1.0 Background

The knowledge of flame structure at high turbulent conditions is very crucial to develop and optimize the next generation of rocket engines, ramjets, scramjets, diesel engines and turbines [1-2]. The experimental investigation on flame fronts at high turbulent conditions remains limited [3-6]. Laser diagnostics such as kHz level PLIF allows for an understanding of the flame evolution at high Reynolds number. The outcome results from this effort will provide an insight into the flame dynamics and help to validate the models used in combustion research [6-9].

There are many tracers that can trace the flame fronts during the combustion such as OH, CH, CH_2O and Toluene. There is a large amount of information on OH PLIF imaging, however, little research has been done on CH PLIF imaging. More investigation needs to be carried out on CH PLIF. There is a correlation between the heat release and the CH signals [3], [10]-[11]. Therefore, methylidyne (CH) PLIF could be an effective marker in investigating the flamelet structures at Re = 15000 [7]-[9], [12]. However, capturing the CH PLIF signal in high speed and complex flow-fields is difficult as it has a low relative concentration in the flames [10]-[11], [13]-[14].

The CH-PLIF has mainly been conducted using the A-X and B-X bands [14]-[16]. These wavelengths cannot be reached using a common YAG pump-dye laser like the one available at the UTEP. Carter et al. [11], [14] revealed that the detection of the CH in hydrocarbon flames is possible using the KHz level CH PLIF at C-X ≅ 314nm. This band falls within the capacity of the YAG pump-dye laser like the one commonly used for OH detection [10], [12]-[13]. The CH bands had been first reported in

literature since the 1950s, however, because of their lower emission energy level and overlapping with the OH band, it has not been the choice among combustion researchers.

Nonetheless, Carter's group reported the detection of the CH in turbulent flame in a Busen burner [11], [14], [16]. However, the study was limited to open flame systems. In addition, the majority of research work has been conducted on 2D flame systems and/or on open flame systems [4], [12], [17]-[19]. This research work presents an experimental methodology to characterize flame evolution of turbulent premixed mixture over a backward facing step, inside a windowed combustor, using the CH-CX PLIF.

2.0 METHODOLOGY AND CHALLENGES

A small-scale windowed combustor with a backward a facing step (Fig. 1) is used in this study [13], [20]. The backward facing step induced a low-speed recirculation zone at the edge of the step. The recirculation zone helped to stabilize the flame and hence prevented flame extinction. A grid (perforated plate) with 61% blockage ratio was placed at the inlet of the chamber. The grid induced uniform isotropic turbulence in the flow, which made the flow inside the chamber more turbulent. A pilot ignition system (hydrogen-air) is used to initiate the ignition of the combustible mixture inside of the chamber. Figure 2 shows the position of the grid and pilot flame. A solenoid-based feed system is used to control the main flow, pilot flow and the cooling system.

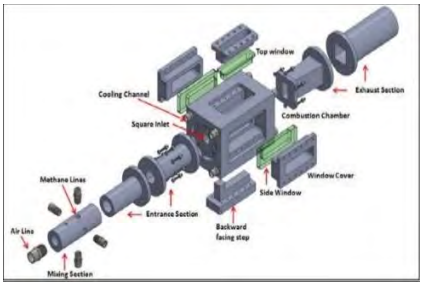

Fig.1. The 3d view of combustor and its subsystems [20]

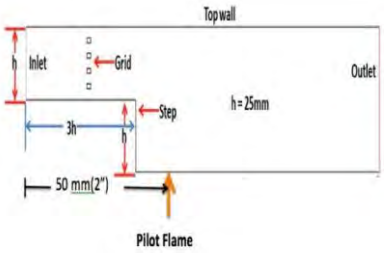

Fig.2. The pilot flame and grid position [13]

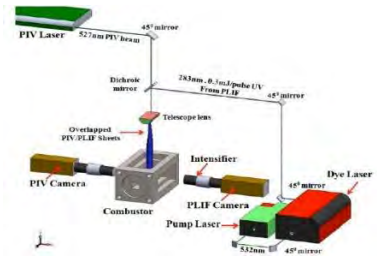

Fig.3. Schematic of the PLIF system [13]

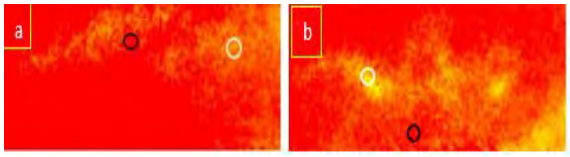

Fig. 4. Flame profiles with HSV colormap at Re = 15000 and with (a) ϕ = 0.7 and (b) ϕ = 1.0

A PLIF system (Fig. 3) consists of a pump laser, a dye laser and a high-speed camera and is used for flame characterization. The pump laser (Nd-YAG Edgewave IS series) pumps a 532nm laser beam through the frequency doubled dye laser (Radiant Dyes HighRep Dye laser). The dye laser tunes the wavelength of the system to CH excitation wavelength using the dyelaser oscillator and BBO crystal assembly. The DCM is used in the dye laser. The dye laser was operated at 3.5kHz because at this frequency the maximum energy output was attained. The pump laser could produce

a maximum of 20W at 10kHz i.e. 2 mJ/pulse of laser energy, whereas, the dye laser could produce a maximum of 0.2 mJ/pulse. A speed sense 9070 high frame rate CCD camera integrated with the intensifier unit (Hammatsu) was used to detect the laser fluorescence from the flame. A LabView program coupled with the data acquisition system was used to monitor and record the data during the combustion. To facilitate the detection, a Cerco 10mm f/2.8 lens was placed in the intensifier unit. A UG-5 colored glass was equipped with a lens to block the noises from visible light and allow the fluorescence to pass into the camera. This investigation was conducted at Re = 15000 at two different equivalence ratios. The experimental operating conditions are listed in table 1.

Table 1. The test operating conditions

Reynold Number, Re	Combustion Mixture	Flow Nature	Bulk Mixture Flow Rate (LPM)	Methane Flow Rate (LPM)	Air Flow Rate (CFM)	Equivalence Ratio, ϕ
15000	Premixed methane-air	Turbulent	353.7	24.2	11.6	0.7
			353.7	33.6	11.3	1.0

Table 2. Operating conditions for pump laser and intensifier unit

Parameters to Control	Magnitudes with Units
Pump Laser Capacity	532 nm
Dye Laser Maximum Output	355 nm
Pump Laser Pulse Energy	2 mJ/pulse
Dye Laser Pulse Energy	0.2 mJ/pulse
Gate Exposure Time, Gate Delay Time, Gate Pulse Width	15 μs, 10ns and 70 μs
Intensifier Gain	750
Excitation Wavelength for CH-CX Band	310-320 nm

In the experimental and post-experimental stages, many challenges were encountered. The initial challenge was to set the concentrated laser on the interrogation plane inside the combustor. The second challenge was to tune the wavelength for the CH C-X. A wavelength scan was performed and a wavelength of 314.415nm was found to be the optimum wavelength for the CH C-X band. However, the extraction of the CH C-X signal from the flames was very difficult. This happened because the bandwidth of the CH C-X signal overlaps with OH signal. This issue has been resolved by iterating several camera and intensifier parameters such as gate pulse width, exposure time, and gate delay. After several iterations, it was found that the OH signal reduces with the decrease in the gate time and the exposure time. A gate delay of 10 ns, gate pulse width of 70 μs, intensifier gain of 750, and gate exposure time of 15 μs were detected as the optimum conditions for CH-CX detection. Table 2 lists the operating parameters for the CH-CX PLIF system.

An adaptive MATLAB based image processing code was developed. The code was adjusted to the flame image pixel matrix. During each run, the code abstracted the base image from the raw image. This allowed for minimal unwanted laser reflections, and background noise from the flame image. Moreover, the code automatically adjusted the interrogation area with the flames, thus eliminating the scaling errors in the flame frame. Afterwards, a separate code was developed for color-scale imaging of the flame profiles. The code allowed for investigations of the effect of color maps on the flame profiles. It was observed that the grayscale colormap has potential to trace the flame profile effectively. The flame profiles generated by grayscale color map had almost no background noise. Because of this, only the grayscale associated HSV colormap is reported in this paper.

One of the goals of this study was to detect the flame edges. For this, a separate MATLAB code was developed. The code transformed the raw images to RGB images. After that, the RGB images were converted to binary images. Finally, the MATLAB edge detection command was used to generate the flame edges.

3.0 Results and Discussions

The flame profiles detected at Re = 15000 and with equivalence ratios (ϕ) of 0.7 and 1.0 are presented in figure 4. The presence of the burned gases (represented by the white circle) and unburned gases (represented by the black circle) within the flame profile was also noticed. It was

observed that the flame profiles have some discontinuity. This discontinuity occurred because of the detachments and reattachments of the flamelets from the flames. The flame evolution profiles of turbulent premixed combustion inside the windowed combustor are shown in figure 5. It shows the effect of the turbulence (Re = 15000) and methane-air flow rates on the flame evolution. It was noticed that the flame evolution is greatly affected by the turbulence. The flame width increased as the flame progressed downstream. There is a formation wrinkle (loop of burned gases) in the flame profiles (see fig. 5(b)). The wrinkle formed because of the change in local pressure in the flame fronts. The pressure fluctuation caused the change in flow momentum. The change in flow momentum helped to form more wrinkles in the flame fronts (see fig 5(c)). The wrinkles continuously formed as the flame moved downstream. It was observed that the gap between the wrinkles reduced as the flame progressed downstream.

The wrinkles began to break down from the flame core. This happened because part of the burned gases at the flame edges reached a very high thermal energy. In addition, the higher order turbulence and local pressure fluctuation were also responsible for this breakdown. This phenomenon is called pinch-off or break down event (see fig 5(d)). The detached burned gases reached a very high temperature and ultimately burnt out from the flame core. This event is called quick burn out of the burned gases (see fig 5(e)). It was also observed that the change in the equivalence ratio of 0.7 to 1.0 did not affect the flame evolution. Although methane and airflow rates are different, flame evolution was the same because the turbulence (i.e. Re) was the same in both cases.

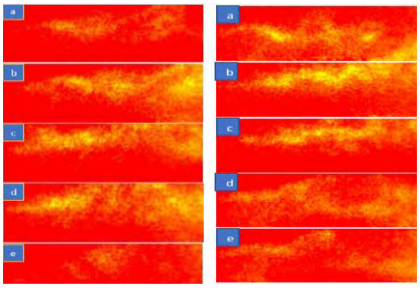

Fig.5. The flame evolution profiles (a→e)

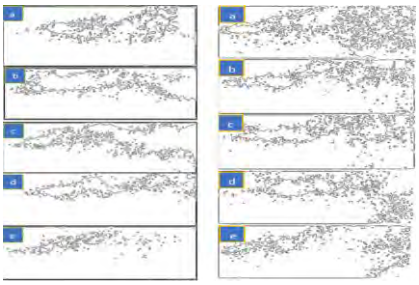

Fig.6. The flame edges (a→e)

(Where, a = Initial flame profile, b = Wrinkle formation, c = More wrinkle formation, d = Pinch Off (Break Up) from the reactant core, e = Quick burnout of the turned gases from the reactant core; data is presented at Re = 15000, and with $\phi = 0.7$ (first column of each figure) and $\phi = 1.0$ (second column of each figure))

The flame evolution could also be explained with the flame edge profiles (Fig 6). For this, a separate MATLAB code was developed. The flame edges clearly showed how the wrinkles initiate and continued to grow. (Fig. 6(b) and 6(c)). There is a rapid change in wrinkle shape in the flame fronts. This change is more noticeable as the flame moves downstream. This happened because of the turbulence induced by the grid. The turbulence increased along the flow path and made the wrinkles even more irregular in shape. It was also noticed that the flamelets became detacheded from the flame core. This happened because of the local pressure fluctuation in the flame fronts. This change in local pressure caused the discontinuity in the flamelets. In addition, the turbulence caused some portion of the flame to extinct. However, a backward facing step was used to stabilize the flame and prevent the flame extinction. Low-velocity recirculation zones were created on the onset of the step. This caused the formation of favourable eddies and vortices in the flow. This

helped to reattach the detached flamelets to the flame core. Consequently, the flame became stabilized and flame extinction was minimized.

After the winkle's growth, the flame began to breakdown from the flame fronts (see Fig. 6(d)). This happened because some part of the burned gases reached a very high pressure. This is called the pinch-off or breakdown event. Furthermore, it was noticed that the pinch-off event was more dominant downstream, near the wall. At the wall, there was a formation of small eddies that infused to the flame and caused the burned gases to breakdown from the flame fronts. Subsequently, some part of the burned gases reached a very high temperature and burnout from the flame core. This process is called the burnout of the burned gases (see Fig. 6(e)). It was found that the flame evolution is more visible and understandable with the flame edge profiles. The flame edge profiles also showed that there is no difference in flame evolution (a→e) at both $\phi = 0.7$ and 1.0. Since the same grid is used and the same bulk mixture flow rate is considered, the resultant turbulence was also the same. Although the equivalence ratio is different, the flame evolution, or flame dynamics, was the same.

The flame profiles and flame edges together gave qualitative information on flame thermodynamics. There was a presence of the highest CH concentration gradient in the flame fronts. This indicated that the flame fronts have the highest thermal energy. This also indicated that the combustion at the flame fronts was complete. It is reported in the literature that the total energy released during the combustion is related to the area of the flame front structure [21]. Thus, if the total heat release is quantified, the area of the flame structure could also be measured or vice-versa. There was an increase in combustion heat release at an equivalence ratio (ϕ) of 1.0. This happened because, at $\phi = 1.0$, the rate of methane flow was higher than what it was at $\phi = 0.7$. Therefore, better detection of the flame edges could bring a better understanding of flame thermodynamics.

4.0 Conclusions

This study introduced a complete scheme of detecting and processing the flame fronts of premixed turbulent combustion inside a windowed type combustor. The flame profile showed that the flame evolution was greatly influenced by flow physics, such as turbulence, local pressure, and temperature. There was no change in flame profile at equivalence ratios (ϕ) of 0.7 and 1.0. This happened because the turbulence is the same in both cases. The flame edges provided sound information on flame evolution. It was found that the turbulence increased as flames progressed downstream. The infusion of some eddies to the flame core made pinch-off events more dominant on the bottom wall of the combustor. The backward facing step stabilized the flame by reattaching the detached flamelet to the flame core and hence prevented flame extinction. It was found that the heat released during the combustion increased with the increase in methane flow rate.

References

[1] Bobba, Mohan Krishna. *"Flame stabilization and mixing characteristics in a stagnation point reverse flow combustor"*. PhD Dissertation. Georgia Institute of Technology, Atlanta, GA. 2007. http://hdl.handle.net/1853/26502

[2] Hossain, Mohammad A. *"Design of a high intensity turbulent combustion system"*. Master's Thesis. The University of Texas at El Paso, El Paso, TX. 2015. https://digitalcommons.utep.edu/dissertations/AAI1593092

[3] Chen, YunTao. "*Investigation of Partially Premixed Combustion Instabilities through Experimental, Theoretical, and Computational Methods".* PhD Dissertation. University of Michigan, Ann Arbor, MI. 2015. http://hdl.handle.net/2027.42/111342

[4] Filatyev, Sergei A., Driscoll, James F., Carter, Campbell D. and Donbar, Jeffrey M. "Measured properties of turbulent premixed flames for model assessment, including burning velocities, stretch rates, and surface densities." *Combustion and Flame,* Vol.141, No. 1-2, 2005, pp. 1-21. https://doi.org/10.1016/j.combustflame.2004.07.010

[5] Periagaram, Karthik Balasubramanian. *"Determination of flame characteristics in a low swirl burner at gas turbine conditions through reaction zone imaging".* PhD Dissertation. Georgia Institute of Technology, Atlanta, GA 2012. http://hdl.handle.net/1853/45828

[6] Vagelopoulos, Christina M. and Jonathan H. Frank. "An experimental and numerical study on the adequacy of CH as a flame marker in premixed methane flames." *Proceedings of the Combustion Institute,* Vol. 30, No. 1, 2005, pp. 241-249. https://doi.org/10.1016/j.proci.2004.08.243

[7] Abu-Gharbieh, Rafeef. "*Laser sheet imaging and image analysis for combustion research*." PhD Dissertation. Chalmers University of Technology, Göteborg, Sweden. 2001. http://www.ece.ubc.ca/~rafeef/papers/phd2001.pdf

[8] Hammack, Stephen Daniel. *"Development of high-speed laser diagnostics for the study of advanced propulsion systems".* PhD Dissertation. University of Illinois at Urbana-Champaign, Champaign, IL. 2015. http://hdl.handle.net/2142/89121

[9] Grisch, Frédéric, and Mikaël Orain. "Role of Planar Laser-Induced Fluorescence in Combustion Research." *AerospaceLab, Vol.* 1, 2009, pp.-1. http://www.aerospacelab-journal.org/al1/Role-of-Planar-Laser-Induced-Fluorescence-in-combustion-research

[10] Tanahashi, Mamoru, Murakami, Shinichirou, Choi, Gyung-Min, Fukuchi, Yuichi and Miyauchi, Toshio. "Simultaneous CH–OH PLIF and stereoscopic PIV measurements of turbulent premixed flames." *Proceedings of the Combustion Institute*, Vol. 30, No. 1, 2005, pp. 1665-1672. https://doi.org/10.1016/j.proci.2004.08.270

[11] Carter, Campbell D., Donbar, Jeffery. M. and Driscoll, James F. "Simultaneous CH planar laser-induced fluorescence and particle imaging velocimetry in turbulent nonpremixed flames." *Applied Physics B: Lasers and Optics,* Vol. 66, No. 1, 1998, pp. 129-132. https://doi.org/10.1007/s003400050366

[12] Sjöholm, Johan, Rosell, Joakim, Li, Bo, Richter, Mattias, Li, Zhongshan, Bai, Xue-Song and Aldén, Marcus. "Simultaneous visualization of OH, CH, CH_2O and toluene PLIF in a methane jet flame with varying degrees of turbulence." *Proceedings of the Combustion Institute,* Vol. 34, No. 1, 2013, pp. 1475-1482. https://doi.org/10.1016/j.proci.2012.05.037

[13] Acosta-Zamora, Arturo. *"Flame front structures studies of highly turbulent reacting flow over a backward facing step using KHz OH-CH planar laser induced fluorescence".* PhD Dissertation. The University of Texas at El Paso, El Paso, TX. 2016. https://digitalcommons.utep.edu/dissertations/AAI10251418

[14] Carter, Campbell D., Hammack, Stephen and Lee, Tonghun. "High-speed flamefront imaging in premixed turbulent flames using planar laser-induced fluorescence of the CH C− X band." *Combustion and Flame,* Vol. 168, 2016, pp. 66-74. https://doi.org/10.1016/j.combustflame.2016.03.024

[15] Li, ZhongShan, Kiefer, Johannes, Zetterberg, Johan, Linvin, Martin, Leipertz, Alfred, Bai, Xue-Song and Aldén, Marcus. "Development of improved PLIF CH detection using an Alexandrite laser for single-shot investigation of turbulent and lean flames." *Proceedings of the Combustion Institute, Vol.* 31, No. 1, 2007, pp. 727-735. https://doi.org/10.1016/j.proci.2006.08.015

[16] Skiba, Aaron W., Carter, Campbell D., Hammack, Stephen D. and Lee, Tonghun. "A simplified approach to simultaneous multi-scalar imaging in turbulent flames." *Combustion and Flame,* Vol. 189, 2018, pp. 207-211.

[17] Ganji, A. T., and Robert F. Sawyer. *"Turbulence, combustion, pollutant, and stability characterization of a premixed, step combustor*". 1980.

[18] Ganji, A. R., and R. F. Sawyer. "Experimental study of the flowfield of a two-dimensional premixed turbulent flame." *AIAA Journal*, Vol. 18, No. 7, 1980, pp. 817-824.

[19] Cohen, Jeffrey M., Brian E. Wake, and Dochul Choi. "Investigation of instabilities in a lean, premixed step combustor." *Journal of Propulsion and Power*, Vol. 19, No. 1, 2003, pp. 81-88.

[20] de la Torre, Martin Alexandro. *"Characterization of high intensity turbulent flows through time resolved particle image velocimetry in a backward facing step combustor".* 2016.

[21] Seyfried, Hans, Jimmy Olofsson, Johan Sjöholm, Mattias Richter, Marcus Aldén, Andreas Vressner, Anders Hultqvist, and Bengt Johansson. High-speed PLIF imaging for investigation of turbulence effects on heat release rates in HCCI combustion. *SAE Technical Paper*, 2007, No. 2007-01-0213.

MATERIALS OPTIMIZED FOR ADDITIVE MANUFACTURING: KICKING OFF THE NEXT GENERATION OF MATERIAL DESIGN

H. Taylor , R. Wicker
W.M. Keck Center for 3D Innovation, El Paso, TX 79968, USA;
* Corresponding author (hctaylor@miners.utep.edu)

Keywords: *Additive manufacturing, Metal, Characterization, Laser powder bed fusion, Alloy design*

ABSTRACT

Additive manufacturing (AM) has progressed beyond eye-catching lattice structures and showpieces into a full-fledged manufacturing industry. AM cuts across all engineering fields, relying heavily on materials science to develop the cause/effect relationship of numerous processing parameters and performance characteristics. It is not novel to develop material systems specifically for the manufacturing method, yet AM has only recently reached a maturity level to support focused material development. In recent years, metal AM has made huge strides by fielding many FDA and FAA qualified components using traditional alloys like Ti-6Al-4V and CoCr. This important success paves the way for the next milestone in AM, a qualified AM component made of a novel alloy. The unique processing environment offered in AM will enable the creation of exotic materials by opening the door to a relatively unexplored realm in materials design. Although alloys designed for AM will push beyond current performance limitations, effectively designing and qualifying these materials requires a broad range of analytical and manufacturing equipment. In addition to having the right tools, it is imperative to have control over the entire workflow, from base material to processing parameters and materials characterization. With the major additive technologies and required analytical equipment under one roof, the W.M. Keck Center for 3D Innovation is positioned to become a leader in developing next generation materials. This paper will briefly review what specifically allows AM to target new materials and the required equipment to effectively develop these materials.

1 Introduction

1.1 Key Metal Additive Manufacturing Technologies

Additive manufacturing (AM) creates design optimization opportunities and allows for rapid iterations of functional prototypes. These benefits are easily conceptualized but are not the only aspects of AM making it attractive. Additive processes create additionional opportunities due to the iterative layerwise process including conductive traces or embedded sensors [1]. Materials design for AM is another subset of the industry beginning to take shape that accounts for the unique processing conditions available through this production method. In fact, the Max-Planck Institute's department for Microstructural Physics and Alloy Design established a research group called Alloys for Additive Manufacturing back in 2015. In laser

powder bed fusion (L-PBF) the cooling rates have been reported to exceed $5x10^6$ kelvin creating fine grain structures, access to metastable phases, and in many cases are adequate for printing metallic glasses with no critical radius limitations [2,3,4]. These extreme conditions are not entirely positive and can prevent many commonly used alloys such as Al 6061 and Al7075 from being easily adapted to L-PBF.

There are five AM techniques available for metal part fabrication; powder bed fusion (PBF), directed energy deposition (DED), binder jetting, sheet lamination, and material jetting. The W.M. Keck Center for 3D Innovation (Keck Center) houses three L-PBF machines, EOS M-290 (Krailing, Germany), SLM Solutions SLM 125^{HL} (Lubeck, Germany), and Aconity3D AconityONE (Herzogenrath, Germany), two electron beam PBF machines, Arcam A2 and S12 (Molndal, Sweden), and two binder jetting machines, ExOne M-Flex and M-lab (North Huntingdon, Pa). These encompass the key metal AM technologies in the commercial sector from the state of the art in serial production AM (EOS) and research and development (Aconity3D) relevant to L-PBF. The AconityONE has sever unique features such as complete open access to all controls and a pre-heated bed capable of 1000^{o}C allowing the user to print materials that fail from the extreme thermal stresses. L-PBF will be used in most examples throughout this overview but all claims can be adjusted for for materials development needs in other additive manufacturing systems.

1.2 Currently Available Materials

Alloys used in AM focus on higher end applications where the cost of AM can be justified. Typical PBF alloys include Ti-6Al-4V, Nickel-based superalloys 625 and 718, several stainless steels, Co-Cr, and some specialty steels. These alloys can be printed with high levels of control that meet the standard set by their traditionally manufactured counterpart.
Although aluminum alloys are critical to the automotive and aerospace industries, most cannot be reliably made via L-PBF due to hot cracking [5]. AlSi10Mg can be easily manufactured via L-PBF and is the only one commonly used. This alloy overcomes cracking with the increase Si content and while it possesses good strength, it has low ductility and is not a good choice to replace alloys like Al6061. The lack of a quality aluminum alloy in AM that can perform at least as well as Al6061 is a great example of the need to design new alloys for AM. In order to develop a material for AM, hundreds of parameters and characteristics must be controlled through the process, from the raw material to the end product.

2 Controlling the Process from Start to Finish

2.1 Feedstock Materials

Powder properties are a critical aspect of the metal AM industry and add additional variability to the process. Powder metal (PM) is a well-established industry and parts are commonly made via press and sinter, hot isostatic pressing, hot pressing, liquid phase sintering, metal injection molding, etc. Sadly, many of the techniques used to create feedstock for these consolidation methods do not work well for metal AM. All metal AM technologies require excellent flowability and loose pack densities. For this reason, the AM industry has created its own feedstock manufacturing subset that focuses on creating spherical powder. Spherical powder is typically produced via gas or plasma atomization.

Each of these processes are expensive when compared to other powder production methods that do not produce spherical powder, adding additional cost to an already expensive process.

In order to properly develop new alloys and establish a reliable process, the material needs to fully characterized from the as-received powder state. This will include elemental analysis, particle size and shape distributions, flowability, and other characteristics specific to AM related to layer packing and spreading.

Particle size distribution and morphology have significant effects on how the material behaves during the layering process. The optimal powders have near perfect spherical morphologies but optimal particle size is less straight forward [6]. Smaller particles result in improved surface finish but typically have higher oxygen content, flow poorly, and are more flammable. Accurate particle size and shape distribution is difficult to gather when a large number of particles need to be quantified. The Keck Center utilizes Retch Technologies Camsizer X2 (Haan, Germany), shown in Fig. 1, which conducts dynamic imaging of particles they fly-by cameras. The equipment takes millions of size and shape measurements in minutes, resulting in quantitative evaluation of powder characteristics. This instrument has an effect lower detection limit of approximatly 3µm and an upper limit in its current configuation of 3000µm.

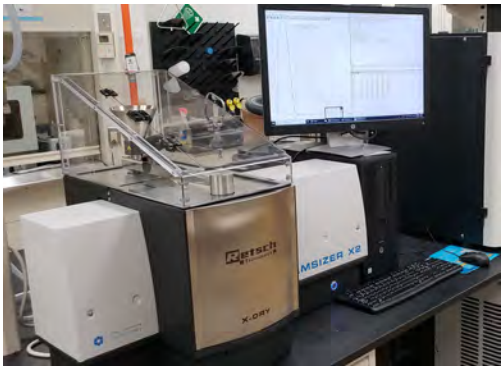

Fig 1. Retch Technologies Camsizer X2 particle analyzer

Powders have high surface area per unit mass compared to a billet of the same material, and increased surface area allows for higher surface oxide content. It is well known that oxygen, nitrogen, and even hydrogen can have significant effects on performance and therefore need carful tracking and control throughout the AM process. Substantial work has been done to gather performance data of additively manufactured Ti-6Al-4V but typically, the variables accounted for only include build direction, and postprocessing methods which can lead to misidentification of performance values [7]. The Keck Center will utilize its ELTRA (Haan, Germany) ONH-p elemental analyzer (Fig. 2) to quantify oxygen, nitrogen, and hydrogen content in powder and bulk printed parts to ensure performance values are properly understood.

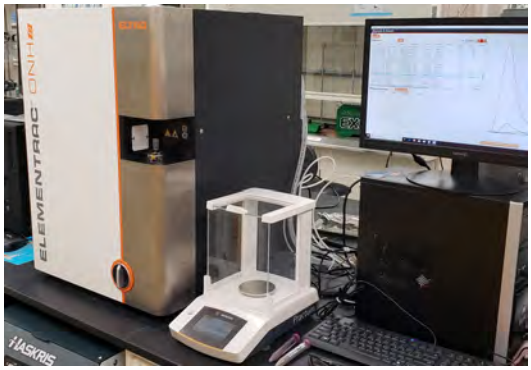

Fig 2. Eltra ONH-p elemental analyzer

Along with ONH the remaining elemental composition of alloys must be quantified and verified frequently as powder gets recycled during the printing process. To obtain quantitative elemental composition inductively, coupled plasma optical emission spectroscopy or mass spectroscopy (ICP-OES, ICP-MS) are the methods of choice. For metal alloy composition, ICP-OES is ideal and can obtain results of most elements down to the parts per billion level. Tracking composition of alloys after printing is important due to evaporation of lower melting point elements. At this time, the Keck Center uses partner facilities to perform these analyses but is working toward adding this analytical capability to the lab.

Finally, powder flowability must be characterized for the layering process. At this time, there is no dedicated flow standard pertaining to AM but the standard flow quantifying measurments, such as Hall flow and angle of repose, can be useful in quantifying flow behavior. In addition, new instruments such as the Mercury Scientific's REVOLUTION dynamic avalanche angle analysis has shown great results in quantifying powder flow for AM. The Keck Center is also working on establishing in-house analysis of flowability as it relates to PBF that relates the powder size, morphology, moisture levels, and loose fill density to spreadability. The goal will be to establish an equation to relate common powder characteristics to spreadability instead of developing a new testing rig and standard.

2.2 Building Components

Developing materials for AM will require expert users of the technology and access to all aspects the equipment. Alloy development will primarily focus on the laser and electron beam powder bed fusion techniques as these technologies open new doors to material structural control. Achieving full density is a prerequisite to alloy development but is by no means the end of the story. Fig. 3 depicts a parameter development test matrix for single track contours and hatching solid cubes. This is the first printing step in the development process and is used to box in the parameters that affect properties of interest.

Fig 3. Ti6242 parameter development in AconityOne with platform preheat to 500ºC to prevent cracking from high cooling rates in L-PBF. Solid cubes used to identify ideal hatching parameters while the hollow cube represent single line contours and help to identify meltpool characteristics.

The powder bed fusion process creates extreme process conditions that can be controlled on a microscopic level. The key condition to control is cooling rates from melt as this has significant effects on the microstructure of the alloy. To control cooling rate many variables must be accounted for including spot size, scan speed, laser power, and bed preheat temperature. In addition, the user must account for part geometry as this has significant effects on cooling rate [3]. To properly design alloys for these production methods, it is important to have comprehensive knowledge of all the variables under user control in addition to a fundamental materials background.

To help users develop parameters and a deeper understanding of the L-PBF process, the Keck Center has two machines with cutting edge in-situ monitoring technologies. The EOS M290 has both the EOSTATE Exposure OT (Optical Tomography) and EOSTATE Meltpool in-situ monitoring technologies for in-beam and off-axis monitoring of the building process. The Exposure OT off-axis monitoring is used in serial production to identify possibly defects and acts as a quality assurance metric. An example of the details revealed by EOS on-axis Melt Pool can be seen in Fig. 4. The build was in IN718 using EOS performance parameters of a commonly printed rook. The selected slice of the first overhang layer near the top of the rook shows the stark difference between in-skin and down-skin parameters. The rook was subsequently sectioned for microstructural analysis to corollate meltpool data to microstructure. The AconityONE system has similar in-situ monitoring but within beam high speed video recording, not only melt pool monitoring. The High-Speed camera can record at 5000 frames per second allowing the user to monitor the melt pool in detail. This advanced technology can be used to better optimize processing parameters such as power, line speed, and spot size. The AconityONE's dual in-line pyrometers can capture the intensity value of the melt to identify over-heating and under-heating of the components. In addition to the monitoring system the AconityONE allows complete open access to all parameters and a pre-heated bed capable of 1000ºC. The high temperature pre-heat opens access to materials like titanium aluminides, tungsten, and other materials that are prone to cracking during rapid thermal cycling [8]. The deeper understanding of the process created by in-situ monitoring allows researchers to push beyond limitations faced when exclusively relying on post build analytics.

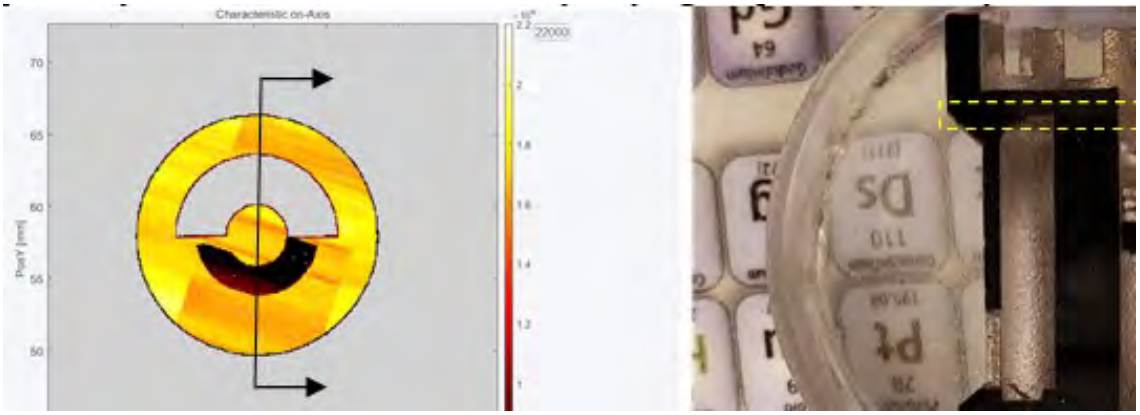

Fig. 4. Left) On-axis meltpool data from EOS M-290 showing the lower intensity of down skin exposure. Right) Sectioned, vacuum impregnation mounted and polished rook from build with highlighted box representing the layer seen in meltpool data.

In addition to scanning parameters the process chamber conditions include many impactful variables such as atmosphere composition, chamber pressure, and flow conditions over the powder bed. The oxygen content must be controlled and, in most cases, the goal is to have no oxygen increase in the material. Flow has also proven to be critically important in the process to remove splatter and smoke produced during the melt process. Splatter particles and smoke created during the laser melting process have been shown to have negative effects on quality [9]. It is critically important to understand these interactions and factor them into performance data post build.

Once the build is complete, most L-PBF components must be stress relieved and possibly heat treated, allowing for further tailoring of properties that may affect part performance and increasing the number of variables one needs to account for.

2.3 Quantifying Performance

After building test articles, detailed characterization must be carried out to relate the process parameters to structure, properties, and performance. This characterization includes elemental analysis, microscopy (optical, scanning electron microscopy, and transmission electron microscopy), mechanical behavior, etc.

Proper sample preparation is critical for all analysis techniques, and metallography is straightforward but not simplistic. When sectioning and polishing samples, it is important to minimize heat input to the specimen as the microstructure can be altered creating possibilities for mis-identification of physical attributes. To minimize this possibility the Keck Center uses an ATM GmbH (Mammelzen, Germany) precision sectioning saw seen in Fig. 5 with a pulsed cutting mode that allows cooling fluid to pass over the cutting surface. The sectioned, polished, and etched samples are then examined on an Olympus GX53 inverted microscope and a JEOL IT500lv scanning electron microscope equipped with back scattered electron (BSE), secondary electron (SE) and an EDAX brand energy dispersive spectroscopy (EDS) detector for elemental analysis.

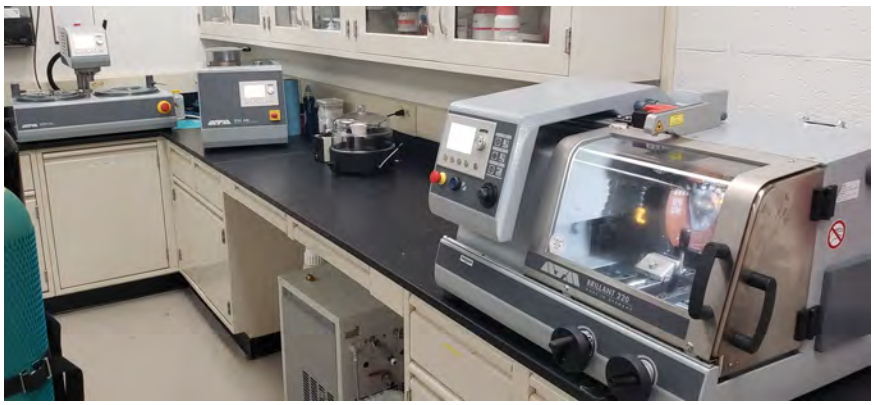

Fig. 5 ATM metallography sample preparation equipment featuring Brialliant 220 precision section saw, vacuum impregnation cold mount station, Opal 460 hot mounting press, and Saphir 530 automated polisher

Mechanical performance of the printed materials must also be quantified with a variety of methods. Hardness, compression, and tensile properties are important but only reveal a small portion of the relevant performance criteria. Fatigue performance is critical in many applications and PBF components have historically performed poorly in this area [10] The Keck Center has multiple mechanical testing machines with capabilities to perform tests to 100kN and the ability to perform fatigue testing up to 4hz.

There are limitless characterization techniques, many of which are specific to the application. While it is not financially feasible to have all techniques in one lab, the Keck Center is well equipped to perform its own analysis in many areas and has partnerships with other labs in the university to expand its capabilities even further.

3.3 Conclusion

The W.M. Keck Center for 3D Innovation has built a multidisciplinary lab with broad capabilities in nearly all additive manufacturing fields. The difficulty in new alloys and composites is in reliable and repeatable data. There must be tight control over the experimental process in order to properly understand and evaluate properties. The experience the staff and students have in design, building, and characterizing AM components allows for a natural transition to materials design and development tailored to AM. There are thousands of papers published every year with respect to new metal alloys and composites, yet the alloys developed half a century ago still dominate the market. Often times the new research fails to be repeatable and this is critical if there is hope to commercialize a certain material. With all pieces in place, the Keck Center can overcome common pitfalls by reliably producing new materials with improved performance.

References

[1] Steven Ambriz, Jose Coronel, Bob Zinniel, Ron Schloesser, Chiyen Kim, Mireya Perez, David Espalin, Ryan B. Wicker, Material handling and registration for an additive manufacturing-based hybrid system, Journal of Manufacturing Systems, Volume 45, 2017, Pages 17-27.

[2] Simon Pauly, Pei Wang, Uta Kühn, Konrad Kosiba, Experimental determination of cooling rates in selectively laser-melted eutectic Al-33Cu, Additive Manufacturing, Volume 22, 2018, Pages 753-757.

[3] Paul A. Hooper, Melt pool temperature and cooling rates in laser powder bed fusion, Additive Manufacturing, Volume 22, 2018, Pages 548-559.

[4] Xiao-Jun Shen, Cheng Zhang, Yan-Ge Yang, Lin Liu, On the microstructure, mechanical properties and wear resistance of an additively manufactured Ti64/metallic glass composite, Additive Manufacturing, Volume 25, 2019, Pages 499-510.

[5] Cassiopée Galy, Emilie Le Guen, Eric Lacoste, Corinne Arvieu, Main defects observed in aluminum alloy parts produced by SLM: From causes to consequences, Additive Manufacturing, Volume 22, 2018, Pages 165-175.

[6] Jun Hao Tan, Wai Leong Eugene Wong, Kenneth William Dalgarno, An overview of powder granulometry on feedstock and part performance in the selective laser melting process, Additive Manufacturing, Volume 18, 2017, Pages 228-255.

[7] Shunyu Liu, Yung C. Shin, Additive manufacturing of Ti6Al4V alloy: A review, Materials & Design, Volume 164, 2019.

[8] Joachim Gussone, Yves-Christian Hagedorn, Human Gherekhloo, Galina Kasperovich, Tarik Merzouk, Joachim Hausmann, Microstructure of γ-titanium aluminide processed by selective laser melting at elevated temperatures, Intermetallics, Volume 66, 2015, Pages 133-140.

[9] Alexander Ladewig, Georg Schlick, Maximilian Fisser, Volker Schulze, Uwe Glatzel, Influence of the shielding gas flow on the removal of process by-products in the selective laser melting process, Additive Manufacturing, Volume 10, 2016, Pages 1-9.

[10] R. Dörfert, J. Zhang, B. Clausen, H. Freiße, J. Schumacher, F. Vollertsen, Comparison of the fatigue strength between additively and conventionally fabricated tool steel 1.2344, Additive Manufacturing, 2019.

Mechanically Activated Self-Propagating High-Temperature Synthesis (MASHS)

L. Calvo, V. Avalos, L. Gandara-Mendez
[1] Mechanical Engineering Department, The University of Texas at El Paso, El Paso, TX 79968, USA;
Luis Calvo (lccalvo@miners.utep.edu) Victor Avalos (vlavalos@miners.utep.edu)
Luis Gandara-Mendez (lngandaramendez@miners.utep.edu)

Keywords: *MASHS, SHS, MA, Ball Milling, Grinding Media*

ABSTRACT

Producing advanced materials through powder based exothermic reactions is a process that has been around for several decades. Mechanically activated self-propagating high-temperature synthesis (MASHS) is a short-term high energy ball milling process prior to self-propagating high-temperature synthesis (SHS). There are multiple types of milling that can be performed. However, the main types of milling that will be focused on in this paper are wet grinding and dry grinding, which is performed by grinding with different media, such as balls and cylpeds. The advantages and disadvantages of MASHS will be discussed along with how to overcome some of these disadvantages, such as porosity, by using a method known as spark plasma sintering (SPS).

Introduction

Discovered in the 1960's, self-propagating high-temperature synthesis (SHS) is a method of creating organic [1] and inorganic compounds through combustion reactions. MASHS is a self-sustaining reaction that takes place during high energy ball milling of the reaction media [2]. A type of SHS, it raises the exothermicity of mixtures, thus enabling an easier ignition and stable combustion. Today, MASHS is used mainly for its simple method of creating ceramic, composite, and intermetallic compounds. Mechanical activation (MA) is needed for several reasons, including:

1) To modify the thermal parameters of the combustion front, such as the combustion front velocity and the thermal heating rate in order to produce the desired end products with expected microstructure
2) To initiate a combustion front in the case of systems having a low exothermicity.

Powdered material, pressed into pellet form, is the most common form of conducting MASHS because it assists in the loading of the reactants and makes it simpler to regulate the porosity. There are sometimes inabilities for powder systems to undergo the processing of SHS such as low exothermicity, and in order to enhance this process, MA is utilized. This can be done through various types of MA such as powder ball milling, field activation, and microwave activation [3].

There are several ways of performing powder ball milling, with wet or dry grinding. Planetary ball mills and overflow discharge mills are among several different powder ball milling mechanisms [4]. Different types of grinding media, such as balls and cylpeds are used to perform these different milling methods [5].

The procedures that take place prior to the combustion include selecting powders and mixing them. Milling then takes place within a ball mill. The powder is then poured into a die and pressed into a pellet. Once pellet samples are ready, they are placed within a reaction chamber that is filled with an inert or reactive gas such as Ar, He, CO, or others alike. The pellets are then ignited using either a tungsten coil or laser [6]. With a tungsten coil, the combustion front starts from the top of the pellet and continues downward as shown in Figure 1 below. The reaction heat that is produced from the surface combustion of the pellet would then transfer to the core of the pellet. Temperatures of the wave-front can reach as high as 350-525 K for organic systems and 1500-4400 K for inorganic systems [1]; these temperatures are measured by a pyrometer or thermocouple that is embedded within the sample.

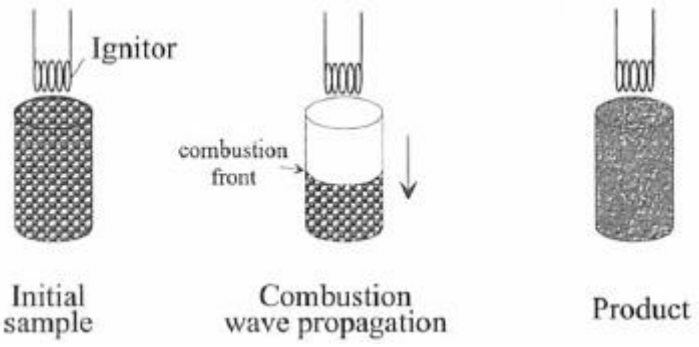

Figure 1. The mode of combustion synthesis in MASHS [7].

Grinding Media

The purpose of grinding media during the milling process is to disrupt the binding forces of the particles within the mills, and during the collision, powders are subject to undergo stresses from 200 MPa to 2 GPA. There are three factors taken into consideration for size reduction: media mass, media surface area, and media size distribution [8]. Typically, there are two types of grinding media that are used in ball mills. These include balls, normally made of steel, zirconia, high-density ceramic, etc., or cylpebs, which are cylindrical metal bodies [5]. Cylpebs are cylindrical grinding media with edges that are rounded off. They have a greater surface area and higher bulk density than balls, which, is impractical, because it was indicated that cylpebs use up 21% more energy than balls [8]. Because of this, the increase of surface area also increases the power.

A reduction in powder size can result in three different ways: abrasion, cleavage, and fracture. When the powder undergoes abrasion, there are low-intensity stresses that are applied to the initial particle, resulting in fine particles taken from the surface. Cleavage of the particles occurs when there are slow, but intense stresses applied, producing fragments of about 50-80 % of the size of the original particle. Fracture, on the other hand, is the result of rapid and intense stress being applied, making small fragments of multiple particle sizes occur. After the deformation of the powders from the impact of the grinding media, hardening, and fracture take place, as well as re-welding. Alloyed powders are generated as the result of repeating this process. Examples of each type of size reduction are shown in Figure 2.

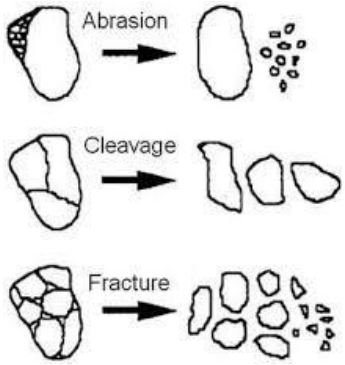

Figure 2. Size reductions due to abrasion, cleavage, and fracture [5].

Milling

MA can be done through the most popular way which is powder ball milling. There are several different types of ball mills available for the process. A couple of powder ball milling that is known are the planetary ball mill and the overflow discharge mill [5]. These can be done by wet or dry grinding, where wet grinding uses a liquid during the milling process, and dry grinding uses air as a gas.

A planetary ball mill is a type of dry grinding that uses high centrifugal forces, resulting in high pulverization energy. It is made up of a rotating sun disk with up to four grinding chambers (GC) located within the mill, as seen in Figure 3. While the sun disc is rotating in one direction, the grinding chambers will rotate in the opposite direction at high speeds to ensure high forces and a random motion and collision pattern of the grinding media, as displayed in Figure 4 [9]. There are also counterweights for balancing purposes within the planetary mill in order to avoid oscillations of the machine.

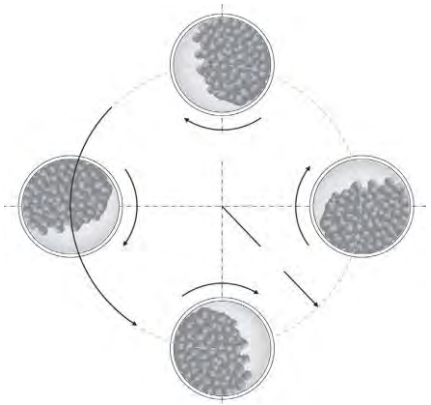

Figure 3. Planetary ball mill with four grinding chambers rotating in the opposite direction to sun disc [9].

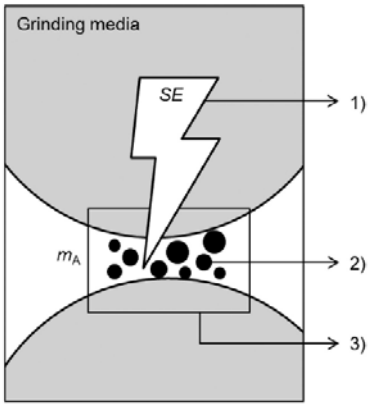

Figure 4. Particles between colliding grinding media where 1) is the amount of dissipated energy, 2) is where breakage and deformation take place within the particle bed, and 3) is where each particle receives part of the stressing energy [9].

There are essential parameters within each milling condition: rotation speed, or angular velocity of revolution (Ω), the speed of the disc, or angular velocity of rotation (ω), and the time of the milling process, or grinding time (Δt), etc. [10]. When changing these parameters during the milling process, they can affect things such as the grinding rate and the impact energy. Speed ratios also have an influence on how the grinding media moves within the grinding chambers. As the speed ratios within the chambers increase, the motion of the media goes from cascading, to cataracting or free-fly, followed by rolling [11] as shown in Figure 5.

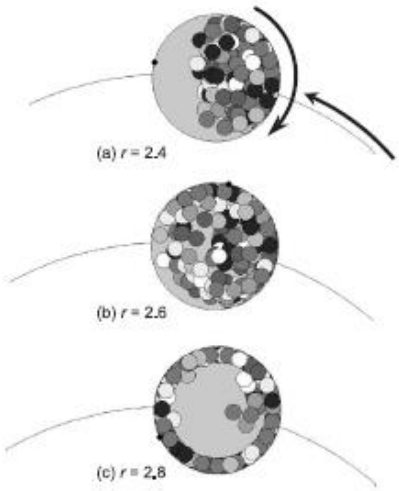

Figure 5. Media motion during milling at different speed ratios: a) cascading, b) cataracting, and c) rolling [11].

The free-fly trajectories are preferred since that is when most of the collision occurs. This happens when the media detaches itself and collides with media or with the wall [12]. The grinding media's motion is rolling when the speed ratio is too high due to the centrifugal force that is caused by the grinding chamber. This motion makes it ineffective during the grinding process since the collision of the media against each other or the wall is considerably reduced; reducing the specific impact energy (E_w).

Another type of powder ball milling is an overflow ball mill, or an overflow discharge mill, that is a type of wet grinding, other than a planetary ball mill that can also be used as wet grinding, where a high specific surface is wanted without any respect to the particle size. The water flow is what considers overflow ball milling wet grinding. This mill works by having a transmission device rotating the cylinder inside, and having materials fed through the inlet of the cylinder to be crushed by the grinding media inside. Since the material is continuously being fed, the pressure is what causes the ground material to be discharged from the outlet of the cylinder through water flow as shown in Figure 6. Backpitch impellers are located within the hollow shaft to return the grinding media to the mill.

Overfilling a mill is essential for engineering in order to conduct circuit design and simulations; ball mill capacity is also something to keep track of for increasing productivity. The main parameters needed to take into consideration for overflow ball mill are slurry pool volume, mill feed rate, and mill power draw. Within this mill, the power draw data cannot be used as an indicator for overfilling [13]. Due to this, unrealistic simulations of the mill capacity are the result. In order to counteract this, a slurry time residence is used to identify the onset point of overfilling.

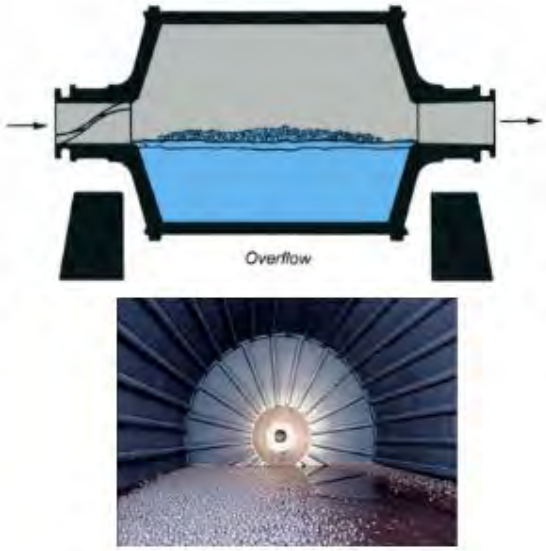

Figure 6. Depiction of overflow ball mill [14].

Unlike other mills that are analyzed using mass-based residence time ($\tau_m = \frac{60H}{F}$), the residence time for overflow ball milling is calculated using volume-based residence time ($\tau_v = \frac{60V_{total}}{Q}$). Figure 7 below shows the most frequently used residence time in a survey to be 3-4 minutes. In this type of ball mill, the mill power draw is dominated by the volume for a given rotational speed. Increasing the mill feed rate will increase the slurry pool volume, but not increase the ball mill power draw. The reason for this is because the slurry pool counters the torque required to rotate the mill shell and lift the ball media, which in turn, leads to decreasing mill draw power [15].

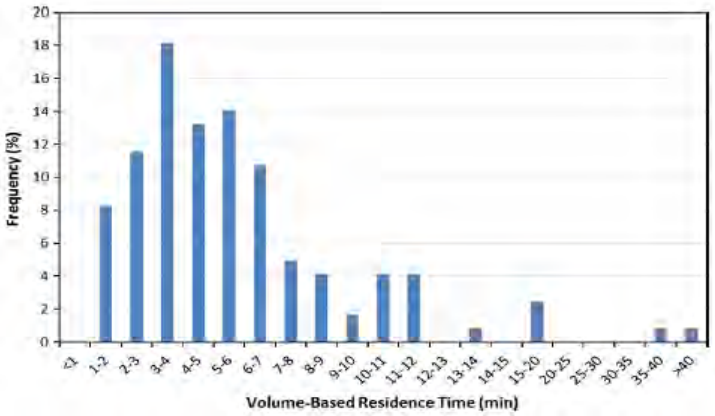

Figure 7. Distribution pattern of volume-based residence time in overflow ball mills [13].

Advantages/Disadvantages

MA comes with many advantages, including, reducing ignition temperatures, producing nanostructured products, removing the need for an oxidizer for reaction (detonation wave), and increasing the combustion front velocity. The increase in the combustion front velocity is preferred so that the milled powder is easily activated without the need of any extra external sources. Along with the optimizations that come with MA, there are also complexities that can occur, such as the MA process step taking long periods of time opposed to non-mechanically activated materials, the potential for powder contamination during MA, and high levels of porosity in the final product [3].

A significant problem for MASHS and SHS alike that has continued throughout the process is unwanted porosity of the finished product. This imperfection can occur by the sudden evaporation of low boiling point impurities, adsorbed moisture on the surfaces of the powder, or in some cases the atmosphere [3]. This can be avoided by carefully selecting the powder size, the environment in which the process is taking place, and in other cases, introducing spark plasma sintering (SPS) [16] [17].

SPS is a type of sintering, in which, the powder is placed within an electrically conducting die andF then sintered under uniaxial pressure. This can be considered a setup of hot pressing, but SPS has its heat generally provided by a direct pulsed electric current [3], while hot pressing is a high-pressure process which induces sintering at high temperatures [8]. As shown in a study done by Meri and Miyamoto [3], the temperature is the predominant process parameter for both SPS and hot pressing.

Planetary ball milling is quick and powerful enough to be able to grind the powder material to the nano-range without contamination, making this preferable in order to counteract this problem [18]. The user is able to control the speed and energy during long-term trials for replicated results. A reaction that is worked on to be avoided during powder ball milling is mechanically induced self-propagating reaction (MSR). This is where the powder reactants transfer to products through an SHS type reaction inside the milling vial [3]. It is crucial to mill the powders to a lower time than what causes MSR to occur in order for the powders to remain in an elemental powder form with high reactivity and not cause a reaction to occur early.

Conclusion

Research of MASHS and the materials used in this method have become more prominent within both research and industrial use. With its ability to be used for the improvement of reaction needed in order to modify the microstructure for products and developing composites with a combination of unique properties, MASHS is slowly becoming a standard process. A higher level of strength and durability could be much more difficult to achieve by other technologies.

MA has helped in increasing the combustion front velocity and reduce the problem of porosity, which can be viewed as the most troublesome challenges during combustion synthesis. A focus on the milling process shows that there is an increase in the contact surface between the reactants, improving the self-sustaining reaction compared to that of the normal SHS process. Control of all parameters is needed in order to prevent unwanted results as well as improving grinding performance.

References

[1] Klimchuk, E. G. (2017). Organic SHS. *Concise Encyclopedia of Self-Propagating High-Temperature Synthesis,* 227-230.

[2] E. A. Levashov, A. S. Mukasyan, A. S. Rogachev & D. V. Shtansky (2017) Self-propagating high-temperature synthesis of advanced materials and coatings. *International Materials Review,* 203-239, 2017.

[3] K. Morsi, "The diversity of combustion synthesis processing: a review," *Journal of Materials Science*, vol. 47, no. 1, pp. 68–92, 2011.

[4] D. V. Shtansky, "Materials and Coatings for High-Temperature Applications," *Concise Encyclopedia of Self-Propagating High-Temperature Synthesis*, pp. 188–189, 2017.

[5] V. Monov, B. Sokolov, and S. Stoenchev, "Grinding in Ball Mills: Modeling and Process Control," Cybernetics and Information Technologies, vol. 12, no. 2, pp. 51–68, Jan. 2012.

[6] J. Yang, L. Han, Y. Chen, G. Liu, Z. Lin, and J. Li, "Effects of pelletization of reactants and diluents on the combustion synthesis of Si3N4 powder," *Journal of Alloys and Compounds*, vol. 511, no. 1, pp. 81–84, 2012.

[7] M. M. Pacheco, *Self-sustained high-temperature reactions: initiation, propagation and synthesis*. S.l.: s.n., 2007.

[8] F. Shi, "Comparison of grinding media—Cylpebs versus balls," *Minerals Engineering*, vol. 17, no. 11-12, pp. 1259–1268, 2004.

[9] C. Burmeister, L. Titscher, S. Breitung-Faes, and A. Kwade, "Dry grinding in planetary ball mills: Evaluation of a stressing model," *Advanced Powder Technology*, vol. 29, no. 1, pp. 191–201, 2018.

[10] C. Gras, D. Vrel, E. Gaffet, and F. Bernard, "Mechanical activation effect on the self-sustaining combustion reaction in the Mo–Si system," *Journal of Alloys and Compounds*, vol. 314, no. 1-2, pp. 240–250, 2001.

[11] H. Mio, J. Kano, F. Saito, and K. Kaneko, "Optimum revolution and rotational directions and their speeds in planetary ball milling," *International Journal of Mineral Processing*, vol. 74, 2004.

[12] A. Rogachev, D. Moskovskikh, A. Nepapushev, T. Sviridova, S. Vadchenko, S. Rogachev, and A. Mukasyan, "Experimental investigation of milling regimes in planetary ball mill and their influence on structure and reactivity of gasless powder exothermic mixtures," *Powder Technology*, vol. 274, pp. 44–52, 2015.

[13] F. Shi, "An overfilling indicator for wet overflow ball mills," *Minerals Engineering*, vol. 95, pp. 146–154, 2016.

[14] "Overflow VS Grate Discharge Ball or Mill - Why Retrofit," *Mineral Processing & Metallurgy*, 24-Apr-2018. [Online]. Available: https://www.911metallurgist.com/blog/overflow-vs-grate-discharge-ball-mills. [Accessed: 20-Nov-2018].

[15] A. B. Makokha, M. H. Moys, and M. M. Bwalya, "Modeling the RTD of an industrial overflow ball mill as a function of load volume and slurry concentration," *Minerals Engineering*, vol. 24, no. 3-4, pp. 335–340, 2011.

[16] V. Kurbatkina, E. Patsera, E. Levashov, and A. Timofeev, "Self-propagating high-temperature synthesis of single-phase binary tantalum-hafnium carbide (Ta,Hf)C and its consolidation by hot pressing and spark plasma sintering," *Ceramics International*, vol. 44, no. 4, pp. 4320–4329, 2018.

[17] Y. F. Yang and M. Qian, "Spark plasma sintering and hot pressing of titanium and titanium alloys," *Titanium Powder Metallurgy*, pp. 219–235, 2015.

[18] F. Bernard, S. Paris, and E. Gaffet, "Mechanical Activation as a New Method for SHS," *Advances in Science and Technology*, vol. 45, pp. 979–988, 2006.

MECHATRONIC DESIGN AND CONTROL IMPLEMENTATION OF A CUSTOM WIRE EMBEDDING TOOL FOR LARGE SCALE 3D PRINTING

Xavier A. Jimenez[1,2*], Eduardo Meraz Trejo[1,2], David Espalin[1,2], Ryan Wicker[1,2]
[1] Department of Mechanical Engineering, The University of Texas at El Paso, El Paso, USA
[1] W.M Keck Center for 3D Innovation, El Paso, USA
* Corresponding author (xjimenezgu@miners.utep.edu)

ABSTRACT

Additive manufacturing (AM) technologies combined with micro-dispensing or wire embedding tools, enable the opportunity to create 3-dimensional multi-functional components in an accelerated time frame. Although it is possible to create products like an RF antenna and a CubeSat module, the embedding rate is limited to 10 mm/s. Newer AM systems with large build volumes (>20 m^3), high material deposition rates (>40 kg/hr.) and fast printing speeds (>76 mm/s) have been developed in recent years to leverage the advantages of AM in large scale applications. A wire heating method within a custom wire embedding tool needs to be developed to create multi-functional components in a large-scale setting. The work presented in this paper focuses on the mechatronic design and controls implementation of a wire embedding tool into the Big Area Additive Manufacturing (BAAM) machine. This document will describe the design requirements and provide a brief introduction to the mechanical design. Finally, the control implementation, G-code customization and overall embedding process are going to be described.

1 Introduction

In traditional manufacturing, multi-functional components are created in a series of steps using several processes. When creating new products, time to market (TTM) is an important measure to quantify success and profitability [1]. The need for multiple steps, processes and specialized tooling reduces the TTM, which can result in less profit or a compromised opportunity. Similarly, when parts need to be created to perform as tooling for the manufacturing of more complex products, the production time needs to be optimal as not to slow manufacturing. Moreover, because traditional manufacturing requires the use of multiple processes, the parts need to be transferred across different groups within a single company. The use of 3D printing technology coupled with electrical interconnect placement can reduce production time and cost for low volume high-value applications.

Additive Manufacturing (AM) also known as 3D printing, is a manufacturing process that builds 3-dimensional objects in a layer-by-layer form. Although this technology started as a prototyping method for single function parts, multi-functional parts are now being fabricated using AM. Modified stereolithography (SL) and fused deposition modeling (FDM) systems

integrated with micro-dispensing or wire embedding technology can create 3D parts with electrical interconnects and components [2,3,4,5,6]. Micro-dispensing is a technology similar to AM, but instead of depositing material on a plane, it deposits conductive material. The disadvantage of using this technology is that the conductive material within the part cannot be cured as it is traditionally done with PCB boards, because the thermoplastic is not able to withstand the required high curing temperatures. An in-situ laser curing system for silver-based conductive inks proved successful at curing less viscous inks [7]. Overall, the resistivity of those traces was very high, which did not allow for the creation of parts with higher power applications. Due to this, efforts were made to developed a system to place solid wire onto the printed part [8]. The wire placement technology, also called wire embedding technology, uses either thermal energy or ultrasonic energy to embed not only solid wires but also metal foil. Wire embedding has been used to create different parts including embedded RF antennas, CubeSat modules, and a microwave path antenna [9,10]. This technology was transferred into a system named Multi^{3D} system which combines multi-material FDM 3D printing, micro-machining, component placement, and wire embedding. The multi-process is enabled by the implementation of material handling robotics and a heated portable platform [11,12].

As to leverage all of the advantages of AM in a large-scale environment by the creation of complex low volume parts, many organizations have started developing large scale thermoplastic 3D printers [13,14,15]. From all the variety of printers available in the market, three printers stand put from the rest due to their build volume and material deposition rate. The systems are the Large-Scale Additive manufacturing (LSAM, Thermwood Corp., Dale, IN US) machine, Wide and high Additive manufacturing (WHAM, Ingersoll machine tools, Rockford, IL US) machine and the Big Area Additive manufacturing (BAAM, Cincinnati Inc., Harrison, OH US) machine.

The BAAM was developed by Oak Ridge National Labs (ORNL), and Cincinnati incorporated and when introduced (2015), it became the first ever large-scale material extrusion printer in the world [16]. This machine has a build volume of 6 x 2.3 x 1.8 meters (20'x 7.5' x 6') and can print up to 45 kg of thermoplastic material per hour traveling at speeds of >76 mm/s, which is about 250 times faster than other AM material extrusion system (e.g., FDM). To avoid slowing down the printing process (current embedding at 10 mm/s), a method for high deposition of wire is necessary. The objective of this research paper is to describe the mechatronic design and control implementation of a wire embedding tool into the Big Area Additive Manufacturing (BAAM) machine. The document starts with a brief description of the tool and heating method used to embed wire. The rest of the document will concentrate on machine communication and controls, G-code customization, and the overall embedding process control.

2 Mechatronic design and control implementation of wire embedder tool

2.1 Project overview and design requirements

The project "Multi-Functional BAAM: Big Area Additive Manufacturing with multi-purpose wire embedding" was granted by America Makes, one of the institutes created by the national network for manufacturing innovation, which focuses in accelerating the development of

additive manufacturing (AM). Design requirements were defined to create a tool suitable for the BAAM system. The requirements were set as follows:

1. Increase the throughput of the wire embedding technology
2. Integrate wire embedding hardware with BAAM controller
3. Mechanically integrate the wire embedding tool on the BAAM machine
4. Identify CAM software for producing 5-axis, wire embedding G-code
5. Develop a CAD/CAM post processor to prepare BAAM G-code specific to wire embedding

The increase of throughput outlined in objective one is necessary because of the high printing speed that the BAAM possesses. Also, the diameter of the wire that can be embedded needs to be increased from previous tools to accommodate for high power applications (~1 mm diameter, 14-gauge wire). The speed of wire embedding used in smaller FDM systems is about 10 mm/s, and it has to be increased to 100 mm/s. Objective 2 and 3 outlines the process of integrating the new components into the current firmware of the machine both in terms of controls and mechanics. A piece of software will have to be identified to create five-axis instructions for the machine. Finally, a G-code post processor will serve to integrate the wire embedding and printing instructions.

2.2 Mechanical Design and Arc Welding

Previous methods that were used to embed interconnects into FDM parts were based on ultrasonic energy or micro-dispensing of conductive material. Solid wire must be used to achieve low resistivity within those interconnects, which negates the use of micro-dispensing. The problem with using ultrasonic energy relies on that with the larger diameter wire and a faster speed; the process is not able to transfer energy fast enough to achieve the required temperature increase in the wire (~250 °C). The next idea was to use heated air to provide energy to the wire to increase its temperature before embedding it to the plastic. Experiments were performed, but this method was unable to provide the required energy to embed the wire. A method of heating the wire using a discharge arc was found to be successful by providing the required temperature increase with a low current consumption if compared to resistive heating (Fig. 1) [17]. The target material for the interconnects is copper (low resistivity), whose

Fig. 1: Embedded wire into a BAAM printed part

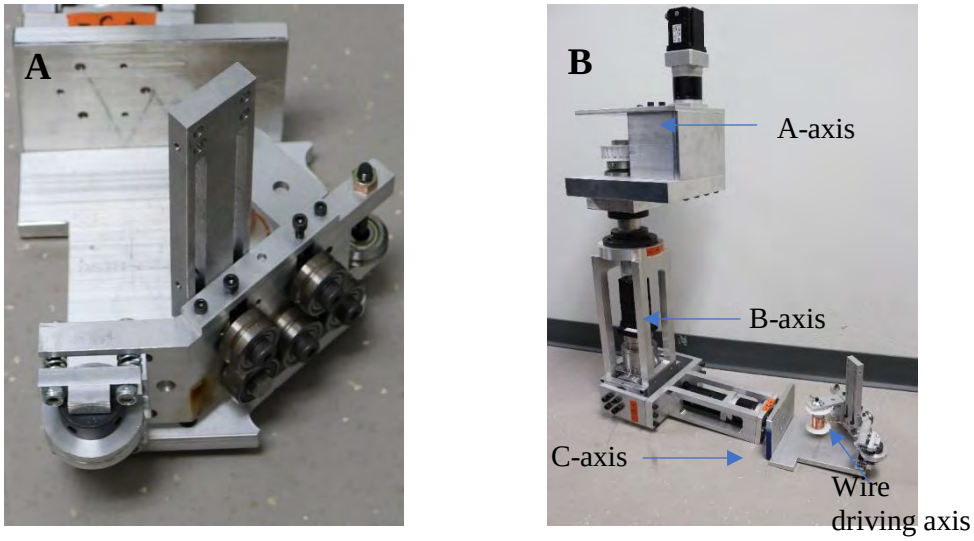

Fig. 2: Wire embedder tool (A) and tool arm (B)

resistivity value is low enough to render resistive heating ineffective for this application. The selected arc heating approach is very similar to inert tungsten gas (TIG) welding. In this process, a non-consumable electrode made of tungsten is used to create an arc towards the metal part being welded. Similarly, this process was studied and optimized to heat the wire (i.e., metal being welded) with the non-consumable electrode. Argon is used to shield the area to avoid contamination of the wire and electrode. Additionally, the gas also serves as a cooling agent for the torch. The wire arc heating system is comprised of different components including a power supply, torch (i.e., electrode), arc starter and a gas flow valve. From the control's perspective, the power supply needs to be controlled in order to adjust voltage and amperage parameters prior to and during wire embedding operations. The arc starter, used to provide the initial energy to create the arc, needs to be actuated at the beginning of every path. Finally, the gas valve open starts the controlled flow of gas toward the torch.

Up until this project, most of the efforts on wire embedding were centered on planar surfaces. For this project, the goal was to create a tool able to place the wire on multi-axis surfaces (contoured and planar). This would allow for the wire to be placed during or after the printing process in any side of a part. To achieve this, the tool needed to have three axes (A, B, C and wire driving) which complemented with the X, Y and Z of the BAAM creates a 6 degree of freedom (DOF) non-standard robotic arm. The tool has two major components, the embedding tool (Fig. 2-A) and the tool arm (Fig. 2-B). The embedding tool houses the wire driving motor, sensors, wire spool, torch and application roller. The tool arm houses the rest of the motors and an electrical panel.

2.3 Controls

Two strategies for controlling the tool and communicating with the BAAM system were devised. The first strategy was to have a separate programmable logic controller (PLC) that would control the tool axis based on commands sent by the BAAM's PLC. Using this approach would result in possible problems with synchronization and timing making the tool follow an

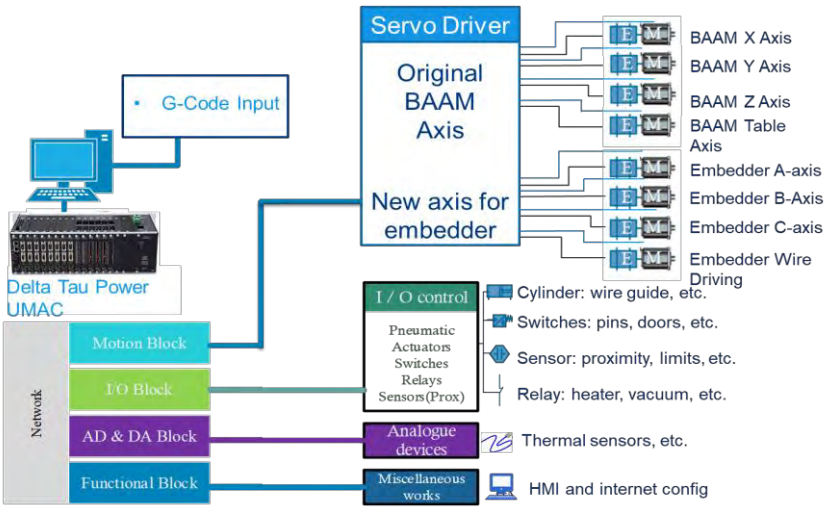

Fig. 3: Control schematic for the wire embedding tool

incorrect path. The second alternative was to integrate all the new components into the BAAM's PLC (Fig. 2). This was the chosen alternative due to the simplified integration and because Cincinnati Inc. would support this effort. The equipment selection, process development and G-code development would be managed by UTEP, while Cincinnati Inc. would modify the machine's firmware, create new electrical panel for components and perform initial testing.

The first part of the control work is to understand all the different components and their control mode (table 1). The table provides the name, function and control mode for each component.

Table 1: List of devices to be controlled

System	Device	Control
Embedder movement	Pneumatic actuator	M-code
	A-axis	G-code
	B-axis	G-code
	C-axis	G-code
Wire Driving	Wire driving axis	G-code
Arc Welding	Power Supply	M-code/code
	Arc starter	M-code
	Gas flow valve	M-code
Sensors	Before embedder pyrometer	M-code
	After embedder pyrometer	M-code
	Proximity sensor	M-code

All the devices need to be controlled using G-code, a method of controlling a gantry system based on positions for all the motors. Also, G-code can transfer information to the machine via M-codes to control the additional components (i.e. power supply). Although there are some standard M-codes across multiple platforms, many of the M-codes are created from scratch and

are custom to a specific system. For this project, many codes were created to control all the different devices mentioned before. For example, some codes are used to provide voltage and amperage information to the machine or to turn the pneumatic actuator on.

3.4 G-code

The process for the creation of multi-functional components starts by designing the circuit in Autodesk Eagle software (figure 4). The circuit is then exported from Eagle and imported into Fusion 360 using a modified and custom file developed during this project. The next step is for the user to design the component and move the components to the desired places. Then, the software is going to map the whole 2D surface where the wire needs to be placed and it will autoroute all connections. At this point, the information needs to be transferred to machine instructions for the manufacturing process to start.

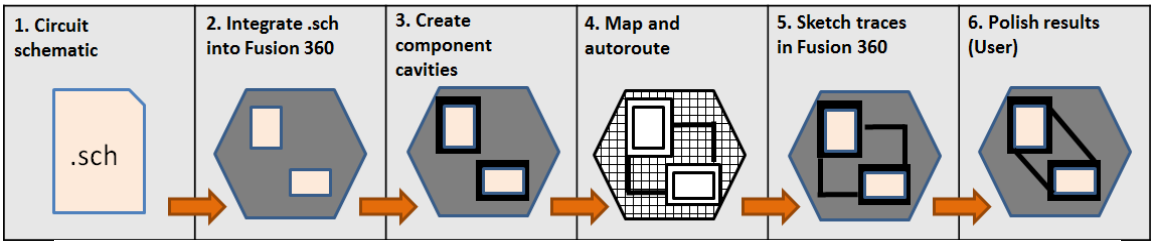

Figure 4: 3D routing software pipeline

Autodesk Fusion 360 offers a computer-aided manufacturing (CAM) environment, where the user can create instructions for computer numerical control (CNC) manufacturing. Fusion 360 supports different subtractive processes including but not limited to milling, turning and water jet cutting. The software can output information for machines with two, three, four and five axes. The CAM functionality can be modified to output machine instructions for wire placement through the use of a custom post. In a CAM software, a post adds all the specific commands needed to run a machine like the toolpaths, speeds and M-codes. A custom post was developed in partnership with Autodesk and Cincinnati Inc to obtain machine instructions for the BAAM tool.

4 Wire embedding process

As it was explained in the previous section, the wire embedding process starts by creating G-code using Fusion 360. The code is then transferred into the BAAM system, where it read by the PLC. The process continues by starting the code using the BAAM, then the tools in the BAAM offset following G-code (Fig. 5-B). Once the wire embedder is at the correct height, then the machine can move to the starting position (Fig. 5-C). Then, the arc starts heating the wire while simultaneously beginning movement (Fig. 5-D, E). Once the wire trace is completed, the tools move up to leave some wire protruding (To connect the components). Then wire stops moving while the arc heats the wire to the point that it breaks (Fig. 5-F). The final step is to push wire out of the tool and reset all controls to start another trace.

Three sensors are placed on the tool: two pyrometers, and a proximity sensor. The pyrometers record information about the temperature of the plastic and wire before and after embedding. This is relevant information from a research perspective to make sure experimentation is always consistent. Similarly, the proximity sensor is used to record the distance away from the plastic that the tool is at. Because the roller in the tool has springs, the user could place the tool at different heights causing inconsistencies with experimentation. Currently, this tool has been fully implemented in a BAAM system at Cincinnati Inc headquarters and is awaiting further testing.

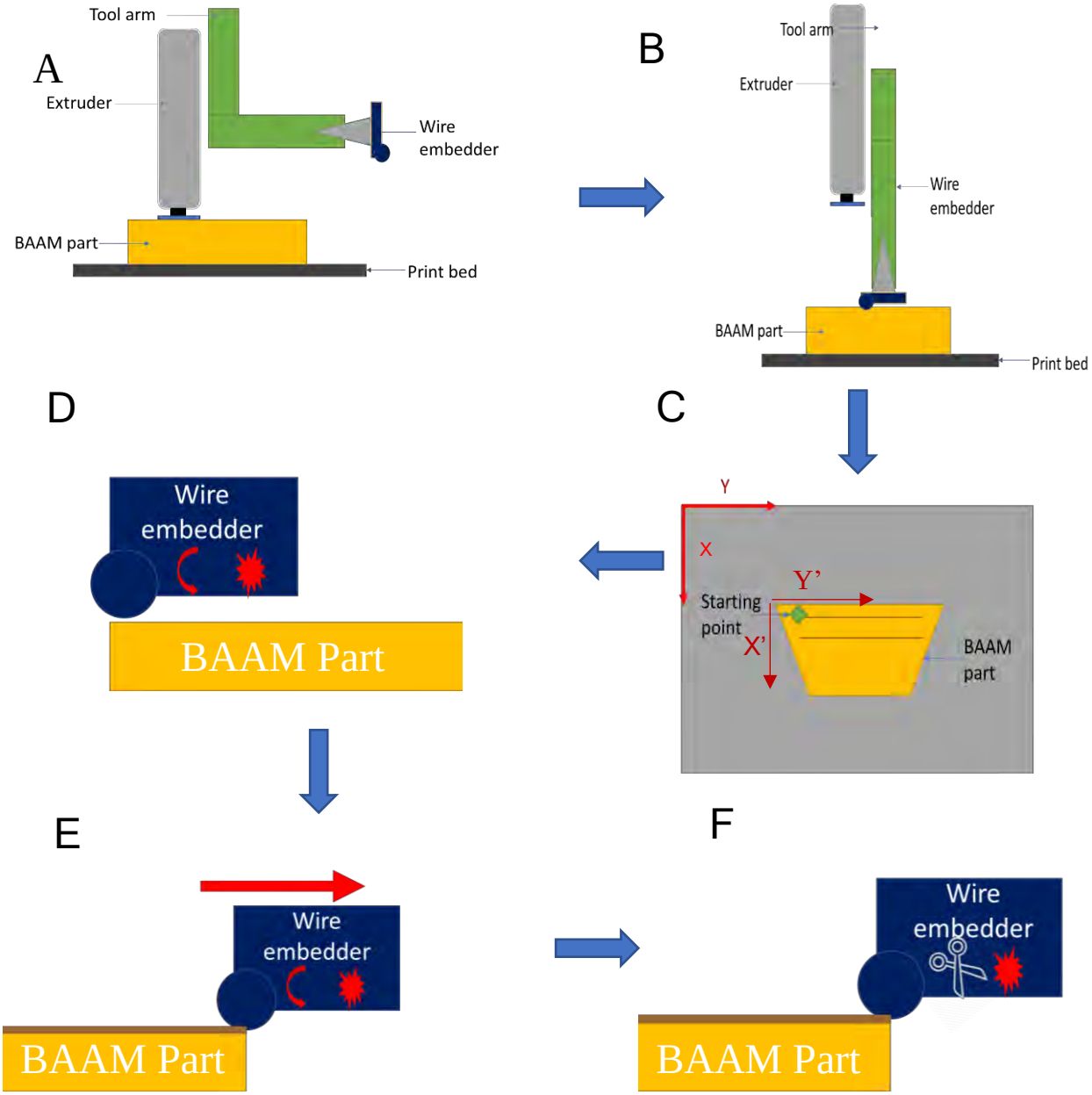

Figure 5: Wire embedding process; 1) Printing process is interrupted, 2) Offset BAAM tool (Fig. 5-B), 3) move to starting position (Fig. 5-C), 4) Start wire arc (Fig. 5-D, E), and 5) Cut wire (Fig. 5-F).

5 Conclusions

Although this work only presents a brief overview of the control mechanism for a large area 3D printing wire embedder tool, it is easy to realize the expertise necessary to perform control work is broad. Not only is a vast knowledge of PLC control required, but familiarity with the management of electrical systems and understanding of mechanical concepts is necessary to ensure a robust control system. During the development of this tool, one of the biggest challenges was to make sure the mechanical worked well in conjunction with the control system of the tool. Multiple iterations of the design were created to attain at the final version presented in this work. Understanding the mechanical requirements, such as torque and maximum loading conditions in a multi-axial environment was challenging – a task that required the collaboration between different private and public entities to arrive at the work presented here. In addition, the development of an adequate G-code presented its challenges - because there is no current method of simulating the process, the code had to be manually analyzed line by line, while visualizing the physical implications of every instruction.

6 Acknowledgment

This research was performed through the National Center for Defense Manufacturing and Machining under the America Makes Program entitled “Multi-Functional BAAM: Big Area Additive Manufacturing w/ Multi-Purpose Wire Embedding” and is based on research sponsored by Air Force Research Laboratory under agreement number FA8650-12-2-7230. The U.S. Government is authorized to reproduce and distribute reprints for Government purposes notwithstanding any copyright notation thereon. This research was conducted at The University of Texas at El Paso (UTEP) within the W.M. Keck Center for 3D Innovation (Keck Center) with support, in part, provided through the Mr. and Mrs. MacIntosh Murchison Chair I Endowment at UTEP (RBW).

References

[1] Kahn, K. B., Castellion, G., & Griffin, A. (Eds.). (2005). *The PDMA handbook of new product development*. Hoboken, NJ: Wiley.

[2] M. Navarrete et al., *"Integrated layered manufacturing of a novel wireless motion sensor system with GPS"*, Proc. Solid Freeform Fabrication Symp., pp. 575-585, 2007.

[3] R. Olivas, R. Salas, D. Muse, E. MacDonald, R. Wicker, *"Structural electronics through additive manufacturing and micro-dispensing"*, Proc. IMAPS Nat. Conf., pp. 940-946, 2010.

[4] A. J. Lopes, E. MacDonald, R. B. Wicker, *"Integrating stereolithography and direct print technologies for 3D structural electronics fabrication"*, Rapid Prototyping J., vol. 18, no. 2, pp. 129-143, 2012.

[5] D. Espalin, D. W. Muse, F. Medina, E. MacDonald, R. B. Wicker, *"3D Printing multi-functionality: Structures with electronics"*, Int. J. Adv. Manuf. Technol., Mar. 2014.

[6] R. B. Wicker, E. W. MacDonald, *"Multi-material multi-technology stereo-lithography"*, Virtual Phys. Prototyping, vol. 7, no. 3, pp. 181-194, 2012.

[7] Lopes, A. J., Lee, I. H., MacDonald, E., Quintana, R., & Wicker, R. (2014). *Laser curing of silver-based conductive inks for in situ 3D structural electronics fabrication in stereolithography*. Journal of Materials Processing Technology, 214(9), 1935-1945.

[8] Espalin, D., Muse, D. W., MacDonald, E., & Wicker, R. B. (2014). *3D Printing multifunctionality: structures with electronics*. The International Journal of Advanced Manufacturing Technology, 72(5-8), 963-978.

[9] Shemelya, C. M., Zemba, M., Liang, M., Espalin, D., Kief, C., Xin, H., ... & MacDonald, E. W. (2015, May). *3D printing multi-functionality: Embedded RF antennas and components*. In 2015 9th European Conference on Antennas and Propagation (EuCAP) (pp. 1-5). IEEE.

[10] Liang, M., Shemelya, C., MacDonald, E., Wicker, R., & Xin, H. (2015*). 3-D printed microwave patch antenna via fused deposition method and ultrasonic wire mesh embedding technique*. IEEE Antennas and Wireless Propagation Letters, 14, 1346-1349.

[11] Coronel Jr, J. L. (2015). *Multi 3D system: Advanced manufacturing through the implementation of material handling robotics*. The University of Texas at El Paso.

[12] Ambriz, S. D. (2015). *Design and development of the portable build platform and heated travel envelope for the Multi 3D manufacturing system*. The University of Texas at El Paso.

[13] Industrial 3D Printers | Advanced Additive Manufacturing Solutions. (n.d.). Retrieved from http://www.titan3drobotics.com/

[14] Large-Scale 3D Printers | BigRep GmbH Industrial Additive Manufacturing. (n.d.). Retrieved from https://bigrep.com/

[15] 25 Best Large 3D Printers of Winter 2018-19. (2019, February 09). Retrieved from https://all3dp.com/1/best-large-3d-printer-large-format-scale-3d-printers/

[16] Love, L. J., & Duty, C. (2015). Cincinnati Big Area Additive Manufacturing (BAAM). *info. ornl. gov. http://info. ornl. gov/sites/publications/files/Pub54708. pdf*.

[17] Espalin, David, *"High Feed Rate Wire Heating and Embedding for Large Area Additive Manufacturing of Parts Containing Embedded Electronic Functionality"* (2017). ETD Collection for University of Texas, El Paso. AAI10825126. https://digitalcommons.utep.edu/dissertations/AAI10825126

METAMODELING OF MINIMUM CREEP STRAIN RATE MODELS WITH TEMPERATURE DEPENDENCE

R. Vega, C. Stewart
Mechanical Engineering, The University of Texas at El Paso, TX 79968, USA;
Calvin M. Stewart cmstewart@utep.edu

Keywords*: Minimum Creep Rate, Metamodeling, MATLAB*

ABSTRACT

Creep is a mechanism that occurs in materials that are used in conditions in which stress is constantly applied at elevated temperatures. The elevated temperatures affect the materials operational life which results in a need for knowing when a part needs to be replaced in a system before it fails. There are many models that can predict this failure but one of the first steps in using these models is knowing the minimum creep strain rate (MCR). The minimum creep strain rate is present in creep prediction models as it is the base for creep mechanics, it is the slope of the secondary creep regime and is necessary for building a creep rupture curve. The MCR can be calculated with a multitude of models, and as a result, there is always an uncertainty as to which model is the best for any given material and situation. A computational tool was developed to aid in the process. The tool uses a "metamodel" and optimization processes to help find the best possible model for a set of data for a material. A metamodel is a model that is derived by combining multiple base models, in this case, 9 different models. The benefits of metamodeling are the ability to rapidly regress into any of the base component models while leaving an opportunity for automatic regression and new model discoveries. The metamodel and tool were used to find the best model for a set of data for 9Cr-1Mo-V-Nb (ASTM P91) at varying temperatures. Based on the available data, the metamodel found that the best base model was the Johnson-Henderson-Kahn model as it generated the best fits for the available data.

1 INTRODUCTION

A metamodel is generated by combining different base models through mathematical rules and setting constraints. A metamodel should be able to revert into any of its base models by changing constants that are present within it, essentially turning "on/off" different sections of the model as needed. With a metamodel, calibration of the base models becomes consistent as all the models will go through the same process which results in simpler optimizations. A metamodel can be used in a "constrained" and "pseudo-constrained" approach. The constrained approach forces the metamodel to regress into any of its base models by forcibly setting the values of constants to 0 or 1. This allows the model to change form into one of the 9 MCR models that are shown in Table. 1.

Model	Parameter Equation	Eq.
Norton (N), 1929[1]	$\dot{\varepsilon}_{\min} = A\left(\frac{\sigma}{\sigma_0}\right)^n * \exp\left(\frac{-Q_c^*}{RT}\right)$	(1)
Simplified Norton (SN), 1929[1]	$\dot{\varepsilon}_{\min} = A\sigma^n * \exp\left(\frac{-Q_c^*}{RT}\right)$	(2)
Nadai (Na), 1931[2]	$\dot{\varepsilon}_{\min} = A\exp(\frac{1}{\sigma_0} + c\sigma) * \exp\left(\frac{-Q_c^*}{RT}\right)$	(3)
Soderberg (S), 1936[3]	$\dot{\varepsilon}_{\min} = A\left\{\exp\left(\frac{\sigma}{\sigma_0}\right) - 1\right\} * \exp\left(\frac{-Q_c^*}{RT}\right)$	(4)
McVetty (M), 1943[4]	$\dot{\varepsilon}_{\min} = A\sinh\left(\frac{\sigma}{\sigma_0}\right) * \exp\left(\frac{-Q_c^*}{RT}\right)$	(5)
Dorn (D), 1955[5]	$\dot{\varepsilon}_{\min} = A\exp\left(\frac{\sigma}{\sigma_0}\right) * \exp\left(\frac{-Q_c^*}{RT}\right)$	(6)
Johnson-Henderson-Kahn (JHK), 1936 [6]	$\dot{\varepsilon}_{\min} = [A_1\left(\frac{\sigma}{\sigma_0}\right)^{n_1} + A_2\left(\frac{\sigma}{\sigma_0}\right)^{n_2}] * \exp\left(\frac{-Q_c^*}{RT}\right)$	(7)
Garofalo (G), 1965[7]	$\dot{\varepsilon}_{\min} = A\left\{\sinh\left(\frac{\sigma}{\sigma_0}\right)\right\}^n * \exp\left(\frac{-Q_c^*}{RT}\right)$	(8)
Wilshire (W), 2007[8]	$\dot{\varepsilon}_{\min} = \left[-\ln(\frac{\sigma}{\sigma_{TS}}) \Big/ k_2\right]^{\frac{1}{v}} * \exp\left(\frac{-Q_c^*}{RT}\right)$	(9)

Table 1. MCR models where σ is stress, T is temperature, R is global gas constant and $A_1, A_2, \sigma_0, n_1, n_2, c, k_2, v, Q_c^*$ are material constants

The metamodel that was derived is represented in Eq. 10.

$$\dot{\varepsilon}_{\min} = [A_1(\frac{\sigma}{\sigma_0})^{n_1} + A_2(\frac{\sigma}{\sigma_0})^{n2} + A_3\sinh(\frac{\sigma}{\sigma_0})^{n_3} + A_4\exp(\frac{a_1}{\sigma_0} + c\sigma - a_2) + a_3\{\frac{-\ln(\frac{\sigma}{\sigma_0})}{k_2}\}^{\frac{1}{v}}] * \exp(\frac{-Q}{RT}) \quad \textbf{(10)}$$

The metamodel generated combines all 9 models and has generated 3 more constants, $a_1, a_2,$ and a_3 . These constants are binary, meaning that they can only have 1 of 2 possible values at a time. If the constant is to be used, it is assigned a value of 1, whereas if a constant is not needed, it is set to 0. This metamodel was adapted from a model done in a previous study where the Nadai and Wilshire models were not included [9]. The temperature dependence was also not included in the previous study, allowing for a new optimization method to be explored in this study.

2 CALIBRATION

The inclusion of temperature dependence requires the calibration of material constant Q . This constant is known as the creep activation energy which varies from on a material basis. On a log-log scale, stress is plotted on the x-axis while $\dot{\varepsilon}_A$, a modified MCR, is plotted on the y-axis. The value of $\dot{\varepsilon}_A$ is found trough Eq.11.

$$\dot{\varepsilon}_A = \dot{\varepsilon}_{\min} / \exp(\frac{-Q}{RT}) \quad \textbf{(11)}$$

The value of the activation energy is found optimizing Q such that the points that are plotted on the graph are as close to each other as possible by maximizing the R^2 given from an exponential trendline. In Fig. 1, the best possible activation energy value that was found was that of 319kJ/mol.

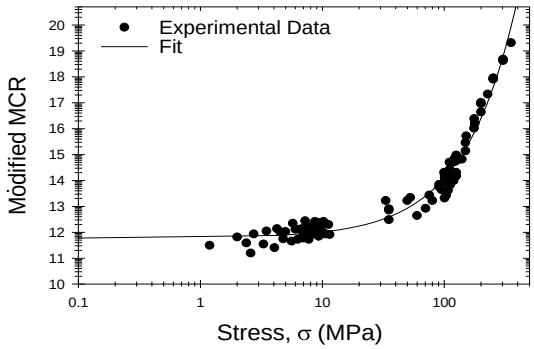

Fig. 3. Calibration for activation energy[10-16]

3 RESULTS

All the models were optimized using a MATLAB script. The MATLAB script uses the same process in the previous study, only differing in the constants that are generated as only one set of constants will be reported for the material [9]. The MATLAB code is also able to report the *NMSE* and the *RSS*, the normalized residual squared value. The model that was able to fit the data used with the smallest amount of error was the JHK model. In Fig. 2, the model fits for the JHK model are shown.

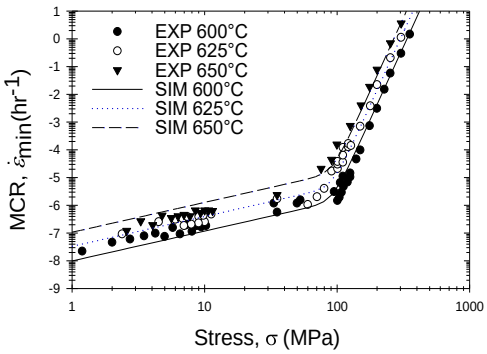

Fig. 2. JHK MCR simulated fits[10-16]

The new material constants for the JHK model were found to be drastically different from the constants without temperature dependence. The generated values differ by more than 200% than that of the previous study, demonstrating how temperature dependence affects the material constants for each model drastically.

References

[1] Norton, F. H. "*The Creep of Steel at High Temperature"*. McGraw-Hill Book Company Incorporated. New York .(1929)

[2] Nadai. Arpád, A. Wahl. "*Plasticity"*. McGraw-Hill Book Company, inc., 1931.

[3] Soderberg, C. R. (1936). "The Interpretation of Creep Tests for Machine Design". *Trans. ASME*, 58(8): 733-743.

[4] McVetty, P. G. (1943). "Creep of Metals at Elevated Temperatures-The Hyperbolic Sine Relation between Stress and Creep Rate". *Trans. ASME,* 65: 761.

[5] Dorn, J. E. (1962). "Progress in Understanding High-Temperature Creep". *H. W. Gillet Mem. Lecture*. Philadelphia: ASTM.

[6] Penny, R. K., and Marriott, D. L., 1995, "*Design for Creep"*. Springer, pp.11.

[7] Garofalo, F. (1965). "*Fundamental of Creep and Creep Rupture in Metals*". New York: Macmillan

[8] Wilshire, B., P. J. Scharning, and R. Hurst. "New methodology for long term creep data generation for power plant components." *Energy Materials* 2, no. 2 (2007): 84-88.

[9] Vega, R. and Stewart, C. "Validation of the Development and Application of Minimum Creep Strain Rate Metamodeling". *ASME Turbomachinery Conference and Exposition*, Phoenix, AZ, 2019.

[10] Gorash, Y. "Development of a creep-damage model for non-isothermal long-term strength analysis of high-temperature components operating in a wide stress range," *Martin Luther University of Halle-Winttenberg, Halle Germany*(2008).

[11] Gaffard, V., Besson, J., and Gourgues-Lorenzon, A. F., "Creep failure model of a tempered martensitic stainless steel integraiting multiple deformation and damage mechanisms," *Int. J. Fracture*, vol. 133, pp. 139 – 166, 2005.

[12] Gaffard, V., Gourgues-Lorenzon, A. F., and Besson, J., "High temperature creep flow and damage properties of the weakest area of 9Cr1Mo-NbW martensitic steel weldments," *ISIJ International*, vol. 45, no. 12, pp. 1915 – 1924, 2005.

[13] Kloc, L. and Fiala, J., "Viscous creep in metals at intermediate temperatures," *Kovov´ e Materi´aly*, vol. 43, no. 2, pp. 105 – 112, 2005.

[14] Kloc, L. and Skleniˇcka, V., "Transition from power-law to viscous creep behaviour of P-91 type heat-resistant steel," *Mater. Sci. & Eng*., vol. A234-A236, pp. 962 – 965, 1997.

[15] Kloc, L. and Skleniˇcka, V., "Confirmation of low stress creep regime in 9% Chromium steel by stress change creep experiments," *Mater. Sci. & Eng*., vol. A387A389, pp. 633 – 638, 2004.

[16] Skleniˇcka, V., Kuchaˇrov ´ A, K., Kudrman, J., Svoboda, M., and Kloc, L., "Microstructure stability and creep behaviour of advanced high chromium ferritic steels," *Kovov´e Materi´aly*, vol. 43, no. 1, pp. 20 – 33, 2005.

MODEL OF PIEZOELECTRIC SENSOR WHEN SUBJECT TO VARIOUS FLOWS

A. Castellano[1], M. Hernandez[1], D. Morales, R. Valles Martinez[1], J. Aboud, and N. Love[1]*
[1] Mechanical Engineering, Department of Energy, El Paso, TX 79968, USA;
* Corresponding Author: ndlove@utep.edu

Keywords: *Piezoceramic, air flow sensor, lead zirconate titanate*

ABSTRACT

This paper shows research gathered concerning piezoelectric materials, with an end goal using that information to create a sensor. In partnership with the Department of Energy, the goal is to create a sensor out of piezoelectric material for a turbine to be able to detect the pre-stages of surge and stall to be able to protect the turbomachinery. Surge and stall can be prevented by a feedback control that tries to provide data of high unsteady conditions and tries to indicate when cold air bypass goes through cycle configuration to avoid a turbomachinery catastrophe. It can also provoke a volume increment between the compressor and the turbine. When surge and stall occurs, airflow separates from the blades due to a sudden increase on the angle of attack. We are looking into using piezoelectric materials, PZT in particular to design a sensor capable of measuring a difference in pressure, temperature, or velocity, inside a compressor to avoid possible catastrophic failure due to surge or stall. Despite having advantageous sensitivity and monitoring features, their brittleness enables a limited use for directly impacted regions only. In a research study, flutter and active control of piezoelectric performance/actuation are analyzed. While there have been applications of PZT in turbines, an application focusing on mass flow rate has yet to be researched.

1 Literature Review

1.1 Piezoelectric Materials

Piezoelectric materials have the property of converting mechanical energy to electrical energy. This property can be utilized to relate these electrical signals to other factors, including flow velocity. This has previously been researched before is by embedding a piezoelectric structure into a cantilever beam and recording the voltage output that occurs. Next, the different resonant frequencies of the voltage outputs caused by the vibrations of the wind hitting the beam are measured. A chart can be made relating several flow velocities and the resonant frequencies that those produced. These values can be affected by the geometry of the beam, so any changes to it have to be considered.

Piezoelectric materials have high strength, an easy manufacturing process, low maintenance, and superior compactness. Piezoelectric-based ceramics include properties such as high impact sensitivity and frequency signals and detection for locating impacts and vibrations. Lead zirconate titanate, or PZT material, was chosen for this experiment because of its highly

efficient piezoelectric properties. PZT-based ceramics exhibit convenient characteristics, such as shaping flexibility and high functioning temperature.

When a piezoelectric is placed in an air flow system—whether to harvest energy or as a sensor—having laminar flow versus turbulent flow gives different readings. Because piezoelectric materials read an instantaneous measurement, when there is a laminar flow it only signals the first contact between air flow and the piezoelectric which in turn does not provide a reading over a time period. This scenario can be solved by placing a body in front of the sensor (most often a cylinder) to create vortices and therefore turbulent flow. The wind can then hit the sensor causing it to vibrate, allowing the sensor to work more efficiently.

Not only is the geometry important in the readings, but also the placement of the beam itself. [3] A correlation has been made between the placement and orientation of the beam and the output signal of the piezoelectric material. Most of the studies have been conducted using only one wind direction at a time, but the results show which orientation provides the best clarity in the voltage outputs.

2 Modeling

From the literature review, a design for a two-dimensional air flow system is presented. To measure the air flow a clear acrylic box was designed where the piezoelectric ceramics are placed. To ensure that the air flow versus voltage output correlation could accurately be defined, fans are placed at each inlet where the airspeed can be controlled. A honeycomb air filter is placed at the base of each inlet to ensure that the airflow going into the system is laminar flow. With the inlet being a laminar flow, we can manipulate the airflow hitting the piezoelectric ceramic without disrupting the entire stream. The experiment can model a small scale of the sensor then scale up to fit the turbomachines being used at the Department of Energy.

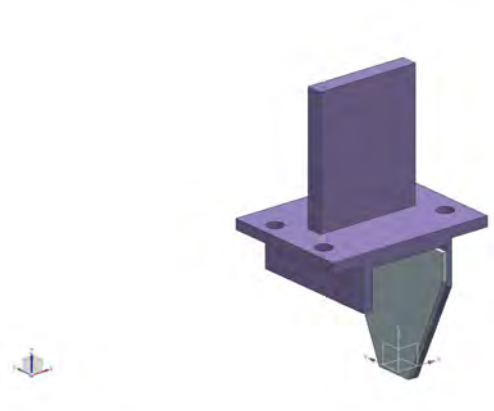

Figure 1 Drawing of piezoelectric ceramic mount with piezoelectric attached

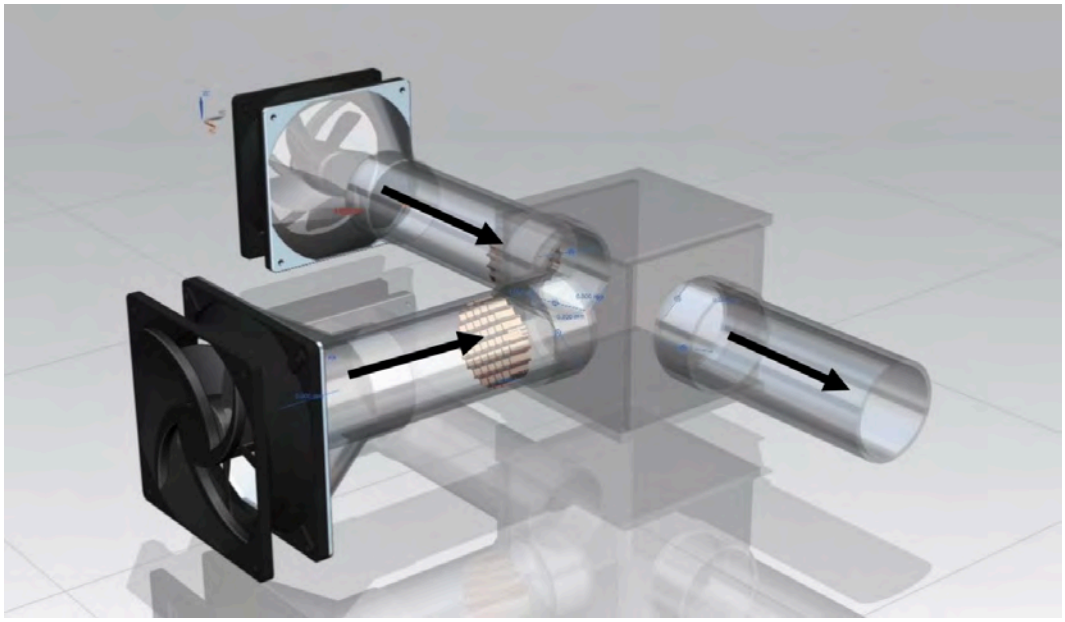

Figure 2 Drawing of experimental setup.

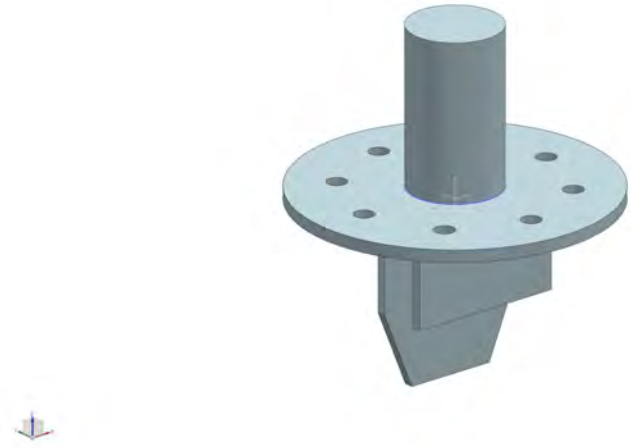

Figure 3 Piezoelectric ceramic mount for a multi-dimensional flow

3 Simulations

As stated previously, our sensor design incorporates a obstruction in front of our PZT plate to create turbulence. By bringing our designs into 2D and 3D modeling and CFD (computational fluid dynamics), testing and adjustments to our sensor prior to our prototype may be done.

3.1 Obstruction Length

One of our first tasks in simulations was to determine the dimensions of our obstruction in comparison to our PZT plate. Since the goal of the obstruction is to create turbulence in the flow hitting the PZT, the appropriate length must be determined to maximize this effect. To begin and simplify our simulations, we began with 2D one directional flow over a simplified version of our sensor. In order to get an idea of how the obstruction length will affect our results we maintain our boundary conditions and PZT geometry with only our obstruction varying in length. Through simulations we came to a decision to use a 50% proportional obstruction length to our PZT plate. Our reasoning behind this was that our 75% length was too close to the length of our PZT that we weren't getting a large pressure difference in front of and behind the PZT. In a similar fashion, the 25% length was to small that its effects were nearly negligible. In conclusion we chose to have a 50% length to maximize the pressure difference and effectiveness of the obstruction.

3.2 3D 1 Directional Flow Over v.1 Sensor

Following the research on our obstruction length 3D simulations on a more detailed model of our design are under investigation. Our geometry was designed using Ansys software. Boundary conditions for flow analysis included inlet, outlet and walls. These results will be presented during the symposium. Simulations show that the highest-pressure regions exist along the midsection of our rectangular obstruction and PZT plate with a max pressure of 3.9 kPa. In addition, we had flow disruption due to the obstruction as desired.

References

[1] *A self-resonant micro flow velocity sensor based on a resonant frequency shift by flow-induced vibration Young Ho Seo and Byeong Hee Kim Published 11 June 2010 • 2010 IOP Publishing Ltd*

[2] *Vortex shedding induced energy harvesting from piezoelectric materials in heating, ventilation and air conditioning flows L A Weinstein, M R Cacan, P M So and P K Wright*

[3] *Demir, F., & Anutgan, M. (2017). Effects of the Wind Speed and the Material Emplacement on the Output Signal of PZT Piezoelectric Energy Harvester. Acta Physica Polonica A,131(3), 362-366. doi:10.12693/aphyspola.131.362*

MODIFIED WILSHIRE MODEL FOR LONG-TERM CREEP DEFORMATION

J. A. Cano[1] and Ph.D. C. M. Stewart[1]
[1] Department of Mechanical Engineering, El Paso, TX 79968, USA;
* Jaime A. Cano (jacano2@miners.utep.edu)

Keywords: *Wilshire; alloy P91; constitutive model; creep deformation; interpolation and extrapolations*

ABSTRACT

There exists a challenge in predicting long-term (10^5 hours) creep of materials where 11 years or more of continuous testing is required to physically collect creep data. As an alternative to physical testing, constitutive models are calibrated to short-term data ($<10^4$ hours) and employed to make extrapolative predictions of long-term creep behavior. The Wilshire model has been successful in extrapolating the stress-rupture and minimum-creep-strain-rate behavior of materials. Recently, the time-to-creep-strain equation of Wilshire has been exploited to generate full creep deformation curves. The complexity of the time-to-creep-strain calibration process and nonlinearity of the equation make the resulting creep deformation predictions difficult to obtain and of questionable reliability. In this study, a modified Wilshire model for creep deformation is developed. A database of alloy 91 data is gathered and calibrated to the new model. The modified Wilshire model is shown to maintain the accuracy of stress-rupture and minimum-creep-strain-rate predictions while simultaneous offering easy-to-obtain highly-accurate predictions of long-term creep deformation.

1 Introduction

1.1 Wilshire Model

The Wilshire model was developed by Wilshire and Battenbough in the University of Wales Swansea. Wilshire determine that previous models such as Norton-power law and Monkman-Grant equations have limitations predicting creep behaviors [1-3]. Wilshire proposed alternative rupture time, t_f and minimum-creep-strain-rate, $\dot{\varepsilon}_{\min}$ laws as follows

$$\frac{\sigma}{\sigma_{TS}} = \exp\left(-k_1 \left[t_f \exp\left(-\frac{Q_c^*}{RT} \right) \right]^u \right) \quad (1)$$

$$\frac{\sigma}{\sigma_{TS}} = \exp\left(-k_2 \left[\dot{\varepsilon}_{\min} \exp\left(\frac{Q_c^*}{RT} \right) \right]^v \right) \quad (2)$$

where k_1 (in hr^{-u}) , u , k_2 (in $\left(hr^{-1}\right)^{-v}$), and v are material constants. The $\dot{\varepsilon}_{\min}$ and t_f predictions take the same functional form and are distinguished by different coefficients (k_1, k_2) and exponents (u, v) [4-5]. The Wilshire law has been successful in extrapolating multi-batch short-term stress-rupture data out to 100,000 hours, as well as creep resistance in

material's development stage, and the analytical process is accurate for different material forms [1-3, 6-9].

1.2 Novel Model

Wilshire introduced a third equation for predicting the time-to-creep-strain, t_ε as follows

$$\frac{\sigma}{\sigma_{TS}} = \exp\left(-k_3 \left[t_\varepsilon \exp\left(-\frac{Q_c^*}{RT} \right) \right]^w \right) \tag{3}$$

where k_3 and w are material constants at a constant creep strain, e[2-3, 6-7]. Abdallah and colleagues applied the calibration approach to model full creep deformation curves in the following manner [7]

$$k_3 = f_1(\varepsilon) \tag{4}$$

$$w = f_2(\varepsilon) \tag{5}$$

were regression analysis is performed and material constants k_3 and w are functionalized with respect to strain. Introducing [Eq. (4)-(5)] into [Eq. (3)] creates the following nonlinear function

$$\frac{\sigma}{\sigma_{TS}} = \exp\left(-f_1(\varepsilon) \left[t_\varepsilon \exp\left(-\frac{Q_c^*}{RT} \right) \right]^{f_2(\varepsilon)} \right) \tag{6}$$

where the time-to-creep-strain, t_ε and the creep strain, ε exist together. This equation depends on the creation of a strain vector, depending on the desire stress and temperature, were the time vector, t_ε is later calculated and then the creep deformation curve is created. There is a great uncertanties on how to calculate the k_3 and w and compared to first Wilshire models [Eq. (1)-(2)], these third equation does not have a clear analytical approach.

To create the novel Wilshire equation the framework from the Sin-Hyperbolic (Sinh) is considered [10-11]. The equation is based on continuum damage and has rupture time, t_f and minimum-creep-strain-rate, $\dot{\varepsilon}_{\min}$ dependance. The equations are as follow

$$\dot{\varepsilon}_{cr} = A \sinh\left(\frac{\sigma}{\sigma_s} \right) \exp\left(\lambda \omega^{3/2} \right) \tag{7}$$

$$\dot{\varepsilon}_{\min} = A \sinh\left(\frac{\sigma}{\sigma_s} \right) \tag{8}$$

$$\dot{\omega} = \frac{M\left[1 - \exp(-\phi) \right]}{\phi} \sinh\left(\frac{\sigma}{\sigma_t} \right)^\chi \exp\left(\phi \omega \right) \tag{9}$$

$$t_f = \left[M \sinh\left(\frac{\sigma}{\sigma_t} \right)^{\chi} \right]^{-1} \tag{10}$$

were constants are determined using numerical optimization.

2 Results and Discussion

2.1 Modified Model

To obtained the modified Wilshire model, consider [Eq. (1) and (2)] and isolate t_f and $\dot{\varepsilon}_{\min}$ resulting in the following equations

$$t_f = \frac{\left[-\ln\left(\frac{\sigma}{\sigma_{TS}} \right) \Big/ k_1 \right]^{\frac{1}{u}}}{\exp\left(-\frac{Q_c^*}{RT} \right)} \tag{11}$$

$$\dot{\varepsilon}_{\min} = \frac{\left[-\ln\left(\frac{\sigma}{\sigma_{TS}} \right) \Big/ k_2 \right]^{\frac{1}{v}}}{\exp\left(Q_c^* / RT \right)} \tag{12}$$

which are then apply to the existing Sinh framework. Substituting [Eq. (10)] for [Eq. (11)] and then plugin to [Eq. (9)] gives the damage model that is then plug into [Eq. (7)]. Similarly, [Eq. (8)] for [Eq. (12)] and then plug it into equation [Eq. (7)] leads to the new modified model. The modified model is given in the following form

$$\dot{\varepsilon}_{cr} = \dot{\varepsilon}_{\min} \exp\left(\lambda \omega^{3/2} \right) \tag{13}$$

were the remaining variables to solve are λ which is solve using the minimum-creep-rate and the final rate and ϕ which is solve using numerical optimization.

Constants Q_c^*, k_1, u, k_2, and u are obtained from previous studies considering the plate form [9]. Contants λ and ϕ are describe in Table 1 at a single temperature 600 $^\circ C$ and stresses 100, 110, 120, 140, 160 and 200 MPa.

Stress, MPa	100	110	120	140	160	200
λ	5.51	5.52	5.00	4.00	3.84	3.57
ϕ	3.60	7.10	7.50	3.80	4.20	3.70

Table 1. Material constants λ and ϕ for constant temperature 600 $^\circ C$ at various loads.

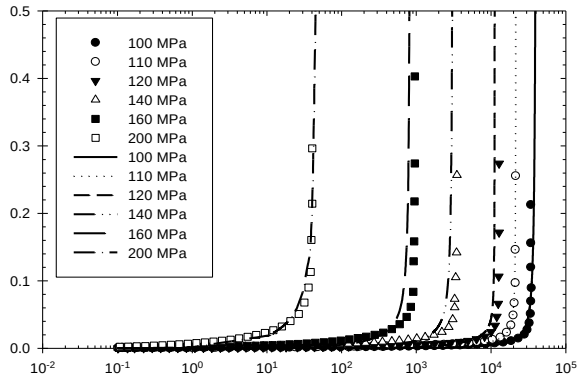

Fig. 1. Modified Wilshire model for a single temperature 600 $°C$ at 100, 110, 120, 140, 160, and 200 MPa for Strain, ε vs Time, hr .

The modified Wilshire [Eq. (13)] is plug using the material constants and is shown in Fig. 1 for the different loadings. As shown, the current model the ductility and the secondary and tertiary creep regimes. Using the Normalize-Mean-Square-Error (NMSE) the current error for the model is 6.51, 0.13, 4.54, 88.15, 1.29, and 0.01 for stresses of 100, 110, 120, 140, 160 and 200 respectively.

3 Conclusion

The modified model has proven to fit the long-term creep curve using the conventional Wilshire approach and the Sinh framework. The error given gives reliability for the prediction model. Future work is to implement a method to find λ and ϕ analytically as well.

References

[1] Wilshire, B., & Scharning, P. J. (2007). Long-term creep life prediction for a high chromium steel. Scripta Materialia, 56(8), 701-704.
[2] Wilshire, B., & Scharning, P. J. (2008). A new methodology for analysis of creep and creep fracture data for 9–12% chromium steels. International materials reviews, 53(2), 91-104.
[3] Wilshire, B., & Scharning, P. J. (2008). Prediction of long-term creep data for forged 1Cr–1Mo–0· 25V steel. Materials science and technology, 24(1), 1-9.
[4] Burt, H. & Wilshire, B. Metall and Mat Trans A (2006)37:1005. https://doi.org/10.1007/s11 661-006-0073-3
[5] Wilshire, B., & Battenbough, A. J. (2007). Creep and creep fracture of polycrystalline copper. Materials science and engineering: a, 443(1-2), 156-166.
[6] Wilshire, B., Scharning, P. J., & Hurst, R. (2007). New methodology for long term creep data generation for power plant components. Energy Materials, 2(2), 84-88.
[7] Abdallah, Z., Perkins, K., & Williams, S. (2012). Advances in the Wilshire extrapolation technique—Full creep curve representation for the aerospace alloy Titanium 834. Materials Science and Engineering:176-182.
[8] Whittaker, M. T., Evans, M., & Wilshire, B. (2012). Long-term creep data prediction for type 316H stainless steel. Materials Science and Engineering: A, 552, 145-150.
[9] Cano, J.A, Stewart, C.M (2019). Application of the Wilshire Stress-Rupture and Minimum-Creep-Strain-Rate Prediction Models for Alloy P91 in Tube, Plate, and Pipe Form. ASME Turbo Expo: Turbomachinery Technical Conference and Exposition
[10] Haque, M. S., and Stewart, C. M., 2016, “Finite Element Analysis of Waspaloy Using Sinh Creep-Damage Constitutive Model under Triaxial Stress State,” ASME Journal of Pressure Vessel Technology, 138(3). doi: 10.1115/1.4032704
[11] Haque, M. S., and Stewart, C. M., 2016, “Modeling the Creep Deformation, Damage, and Rupture of Hastelloy X using MPC Omega, Theta, and Sin-Hyperbolic Models,” ASME PVP 2016, PVP2016-63029, Vancouver, BC, Canada, July 17-21, 2016

MULTIFUNCTIONAL SENSING USING 3D PRINTED NANOCOMPOSITES

H. Kim[1], B. R. Wilburn[1]*, E. Castro[2],
C. A. G. Rosales[3], L. A. Chavez[1], T. B. Tseng[4] and Y. Lin[1]
[1]Department of Mechanical Engineering, University of Texas at El Paso, El Paso, TX 79968, USA;
[2]Department of Chemistry, University of Texas at El Paso, El Paso, TX 79968, USA;
[3]Department of Electrical and Computer Engineering, University of Texas at El Paso, El Paso, TX, 79968, USA;
[4]Department of Industrial, Manufacturing, and Systems Engineering, University of Texas at El Paso, El Paso, TX 79968, USA
* Corresponding author (brwilburn@miners.utep.edu)

ABSTRACT

This research studied multifunctional sensing capabilities on nanocomposites composed of poly(vinylidene) fluoride (PVDF), BaTiO3 (BT), and multiwall carbon nanotubes (CNTs) fabricated by fused-deposition modeling 3D printing. To improve the dielectric property within BT/PVDF composites, CNTs have been utilized to promote ultrahigh polarization density and local micro-capacitor among BT and polymer matrix. The 3D printing process provides homogeneous dispersion of nanoparticles, alleviating agglomeration of nanoparticles, and reducing micro-crack/voids in matrix which can enhance their dielectric property. In this research, we demonstrated that by utilizing unique advantages of this material combination and a 3D printing technique, sensing capabilities for temperature and strain can be engineered with different content variations of included BT and CNTs. It is observed that the sensing capability for temperature change with respect to a 25–150C range can be improved as both BT and CNTs' inclusions increase and is maximal with 1.7wt.% CNTs/60wt.%BT/PVDF nanocomposites, while the sensing capability for strain change in a 0–20% range is maximal with 1wt.%CNTs/12wt.%BT/PVDF nanocomposites. In addition, it is found that the best combination for mechanical toughness is 1wt.%CNTs/12wt.% BT/PVDF with 24.2 MPa and 579% in ultimate tensile strength and failure strain, respectively. These results show the technique to 3D print multifunctional nanocomposites with temperature and strain sensing capabilities as well as increased mechanical property. Furthermore, this research demonstrated the feasibility for large-scale multifunctional sensor device manufacturing with freedom of design, low-cost, and an accelerated process.

1 Introduction

Polyvinylidene fluoride (PVDF) and BaTiO3 (BT) are well-known smart materials used as piezo-/di-electric devices for sensor and energy storage due to their unique characteristics.[1–3] In order to improve the piezo-/di-electric performance as well as tensile strength, the introduction of organic fillers such as carbon fiber, carbon nanotubes (CNTs), and carbon black have been extensively investigated by incorporating them in polymer composites.[4–8] Researchers investigated other areas of CNT-based strain sensors using their piezo-capacitive and resistive effects on highly stretchable elastomer substrate or in a polymer matrix for robotics, structural health monitoring, human skin, interactive electronics, smart clothing, and

strain gauge.[9–14] Strain sensing of polymer CNTs nanocomposites is based on the electrical property changes induced by external stresses, concepts of the destruction of the CNTs' conductive networks, and alternation of resistance changes due to variation of the distance between CNTs.[11] These CNTs were used to act as stretchable electrodes or to mix with polymer materials tested within limited lower strain parameters. Recently, it is proved that processes of filament extrusion and fused-deposition modeling (FDM) 3D printing provide homogeneous dispersion of BT and possibly other additives in PVDF as well as alleviating agglomerates and removing voids and cracks.[15] The 3D printed piezo-/di-electric nanocomposites using FDM 3D printing technique was studied to improve both their electrical and mechanical performances by integrating polymer with piezo-/di-electric ceramics. By utilizing the characteristics of CNTs and BT nanoparticles in a PVDF matrix and unique property of FDM 3D printing technique, [16-18] other sensing capabilities can be explored in strain and temperature changes based on capacitance change in the distance variation of CNTs' networks under strain change and in phase transformation of BT ceramics with local micro-capacitor of CNT electrodes under temperature change.

2 Experimental Setup

For the fabrication of filaments that harness a continuous CNTs/BT/PVDF nanocomposite needed for 3D printing, the following materials were used: PVDF powder, BT powder, multi-wall carbon nanotubes (CNTs) powder, and N-Dimethylformamide solvent (DMF). With respect to varying BT nanoparticle sizes, BT powder with 700 nm nanoparticle size withholds its maximum capacitance at 1 kHz in greater loading systems.[19] Supplementary material and was used to mix CNTs/BT/PVDF uniformly. For this uniformly dispersed mixture of BT and CNTs in DMF solvent, the materials were sonicated for 30 min and had a 1:10 weight ratio of PVDF powder. The addition of PVDF powder was inputted after the sonication and the total mixture was placed in a water bath for 10–15 min, or until the PVDF powder visibly dissolved at 80°C. Ultra-sonication was applied to the solution for 15 min that allowed BT and CNTs clusters to be alleviated. Lastly, the nanocomposite solution was treated by evaporating DMF solvent once poured out into a glass substrate and placed to be heated on a hot plate for 12 h at 80°C. Dried solvent casted nanocomposites were heated up at 205°C and 230°C for filament extrusion and 3D printing process, respectively.

3 Results and Conclusion

It was found that the capacitance property of the 3D printed nanocomposites can be utilized in sensing the changes of temperature and strain. The highest sensibility for temperature is observed in nanocomposites containing 1.7wt.%CNTs/60wt.%BT/PVDF which are the maximum loading for BT and CNTs percolation threshold. The highest sensibility for strain is observed in nanocomposites containing 1wt.%CNTs/12wt.%BT/PVDF. The nanocomposites above 1wt.%CNTs resulted in the degradation of the changing rate in the capacitance. This degradation was because the CNT cluster effectively destructs capacitance as the strain is induced. It is observed that the addition of more than 12wt.% of BT particles degrades the changing rate in the capacitance because Poisson's ratio becomes lower as the BT content increases at a higher loading system. The combination between CNTs and BT inclusions contributes to a high changing rate in the capacitance when it comes to the temperature and strain changes. The superior mechanical performance is observed in

nanocomposites containing 1wt.%CNTs/12wt.%BT/PVDF showing 24.2MPa and 579% for mechanical stress and strain, respectively. These improved mechanical properties stem from CNTs and BT reinforcements. However, ultimate tensile strength starts decreasing after 1 wt.%CNTs and 12wt.%BT and failure strain after 1wt.%CNTs and 40wt.%BT. This study demonstrated the feasibility of massive production for multifunctional sensing device manufacturing with freedom of design, low cost, and an accelerated process.

References

[1] Sebastian, Mailadil T., and Heli Jantunen. "Polymer–ceramic composites of 0–3 connectivity for circuits in electronics: a review." *International Journal of Applied Ceramic Technology*7, no. 4 (2010): 415-434.

[2] Salimi, A., and A. A. Yousefi. "Conformational changes and phase transformation mechanisms in PVDF solution-cast films." *Journal of Polymer Science Part B: Polymer Physics*42, no. 18 (2004): 3487-3495.

[3] Xu, Wenwen, Haokai Yang, Wei Zeng, Todd Houghton, Xu Wang, Raghavendra Murthy, Hoejin Kim et al. "Food-Based Edible and Nutritive Electronics." *Advanced Materials Technologies* 2, no. 11 (2017): 1700181.

[4] Park, Kwi-Il, Minbaek Lee, Ying Liu, San Moon, Geon-Tae Hwang, Guang Zhu, Ji Eun Kim et al. "Flexible nanocomposite generator made of BaTiO3 nanoparticles and graphitic carbons." *Advanced Materials* 24, no. 22 (2012): 2999-3004.

[5] Dang, Zhi-Min, et al. "Tailored dielectric properties based on microstructure change in BaTiO3-carbon nanotube/polyvinylidene fluoride three-phase nanocomposites." *The Journal of Physical Chemistry C* 114.31 (2010): 13204-13209.

[6] Jin, Youngho, Ning Xia, and Rosario A. Gerhardt. "Enhanced dielectric properties of polymer matrix composites with BaTiO 3 and MWCNT hybrid fillers using simple phase separation." *Nano Energy* 30 (2016): 407-416.

[7] Kim, Hoejin, et al. "Synthesis and characterization of CeO 2 nanoparticles on porous carbon for Li-ion battery." *MRS Advances* 2.54 (2017): 3299-3307.

[8] Kim, Hoejin, et al. "Porous Carbon/CeO 2 Nanoparticles Hybrid Material for High-Capacity Super-Capacitors." *MRS Advances* 2.46 (2017): 2471-2480.

[9] Cai, Le, Li Song, Pingshan Luan, Qiang Zhang, Nan Zhang, Qingqing Gao, Duan Zhao et al. "Super-stretchable, transparent carbon nanotube-based capacitive strain sensors for human motion detection." *Scientific reports* 3 (2013): 3048.

[10] Cohen, Daniel J., et al. "A highly elastic, capacitive strain gauge based on percolating nanotube networks." *Nano letters*12.4 (2012): 1821-1825.

[11] Georgousis, G., et al. "Strain sensing in polymer/carbon nanotube composites by electrical resistance measurement." *Composites Part B: Engineering* 68 (2015): 162-169.

[12] Dharap, Prasad, et al. "Nanotube film based on single-wall carbon nanotubes for strain sensing." *Nanotechnology* 15.3 (2004): 379.

[13] Yamada, Takeo, et al. "A stretchable carbon nanotube strain sensor for human-motion detection." *Nature nanotechnology*6.5 (2011): 296.

[14] Kang, Inpil, et al. "A carbon nanotube strain sensor for structural health monitoring." *Smart materials and structures*15.3 (2006): 737.

[15] Kim, Hoejin, et al. "Fabrication and characterization of 3D printed BaTiO3/PVDF nanocomposites." *Journal of Composite Materials* 52.2 (2018): 197-206.

[16] Kim, Hoejin, et al. "Integrated 3D printing and corona poling process of PVDF piezoelectric films for pressure sensor application." *Smart Materials and Structures* 26.8 (2017): 085027.

[17] Kim, Hoejin, et al. "3D printing of BaTiO3/PVDF composites with electric in situ poling for pressure sensor applications." *Macromolecular Materials and Engineering* 302.11 (2017): 1700229.

[18] Kim, Hoejin, et al. "Increased piezoelectric response in functional nanocomposites through multiwall carbon nanotube interface and fused-deposition modeling three-dimensional printing." *MRS Communications* 7.4 (2017): 960-966.

[19] Dang, Zhi-Min, Sheng-Hong Yao, and Hai-Ping Xu. "Effect of tensile strain on morphology and dielectric property in nanotube/polymer nanocomposites." *Applied Physics Letters*90.1 (2007): 012907.

N-type Silicon Solar Cells Doped with Boron and Phosphorus

Clara Camarillo[1], Cesar Valenzuela[1], Juan Jaramillo[1], and Christopher Serrano[2]

[1]Electrical and Computer Engineering, The University of Texas at El Paso, El Paso, TX 79968, USA
[2]Mechanical Engineering, The University of Texas at El Paso, El Paso, TX 79968, USA

***Abstract*-Photovoltaic cells are an important device to produce electricity by direct sunlight. The most common cells that are produced are p-type cells, due to their stability and efficiency. They are usually doped with boron and use thermal SiO_2 and SiN_x to passivate the n+ emitters[1]. P-type cells are, however, flawed. There is a direct correlation between their efficiency and their susceptibility to degradation due to light exposure. Alternatively, to p-type cells there are n-type cells that do not possess the same disadvantage of efficiency and light induced degradation. The draw back from n-type cells are the unstable forms of passivating the p+ emitters. Through our research we attempted to produce an n-type device that is both, stable and efficient. To do so we used n-type silicon and tried different methods of doping along with a various materials for the contacts on both the fingers and back side.**

***Index Terms*—Anneal, contacts, doping, n-type solar cells.**

I. Introduction

THE MAJORITY of solar cells produced are p-type silicon solar cells. They are the most common cells because of their high efficiency and well-known ability to passivate the n+ emitters. The most common way to passivate the n+ emitter is by using a thermal SiO_2 and/or SiN_x [1]. The downfall of these p-type solar cells is that it is susceptible to light-induced degradation. This issue is magnified as the efficiency of the cell increases, as there is a direct correlation between the efficiency of the cell and their vulnerability to light-induced degradation.

As an alternative, n-type solar cells may be the solution for avoiding the problems associated with light-induced degradation and its correlation to deficiency. N-type silicon solar cells are not commonly used because passivating the p+ emitters has proven to be more difficult than the previously mentioned cells. There have been attempts to use a similar method, as seen in p-type cells; to passivate the p+ emitters such as thermal SiO_2 and/or SiN_x. The results of this have shown the p+ emitters to be unstable and therefore, less desirable.

In this particular study we are attempting to create solar devices using n-type silicon wafers. We use boron to dope the silicon wafer and make various attempts to create a device that is efficient at producing voltage and current. Our study was conducted in a manner that followed a previous experiment that produced a n-type silicon solar cell with 20% efficiency. Through their study they were able to conclude that texturizing both sides and firing the device, they were able to create cells that had a low current density which would allow for voltage detection.

II. Experimental Procedure

The solar cells that were created, started off as a silicon wafer that was cut into 4-cm^2 squares. The first step of the experiment was to create an etching on the surface of the silicon squares. Using a 5% hydrofluoric acid, we dipped each sample in the acid for 10 seconds, proceeded to rinse the sample using de-ionized water, and drying each sample using nitrogen gas. The second step was to create a textured surface that would create pyramid-like structures on the surface of the silicon; which can be seen in figure 1. These structures are useful in trapping light by keeping it in the valley of the pyramids [3]. This step was accomplished by using a 2% potassium hydroxide solution. We then placed the silicon squares in the 2% KOH bath and agitated them for thirty minutes. Then after agitation, they rested in the solution for ten minutes before being rinsed and dried. These first two steps were the same throughout the different experiments. After this step there were variations on the steps that follow.

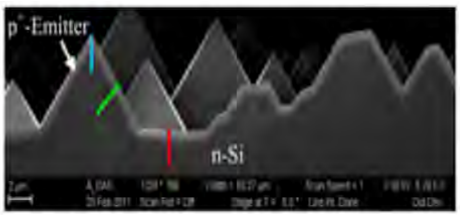

Fig. 1. SEM image of p+ emitter on a textured surface [1].

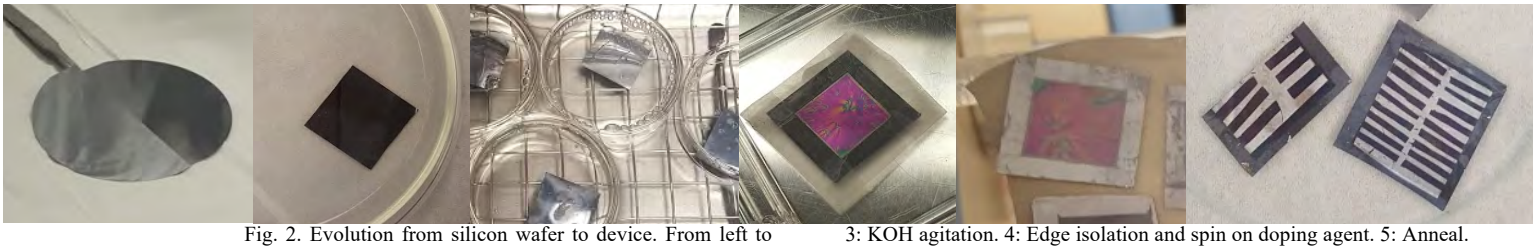

Fig. 2. Evolution from silicon wafer to device. From left to right. 1: silicon wafer. 2: Cut in 4 cm^2 squares. 3: KOH agitation. 4: Edge isolation and spin on doping agent. 5: Anneal. 6: Fingers and contacts.

In step three we did an edge-isolation on the silicon cell and doped the wafer. For the first round, we only doped the front side of the device with boron. For the second round, we doped both the front and back side of the device. The front side was doped with boron and the backside was doped with phosphorus. This process of doping the silicon wafer was done through spinning the doping agent at a speed of 3k rpm for 10 seconds. After drying for one minute on a hot plate at 100°C, it was annealed at 950°C for 10 minutes. In step four, we did another etching by dipping each device in a Buffered-Oxide-Etching (BOE) solution for 10 seconds the first time and for three seconds the second time around.

In step five we added aluminum contacts to both sides of the device. For the front side we applied the aluminum using a toothpick and we applied a small layer on the backside; this method was used for the first round. In the following attempts, we used a physical vapor deposition system to make the contacts more uniform, even, and neat. The idea was that we would be making a device that was more precise and allowed for a higher voltage, current, and overall efficiency. In later trials, there were various anneals added to the process in the making of these devices. The first anneal added was 250°C for 30 minutes, then 400°C for twenty minutes, and lastly 750°C for one minute. The process of the steps can be seen in figure 2 from intrinsic wafer to a solar device.

A. Challenges

Through these experiments, we found that doping both sides of the devices with both boron and phosphorus there was a greater amount of current collected. We also used several types of tape that had a weaker adhesive. This weaker adhesive allowed us to handle the silicon wafer with more care and less breakage. Breaking the devices was one of the biggest disadvantages we had as a group. The wafers are very thin and fragile; the only solution was to proceed with the utmost care and diligence. We also experienced some quality loss due to the phosphorous we were using. It was expired and had a gel-like consistency that did not allow for proper spin-on application. This was considered problematic during the first anneal, when the devices were fired at 950°C for ten minutes. It was at this stage that the devices visibly displayed noticeable loss to the phosphorus dopant. This will be corrected in future experiments, as the phosphorus' proper physical state and potency should resolve these issues.

Another challenge that persisted throughout the study was the application of the contacts. This problem applied to both the fingers and the back contacts. We started the experiment using aluminum for both sides and then switched to using aluminum for the back contact and silver for the front contacts. We also switched the method of applying the contacts from manual application to using the physical vapor-deposition system. This system used a series of programs to turn the aluminum and silver materials from solid form to gas form. The program then dispositioned the vapor on the devices making the contacts an even layer and a specific thickness. We attempted to use tape as a form of "pattern making" for the front contacts. Frustratingly, this proved to be challenging because we could not make the fingers small enough and we often damaged the device in the process of removing the tape. We then moved onto using a mask that would prevent the damage due to the tape. However, this also had its own set of challenges, which forced us to use a mask that would prevent the

Fig. 3. On the left we can see the manual mask made of tape and the damage that was caused. On the right we can see the mask method after an application.

damage caused by tape. Again, this method presented some

difficulties because the mask did not always lay flush. Additionally, the fingers and bus bar just became an indistinguishable marriage of metal. The different methods we attempted can be seen in figure 3. We later discovered that the fingers and bus bar needed to be very thin and tall so that we could achieve the desired currents and voltages. After sorting the issues with the contact dimensions, we noticed that with additional anneals and heating cycles of varying degrees, we could passivate the p+ emitter. This result was desired because it would produce a current density low enough to produce a voltage.

II. Results

Results were obtained by using the QEXL Solar Cell Quantum Efficiency Measurement System. Samples must have their area measured before placing it on the machine. Once the area is calculated, the sample can now be placed on top of a copper strip and place one of the contacts on top of the silver or aluminum finger/bus bar. The computer will use a I-V characteristics graph. After naming the file and selecting a save folder, the measurement is done. On the right side of the screen, the program will show important information such as open circuit voltage, short circuit current, current density, shunt resistance, fill factor and finally the efficiency of the sample. Below are the results of the samples along with a description of the different steps taken on each result. Only the best result will be shown for same batches of silicon samples.

First batch consisted of the steps described on the fabrication process. Nothing was changed on the step procedure. On this n-type sample had an efficiency of 0.05%, V_{OC} of 0.255, and I_{SC} of 1.27 mA as seen in Fig. [4].

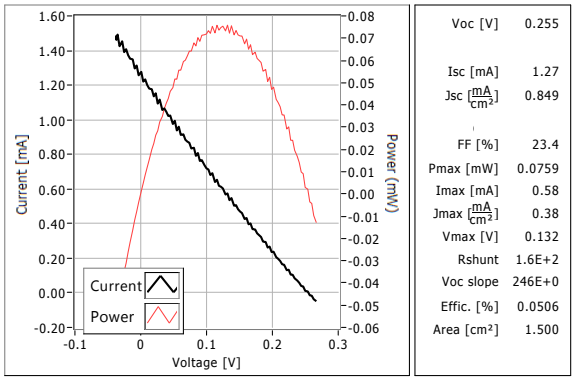

Fig. 4: First batch results.

For the second batch, the same procedure was followed. However, the back side of the sample n-type doping, phosphorous jelly, was applied to see if it can increase the sample performance. And the PVD machine was used to do both back and front side contacts. On this n-type sample had an efficiency of 0.001%, V_{OC} of 0.308, and I_{SC} of 0.0109 mA, Fig. [5, 6].

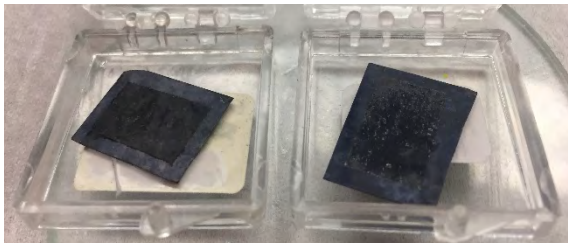

Fig. 5: Solar cells after initial anneal, prior to contacts.

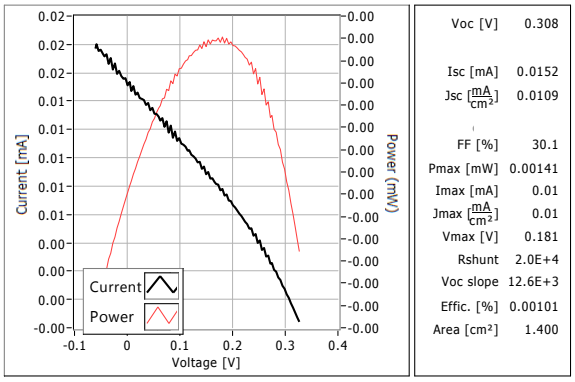

Fig. 6: Second batch results.

Annealing the sample at 250ºC for 30 minutes on a hot plate after measurement proved to increase their performance by a little bit (Picture below). The sample had an efficiency of 0.009%, V_{OC} of 0.399, and I_{SC} of 0.161 mA, Fig. [7].

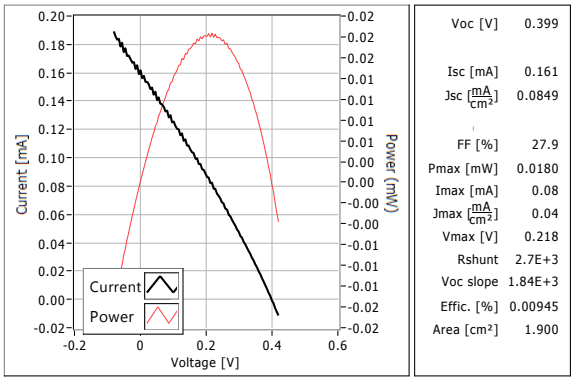

Fig. 7: Final results after second anneal.

III. Conclusion

Solar power is a clean way of harvesting energy, it can be considered an untapped source of everlasting energy. We all use electricity in our everyday lives whether it is for powering up our laptops, cell phones, or even our vehicles. Solar cells convert light into energy and with our unlimited need for energy there is demand for more efficient solar cells. These n-type cells are important because they are less susceptible to light degradation, will therefore last longer than p-type cells, and will in turn be more cost effective.

While making these n-type silicon solar cells we came across many issues. Some that had an obvious solution and others that were more difficult to figure out. We quickly noticed the trend from doping one side to doping both sides. When we doped both sides we were able to get an overall more efficient device. Along with the n-type silicon solar cells, we were able to make some cells that were produced from a p-type silicon. Without, many trials we came up with great results the first time around, the results can be seen in Table II and can be compared to the results in Table I, that have the values of the n-type silicon.

IV. Discussion

The solar cells produced would make a great impact on the cells that are in the market already. N-type solar cells would be more beneficial because they would last longer and would in turn be more cost efficient. Successfully making n-type silicon solar cells is important in the harvest of solar energy to be more affordable and more efficient.

References

[1] A. Das, K. Ryu and A. Rohatgi, "20% Efficient Screen-Printed n-Type Solar Cells Using a Spin-On Source and Thermal Oxide/Silicon Nitride Passivation," in *IEEE Journal of Photovoltaics*, vol. 1, no. 2, pp. 146-152, Oct. 2011.

[2] Bock, R. , Schmidt, J. and Brendel, R, “n-type silicon solar cells with surface-passivated screen-printed aluminium-alloyed rear emitter,” *Physica Status Solidi (RRL)*, 2008, 2: 248-250.

[3] G. Kumaravelu, M. M. Alkaisi and A. Bittar, "Surface texturing for silicon solar cells using reactive ion etching technique," *Conference Record of the Twenty-Ninth IEEE Photovoltaic Specialists Conference, 2002.*, 2002, pp. 258-261

[4] Rothhardt, P., Meier, S., Jiang, K., Wolf, A., & Biro, D. (2014). *19.9 % EFFICIENT BIFACIAL N-TYPE SOLAR CELL PRODUCED BY CO-DIFFUSION-COBIN.* Amsterdam: 29th European PV Solar Energy Conference and Exhibition.

[5] Schmiga, C., Nagel, H., & Schmidt, J. (2006). *19% Efficient n-type Czochralski Silicon Solar Cells with Screen-printed Aluminium-alloyed Rear Emitter.* Wiley InterScience.

[6] SVMI. (n.d.). Retrieved from Wafer Annealing: https://www.svmi.com/wafer-services/wafer-annealing/

OF II Payload Control

Eduardo Macias Zugasti[1], Alan Caldelas[2], Joel Quintana Ph.D.[3]
University of Texas at El Paso, El Paso, Texas, 79968, United States

In October 2019, Orbital Factory II (OF-II) team will be launching a CubeSat into a 400 km Low Earth Orbit (LEO). Part of the OFII CubeSat mission includes photographing the Earth as well as photographing the experiment from inside the CubeSat. A 5-megapixel camera will be used for Earth observation, and a 0.3-megapixel camera was selected for photographing the experiment. For communication with cameras and data transmission it was decided to use a microcontroller. However, some experiments needed to take place in order to assess whether the cameras would be effective in space. After doing some vacuum chamber trials and arduous testing, the team concluded that these cameras would be effective for the work conducted in space. The experiment also needed to be driven with an embedded system, so an FPGA was implemented for its control.

I. Introduction and Background

The Communications and Electronics team was selected to develop a system that will be photographing on the CubeSat while in space. The system was put under an experiment to gather more information about the mission. To accomplish this task an embedded system was concluded to be the optimal choice for the experiment. The paper includes descriptions of several problems the team encountered and the most fiscally responsible ways of solving the problems. The paper has been constructed with solutions and scenarios in the order they occurred. The first part discusses the microcontroller that was chosen for the experiments. The next section presents the types of cameras chosen and protocol for communication that was employed as well as the experiments exercised. The third section of the paper focuses on the motor control and FPGA communication used during the experiment inside the cubic satellite. The fourth and final section describes the conclusion.

II. Microcontroller Chosen

The microcontroller that was purchased for the mission was a STM32F427IIT6, which uses an Arm Cortex-M4 CPU. Since this microcontroller is not sold with a development board, the team decided to use an STM34F401RE, which is compatible with the same libraries that the STM32F427IIT6 uses. After conducting research, it was found that there is an easy way to program the microcontroller. An online Integrated Development Environment (IDE) called Mbed, where it is possible to program and compile programs to be uploaded to a microcontroller. After looking at some examples of how to do some data communication and GPIO the microcontroller was ready to communicate with cameras.

III. Cameras and Communication

The cameras necessary for this mission needed to be easy to program and use because the data was going to the transmitted via antennas. Some inexpensive but comparable cameras were selected from Spinel Electronics. The camera that was chosen to take photographs of the Earth was the SC50MPA model, which is a simple 5.0-megapixel camera. The experiment did not require a high resolution photograph, so the camera chosen for this part was a SC03MPA model. This camera has a resolution of 0.3-megapixels. Both cameras use a simple communication

---

[1] Graduate Research Assistant, Department of Electrical Engineering.
[2] Undergraduate Research Assistant, Department of Computer Science.
[3] Research Assistant Professor, Department of Mechanical Engineering.

protocol to take the photographs. A Universal Asynchronous Receiver Transmitter is a digital communication mode that cameras use to transmit image data. The images are sent in hex code, so once the data is received it needs to be converted from hex to .jpeg to see the actual image. An important advantage of using UART is that there is no need to synchronize the microcontroller with the cameras, however both will need to work in the same baud rate, which is 115200 by default. The algorithm to take pictures is presented in Fig. 1.

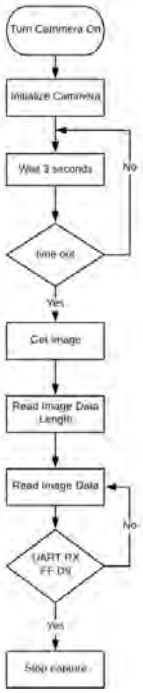

Fig. 1 Algorithm used to take photographs.

It is important to know exactly how much data the microcontroller is going to be receiving. For instance, when the microcontroller sends “56 00 34 01 00” which is Read Image Data Length, the camera will answer “76 00 34 00 04 00 00 XH XM XL”[1] where “XH XM XL” is the image data length. XH is the most significant bit and XL is the least significant bit. So in the next instruction “56 00 32 0C 00 0A 00 MM MM MM 00 KK KK KK 00 0A” which is Read Image Data, the microcontroller needs to specify data length from most significant bit to least significant bit in the “KK KK KK ” bytes. If the microcontroller sends the incorrect data, bytes “FF D9” will never be transmitted and the images that the microcontroller will be received corrupted. There is no image that will be processed after converting data from hex if these instructions are not sent correctly.

One important consideration was if the cameras would be able to survive in space. There is always the possibility of the temperature becoming so high that the equipment overheats or problems with the images being processed in a vacuum. In order to test whether these off-the-shelf cameras would be able to survive space conditions, vacuum chamber testing was implemented.

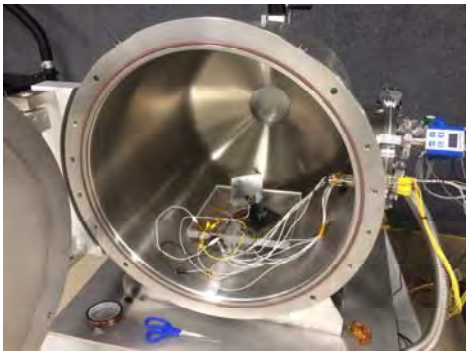

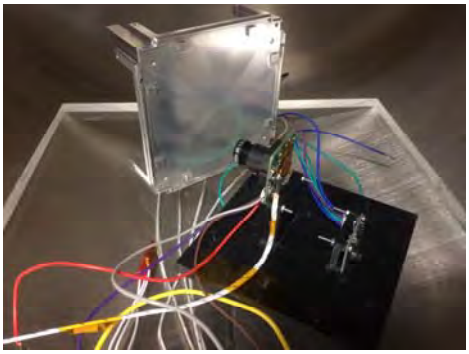

Fig. 2

The experiment consisted in putting the cameras inside of the vacuum chamber and taking 100 pictures one after the other without any breaks. Fig. 2 displays the setup of the experiment in the vacuum chamber. During the experiment all the data from the images was stored. Also, there were thermocouples connected to the cameras to track any temperature change.
After taking 100 pictures and being two hours under zero atmospheric pressure, the cameras survived and no overheating was detected. Both cameras work optimally below 80 C degrees. During the vacuum chamber test the cameras' temperature kept stabilized on 60 C degrees, even when pictures were taken. After processing data and checking the images the team concluded that these cameras would withstand the task without any problems.

The images shown in Fig. 3, are pictures taken inside the vacuum chamber at the beginning and at the end of the experiment. The only difference in these two images was caused by the light angle.

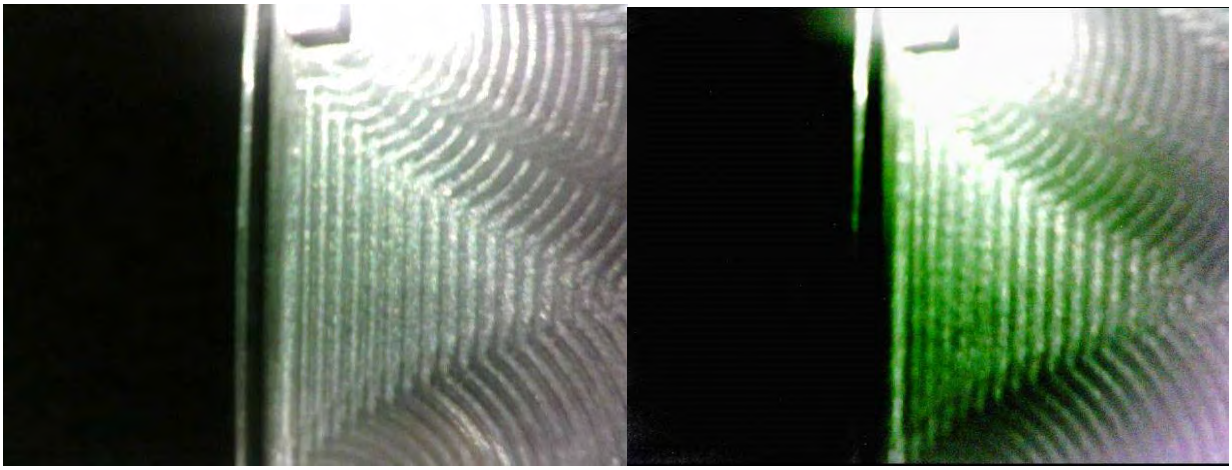

Fig. 3

IV. Motor and FPGA

In order to move the printer in the experiment a stepper motor was needed. After some discussion the team decided to use an FPGA to move the stepper motor and do conductivity tests. The idea was to implement Inter Integrated Communication (I^2C) between the microcontroller and the FPGA. Once communication was established, the microcontroller needed to send data to the FPGA. After the FPGA received the data, it processes it and sends it to different ports that will move the stepper motor and change the position of the printer. Also, the FPGA would turn on some LEDs, in order to provide lighting for better images. The algorithm for the experiment is presented in Fig. 4.

First, the microcontroller needs to establish communication with the FPGA via I^2C. After communication is established, the microcontroller checks if the printer is in home position before starting the experiment. If the printer is not in home position it will be moved to home. Once the printer is in home position, the camera for experiment will be turned on. After that moment, the experiment is ready to start and it is documented by the camera. Once the experiment is completed the camera will be turned off and the stepper motor will be stopped.

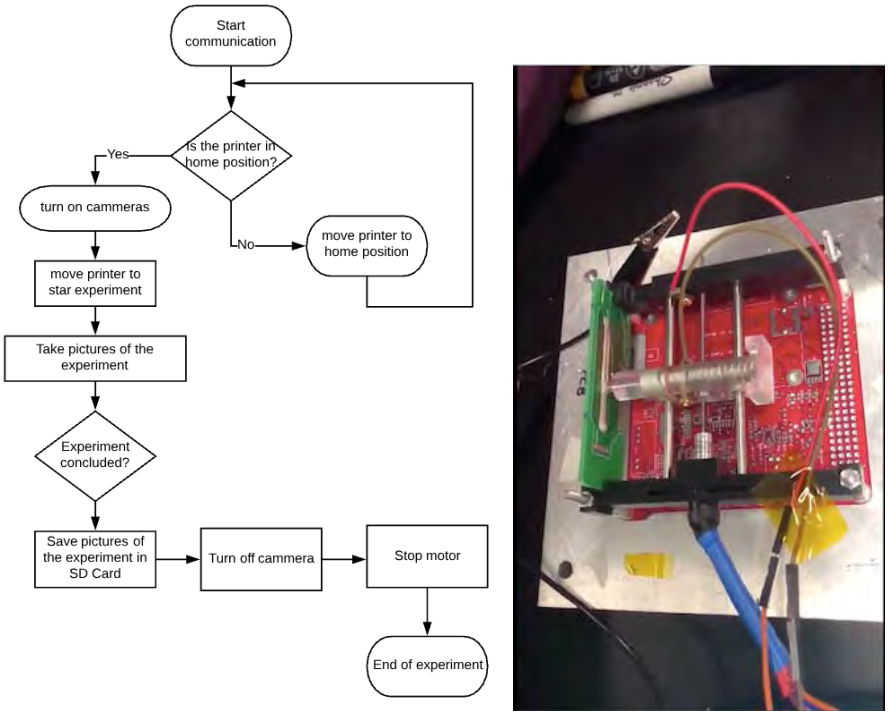

Fig. 4

V. Conclusions

Spinel Electronics cameras are a simple, inexpensive and a vacuum-proof option for photographing in space. The communication protocol is simple and easy to correct if there is any bug found. They do not cost more than $40 USD; they are cost effective since they can work in a non-atmosphere area without overheating. An FPGA is also a good option to control multiple devices, as well as controlling stepper motor and for processing data. An FPGA can receive the bits and directly send them as inputs or outputs to turn on LEDs and they are good to check conductivity in different current points.

References

[1] Endurosat On-Board Computer Type II [User Manual]. (2018, June 20). OBC, Rev 1

[2] SC03MPA: 0.3 Mega Pixels Serial JPEG Camera User Manual. (2018). Rev. D

[3] ALI MAZIDI, M. (2018, October 12). STM32 Arm Programming From Embedded Systems . *Mcontrollers*

Orbital Factory II: 3D Printer

Perla R. Perez[1], Brian O. Valdez[1], Dr. Ashan Choudhuri[2]
University of Texas at EL Paso, El Paso, Texas, 79968, United States

As additive manufacturing is becoming an established technology in space, new emerging strategies improve the efficiency of the printing processes. Orbital Factory II (OFII) is a small satellite—or CubeSat—being developed at the University of Texas at El Paso (UTEP) launching in low earth orbit (LEO) on December 2019. OFII is a 1U (10x10x10cm) CubeSat that will carry a one-axis 3D printer experiment as its primary payload. This printer is being developed and tested in-house. The experiment focuses on printing electrically conductive ink on a printing circuit board that verifies the conductivity on the trace once cured. This could potentially allow for the repairs of solar cells while in orbit. The printer assembly utilizes materials made from conventional additive manufacturing processes which are also space-grade to comply with space regulations, and is housed inside the chassis with the other electronic modules. Several feedbacks will be implemented in the design, allowing to track the progress of the printing process during its different stages. This paper discusses the design and development of the 3D printer as well as the challenges and changes encountered throughout the process.

I. Introduction

Orbital Factory II is a CubeSat under development at the University of Texas at El Paso. The 1U structure carries as its primary payload a 3D printing experiment that aims to print a conductive trace while in orbit. This technology would allow for solar cell repairs by closing a circuit[1]. OFII would have initially launched in 2023 on GTO due to a school competition won through the United Launch Alliance. In an effort to get the satellite in space at an earlier date, changes were made to accommodate the near-launch date of October 2019. OFII will launch through NanoRacks, LLC to low earth orbit (LEO), where it will berth outside the ISS on a resupply mission. The satellite will remain aboard NanoRacks' outside deployer before being released into orbit in December 2019.

OFII will carry different payloads, with the printer being the primary mission objective. Inside the satellite there are four other modules, a UHF transceiver, an S-band transmitter, an Onboard Computer (OBC), and an Electrical Power System (EPS). The arrangement of the modules will follow the PC-104 architecture due to its simplicity to deal with the issues of limited weight and volume[2]. The space occupied by the printer is constrained by the empty volume within the confines of the CubeSat after assembling the other components, thus limiting the range of motion of the printer nozzle. Printer operation is carried through a field-programmable gate array (FPGA) which controls the motor through I^2C communication. Universal Asynchronous Receiver Transmitter (UART) serial communication will be used by the cameras which will be controlled by the OBC. The EPS will power all the systems utilized. The libraries used in the programming, the environmental testing, the PCB boards, and other components related to the printer are being developed by UTEP due to the nature of the project. Testing has revealed important information that has prompted design changes in the printer assembly, and it continues to be an important factor in moving forward with the experiment. Printer design and development will be discussed in this paper as well as the testing being conducted after a major redesign.

II. Design Development

OFII has seen a major design change of its printer, mainly due to the results after testing. Originally, OFII was set to fly in GTO (Geostationary Transfer Orbit) and the design of the CubeSat was a different configuration. In preparation for the high concentration of ionizing radiation in GTO[3], the chassis structure was designed to completely enclose all the electronic modules inside solid walls of the chassis. The thickness of the walls was set to three millimeters after running an analysis that calculated a ratio of weight versus radiation protection to ensure that the

[1] Graduate Research Assistant, Department of Mechanical Engineering.
[2] Engineering and Director, NASA MIRO Center for Space Exploration & Technology Research, Department of Mechanical Engineering

satellite would survive a minimum duration of five days. The first iteration of the CubeSat's design consisted in having the printer assembly outside the thick-walled chassis, the decision mainly driven by the risk of having electrical conductive ink confined in a nozzle of inconsistent results. The design of the nozzle consisted of an intricate mechanism that was co-dependent of its own neighboring components.

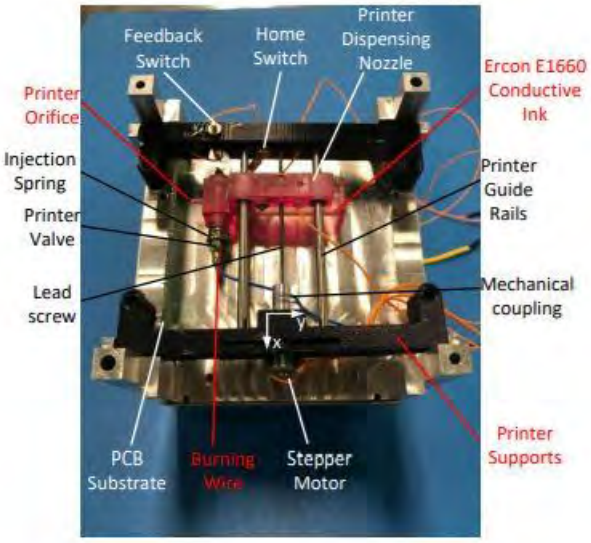

Figure 1: Design of first printer assembly[4]

The nozzle body housed the conductive ink, a spring that would always be exerting pressure on a pusher behind the ink, and an end cap to hold the components inside of the nozzle body. A copper pin close to the tip would block the flow of the ink and contain the ink inside the nozzle. The spring-loaded pin was held together to the nozzle with the use of nylon monofilament. Type C Nichrome burn wire would be wrapped around the monofilament a couple of times to ensure contact. During the printing operation, the printer would first move to the right until reaching the homing mechanism (a switch that would activate once the nozzle assembly reached the rails), and subsequently, the pin would also touch the feedback system. Current would be passed through the burn wire, heating up the nylon eventually breaking it, causing the spring to decompress and force the pin out. This action allowed a small grove on the pin to align to the nozzle tip, permitting for the ink to start flowing. While the motor rotated in the opposite direction, a trace of ink was deposited onto the PCB board. Although the design proved to work from a mechanical point of view, testing with ink inside the nozzle proved to be difficult. All design decisions were made considering the allowable ranges stablished in NanoRacks Interface Control Document[5].

Testing the burn wire mechanism once the nozzle was loaded gave insight into some of the issues happening. Although the nozzle assembly was closed as seen in Fig. 2, there was leakage from the nozzle tip and from one of the sides of the pin. Several attempts were made to try and correct the issue including making the pin hole smaller to contain the

Figure 2: Nozzle failure of previous design iteration

ink. As the hole became smaller, it was observed that it was harder for the spring to be able to move the pin. The tight fit did improve the sealing of the nozzle as ink could not escape from the tip. However, the result of it was 'backflow' of the ink inside the nozzle body. No combination of pusher and pin hole was able to solve the issues. The problems encountered throughout the testing raised concerns of the ink not being properly sealed and able to deploy. Since the design itself was too intricate, a simpler solution was sought to ensure the printer assembly would survive the environment. This simpler solution also was easily repeatable for testing.

While most of the components have virtually remained the same, the nozzle design has seen the most changes. The new nozzle design, although much simpler than its predecessor, has been successful at containing the ink. A change of orbit as well as the procurement of new modules prompted the first changes in the design of the current printer assembly. As the CubeSat will be deployed in LEO and the wall thickness was no longer of concern, more space could be utilized on all sides of the chassis. The printer was moved inside with the rest of the modules to simplify the chassis design by connecting it directly through the PC-104 header pins. The rails were modified to fit in the PC-104 architecture. To reduce the risk of the modules becoming damaged should the ink not be contained while in orbit, the printer sits at one end of the CubeSat, with its PCB board facing the rest of the modules. A Kapton enclosure will also be utilized to isolate the printer assembly from the other components.

The solution to keeping the ink enclosed in the nozzle was to add a wax seal at the nozzle tip, eliminating the intricate pin design of the previous assembly, greatly simplifying the design of the nozzle. The tip of the nozzle is dipped in wax and the rest of the components are added the same way as before (ink, pusher, spring, endcap). As before, the ink is always under pressure since the spring inside the nozzle body is compressed against the pusher/ink. Nichrome wire is still utilized as a burn wire and is placed close to the tip of the nozzle. When voltage is passed through the burn

Figure 3: CAD of current nozzle design

wire, it heats up, causing the wax to melt. Once the wax becomes soft it can no longer hold the pressure inside and ink begins to leak from the tip. When the wax melts, the motor starts turning to deposit the ink trace. The current design of the nozzle is seen in Fig. 3.

A ridge around the nozzle tip was implemented to keep the burn wire in place, making sure it does not detach during launch due to the vibrations. The tip allows for easy maneuvering into the wax and so that the body does not get covered in the wax as well. A second slot was added to the nozzle to have a second point of contact in the threaded rod and eliminate play, which may cause misalignment.

III. Current Design Assembly

The overall current design of the printer did not change much from the original design seen in Figure 1. However, eliminating the pin from the nozzle removed the feedback system that would indicate when the pin had been moved out, which was key in knowing the ink was released. The home switch mechanism will still be implemented to know when the nozzles reaches that position. An inward facing camera will take continuous photos once the printer experiment is running to track the progress of the printing process which is expected to last less than a minute.

The nozzle is guided through two metal rods that keep the nozzle in place. A threaded rod through the middle provides the structure which allows the nozzle to move with the use of a stepper motor connected through a coupling. While most of the components are made from metal which are compatible with space requirements, the main rails are 3D printed out of Ultem and the nozzle is 3D printed out of ProtoTherm, both of which have low outgassing. The substrate

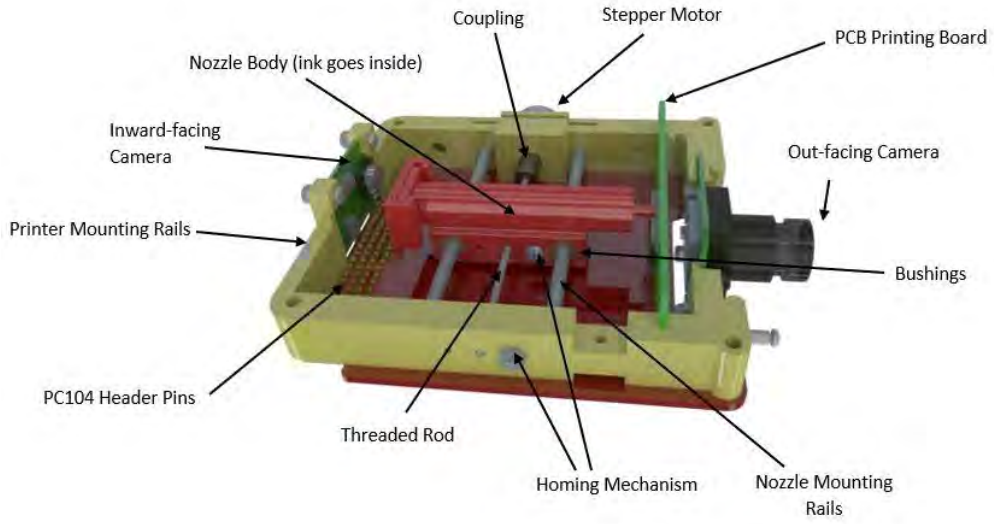

Figure 4: CAD of current printer assembly

used to print is a silver-based ink which is conductive upon curing. Upon printing the ink trace on the printing PCB board, it will be tested for conductivity shortly after, via various test points in the board. If the ink were to deposited nonuniformly (i.e. there is a break in the print), the conductivity can still be measured at different points. Success will be determined by obtaining conductivity at any point of the print. A current design of the printer assembly is seen in Figure 4. An external camera also forms part of the printer assembly but will be used to take pictures of the Earth and Space and has no influence on the printer assembly.

IV. Testing

Different tests have been performed on the printer structure to ensure it will survive the launch as well as the vacuum environment in space. The first test that the printer will experience is the vibration environment at launch. NanoRacks as the satellite integrator provides testing launch loads to test that comply with NASA guidelines per random vibration[6]. Considering that the 3D printing experiment is the primary payload of the satellite and that no specific requirements exist for it, the testing requirements were derived from the ones already established. For the printer, this means that all the connections will stay connected, the threaded rod does not bend and prevents turning, the rails do not break, and finally that the nozzle keeps the ink contained. Afterwards, a functional testing will be performed in vacuum to assure all the components still function properly and are able to perform in space. In actuality, the CubeSat will remain in the docking service module outside the ISS for two months before being put in orbit.

Several tests have been performed prior to check the functionality at different stages. To test the conductivity of the ink in vacuum, traces of ink were placed on a PCB board that would form a conductive path once cured. Positive and negative connections were attached to the board and connected to a voltage source outside the vacuum chamber. Even though the vacuum had not yet reached high vacuum (below -4 Torr), the ink started conducting shortly after being placed inside. Thus, the ink will cure rapidly while in vacuum.

Static vacuum testing was performed after adding the wax seal to see the behavior of the nozzle assembly. Two nozzle assemblies holding ink were placed inside until reaching high vacuum. After leaving them in high vacuum for over an hour, the burn wire was activated, and ink was deposited. Since it was a static test, the ink congregated at the nozzle

tip as seen in Fig. 5. The testing was successful, as the wax and burn wire mechanism worked as expected in high vacuum.

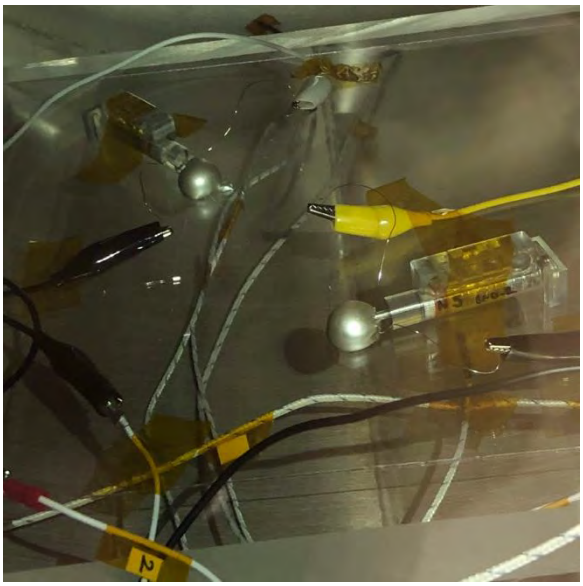

Figure 5: Nozzle assemblies with ink deployed in vacuum chamber

Dynamic testing of the printer assembly confirmed that the motor can move back and forth to deposit a trace of ink onto the PCB test board. Ink was loaded in the nozzle and moved through the printer assembly, conducting the sequence as if it were in space. First, the program checks if it is in the homing position and moves to the right if it is not. Upon touching the homing switch, the motor stops. Power is then passed through the burn wire until the wax melts. The stepper motor then moves to the left as the ink is leaving, leaving a trail of ink on the board. Several passes of the nozzle are conducted (back and forth two times) to ensure a smooth deposition. The programming is still under development and the test was carried by physically manipulating buttons, but the movement of the printer remains unchanged. The conclusion from the test was that the motor can move from side to side as needed, leaving a clear print on the test board. Less ink should be utilized when printing since there was ink left inside the nozzle that started dripping once the printing sequence was finished. The ink trace on the PCB board can be appreciated in Fig. 6 below.

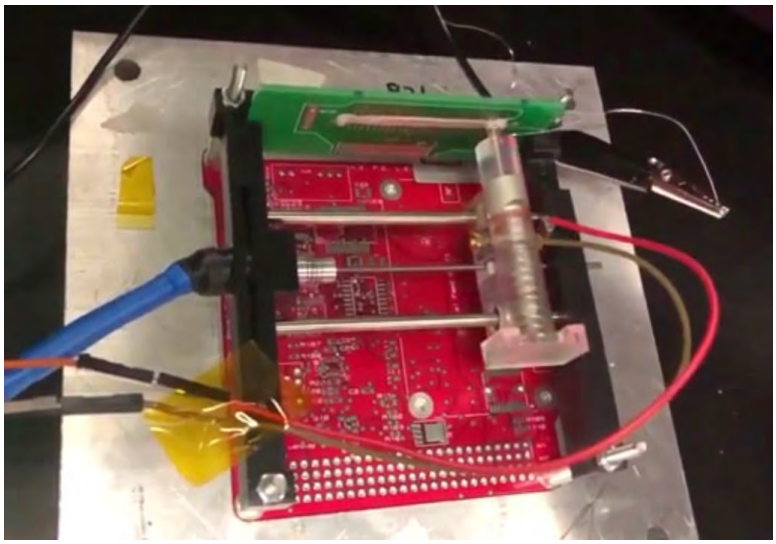

Figure 6: Deposition of ink through a dynamic test of the printer

Testing of the printer assembly will continue up until delivery. Conducting vibration testing followed by a functional test in the vacuum chamber will most closely resemble the environment to which the printer/satellite will be subjected. Multiple testing will ensure repeatability and a successful experiment of the OFII 3D printed in space.

V. Conclusion

Orbital Factory II is a CubeSat developed at the University of Texas at El Paso that will launch through NanoRacks, LLC on a resupply mission to the ISS. The satellite will remain outside of the ISS in NanoRacks' deployer for two months before being released into low earth orbit two months later. The 1U CubeSat carries as its primary mission a one-axis printer that will deposit a conductive ink trace to simulate the repair of solar cells while in orbit. Design iterations and testing have been performed on the printer assembly to make sure that the experiment is successful and can survive the launch and environment conditions.

A change of mission caused the first minor changes to the assembly to simplify the structure and design of the assembly. An intricate spring-loaded pin design in the nozzle was able to work mechanically but was unable to contain the ink inside. Following this problem, a major nozzle redesign was needed, resulting in a simpler design needing to be tested for reliability and repeatability. A wax seal contains the ink inside the nozzle until the burn wire melts the plug, allowing ink to flow out. Several tests have been conducted on the printer at different stages to test each subassembly. The wax sealing mechanism tested in vacuum and the motor dynamic test in the atmosphere, both successful, are positive indicators that the printer assembly is on its way to being successful. Further testing will be performed in the following months simulating the launch environment and performing a functional test on a fully integrated system to confirm that the experiment will be successful while in orbit.

VI. References

[1] Everett, Michael, Flores-Abad, Angel, Khan, Arifur, Masum Billah, Kazi Md, Herzog, Emily, Rahman, Ashiqur, "A 1U Cube-Satellite for Electrically Conductive 3D Printing in GTO", *AIAA SPACE and Astronautics Forum and Exposition*, 2018.

[2] Abbott, Larry, Cox, Gary, Nguyen, Hai, "Adapting PC104Plus for Space" *NASA Johnson Space Flight Center*, Technical Report JSC-CN-6003.

[3]Berrier, D. J., "The combined release and radiation effects satellite, a joint NASA/DOD program" *NASA Goddard Space Flight Center*, Technical Report 19880001469.

[4] Everett, Michael, Flores-Abad, Angel, Khan, Arifur, Maxum Billah, Kazi, Herzog, Emily, Rahman, Ashiqur, R. Choudhuri, Ashan, *"Orbital Factory II: a 3D Printer CubeSat with Self-repairing Purposes"*, 10.2514/6.2018-5231, 2018.

[5] NanoRacks, LLC, "NanoRacks CubeSat Deployer Interface Control Document", NanoRacks, Houston, TX 2013.

[6] NASA, "Launch Services Program", *National Aeronautics and Space Administration*, 2014.

VII. Acknowledgements

Orbital Factory II is an experimental solution supported by NASA under award NNX15AQ04A

Orbital Factory II Integration and Orbital Analysis

James P. Holt,[1] Ashiqur Rahman,[2] and Joel Quintana[3]
University of Texas at El Paso, El Paso, Texas, 79968, United States

Orbital Factory II (OF-II) is a 1U CubeSat project which will be launched in October 2019 into Low Earth Orbit (LEO). OF-II will travel to the International Space Station (ISS) as part of a Cygnus resupply mission. Approximately three months later after Cygnus has completed its mission, OF-II will be deployed. OF-II will orbit the Earth every 90 minutes, and pass over El Paso approximately six to eight times per day. OF-II's primary payload is an experiment to test repair of a device in orbit using additive manufacturing. OF-II's secondary payload is a test of an experimental S-band patch antenna developed by Lockheed Martin Space Systems corporation. Lastly, OF-II will also attempt to take pictures of the Earth and test methods for attitude control using magnetorquers. A ground station will be built in El Paso, TX to receive downlink from OF-II. Several methodologies for attitude control using magnetorquers are under evaluation, which is important for pointing of the S-band patch antenna.

I. Introduction and Background

Orbital Factory II (OF-II) is a 1U CubeSat under development at The University of Texas at El Paso (UTEP). OF-II's primary payload is a test of a novel method of performing in-space electrical repairs using additive manufacturing. By dispensing a conductive paste, open circuits on satellites caused by physical damage could be repaired. OF-II will feature a printed circuit board that simulates a damaged electrical connection, which will be repaired. Additionally, OF-II will test an experimental S-band patch antenna manufactured by Lockheed Martin Space Systems using proprietary nanocopper, as well as an experimental S-band transmitter provided by EnduroSat. Design of OF-II began in 2016 when the project proposal was awarded first place in the inaugural United Launch Alliance (ULA) CubeCorp CubeSat competition. Through this competition, UTEP was awarded a launch opportunity on an Atlas V into a geostationary transfer orbit (GTO). However due to delays in the Atlas V GTO launch manifest, it was decided to launch the first iteration of OF-II into low earth orbit (LEO) through NanoRacks LLC.

II. Launch Opportunity and Target Orbit

OF-II is manifested to launch on the Cygnus NG-12 resupply mission to the International Space Station (ISS). OF-II will be integrated into the NanoRacks External CubeSat Deployer (ENRCSD) mounted on panel five of the Cygnus service module. The launch is scheduled to take place on October 1, 2019 from Wallops, VA aboard an Antares rocket. Approximately three days after launch Cygnus will berth with the space station, where the spacecraft will remain for two to three months. After the space station resupply mission is complete, the astronauts will unberth Cygnus, which will raise its orbit to approximately 455 km. Cygnus will remain at the space station's 51.6-degree orbital inclination.

Commented [j1]: Changed to "delivered." You used "launched" in the previous sentence.

Commented [j2]: I would specify here that the physical damage could be repaired on other satellites or spacecrafts. This sentence makes it sound like you are repairing yourself.

Commented [j3]: Why is this sentence important?

[1] Graduate Research Assistant, Department of Mechanical Engineering.
[2] Graduate Research Assistant, Department of Mechanical Engineering.
[3] Research Assistant Professor, Department of Mechanical Engineering.

Fig. 1 Launch and deployment of OF-II.

III. CubeSat Deployment and Concept of Operations

Approximately three days after the orbit raise maneuver, OF-II—along with the other CubeSats flying on NG-12—will be deployed. It is expected that there will be a deployment deltaV of approximately 0.5 to 2.2 m/s. Shortly after deployment, OF-II's electrical power system (EPS) will activate and the mission will begin.

OF-II's mission has been scheduled into five phases. Each phase has a duration of approximately eight hours. In phase one the EPS built-in firmware will turn on and measure the battery voltage and temperature, as well as check the solar cell states. If all conditions are suitable then the system will turn on the power buses. Next the on-board computer (OBC) will boot. Then the UHF dipole antenna deployment. A system checkouts will be performed periodically, which contains data regarding OBC status, temperature, EPS state, and solar cell status.

In phase two OF-II will acquire data and take pictures with both cameras. First UHF communication will be established in this phase. Also, the system will prepare itself for performing the printer activity. In phase three printing will be performed. Necessary data for printing will be acquired and stored in memory and will be transmitted over UHF during a suitable communication pass. In phase four, data will be transmitted through S-band which will be used to test performance of the patch antenna. In phase five, a tentative mission objective has been planned which includes a commemorative broadcast of a speech from UTEP President Diana Natalicio. After that the system will step into the extended mission phase. During this period, OF-II will be acquiring data from its sensors to downlink. Data received from the extended mission includes tumbling rate, temperature, and power consumption. which will be examined for educational purposes in the future. Additionally, it is planned to experiment with algorithms for using OF-II's magnetorquers for attitude control.

IV. Orbit Analysis

In order to plan out the mission ConOps, the orbit had to be characterized. While the orbit altitude and inclination are approximately fixed, other orbital parameters such as the right ascension of the ascending node (RAAN) and the argument of perigee can vary based on the deployment epoch. This has a significant effect on when ground station passes will occur. Orbital state data for two previous ENRCSD deployments from mid-2018 were provided by NanoRacks. This included the cartesian position and velocity relative to the J2000 frame, as well as the deployment epoch and deployment deltaV vector. These states were then converted into Keplerian elements using Systems Toolkit (STK). The space station orbital elements at the same epochs were also noted. The difference between the CubeSat RAAN and argument of perigee and the space station RAAN and argument of perigee was calculated, and an average was taken for both deployments. This offset—along with a predicted space station orbit in December 2019—was then used to estimate the CubeSat deployment orbit for OF-II. Though variations in deployment time as well as other

factors—such as alterations of the Cygnus orbit—can cause significant changes in the orbit ground track, this method at least provides a realistic guess for the OF-II orbit for analysis. The resulting orbit has an orbital period of approximately 94 minutes.

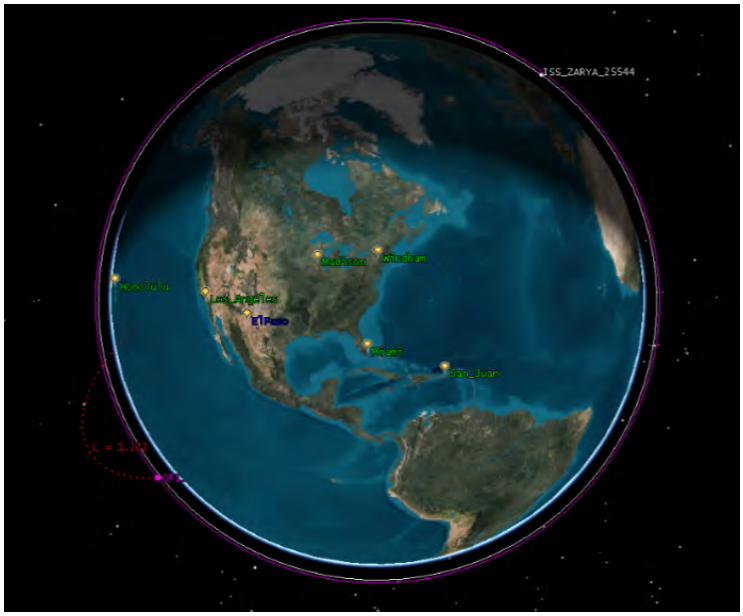

Fig. 2 Orbits for OF-II (purple) and the space station (white).

Next, ground station access had to be calculated. Initially for the OF-II mission, it is planned to utilize only one ground station located at TMD Defense and Space LLC near El Paso, TX. It was found that for this ground station, approximately six to eight passes could be expected per day. Each pass could last a maximum of nine minutes.

One of the biggest challenges of the OF-II mission is the pointing of the S-band patch antenna. While the UHF dipole antenna is omnidirectional, the patch antenna is expected to have a maximum field of view of sixty degrees. The ground station must be within this field of view for downlink to be possible. Otherwise the link budget cannot close. Using STK, the Earth magnetic field can also be modeled. This is being used to evaluate methods of attitude control for OF-II using magnetorquers. Magnetorquers function by creating a magnetic field vector, which will interface with the Earth's magnetic field producing a torque. Several different methodologies of attitude control are currently under evaluation. These include passive control—where the magnetorquers will emulate a passive magnet with a fixed magnetic field vector; control via table lookup—where a lookup table of the ideal magnetic field vector direction over time will be calculated for each pass; or utilization of an active control algorithm—where sensing will be used by the satellite to autonomously calculate the ideal magnetic field vector to keep the patch antenna pointed nadir to the Earth. Due to time constraints, it is likely that methodology one or two will be selected, with methodology three potentially being used during OF-II's extended mission via uplink of a new software package.

Preliminary analysis of methodology one is promising, showing that on average approximately 3.7-minute access can be expected per pass if the CubeSat Z-axis is aligned with Earth's magnetic field. However further analysis will have to be performed to characterize RF losses—such as atmospheric losses or dropoff—caused by the long distance and

Commented [j4]: One thing I noticed is that at times you spell out numbers such as "one, two, or three" Other times you just type the number "1, 2, or 3." Typically the rule is spell out whole numbers that are less than ninety-nine, unless it is a title.

shallow elevation angle as shown in figure 3. Currently the patch antenna and ground station are being modeled with STK's RF toolbox to analyze this further.

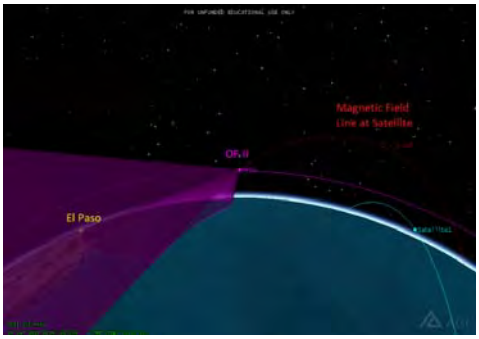

Fig. 3 S-band patch antenna field of view (purple) when the CubeSat Z-axis is passively aligned with the Earth magnetic field vector (red).

V. CubeSat Payloads and Subsystems

OF-II's main payloads are one OBC, one UHF transceiver, one S-Band transceiver, one EPS, a custom payload board, printer module, two cameras, five solar panels, one UHF antenna with four deployable antenna rods and one S-Band antenna. Onboard computer is the brain of the satellite which will control rest of the modules establishing I2C communication using a shared PC104 bus connector. Cameras will be connected through UART with the OBC. Transceivers are used to process data instruction received from OBC using modulators and amplifiers which are further forwarded to the antennas. Antenna converts the electronic signals to Radio frequency and start propagating. Transmitted signal from the satellite is received by ground station antennas. Reconstructing the original signal satellite condition can be realized. Payload board consists of FPGA circuitry which will be used to control the printer motor, blinking LEDs, and to check continuity after the printing is complete. Electronic power system consists of a single cell battery which can provide 10.4 Whr of power through two power buses. Most of the devices are operated with 3.3V bus however a 5V bus is available if high amount of power is required.

Commented [j5]: For example, here you need to spell out five.

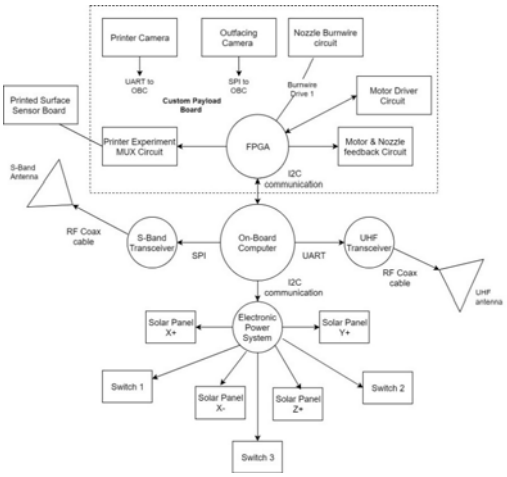

Fig. 4 OF-II system schematic

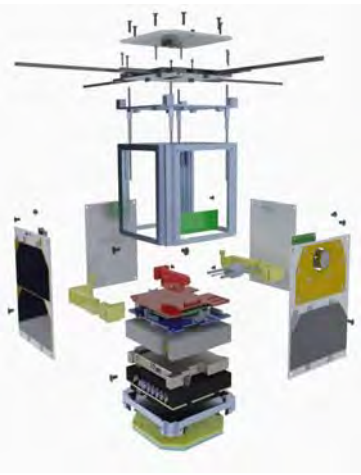

Fig. 5 OF-II Hardware Integration

Orbital Factory II Subsystems and payloads:

OF-II includes flowing subsystems and payloads:

- Onboard computer
- UHF Transceiver
- S-Band Transceiver
- Electrical Power Subsystem
- Payload board & Printer experiment
- Cameras
- UHF Antenna
- S-Band antenna
- Structure subsystem

OF-II incorporates a high-performance computing platform manufactured by EnduroSat which is fully compatible with the CubeSat standard. It is based on ARM Cortex M4 with frequency rate up to 180MHz. It comes with integrated double redundancy sensors: 3-Axis accelerometers and compass. PWM drivers for magnetorquers and inputs for sun sensors, temperature sensors and gyroscope allow the implementation of the attitude determination and control systems. A PC104 bus connector is used to establish communication among the Satellite payloads using I2C method.

OF-II includes a UHF transceiver manufactured by EnduroSat which can be configured between 430-440MHz band. By default, the transceiver works in half-duplex mode with configurable data rate and modulation index. Maximum Data rate in the air is up to 100kbps. Radio has a configurable telemetry beacon broadcast option.

OF-II's one of the primary mission objectives is to test an experimental S-Band patch antenna. A Custom S-Band transceiver also made by Endurosat will be used with an approximate 2400 – 2500 MHz frequency range.

OF-II's EPS comes with integrated one or two Li-Po battery packs encapsulated inside the aluminum box. Capacity of one battery pack is 10.4 Watt-hour. The EPS manufactured by EnduroSat has three photovoltaic input channels for supplying the power from each axis of solar panels. Two latch up protectors are available to protect systems from overcurrent and overvoltage.

Commented [j6]: 10.4 what?

OF-II uses five EnduroSat Solar Panels which are equipped with 2 CESI Solar cells CTJ30 with 29.5% efficiency. The wide effective cell area (the largest possible for solar panels suitable for 1U CubeSats) provides up to 2.4 Watts in LEO per panel. Solar power will be used for extended mission.

OF-II's primary mission objective is to study additive manufacturing in microgravity. This will be accomplished by using the small printer to deposit electrically conductive ink on a printing circuit which will verify the conductivity on the trace once cured. The experiment aims to simulate the repair of solar arrays by adding the conductive trace between a tear on a solar panel. The printer assembly has a stepper motor and a nozzle which contains the conductive ink. A compressed spring puts force on the pusher with O-rings (to prevent backflow) against the ink which is being contained by the wax seal at the tip of the nozzle. Once a burn wire is activated, it heats up and melts the wax, allowing for the spring to decompress and deposit ink on the printing board as it moves across it with the use of the stepper motor.

OF-II contains two cameras one internal and one external camera. Purpose of the internal camera is to observe the printing status which is one of the primary mission objectives. External camera will be used to take pictures of the earth.

UHF antenna has four monopole antenna rods designed for UHF band for amateur satellite communications 435 – 438MHz. Antenna is manufactured by EnduroSat as well. Circularly polarized RF signal has a gain > 0dB. Burn wire mechanism available with feedback for deployment.

OF-II's S-Band antenna manufactured by Lockheed Martin Corporation is an experimental patch antenna which can be operated within 2400 – 2500 MHz frequency band. The aluminum chassis consists of a main body which houses all the modules inside and is covered with two plates at the top and bottom acting as lids to help contain the structure. Four threaded-rods inside the structure are positioned using the PC-104 architecture to stack up the modules which use PC-104 header connectors. Solar panels are mounted to the outside of the structure: three and a half panels around the main body –the half panel used on the same face where the outside camera is facing and the other panel in the top cover above the UHF antenna. S-band antenna is mounted at the bottom cover.

A scheduler outline is provided in the following section:

Phase 1	Phase 2	Phase 3	Phase 4	Phase 5
1. EPS built-in firmware turns on 2. Measure battery voltage and temperature 3. Check for solar cell state 4. Turn on Power buses 5. OBC boots process 6. UHF antenna deployment 7. System Checkout: OBC Status, Temperature, EPS State, Solar cell	1. Take one picture with each camera 2. Check battery status 3. Turn on low power mode if required 4. Get the battery fully charged 5. Check for printer home position 6. Return printer to home if not at home	1. Burn printer wire 2. Turn on stepper motor for 25 seconds 3. Take slideshow-video with 0.5MP camera 4. Wait for 5 minutes 5. Check conductivity via feedback circuit 6. Take 3 pictures with internal camera 7. Store data & image in memory	1. Check battery status 2. UHF transmission for 10 minutes 3. Activate S-Band module 4. Process data packets with GMSK modulation 5. Transmit the digital packets for 2 minutes at every other 8 minutes for 1 hour 6. Check battery status	1. Transmit speech for 10minutes **Extended mission** 1. Read & store temperature data, Tumbling status, EPS status 2. Take pictures with external camera 3. UHF transmission

VI. Conclusion

Orbital Factory II (OF-II) is a 1U CubeSat project which will be launched in October 2019 from Wallops, VA into a 455 km Low Earth Orbit (LEO). The launch integration will be handled by NanoRacks LLC, and the launch will be aboard an Antares rocket to the International Space Station (ISS) as part of a Cygnus resupply mission. Approximately three months later, OF-II will be deployed from the Cygnus spacecraft. OF-II will orbit the Earth every ninety minutes, and pass over El Paso approximately six to eight times per day. OF-II's primary payload is an experiment to test repair of a device in orbit using additive manufacturing. OF-II's secondary payload is a test of an experimental S-band patch antenna developed by Lockheed Martin Space Systems corporation. Lastly, OF-II will also attempt to take pictures of the Earth and test methods for attitude control using magnetorquers. Subsystems onboard OF-II include the Onboard Computer (OBC), the UHF transceiver, the S-Band transceiver, the Electronic Power System (EPS), a custom payload board, the printer experiment, two cameras, five solar panels, the UHF antenna with four deployable antenna rods, and the S-Band patch antenna. A ground station will be built in El Paso, TX to receive downlink from OF-II. Due to the small field of view of the S-band patch antenna, attitude control is critical to close the S-band link budget. Currently, different methodologies for attitude control via magnetorquer are under evaluation, including emulating a passive magnet, utilizing an uplinked lookup table, or using an active control algorithm and sensors. Due to time constraints a simple methodology will have to be selected, and the problem is under further evaluation.

Acknowledgements

The material is based upon work supported by NASA under award No(s) NNX15AQ04A

References

[1] Endurosat On-Board Computer Type II [User Manual]. (2018, June 20). OBC, Rev 1
[2] Endurosat UHF Antenna [User Manual]. (2017, November 17). UHF Antenna, Rev 1.3
[3] Endurosat Electrical Power System (EPS) [User Manual]. (2017, April 13). EPS, Rev 1.1
[4] Endurosat UHF Transceiver Type II [User Manual]. (2018, April 2). UHF Transceiver, Rev 1.2
[5] NanoRacks External CubeSat Deployer (NRCSD-E) Interface Definition Document. (2018, September 5).

Piezoelectric $BaTiO_3$ Ceramics Fabricated Using Paste Extrusion 3D Printing Technique

Anabel Renteria[1], Luis A. Chavez[1], Jaime E. Regis[1], Tzu-Liang Bill Tseng[2], Yirong Lin[1]

[1]Department of Mechanical Engineering, University of Texas at El Paso, El Paso 79968, United States

[2]Department of Industrial, Manufacturing, and Systems Engineering, University of Texas at El Paso, El Paso 79968, United States

Abstract

There are several traditional methods (e.g. tape casting) to process BT ceramics but disadvantages such as difficult handing without shape deformation, demolding, complex geometric shapes, and expansive molds. A paste extrusion 3D printing technique for BT ceramics with polyvinylidene fluoride (PVDF) was developed to overcome the traditional issues. PVDF solution plays multiple roles of binder, plasticizer, and dispersant for excellent manufacturability. It was found that the maximum binder ratio with good viscosity was 1:8.8, while the maximum BT content was 35.45 vol.% in order to achieve maximum density of 3.93 g/cm^3 for 3D printed BT ceramic. Among different sintering temperatures, it was observed that the sintered BT ceramic at 1400 °C had highest grain growth, which affected the piezoelectric and dielectric properties, 200 pC/N and 4730 at 10^3 Hz respectively. This paste extrusion 3D printing technique for ceramic suspensions are expected to enable rapid massive production, customization, and design flexibility of piezoelectric devices.

Keywords: Barium titanate, paste extrusion, additive manufacturing, bulk ceramic, piezoelectric, dielectric

1. Introduction

Functional ceramics have been essential for electronic industries (capacitor, sensor, etc.) for more than five decades [1]. Nowadays, it has been applied to various aspects of practical engineering areas such as energy harvesting, automobile, aircraft, and information storages, due to unique properties including but not limited to electrical, magnetic, and optical properties [2]. Among the electrical properties, ferroelectric materials have been widely used in modern technology aforementioned above. Studies on high-performance lead-free ceramics have been reported due to the concern with environmental pollution caused by lead-based ceramics [3]. Barium titanate ($BaTiO_3$, BT) is a well-known lead-free ferroelectric material [4]. BT ceramic has relatively low piezoelectric (d_{33}: ~190 pC/N) [5] and dielectric (ε: ~1700) properties [6]. However, BT ceramics are more suitable for applications such as capacitors and energy storage devices [6]. There are several conventional methods used for processing bulk BT ceramics, which press BT powders in a mold and fire them at high temperature, such as slip casting, compaction, tape casting, filter pressing, drying casting, and injection molding [7]. They have disadvantages on demolding and subsequent handling without shape deformation during process and limitations to varying geometric [2, 7].

Many research efforts have been made to combine functional devices such as piezoelectric sensor and energy storage with additive manufacturing (AM) [8]. Selective laser sintering and binder jetting techniques have been studied for printing $BaFe_{12}O_{19}$, PZT, and $BaTiO_3$ [9-11]. Some researchers reported that printed structures are porous and not suitable for fabrication of dense structures [2]. Paste extrusion (PE) 3D printing (i.e. robocasting) has been widely studied due to its advantages such as flexibility and low cost equipment [12]. PE does not requires heating since the liquid to solid transition occurs by solvent evaporation [13]. The BT ceramic paste consisted of ceramic powder and various chemicals such as binder, plasticizer, and dispersant to help colloidal suspensions extrude smoothly out of small syringe tip and printed layers retain the shape [12].

A simple method to prepare piezoelectric ceramic suspensions for fabrication of ceramics using polyvinylidene fluoride (PVDF) as a binder was develop. PVDF has been widely used in application of lithium-ion battery to lead to more cohesive particle network and proper viscosity that result in reducing

capacity fading of cathodes during the battery cycling [14]. N-N Dimethylformamide (DMF) is used to dissolve PVDF, also has a property of plasticizer, which decreases viscosity of the material. Therefore, the combination of PDF and DMF solutions plays an important role on the paste formulation. 3D printed samples were studied for piezoelectric and dielectric properties.

2. Experimental details

2.1 Materials, synthesis, and fabrication

$BaTiO_3$ powder (500 nm; Inframat) was used for the fabrication by PE 3D printing. PVDF powder (MW~534,000; Sigma-Aldrich) and DMF solvent (OmniSolv) were used to bind BT powder for ceramic suspensions. To prepare the ceramic suspensions, PVDF powder was first dissolved in DMF under water bath at 80 °C for 15 min with a weight ratio of 1:8.8. BT powder was added to the solution and stirred for 5 min. Additional DMF was added to the ceramic suspensions to meet the ratio of 1:8.8 since the some of DMF solvent evaporated during the water bath process. The suspensions were placed into syringe tube trying to avoid bubble airs inside. A nozzle of 600 μm orifice size was attached to the syringe. Samples were printed in using a *Printrbot Simple metal,* which was modified to extrude paste. The ceramic samples of dimension of 1 × 1 × 0.44 mm were printed with a speed of 1 mm/s and dried at 120 °C for 2 hrs.

2.2 Post processes

The green samples were sintered in an alumina crucible at temperatures of 1100, 1200, 1300, and, 1400 °C with following sintering schedule: 1) heating to 650 °C with a ramp rate of 5 °C/min and holding for 1 hr to allow binder burnout, 2) then heating to 1400 °C (varying with desired temperature) and dwelling for 3 hrs. Table 1 shows the material composition used and changed in weight and volume percent before and after drying the DMF solvent. To test piezoelectric and dielectric properties, surfaces of the sintered samples were then polished with sandpaper (600 grit). Then, silver paint electrodes were applied to the top and bottom surfaces and dried at 60 °C for 2 hrs. After drying, thermal poling was applied on each sample in silicon oil (80 °C) under electric field of 0.66 MV/m for 15 hrs to align dipoles.

Table 1. Weight and volume percent of $BaTiO_3$, PVDF, and DMF in the prepared suspensions.

	$BaTiO_3$	PVDF	DMF
Wt. % (before/after drying DMF)	77.01 / 97.04	2.34 / 2.96	20.65 / 0
Vol. % (before/after drying DMF)	35.45 / 90.66	3.65 / 9.34	60.89 / 0

2.3 Structural, morphological, and functional characterizations

The morphology of the 3D printed bulk ceramics was observed using a scanning electron microscopy (SEM, TM-1000 Hitachi). X-ray diffraction was also performed (Bruker). The piezoelectric coefficient (d_{33}) was measured using d_{33} meter (APC YE2730A). The dielectric constant and loss were analyzed using an LCR meter (1920 Precision, IET lab).

3. Results and Discussion

3.1 Optimization for manufacturability

Figure 2(a) shows part printed with different binder ratios of 1:14, 1:10, and 1:8.8. The suspensions at 1:14 ratio experienced the separation of DMF solvent from suspensions. At 1:10 ratio, no DMF separation was observed and it retained the desired hexahedron geometry. However, it experienced clogging on syringe tip above 1:8.8 ratio, which was found as the maximum binder ratio with good viscosity and retention of desired geometry after printing.

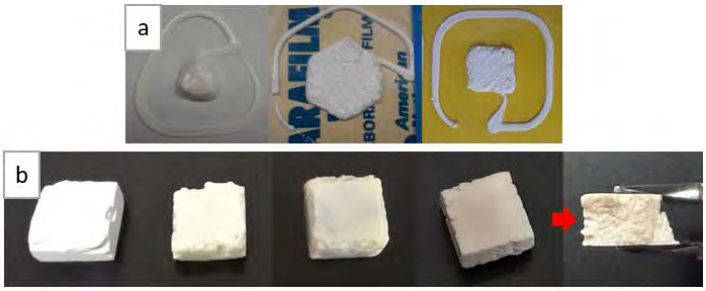

Figure 1. (a) 3D printed samples at different ratios of PVDF-DMF (from left, 1:14 (triangle), 1:10 (hexahedron), 1:8.8 (square)) (b) sintered samples (from left, 1100, 1200, 1300, 1400 °C, and cross-sectional area of the sample sintered at 1400 °C)

With a 1:8.8 ratio, the BT content can be increased by 35.45 vol.% which is printable without clogging. Dimensional accuracy of the 3D printed samples was measured on samples prepared at different BT vol.% of 35.45, 31.91, 28.66, 25.85 and found ± 12, 11, 9, 7 %, respectively compared with a CAD file. After sintering them at 1400 °C, their densities decreased from 3.93 to 3.20 g/cm^3. The sample containing 35.45 vol.%-BT was very rigid; however, the samples became brittle as decrease in BT content due to more porosities created inside from binder burnout. With found BT content (35.45 vol.%) and binder ratio (1:8.8), four different sintering temperatures (1100, 1200, 1300, 1400 °C) were applied to each sample. Figure 1(b) shows that as the sintering temperature increases their appearances are slightly turning from white to brown and the densities were gradually increased from 2.08 to 3.93 g/cm^3.

3.2 SEM and XRD analyses

The morphology of the BT ceramics were analyzed using SEM to observe the grain growth and internal defects. Figure (a) shows microstructure of as-printed part that consisted of BT agglomerates and voids size (ø ≃ 1μm) after DMF evaporation. Sintering at 1100 ˚C seen in Figure (b) occurred grain (ø ≃ 2 μm) and voids growth. These void growths were attributed to a diffusion of BT particles as well as binder burnout. These voids continued but shrank and reduced at 1200 ˚C, meaning that it was densified. The average grain size of ø ≃ 2.5 μm was measured for the sample sintered at 1200 ˚C. Density was increased from 2.08 (34.5 %) to 3.16 g/cm^3 (52.5 %) at increasing sintering temperature from as-printed to 1200 ˚C. Density was calculated based on the theoretical value 6.02 g/cm^3 of pure BT. After 1200 ˚C, few voids remain and significant grain growth occurred to averages of ø ≃ 10 and 40 μm sintered at 1300 and 1400 ˚C, respectively as shown in Figure (d-f).

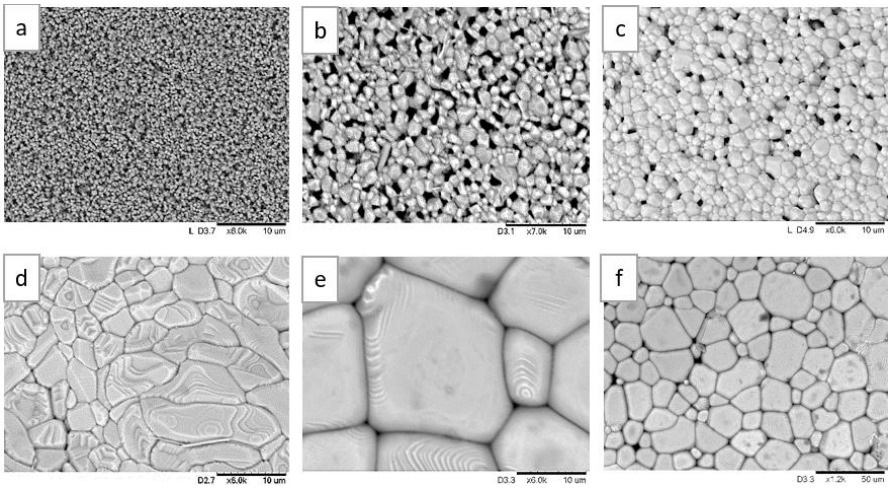

Figure 3. SEM images of samples (a) as-printed, (b) sintered at 1100 °C, (c) 1200 °C, (d) 1300 °C, (e-f) 1400 °C with high and low magnification.

Crystal structures of 3D printed BT ceramics sintered at various temperatures were examined by XRD analysis. The peaks were observed at 2θ = 22.0°, 31.3°, 38.7°, 45.1°, 50.7°, 55.9°, 65.8°, 70.7°, 74.6°, 75.0°, and 79.5° as shown in Figure 1, which indexed for tetragonal crystal structure of BT ceramic [15]. All of these diffraction peaks remain present at all of the sintering temperatures. As the sintered temperature increases, it was observed an increase of peak splitting into two peaks (002) and (200) around 2θ = 44 - 46° as well as peaks around 50.7°, 50.9°, and 75.0° [16]. This peak splitting was occurred because the sintering temperature above 950 °C led to phase transformation from cubic to tetragonal [16-18]. This tetragonality of BT ceramics increases as the sintering temperature increase as evidenced by an increase in extent of peak splitting [34], therefore highest tetragonality among XRD peaks can be seen in the sample sintered in 1400 °C. In contrast, as-printed sample was observed no split of the diffraction peaks at these angles due to no sintering process applied.

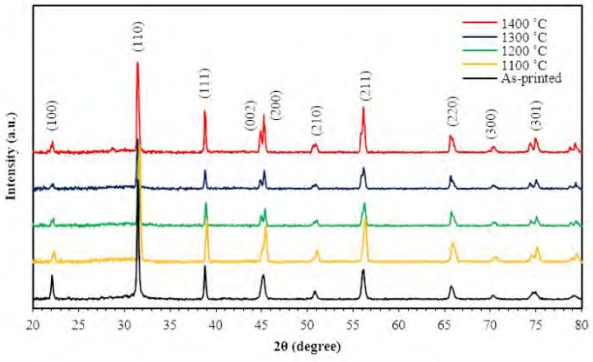

Figure 1. XRD in range from 2θ = 20 to 80 for as-printed sample and samples sintered at 1100, 1200, 1300, and 1400 °C.

3.3 Piezoelectric property

Piezoelectric coefficients (d_{33}) of the sintered samples at various temperature were measured using d_{33} meter. BT ceramic sintered at 1100 and 1200 °C resulted in 103 pC/N, which is lower than the samples sintered at 1300 and 1400 °C. It is assumed that these samples retain high number of voids (as shown in Figure), which means relatively lower density so that it led to low piezoelectric coupling effect when induced by mechanical stress. However, the d_{33} was improved to 128 and 200 pC/N as the sintering temperature increases respectively to 1300 and 1400 °C. It is assumed that the significant increases of d_{33} stems from following reasons: increases in 1) density and grain size and 2) tetragonality that gives higher dipole moment to electrical changes [17].

3.4 Dielectric property

The sintering temperature on the 3D printed BT ceramic increases the dielectric constant at 10^3 Hz from 1580 to 4730 respectively at 1100 and 1400 °C. This high dielectric constant is correlated with its high tetragonality observed in range from 2θ = 44 - 46° in XRD peak [17]. The tetragonality of BT ceramics increased as the sintering temperature increased as evidenced by an increase in extent of peak splitting. Therefore, this increasing dielectric contents are a good agreement with increasing tetragonality. All of dielectric loss measured at 10^3 Hz result in lower than 0.033 as shown in **Error! Reference source not found.**(b), which is desired value for application because of low energy loss [18].

4. Conclusions

BT ceramics were fabricated by PE 3D printing technique and studied in terms of piezoelectric and dielectric properties. To achieve high-density of BT ceramics, the binder (PVDF + DMF) concentration plays an important role in the chemical formulation. The proper chemical interaction and network between BT surface and PVDF solution can be created by the aligned fluorine and hydrogen atoms bonded to BT surfaces through hydrogen bonding within empirical value of 1:10 (PVDF:DMF). To achieve maximum

density of 3D printed BT ceramic, 1:8.8 was found for the maximum binder ratio with good viscosity and retention of desired geometry while holding the maximum BT content of 35.45 vol.%. Highest density of 3.93 g/cm^3 (65.3% of theoretical value) was achieved by sintering at 1400 °C. A high piezoelectric and dielectric properties, 200 pC/N and 4730 at 10^3 Hz respectively were obtained. These results demonstrate the high feasibility in its commercial application for sensor and energy fields such as automobile, biomedical, aerospace, and defense etc. Utilization of the PE 3D printing and simple method of the suspension synthesis are expected to enable massive production, customization, geometrically complex shape of bulk piezoelectric and dielectric devices for next generation technology.

References

1. Qiu, J., et al., *Fabrication of Pb (Nb, Ni) O3-Pb (Zr, Ti) O3 piezoelectric ceramic fibers by extrusion of a sol-powder mixture.* Journal of intelligent material systems and structures, 2004. **15**(8): p. 643-653.
2. Peng, E., et al., *Ferrite-based soft and hard magnetic structures by extrusion free-forming.* RSC Advances, 2017. **7**(43): p. 27128-27138.
3. Karaki, T., et al., *Lead-free piezoelectric ceramics with large dielectric and piezoelectric constants manufactured from BaTiO3 nano-powder.* Japanese Journal of Applied Physics, 2007. **46**(2L): p. L97.
4. Zhu, J., et al., *Phase coexistence evolution of nano BaTiO3 as function of particle sizes and temperatures.* Journal of Applied Physics, 2012. **112**(6): p. 064110.
5. Takahashi, H., et al., *Piezoelectric properties of BaTiO3 ceramics with high performance fabricated by microwave sintering.* Japanese journal of applied physics, 2006. **45**(9S): p. 7405.
6. Vijatović, M., J. Bobić, and B. Stojanović, *History and challenges of barium titanate: Part II.* Science of Sintering, 2008. **40**(3): p. 235-244.
7. Nguyen, D.Q., et al., *Electrical and physical characterization of bulk ceramics and thick layers of barium titanate manufactured using nanopowders.* Journal of Materials Engineering and Performance, 2007. **16**(5): p. 626-634.
8. Kim, H., et al., Increased piezoelectric response in functional nanocomposites through multiwall carbon nanotube interface and fused-deposition modeling three-dimensional printing. MRS Communications, 2017: p. 1-7.
9. Shishkovskii, I., M. Kuznetsov, and Y.G. Morozov, *New methods for development of three-dimensional ceramics based on barium hexaferrite with chromium additives.* Glass and Ceramics, 2003. **60**(5-6): p. 174-178.
10. Gureev, D., R. Ruzhechko, and I. Shishkovskii, *Selective laser sintering of PZT ceramic powders.* Technical Physics Letters, 2000. **26**(3): p. 262-264.
11. Huang, T., et al., *Aqueous-based freeze-form extrusion fabrication of alumina components.* Rapid Prototyping Journal, 2009. **15**(2): p. 88-95.
12. Lu, X., et al., *Solvent-based paste extrusion solid freeforming.* Journal of the European Ceramic Society, 2010. **30**(1): p. 1-10.
13. Cesarano, I. and R. Segalman, *Robocasting provides moldless fabrication from slurry deposition.* Ceramic Industry, 1998. **148**(4): p. 94-100.
14. Barsykov, V. and V. Khomenko, *The influence of polymer binders on the performance of cathodes for lithium-ion batteries.* Rigas Tehniskas Universitates Zinatniskie Raksti, 2010. **21**: p. 67.

tetrafluoroethylene resin. in *American Industrial Hygiene Association Annual Meeting*. 1955.

15. Nagata, K. and T. Kiyota, *Piezoelectric Properties of Low Coercive-Field BaTiO3 Ceramics and Its Application.* Japanese journal of applied physics, 1989. **28**(S2): p. 98.
16. Subramaniam, S., *In situ high temperature environmental scanning electron microscopic investigations of sintering behavior in barium titanate*. 2006, University of Cincinnati.
17. File, P.D., *Joint committee on powder diffraction standards.* ASTM, Philadelphia, Pa, 1967: p. 9-185.
18. Lin, Y. and H.A. Sodano, *Fabrication and electromechanical characterization of a piezoelectric structural fiber for multifunctional composites.* Advanced Functional Materials, 2009. **19**(4): p. 592-598.

Pool Boling Heat Transfer- Setup

Mahamudur Rahman[1] and Jaime Avendano[2]

University of Texas at El Paso, El Paso, Texas, 79902, United States

ABSTRACT

Thermal Engineering has been a subject of extensive research over the last years. Different methods had been employed to augment heat transfer rates. This Pool boiling setup is aiming to try a different approach by using a tube array. Other factor considered on this setup is the ability to withstand 20 bar pressure. This approach will provide new results on the pool boiling area as well as a new method to augment heat transfer rates.

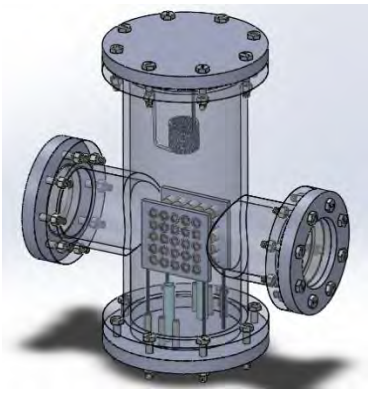

Fig.1. Shows the chamber designed to conduct pool boiling experiments.

Nomenclature

t	= Time
ρ	= Density
v	= Volume
C_P	= Specific Heat in Constant Pressure
T_{sat}	= Saturation Temperature at 10 bar
T_{atm}	= Room Temperature
P	= Power

Chamber Development

The setup requires a chamber design that is capable to withstand a 20 bar pressure. In order for the chamber to operate safely under high pressure conditions, 304 stainless steel was selected for the chamber. A 0.6-inch-thick tempered borosilate glass is going to be used for visualization purposes [1]. The tightening mechanism used for the chamber is 18-8 Stainless Steel Extra-Wide Hex Head Screw, which is able to withstand high pressure and high temperature environment.

The pool boiling experiment is going to be conducted using a tube bundle of 5x5 array. The tubes have a diameter of 20 mm and copper was the selected material. In order to maintain the water temperature at 180°,six heaters were placed in the bottom. In order to obtain accurate readings during the testing the heaters are placed 25mm away from the tube bundle. A representation of the parts discussed can be observed on figure 1.

Calculations

The chamber was designed with a viable small volume in order to avoid the demand of high power required to raise the temperature at 180°. The time to reach 180° can be calculated using the formula (1)

$$t = \frac{\rho v C_P (T_{sat} - T_{atm})}{P} \quad (1)$$

With the design measurements the time needed to reach the temperature is 0.52 hour with a power of 3000 watts.

References

[1] Eric C. Forrest , Lin-Wen Hu , Jacopo Buongiorno & Thomas J. McKrell (2013) Pool Boiling Heat Transfer Performance of a Dielectric Fluid With Low Global Warming Potential, Heat Transfer Engineering, 34:15, 1262-1277, DOI: 10.1080/01457632.2013.793103

PROBABILISTIC EVALUATION OF 304 STAINLESS STEEL USING SINE HYPERBOLIC CREEP-DAMAGE MODEL

Md Abir Hossain[1]*, Calvin M Stewart [1]
[1] Department of Mechanical Engineering, The University of Texas at El Paso, El Paso, TX 79968, USA
* Corresponding author (mhossain9@miners.utep.edu)

Keywords: *Creep-deformation, Minimum-creep-strain-rate, Monte-carlo simulation, Sine-hyperbolic creep damage model, Creep-rupture*

ABSTRACT

An important aspects to be considered in creep testing is repeatability; i.e. the variation in measurements observed in replicate tests. When the results of many replicate creep tests are aggregated together, the minimum-creep-strain-rate, stress-rupture, and creep deformation curves exhibit significant scatter band. Typically continuum damage mechanics (CDM) based constitutive models are applied deterministically where the uncertainty of experiments is not considered. This is also true for the Sine-hyperbolic (Sinh) CDM-based constitutive model where the model is calibrated to represent 50% reliability of creep data. There is a need to implement Sinh in a more stochastic manner. The objectives of this study is to incorporate the probabilistic feature in the Sinh creep damage model to reliably predict the minimum-creep-strain-rate, stress-rupture and creep deformation. This will be achieved using Monte-Carlo methods. Creep deformation data for 304 Stainless Steel is collected from literature consisting of tests conducted at 300 and 320 MPa at 600°C with five replicates. The replicate tests exhibited substantial scatter in the minimum-creep-strain-rate, stress-rupture, and overall creep deformation. Subsequently, upon calibration using the Sinh model, the material constants among the replicates varied. The trends of uncertainty carried by each material onstant is studied. The interdependence of the material constants is evaluated to determine if the uncertainty carried by each material constant can be regressed using a co-dependence function. The uncertainty in the Sinh model is affected by stress variation in the operating condition. Pre-existing and sub-surface defects are evaluated numerically to feed into the uncertainty calculation. The Monte Carlo method was applied to determine the extent that the creep deformation curve varies taking into consideration the variability of the material constants, stress fluctuation and intrinsic defects. Monte Carlo simulations show that the predicted creep deformation persists within the bounds of the experimental data. In future work, this statistical method will be applied to the temperature dependency and inter-dependence of the material constant to quantitatively establish the reliability of the Sinh model in simulating component-level creep deformation to rupture.

1 Sine-Hyperbolic Creep Damage Model

Sine Hyperbolic (Sinh) is CDM-based model has been developed to model the secondary and tertiary creep stages of a typical creep curve[1]. The Sinh model was developed by analyzing classic and contemporary CDM-based models to determine the optimal functional form. Recent studies show the Sinh model exhibits ease of calibration and improved accuracy in creep deformation, damage, and rupture predictions when compared to several constitutive

models[2-4]. The coupled Sinh creep damage constitutive model consists of a creep-strain-rate and damage evolution equation as follows

$$\dot{\varepsilon}_{cr} = A\sinh\left(\frac{\sigma}{\sigma_s}\right)\exp(\lambda\omega^{3/2}) \tag{1}$$

$$\dot{\omega} = \frac{M[1-\exp(-\phi)]}{\phi}\sinh\left(\frac{\sigma}{\sigma_t}\right)^{\chi}\exp(\phi\omega) \tag{2}$$

where $A, \sigma_s, \lambda, M, \phi, \sigma_t$, and χ are material constants, stress, σ is an external variable, and damage, ω is an internal state variable that evolves from zero to unity. All the materials constants are calibrated based on the experimental data gathered from the literature[5]. A detailed monograph of the material constant calibration can be found in Hossain and Stewart[6].

2 Monte Carlo Method

The Monte Carlo (MC) simulation method is integrated into the calibrated material constants of the Sinh model using a subroutine developed in MATLAB. The inputs of the subroutine are the applied stress and temperature and the calibrated average, maximum, and minimum value of each material constant. The amplitude and range for each of the material constant is calculated using the [Eq. (3)] and [Eq. (4)].

$$X_{amp} = \frac{X_{\max} - X_{\min}}{2} + X_{\min} \tag{3}$$

$$\Delta R = \frac{X_{\max} - X_{\min}}{2} \tag{4}$$

where, X_{amp}, $X_{\max}$, $X_{\min}$, and ΔR represent the amplitude, maximum, minimum and range of the each of the material constant. The calibrated amplitude and range is feed into the subroutine with a uniformly distributed random function that generates random number between -1 and 1.

$$X_{unc} = X_{amp} + rand(\Delta R) \tag{5}$$

where, X_{unc} represent the predicted uncertain material constant. For each Monte Carlo simulation, a unique set of uncertain material constant is provided. These material constants are feed into the Sinh model to produce unique minimum-creep-strain-rate, creep-rupture, and creep deformation predictions. The results of many simulations are needed to reliably draw a conclusion about the uncertainty of the creep predictions. In the current study, the minimum number of Monte Carlo simulations per creep curve, N is set equal to the number of uncertain material constants squared. Uncertainty was introduced in 4 material constants of Sinh model, offset of the primary creep regime and the stress fluctuation that steered to 36 Monte Carlo simulations for each creep tests.

3 Result and Discussion

3.1 Creep Deformation using Monte Carlo Method

Monte Carlo simulation technique is applied to establish the creep deformation prediction for the Sinh model. Since the material constants of Sinh model carry the inherent randomness,

the uncertainty was introduced by the application of Monte Carlo method. As the uniformly distributed random number generator function is used for the uncertainty calculation, the predicted material constant always oscillates between the range of maximum and minimum

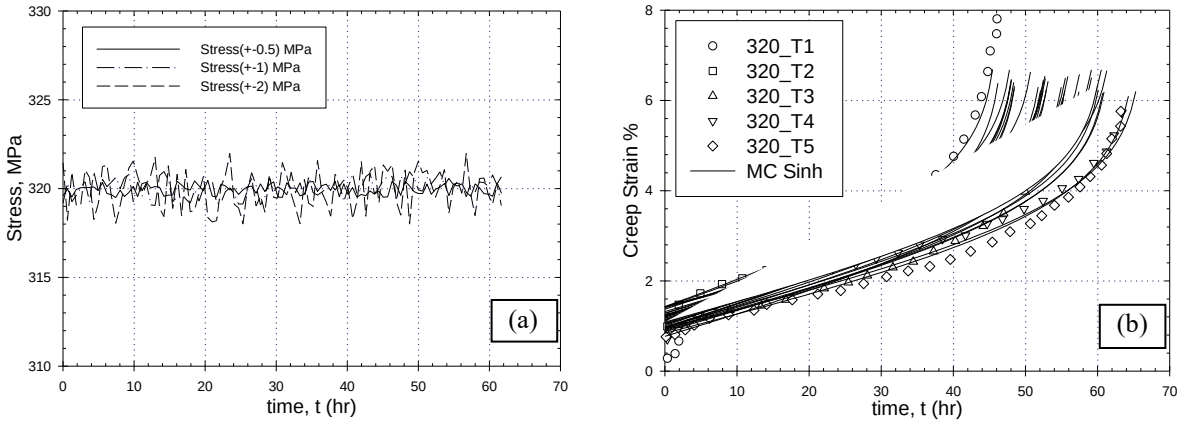

Fig. 1 Monte carlo simulated a) stress fluctuation and b) creep deformation curves at 600 °C subjected to 320

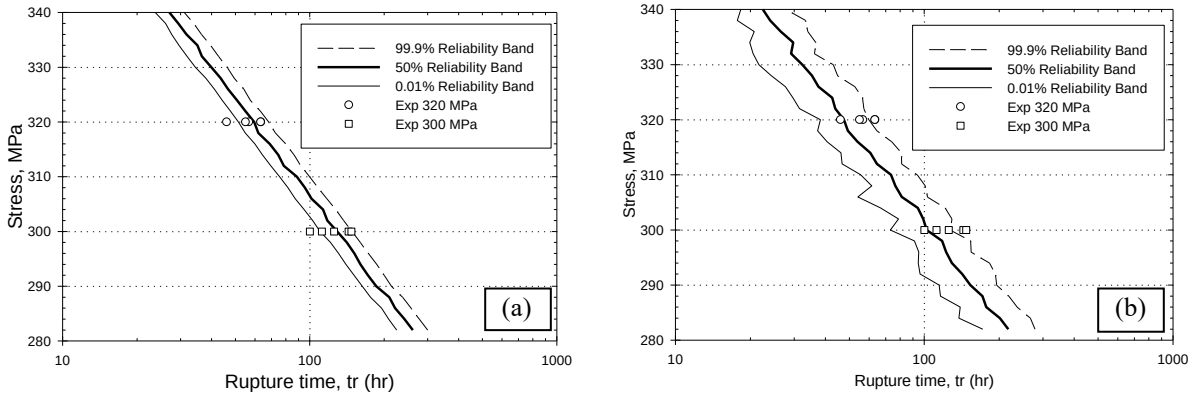

Fig. 2. Reliability band for stress-rupture a) including pre-existing damage uncertainty and b) incorporating pre-existing damage and material constant uncertainty

The stress sensitivity is incorporated in the model at three steps. Stress fluctuation is calibrated at (+/-) 0.5, (+/-) 1, and (+/-) 2 MPa that is illustrated in the Fig. 1(a). The stress dependency is incorporated in the model along with the predicted material constant to generate the creep deformation curve. Fig. 1(b) shows that predicted creep deformation curves remain within the bounds of the experimental data. The width of the predicted curves have a tendency to over predict as the predicted material constants and stress fluctuations are interfering with each other.

Pre-existing and sub-surface defect is considered for the probabilistic assessment of 304 SS. The experimental creep data shows significant scatter and one of the source of this randomness is the presence of pre-existing defect. The test data with the longest rupture time is taken as the base point and initial damage in this case is considered to be 0 i.e. $\omega_o = 0$.

Taking the material constant of this test data as fixed, the rupture time for the test with the shortest rupture time is achieved with only varying the initial damage, ω_o. For calibrating the rupture time, damage rate equation [Eq. (2)] is integrated within the limit from ω_o to 1, resulting in following equation.

$$t_r = \frac{-\frac{1}{1-\exp(-\phi)}\left[\exp(-\phi)-\exp(-\phi\omega_o)\right]}{M\sinh\left(\frac{\sigma}{\sigma_t}\right)^{\chi}} \tag{6}$$

Fig. 2(a) illustrates the reliability bands for the Sinh model with introducing the randomness only in the initial damage ω_o and fixing all the material constants. Fig. 2(b) represents the reliability bands taking into consideration of all the sources of randomness. The reliability bands show good agreement with the experimental results.

3 Conclusion

In this study the research objective was to integrate the probabilistic phenomenon in the Sinh creep-damage model. Sinh model has been applied successfully to describe the creep behavior deterministically. Addition of stochasticity in the Sinh model is going to better equip the model to encompass all the sources of randomness in the conventional creep test. Future work of this current research will include the temperature dependency in the Sinh model. As long-term creep test is a high temperature-stress experiment, so small variation in the temperature regime will affect the creep-rupture. Inclusion of the temperature dependency will be another source of uncertainty. Combining all these sources of uncertainty, final predicted master curves for the creep deformation will be generated. The reliability bands for the minimum-creep-strain-rate and stress-rupture will be established that will enable the application of the Sinh model to predict the creep behavior with more precision and accuracy.

References

[1] Stewart, C. M. “A Hybrid Constitutive Model for Creep, Fatigue, and Creep-fatigue Damage” Doctoral dissertation, University of Central Florida Orlando, Florida. 2013. DOI.momrg.cecs.ucf.edu/theses/StewartC_PhD.pdf

[2] Haque, M. S. and Stewart, C. M. “Modeling of creep deformation, damage and rupture of hastelloy x using mpc omega, theta-projection and sine-hyperbolic models.” *International Journal of Pressure Vessels and Piping (2016)*

[3] Cano, J., Stewart, C. M. “Application of the wilshire stress-rupture and minimum-creep-strain-rate prediction models for alloy p91 in tube, plate and pipe form.” *Proceedings of ASME Turbo Expo 2019: Turbomachinery Technical Conference and Exposition* GT2019-90625. Phoenix, AZ, June 17-21, 2019.

[4] Perez, J., Stewart, C. M. “Assessment of the theta projection model for interpolating creep deformation” *Proceedings of ASME Turbo Expo 2019: Turbomachinery Technical Conference and Exposition* GT2019-90267. Phoenix, AZ, June 17-21, 2019.

[5] Kim, S., Kong, Y., Roh, Y., and Kim, W. “Statistical properties of creep rupture data distribution for STS304 stainless steels.” *Materials Science and Engineering A Vol. 483* (2008): pp. 529–532. DOI.org/10.1016/j.msea.2006.12.153

[6] Hossain, Md Abir, Stewart, C. M. “Reliability assessment of 304 stainless steel using sine-hyperbolic creep-damage model with monte carlo simulation method.” *Proceedings of ASME Pressure Vessel and Piping Conference PVP 2019*: PVP2019-93712. San Antonio, TX, July 14-19, 2019.

Shock and Vibration Testing of the Orbital Factory II CubeSat

Arthur S. Bruno,[1] Hector Echevarria[2]
University of Texas at El Paso, El Paso, TX, 79968, United States

Orbital Factory II is a 1U CubeSat project intended to test the viability of an electronics repair platform and an experimental S-Band antenna. The launch, deployment, and life environments are strongly characterized as part of this mission. Launch will be supplied by the NG12 mission, a Northrop Grumman Antares rocket with the satellite aboard a Cygnus capsule. Deployment will be from the Japanese Experiment Module's airlock aboard the International Space Station, into Low Earth Orbit, or as a part of the Cygnus capsule CubeSat launcher. The purpose of this paper is to describe the various analysis and documentation performed as a part of the shock and vibe study done for the Orbital Factory II project. Early stage testing shows that the new design developed for the printer apparatus survives the vibrational environment with appreciable margin.

I. Nomenclature

LEO = Low Earth Orbit
OFII = Orbital Factory II
TML = Total Mass Loss
CVCM = Collected Vacuum-condensable Materials
ASTM = American Society of Testing Standards
NRCSD-E = NanoRacks External CubeSat Deployer
G_{rms} = G root mean square

II. Introduction

The Orbital Factory II (OFII) satellite is a 1U CubeSat which will perform a preliminary investigation into solar panel repair in a microgravity environment using additive manufacturing methods. This experiment's goal is to serve as a proof of concept test to verify the experimental viability of using a conductive silver paste to mend damaged electronic components in situ. The secondary payload is an S-band antenna manufactured using a novel method. The antenna itself was provide by Lockheed Martin Space Systems Company, manufactured using a proprietary nanocopper surface embedding process. In order for successful operation of the satellite, considerations must be made to account for the different environments that the CubeSat will be exposed to. The Orbital Factory II (OFII) CubeSat must survive both the shock and vibration inherent to the launch. In order to characterize these conditions, the mission's flight provider Nanoracks has issued a document detailing the specific parameters of each environment. Specific strategies and preliminary testing of the Orbital Factory II components is found in this document.

Vibrational testing is mission critical for this satellite. Though the components themselves are built and tested to a specialization by their individual manufacturer that ensure they will survive the launch environments, the primary concern inherent to the shock and vibe testing is the integrity of electrical harnesses and other components. As identified in a comprehensive NASA study[2] on modes of failure for CubeSats, shock and vibration presents a significant risk of Dead on Arrival failures for Cubesats.

[1] Undergraduate Research Assistant, Center for Space Exploration and Technology Research
[2] Undergraduate Research Assistant, Center for Space Exploration and Technology Research

III. Vibration and Shock Testing

As part of the testing requirements, the OFII satellite must be able to withstand a dynamic flight environment of the mission applicable launch vehicle. For the OFII mission, an Antares rocket will be used to achieve Low Earth Orbit (LEO). In order to be qualified for launch as part of provider requirements, vibration testing must be conducted by integrating the CubeSat into the Nanoracks CubeSat External Deployer (NRCSD-E), or a mechanically equivalent test fixture. For testing purposes, a mechanically equivalent test pod will be manufactured in order to conduct the vibration tests. Nanoracks has identified two (2) primary vibration profiles: In-Plane Random Vibration Test Profile and an Out-of-Plane Random Vibration Test Profile[1]. The data used to configure these vibration profiles are shown below:

Table 1: In-plane Random Vibration Test Levels and Duration

Frequency (Hz)	ASD (g^2/Hz)
20	0.016
30	0.025
800	0.025
2000	0.016
G_{rms}	6.55
Duration	60

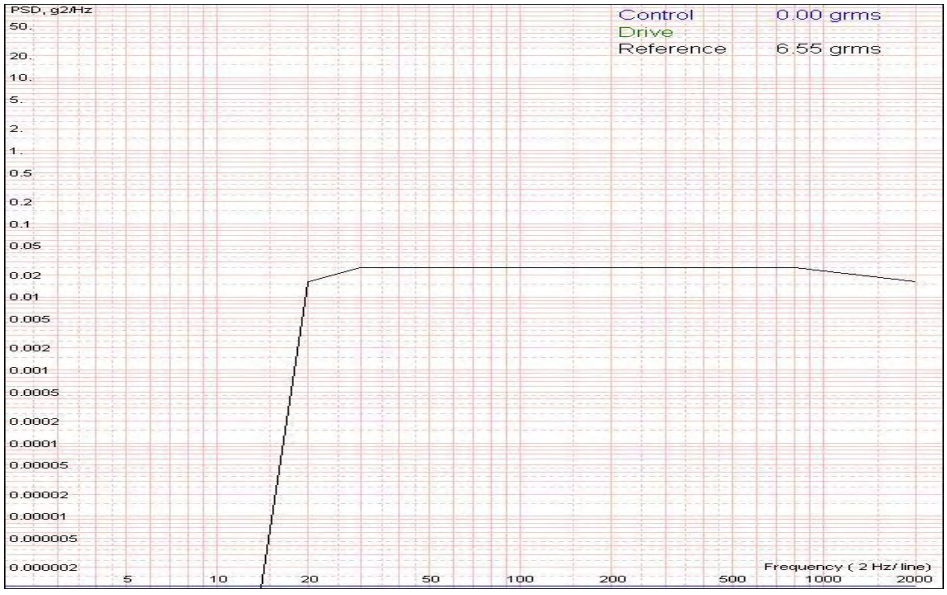

Figure 1: In-Line Random Vibration Profile

Table 2: Out-of-Plane Random Vibration test Levels and Duration

Frequency (Hz)	ASD (g^2/Hz)
20	0.016
30	0.05
800	0.05
2000	0.016

G_{rms}	8.45
Duration	60

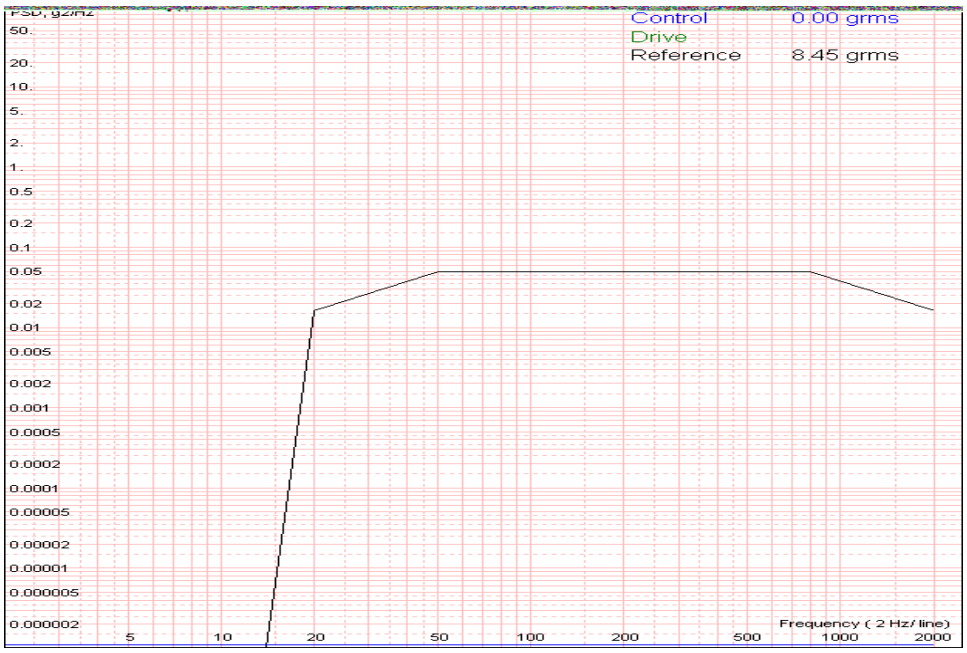

Figure 2: Out-of-Plane Random Vibration Profile

Vibration testing will occur inside the mechanical equivalent test pod with three (3) orientations to ensure that testing is conducted with vibration parallel to all three axis of the CubeSat. Once the test is completed for all three orientations, there will be an inspection of the CubeSat to determine if any damage occurred from the vibration. A post-vibration functionality test, as well as accelerometer response plots will be included in a final test report to Nanoracks for flight qualification.

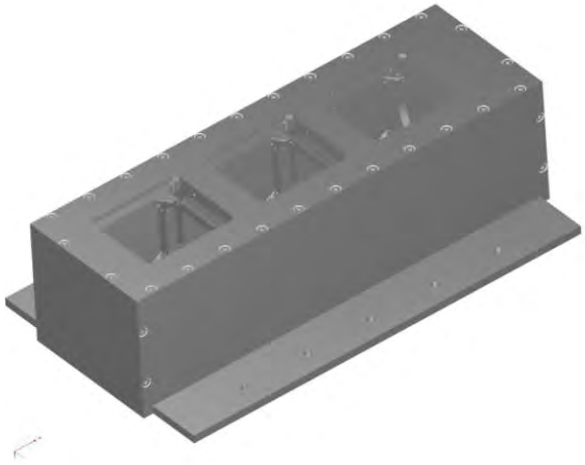

Figure 3 - Mechanically Equivalent 3U Test Pod Design

Post-vibration test records must include evidence that all external components are properly installed and do not an pose an appreciable risk of module or fastener detachment becoming loose. To meet this criterion, all external fasteners will be marked with a straight line after installing them to their specified torque and applying a thread-locker compound. A coincident line will be traced on the OFII Exterior. Any loosening of the fasteners can be visually identified by verifying if the two lines remain coincident after vibration in all three orientations. Following is a figure depicting the fasteners.

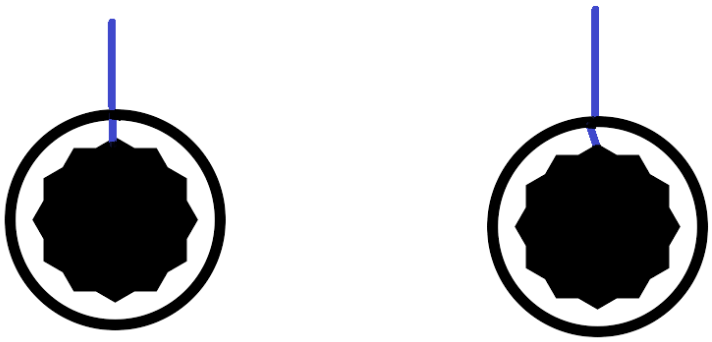

Figure 4 - Illustration of Visual Inspection of Fasteners

This visual inspection will ensure that there was no loosening of the fasteners after vibration; however, this does not out-rule the risk of loosening. The final torque of the fasteners may have been altered during vibration. If there is no visible movement of the fasteners, a first movement torque test will be done using a Tekton Model TRQ-21101 torque wrench. Pictures will be taken of the OFII CubeSat exterior after all vibration test scenarios have been successfully conducted. Individual pictures showing the coincident line between the CubeSat exterior and each fastener must be recorded at this point. First, the fasteners will be checked to see if they can be loosened by hand. Next, a torque wrench will be set to a value 10 in-lb. lower than the specified torque used to install the fastener. The fasteners will then be attempted to be loosened with the torque wrench. If no movement occurs, the torque is increased by one (1) in-lb. increments until arriving at the initial torque value used to install the fastener. If no movement occurs at any torque value, it can be concluded that the fastener remains properly installed and there is no risk of loosening.

IV.Preliminary Testing: Printer Nozzle

Initial vibration testing of individual components has been planned to ensure that the components that have not been qualified by the manufacturer can withstand the dynamic flight environment. Static testing has been planned on the printer nozzle assembly to ensure that the conductive ink remains encapsulated during the entirety of the mission launch. During these preliminary tests, there was no working fluid inside the nozzle of printer. The test was focused on observing the integrity of the wax seal before and after vibration. Once the testing was completed, water was inserted into the printer nozzle to determine if the seal was compromised. The Accelerometer response data for all three test orientations is shown below:

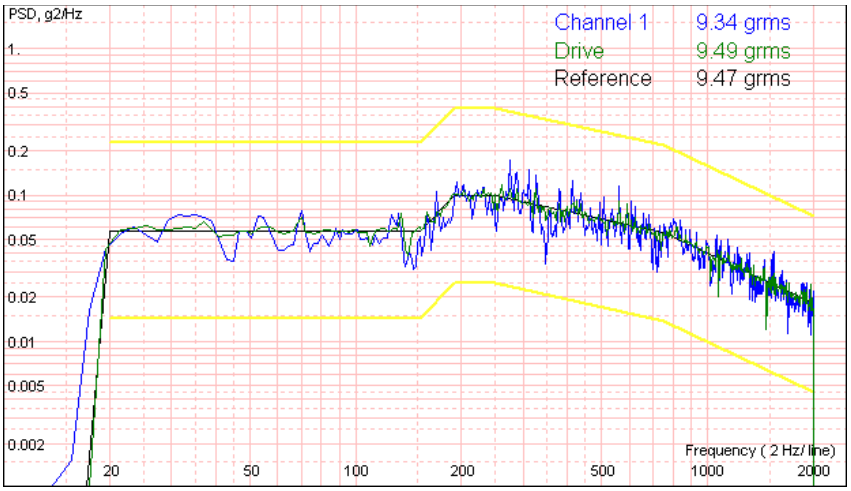

Figure 5 - Accelerometer Response for Nozzle with 2.1 mm of Wax - Orientation #1

Figure 6 - Accelerometer Response for Nozzle with 2.1 mm of Wax - Orientation #2

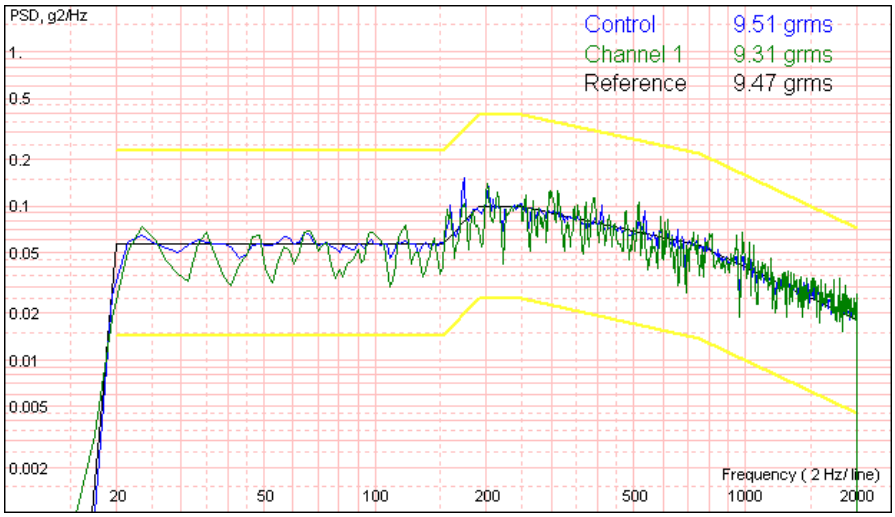

Figure 7 - Accelerometer Response for Nozzle with 2.1mm of Wax - Orientation #3

Post-Vibration inspection of the nozzle determined that there was no damage to the wax seal during all three (3) test configurations. Future testing for the printer assembly will include a vibration test of the complete printer assembly as well as a post-vibration functionality test to prepare for the integrated CubeSat vibration test required by NanoRacks.

The shock environment for the Antares launch has been characterized by Nanoracks. Individual components that are sensitive to shock must be identified and assessed on a case-by-case basis. The characterized shock environment is shown below:

Table 3 - CubeSat Deployer Shock Spectrum

Frequency (Hz)	Protoflight Level (g)
100	40
500	494
1000	989
100000	989

Since there is no verification for this, all efforts will be focused on meeting the random vibration requirements that are detailed above. Time constraints as well as limitations on equipment availability increase the complexity of creating a test scenario for this verification.

V. Conclusion

Environmental testing of the OFII CubeSat is critical to mission success. While many of the individual environmental requirements can be met by inspection or analysis, vibration testing of the integrated system in a test pod that is mechanically equivalent to the NRCSD-E is necessary to ensure proper flight qualification. Individual testing of CubeSat components has a given data set used to characterize the system response and mitigate any risk of failure in the final vibration qualification test or the overall mission. While the vibration testing deliverables necessary for the Nanoracks launch have not yet been met, the testing strategy and dynamic vibration environment have been characterized and detailed in this document, with the schedule for shock and vibe testing to proceed in the near future. The launch itself is scheduled for October/December, 2019, to be launched from Wallops, VA.

Acknowledgements

The material is based upon work supported by NASA under award No(s) NNX15AQ04A

References

[1] Daniels, Nathan, NR-NRCSD-S00004 – NanoRacks External CubeSat Deployer Interface Definition Document (IDD)

[2] Venturini, Catherin, TOR-2017-01689 – Improving Mission Success of CubeSats

Simultaneous Localization and Mapping with an Autonomous Unmanned Aerial Vehicle

Noah J. Lopez[1]
[1] Department of Electrical and Computer Engineering, The University of Texas at El Paso, El Paso, TX 79968, USA
njlopez@miners.utep.edu

Keywords: *SLAM, UAV, ROS, autonomous*

ABSTRACT

Simultaneous localization and mapping (SLAM) is the ability of mapping out an environment and being able to navigate within it. With an increase of unmanned aerial vehicles (UAV) or drones in society, it should only be reasonable to combine a SLAM algorithm with a UAV. Inevitably, there would be a need to create an autonomous solution that can greatly reduce risks when exploring unknown environments that contain harmful elements to a person. With the Robot Operating System (ROS) and open-source programs, these risks can be nullified as exploration can be done by a drone.

Introduction

Traversing through unknown environments can pose many potential risks to people. In order to mitigate these risks, a way to explore an area without sending out a person should be implemented. Simultaneous localization and mapping, otherwise known as SLAM, is used for creating a map of an environment and being able to navigate within it. By combining this technique with an autonomous unmanned aerial vehicle (UAV), this eliminates any risks that a person may be exposed to in unknown environments. The drone of choice for this project is the Intel® Aero Ready-to-Fly (RTF) drone running the PX4 flight stack. It is equipped with the Intel® RealSense™ R200 camera which has depth/infrared and RGB cameras [1].

Fig. 1. Intel® Aero Ready-to-Fly Developer kit [2].

With this drone, work on autonomous SLAM can be expedited due to not creating or building the drone itself. This project can be broken up into two separate problems. The first being to find a suitable algorithm to implement SLAM. As there are multiple solutions to the problem, it is most efficient to find the best suitable program first and foremost. The second problem being to program

the UAV or drone to navigate independently of human interaction. This will be a difficult problem to solve because of needing object detection and thus object avoidance among many other issues.

SLAM Algorithm

Many SLAM algorithms can be found in use with the Robot Operating System (ROS). A benefit of working with ROS is that it is open-source, allowing users to modify most programs to their own accord. Multiple programs for SLAM exist in ROS, however the program of choice will be RTAB-Map, developed by Mathieu Labb´e and François Michaud. From their research, Labb'e and Michaud have programmed a unique solution for the SLAM problem. In figure 2 a comparison of multiple SLAM approaches is shown as researched by Labb'e and Michaud.

	Inputs							Online Outputs			
	Camera				Lidar		Odom	Pose	Occupancy		Point
	Stereo	RGB-D	Multi	IMU	2D	3D			2D	3D	Cloud
GMapping					✓		✓	✓	✓		
TinySLAM					✓		✓	✓	✓		
Hector SLAM					✓			✓	✓		
ETHZASL-ICP					✓	✓	✓	✓	✓		Dense
Karto SLAM					✓		✓	✓	✓		
Lago SLAM					✓		✓	✓	✓		
Cartographer					✓	✓	✓	✓	✓		Dense
BLAM						✓		✓			Dense
SegMatch						✓					Dense
VINS-Mono				✓				✓			
ORB-SLAM2	✓	✓									
S-PTAM	✓							✓			Sparse
DVO-SLAM		✓						✓			
RGBiD-SLAM		✓									
MCPTAM	✓		✓					✓			Sparse
RGBDSLAMv2		✓					✓	✓		✓	Dense
RTAB-Map	✓	✓	✓		✓	✓	✓	✓	✓	✓	Dense

Fig. 2. A comparison of multiple SLAM approaches as researched by Mathieu Labb´e and François Michaud [3].

As seen in figure 2, RTAB-Map can accept a variety of user inputs such as RGB-D, Stereo, and LIDAR to provide depth images. "RTAB-Map (Real Time Appearance-Based Mapping) is an RGB-D, Stereo and Lidar Graph-Based SLAM approach based on an incremental appearance-based loop closure detector" [4]. Using their algorithm, it is possible to map an environment and display depth to the user. One problem with the Intel® RealSense™ R200 camera is its limited range of nearly 3 meters. This greatly affects the effectiveness of RTAB-Maps SLAM approach. As this project progresses, the Intel® Aero will be upgraded to include more advanced camera's such as the Intel® RealSense™ D415 or D435, both with a maximum range of approximately 10 meters [5]. At the moment, there are difficulties in getting RTAB-Map working correctly. There are times when it stops mapping due to either lack of features or too fast of movement. This is an issue and only with time and further research will this problem be solved.

Fig.3. Intel® RealSense™ D415 on left and Intel® RealSense™ D435 on the right [5].

Autonomous Programming

Autonomous programming is a very complex problem, as the SLAM algorithm would have been if not for ROS and open-source solutions. There are a lot of concerns when programming an autonomous vehicle. One must consider object detection and avoidance, as well as not being harmful or destructive to humans. There must be fail-safes involved that can override the UAV manually if a situation calls for it. In the case of not being able to manually take over the drone, one must have some sort of return-to-home function that will activate once it has gone past some distance from the user. One possible solution for programming is using MAVROS, which is a "MAVLink extendable communication node for ROS" [6]. This ROS node allows communication from a ground control station (GCS) to any autopilot that supports MAVLink. MAVLink, Micro Air Vehicle Communication Protocol, is the method of sending messages between drones/UAV's and ground control stations and was released by Lorenz Meier [7]. By using MAVROS with python scrips, one can control MAVLink-enabled autopilots, such as arming the safety or even telling the drone to take off or land. Another approach would be to use Dronecode. Dronecode is the MAVLink library created for the PX4 flight stack specifically [8]. It is very similar to MAVROS, in that it can be used to arm/disarm and tell the drone to land or takeoff. It uses the same communication protocol, MAVLink, as well. In fact, it was Meier who created the Dronecode SDK. Dronecode should work well with the Intel® Aero as it runs on the PX4 flight stack. However, there has not been any tests of the two software, so there is yet experimentation to be done with the programming of an autonomous drone.

Conclusion

Using open-source software, it appears quite feasible to create an autonomous drone or UAV utilizing SLAM algorithms. RTAB-Map is proving to be very user-friendly and able to accomplish SLAM well. There is still the matter of tuning parameters in RTAB-Map to improve the performance of mapping out environments. The programming of the autonomous drone has not been tested as of this writing and will need further research into the matter. This stage is expected to prolong the completion of this project, as there must be extensive testing to ensure that it is safe and can be used without the destruction of property or the drone itself.

References

[1] "Intel® Aero Ready to Fly Drone." *Intel*, www.intel.com/content/www/us/en/products/drones/aero-ready-to-fly.html.

[2] "Intel® Aero Ready to Fly Drone." *Intel*, click.intel.com/intel-aero-ready-to-fly-drone-2515.html.

[3] M. Labbé and F. Michaud, "RTAB-Map as an Open-Source Lidar and Visual SLAM Library for Large-Scale and Long-Term Online Operation," in Journal of Field Robotics, accepted, 2018. (Wiley)

[4] M. Labbé and F. Michaud. "RTAB-Map." RTAB-Map, introlab.github.io/rtabmap/.

[5] "Intel RealSense Depth Cameras." Intel RealSense, realsense.intel.com/depth-camera/#D415_D435.

[6] Ermakov, Vladimir. "Mavlink/Mavros." GitHub, github.com/mavlink/mavros.

[7] Meier, Lorenz. "Introduction." Introduction · MAVLink Developer Guide, mavlink.io/en/.

[8] Meier, Lorenz. "Introduction." Introduction · Dronecode SDK, sdk.dronecode.org/en/.

SIMULTANEOUS MAPPING AND LOCALIZATION OF AN AUTONOMOUS DRONE

N. Habib[1]*, A. Flores-Abad[1], M. McGee[1], A. Choudhuri[1]
[1] Mechanical Engineering, University of Texas at El Paso, El Paso, TX 79968, USA;
*Corresponding author (nrhabib@miners.utep.edu)

Keywords: *Autonomous, Drone, Mapping, Localization*

ABSTRACT

The main goal of this project is to enhance existing, and well-developed technology to support autonomous UAS navigation, obstacle avoidance, and data-link capabilities for airborne inspection of power plants. Through the use of a GPS-denied Inspection System (UGIS), a small, unmanned quad copter is being integrated with autonomous navigation and simultaneous localization and mapping (SLAM). This allows the quadcopter to not only build maps in real time, but also localize itself in these maps. Consequently, the quadcopter can gain the ability to navigate indoor, and eventually outdoor, spaces with machine vision in all directions.

1 Overall Architecture

1.1 Drone Selection

The Intel aero Ready-to-Fly drone offers a low-budget system that is equipped with an Intel Compute Board. It also offers a full Intel RealSense system with prebuilt setup with an integrated flight controller, co-processor, and FPGA based peripheral bus. Additional components required for the drone were limited, allowing for an easy set-up process. This also meant fast track development on SLAM with autonomous navigation and flight-testing was capable right out of the box.

Fig.1. Drone Diagram

1.2 Drone Architecture

The drone was connected to a display monitor along with a keyboard and mouse for a fully functioning computer. Instead of a lithium polymer battery, a power source was created using a power supply and a XT60 connector. Currently, the quad copter is still being equipped for mapping. To do so, Ubuntu was installed to connect to the flight control software and mission planning software called QGroundControl through Wi-fi.

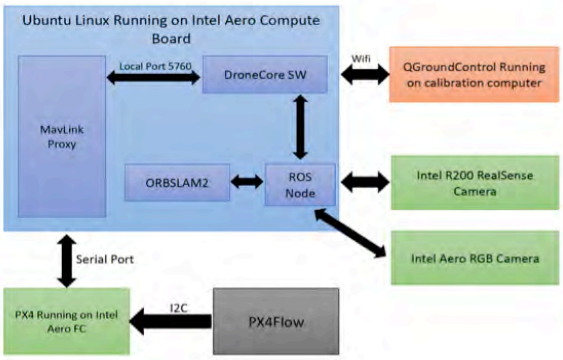

Fig.2. Final design architecture

2 Software Development

2.1 Camera Testing

In order to have a functioning mapping software, the camera has to function as well. The first step to do this is to install the Robotic Operating System (ROS), which is a collection of software frameworks and tools that help build robot applications. Once completed, the camera nodes were launched and then tested to ensure that the mapping software functions properly.

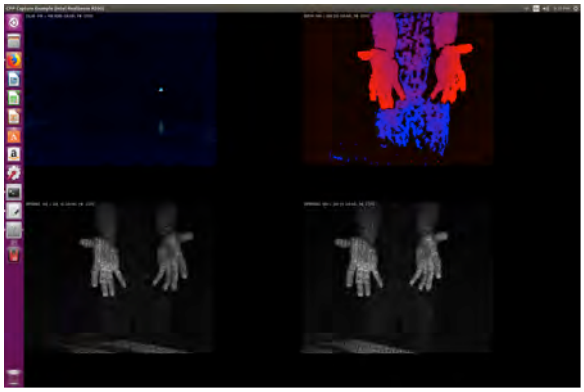

Fig.3. Camera Output

2.2 SLAM Algorithm

The mapping software that was selected was the SLAM (Simultaneous Localization and Mapping) algorithm. This was chosen because it simultaneously maps the unknown environment as well as keeping track of the previously mapped locations. By combining the use of the RealSense camera within the drone and the SLAM algorithm, one cohesive solution for power plant inspection can be created.

2.3 Dependency Installations

Before SLAM could be installed, there were various dependencies that needed to be installed to ensure that SLAM will have full function. The installation of these programs is crucial and can require a great deal of time due to the size of the files. An outline of the dependencies is given below:

RTAB-Map: Loop closure detector to ensure that the same area is not mapped to memory more than once. This allows for storage to be used more efficiently. RTAB-Map also ensures that if a repetition of mapping occurs, that there were no errors within the first mapping.

Pangolin: Development library for managing display and interaction of video input. This helps to modularize 3D video streams without adding any complexity. Pangolin also helps with handling navigation through codes written for several platforms including Linux, which is the platform being used for this project.

OpenCV: Open Source Computer Vision is a library written in C/C++ to be used for real-time applications. The library takes advantage of multi-core processing and takes advantage of the compute platform's specific hardware.

Eigen3: Template library for linear algebra—matrices, vectors, and related algorithms. This is useful for storage of what is being mapped by SLAM.

2.3 Mapping using RTAB-Map

RTAB-Map was first tested to make sure no area is mapped more than once. Before using SLAM, RTAB-Map was tested to ensure proper imaging.

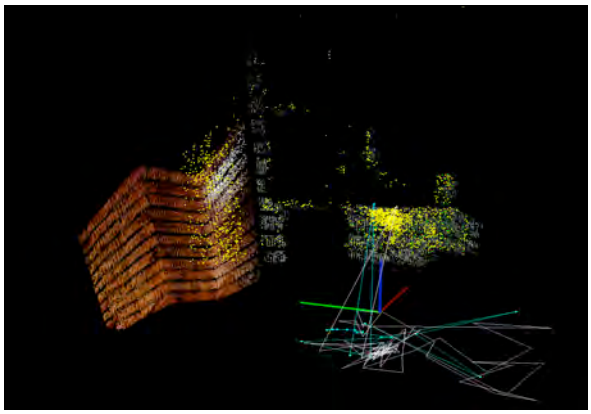

Fig. 3. RTAB-Map output

2.4 Mapping using SLAM

The objective of the initial test is to make sure that certain features of the area are being detected, such as corners and structures. Additionally, the trajectory in which the drone is moved in is also recorded. In the following picture, the drone was only moved in the Z-direction and the trajectory was recorded as such.

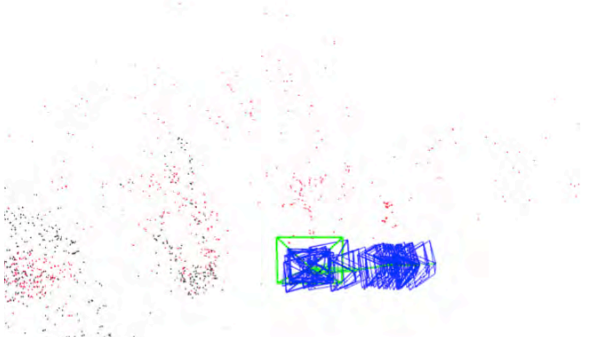

Fig.4. Trajectory

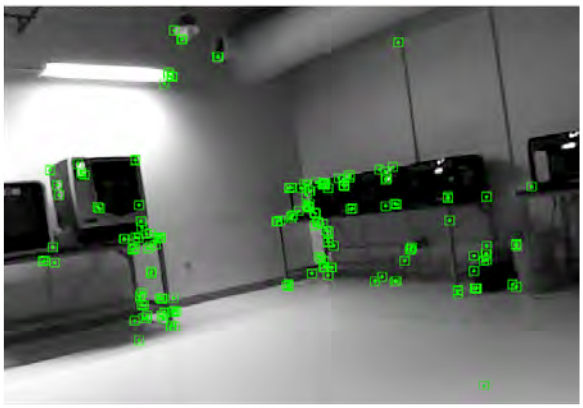

Fig.5. Mapping image output

3. Conclusion

Power plant inspection is important for the health and safety of not only those who work at the power plant but also those who live around it. Human error is inevitable when it comes to manual inspection. By implementing an autonomous drone for inspection, errors can me minimized and therefore the power plant can be more efficient and safe for everyone involved. Through furthering the use of the SLAM algorithm along with future code development, an autonomous drone for this purpose can potentially be created successfully.

References

[1] S. Luthra, *"Simultaneous Localization and Mapping on a Quadcopter"*. Master's Thesis, Cornell University, 2018.

[2] C. Fairchild, T. Harman "ROS Robotics By Example". 1st Edition, Packt Publishing, 2016.

[3] Intel-Aero. "Intel-Aero/Meta-Intel-Aero." *GitHub*, github.com/intel-aero/meta-intel-aero/wiki/01-About-Intel-Aero.

Software Development and Implementation of the tRIAC Data acquisition and control system

R M. Rojo, C Hansen, J. Quintana, A. Choudhuri
The University of Texas at El Paso, El Paso, TX, 79968, United States

I. Abstract

The Technology Research and Innovation Acceleration Park (tRIAC) located at Fabens, Texas, was established for the ongoing development and testing of the cSETR's liquid methane and liquid oxygen rocket engines. These engines range from a 5 lbf Reaction Control Engine (RCE) to the 500 lbf and 2000 lbf Centennial Restartable Oxygen Methane Engines, called CHROME and CHROME-X respectively. Alongside their development, a comprehensive control system managed with National Instrument's LabVIEW software and hardware is used. A lot of care has gone in its design for the safe handling and reliable monitoring and acquisition of the variety of installed pressure transducers, thermocouples, and flowmeters. This control system is housed in the Modular Instrumentation and Control Interface Trailer (MICIT), with a modular software design that eases adaptation to current and future experimental setups. This document goes into further detail of the development of the software to meet the necessary design criteria.

II. Nomenclature

CROME = Centennial Restartable Oxygen Methane Engine
cSETR = Center for Space Exploration and Technology Research
FPGA = Field Programmable Gate Array
LCH4 = Liquid Methane
LOX = Liquid Oxygen
MICIT = Modular Instrumentation and Control Interface Trailer
PT = Pressure Transducer
RCE = Reaction Control Engine
TC = Thermocouple
tRIAC = Technology Research and Innovation Acceleration Park
VI = Virtual Instrument

III. Introduction

The development of a propulsion system is a thorough process that necessitates a unique infrastructure for experimental testing. The Center for Space Exploration and Technology Research (cSETR) under the University of Texas at El Paso (UTEP) established the Technology Research and Innovation Acceleration Park (tRIAC) to provide this infrastructure for the testing of current and future rocket engine designs that utilize a mixture of liquid oxygen and liquid methane.

Engine development can be generally broken down to four stages: component, integration, system, and finally, acceptance level testing in that order. Each step in this process is performed to ensure that the components of an engine operate and work together as intended. Alongside this process is a comprehensive and exhaustive review of experimental procedures to ensure the safety of the personnel and the equipment involved when the engines are in operation.

As of this writing, three designs are planned for: a 5 lbf Reaction Control Engine (RCE) to the 500 lbf and 2000 lbf Centennial Restartable Oxygen Methane Engines, called CHROME and CHROME-X respectively for short. The risk of the substances used as propellants is only exacerbated by the high pressure and cryogenic state they will operate in. While the plumbing includes several safety mechanisms to protect from events such as over-pressurization and flow contamination, the software that controls the electronic valves in the engine offer an additional layer of defense along with recording a suite of test data. The tRIAC facility is constantly under development with new projects on the horizon, and an adaptable system was built to meet these ever-evolving demands.

Recording and monitoring all the sensors installed in any system is the Modular Instrumentation and Control Interface Trailer (MICIT). With the variety of anticipated experimental set-ups, and to reduce the time required to develop programs for new systems, the software is built with the same kind of modularity in its foundational structure.

First and foremost, the system must be safe and reliable. Every modification to the code undergoes QA testing to fix coding errors and to improve the user experience. From small details of making critical sensor readings easier to recognize in a front panel, to developing the logic that automatically initiates an emergency shutdown if necessary. The following sections explores these facets.

Figure 1: (left) Outside view of the MICIT trailer (right) wired compactRIO and compactDAQ

IV. Software overview

The responsibilities of the MICIT is twofold: Data acquisition and electronic valve control. To accomplish this, the MICIT system is equipped with both a compact DAQ (model: cDAQ-9189) and compact RIO system (model: cRIO-9066) pictured above. The installed hardware is outlined in *Initialization and Trouble Shooting of the MICIT system for LO2/LCH4 Engine Testing* by Corey Hensen [2].

A. Data Acquisition

The data acquisition side of the software was built using the *continuous measurement and logging* LabVIEW project template provided by National Instruments. This template sets the groundwork using an assortment of top-level Virtual Instruments (VI)s and sub-level VIs organized into libraries. The collection provides the necessary state machine logic for program initialization, along with displaying and, when prompted, logging all the sensor readings that are installed in any given experimental set-up. The cDAQ comes with three internal sampling clocks and has several modules to interpret signals from thermocouples and voltage readings from both single ended and double ended sensors that include, pressure transducers, load cells, accelerometers, and flowmeters. [3] These modules then dictate the additions and modifications made to the template's groundwork to take full advantage of the cDAQ.

Complementing these VIs and is detailed comments and explanations in both the front panel and underlying wire diagram that sets up the logic for a LabVIEW program.

Processing all the raw data is a host computer using a Windows 7 operating system running on dual 6th Generation, 4-core, 8-threated Xeon processors with 32 gigabytes of error-correcting code (ECC) random access memory. Each of these components were selected to promote overall system stability.

Finally, during data logging, a TDMS binary file is created that stores the sensor readings and valve states. This file format highly memory efficient as it contains only the lightly processed binary data that can either be read using NI's Diadem software, or further processed with other programs such as Matlab when CPU resources are more available.

B. Valve control

On the control side, the cRIO chassis system comes with a built in FPGA module used to dictate the states of the solenoid and motorized valves at any given time [1]. Its onboard 80 MHz clock allows for millisecond logic response times, thus limiting us to only the physical response times of any of the valves. Key thermocouple and pressure transducers have their signals split and shared between both the cDAQ from earlier and the cRIO. This allows the cRIO to directly receive feedback from those sensors and respond immediately and appropriately to any abnormalities even in the event of a loss of connection with the host computer. The advantage of using an FPGA in this configuration is for its ability to operate autonomously once it is active and can perform its function without the overhead of an operating system or program to interpret its readings.

Programming the FPGA is an entirely new feature added to the template mentioned earlier. To use the FPGA hardware, a bitfile is compiled so that the module can adjust itself at a hardware level to complete its programming. It can perform dynamic functions, meaning that the user can adjust the FPGA's variables in real time, such as manual valve control and/or perform its programmed functions that do not require any input from the user, such as an automated valve sequence or red-line response. [4]

The flow chart below illustrates a simplified breakdown of the FPGA logic found in the system:

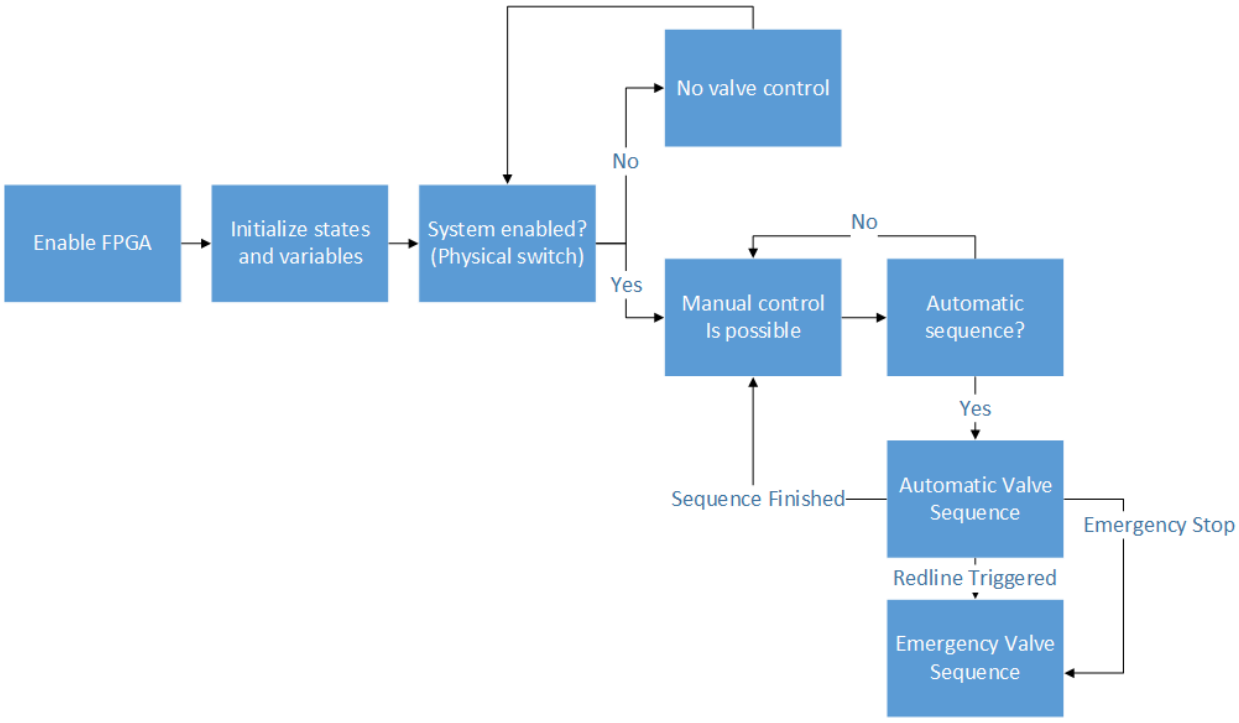

Figure 2: Basic flow chart of the FPGA logic.

V.User Interface

The first of the three current designs that will be tested is the 5 lbf RCE engine. At the time of this writing, the software for this configuration is the most complete and will be previewed and discussed in this section.

The primary RCE VI program is what the lead experimenter will see that will enable the control of the valve states, while also providing real-time sensor readings. As this is the first, it also serves as a trial run and basis for the next VIs that will be tested at tRIAC that will improve upon this overall design.

Figure 3: Front panel for the RCE testing. Allows for direct valve and automatic sequence control. Image shows simulated readings.

One example of a safety feature includes an inability to manipulate any valve and boolean variables unless a physical switch is flipped inside of the trailer, ensuring that the experimenters are aware the system is armed. In addition, a two-step software confirmation is required before the activation of an automatic sequence, reducing the chances of human error better ensuring that the experimenters are aware and prepared.

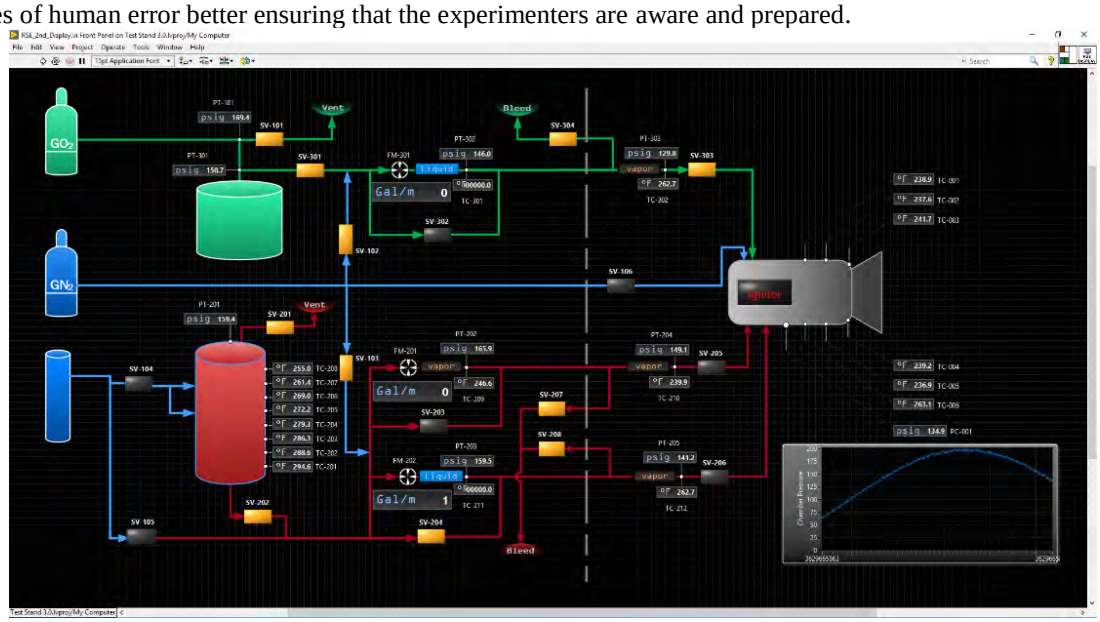

Figure 4: Secondary display that showcases a modified P&ID of the system plumbing and operating conditions. Intended for use in a large second monitor for a testing team to refer to.

It is an invaluable benefit for an entire testing team to be able to see the state of the system and not have to crowd around a monitor. A secondary display that organizes the sensors in a more intuitive manner makes it much easier for others to observe the condition of system.

VI.Future Work

Any kind software development is perpetual. There are always new functionalities to add, more efficient coding methods to implement, and more elegant ways to display and organize the arrays of data to the experimenters. Uninteded bugs that follow coding changes are a fact of life, it requires constant validation to resolve them to validate that a program is test-ready. The entire process behind the development of the existing code is currently being organized into a document for cSETR researchers to educate them of how to operate the system and to also facilitate the development of their overall labview and programming abilties.

References

[1] "NI Labs Includes Pioneer Release of C Interface to LabVIEW FPGA". *National Instruments Newsletter*, 2011.

[2] "Initialization and Trouble Shooting of the MICIT system for LO2/LCH4 Engine Testing" Corey Hensen, *Southwest Emerging Technology Symposium*, 2019

[3] "Getting Started with NI 951x C Series Modules and LabVIEW". pp. 29, 2011.

[4] "Designing High Availability Systems with CompactRIO and Compact FieldPoint". *National Instruments Newsletter, 2016*

SUMMARY ENERGY OUTREACH EFFORT AT UTEP FOR K12 STUDENTS

Daniela Morales[1], Yirong Lin[1], Lourdes Echegoyen[1], Norman Love[1]
[1] Mechanical Engineering Department, University of Texas at El Paso, El Paso, TX 79968, USA;
* Daniela Morales (dmorales23@miners.utep.edu)

Keywords: *renewable energy, engineering education, outreach program, future energy workforce, energy systems*

ABSTRACT

Established with the goal of encouraging prospective engineers to pursue a career in the energy system field, the UTEP Consortium for Integrating Energy System in Engineering and Science Education (CIESESE) organizes outreach events for students in grade levels K-12. During the first year, the CIESESE program at UTEP had a number of over 180 students participate in the outreach program and 30% of those students found that they never had a classroom experience that integrated renewable energy concepts prior to this session.

Currently the UTEP CIESESE program has five educational modules for both students and teachers that include PowerPoint presentations, exercise worksheets, in-class projects, and hands-on activities that educate the future workforce about energy. The modules and in-class exercises are adjusted based on the student's grade level. New educational modules that are more cost-effective and available for local El Paso teachers to adopt in their school programs have been developed. These new activities include projects that emphasize concepts associated with recycling and reusing everyday items for generation of renewable energy. They also include topics of distribution of energy and work output produced by windmills, watermills, wind turbines, and solar cars and use of materials such as plastic bottle caps, Styrofoam cups, popsicle sticks, and DC motors. These modules are publicly available on the UTEP CIESESE website http://engineering.utep.edu/ciesese.

1 Introduction

The Consortium for Integrating Energy Systems in Engineering and Science Education (CIESESE) program at UTEP has the mission of embracing and preparing future generations in the field of engineering and science. The consortium was established to prepare and educate the future energy workforce by implementing educational modules that consist of presentations and interactive videos and by integrating project-based learning exercises in the classroom to help students from K-12 better understand energy-related concepts. Past modules consisted of pre-made LEGO and other lab based activities, thus requiring some hands-on assembly. These modules were too expensive for teachers to adopt in their classroom. Because of school limitations, alternative experiments for broader teacher adoption were developed. New modules are low-cost effective, transferable to classroom curriculum, and promote the usage of recycled materials. In-class projects covered topics such as solar energy, wind energy, fuel cells, and conservation of energy.

2 Recent Efforts Made Within the CIESESE

During the past two years, the Consortium has integrated educational modules into K12 classroom curriculum. These modules have consisted of interactive PowerPoint presentations, videos, and in-class projects that demonstrated concepts such as work output, generation of power, and conservation of energy. The current project works with the NASA MUREP Aerospace Academy (MAA) for the Southwest at UTEP to reach more students and maximize impact. We worked closely with the MAA and their network of teachers. Modules received feedback from Elementary and HS teachers. As part of this project, both student and teacher workshops were developed. Summer and fall sessions were co-hosted with the MAA outreach program.

New modules include concepts on kinetic energy (work output by wind turbines), potential energy (work output by hydroelectric sources), solar energy, and fuel cells. These energy-based projects utilize reusable materials such as plastic bottle caps, Styrofoam cups, and popsicle sticks. The activities are intended to help students effectively communicate as a team and creatively come up with methods and solutions to overcome challenging obstacles. Feedback is gathered from surveys completed by teachers and students.

The modules were divided in categories corresponding to each respective grade level. The first module was developed for students in grade levels K-3rd. This individual project is designed for students to learn in a simple and interactive manner. During these activities, worksheets and instructions sets will be provided to the students so that they may build the windmill and record their observations.

Figure 1: Paper and Plastic Cup Windmill for K-3rd Students

The second module was developed for all grade levels. This project-based activity introduces the concepts from the PowerPoint presentations and videos on these hands-on experiments to the students. It mainly focuses on the power output generated by the DC motor for the wind

turbine to spin. The students are divided into teams of five. The teams have to build the wind turbine on a time limit of 60 minutes. The materials of the activity will be placed on a table and one member from each team shall collect what they need. The teams will be given a set of instructions, which is meant to guide them through every step; however, they can creatively come up with alternative building methods. The students will also be given a worksheet with formulas to calculate the power generated by the wind turbine. A teacher and undergraduate student assistant will be present to help the students if there is any confusion.

Figure 2: DC Motor-Powered Fan

The third module was developed for students in grade levels 5^{th}-12^{th}. This activity helps students put their newly-acquired knowledge from the presentation and videos into practice through this hands-on project. The experiment covers concepts, such as potential and kinetic energy. The modules and activities cover the concepts in greater depth and a high level of understanding is required. The students will be divided into groups depending on the class size. Each student will be assigned a task. Throughout the project, a rotational system will be enforced by the teacher and students will switch roles on a given time frame. A set of instructions, a certain limit of necessary items, and worksheet will be provided for each team, thus there will be no guidance given by the teachers. After building the water wheel project, their observations and calculations are recorded. This activity is intended to help the students work in teams, experience different roles in the project, utilize their time and resources wisely, and rely on one another. The students are expected to follow the set of instructions; however, they can creatively come up with alternative building methods. After the teams finish the activity on the given time limit, students will have to present their project and results to the class.

Figure 3: Homemade Water Wheel for Students in 5^{th}-12^{th} Grade

The last module is designed for students in grade levels ranging from 6^{th}-12^{th}. The activity focuses on the concepts and applications regarding kinetic energy, solar energy, and power output. The concepts introduced in the presentation and videos are to be put into practice into this hands-on activity. The students will be divided into teams. Each group will be provided a set of instructions, worksheet with formulas, and a limited amount of required supplies. A time limit of 90 minutes will be given for the students to complete the experiment. Each student will be given an assigned task. Throughout the project, a rotational system will be enforced by the teacher and students will switch roles on a given time frame. If there are any questions or concerns, the students must rely on their knowledge and team discussion. The projects allow the students to develop creative solutions and alternative methods to build their projects. A teacher and students assistant will be present throughout the activity, but students will have to rely on their knowledge for the majority of the time. After completing the project, the teams must present their findings and demonstrate how their newly-built solar car works.

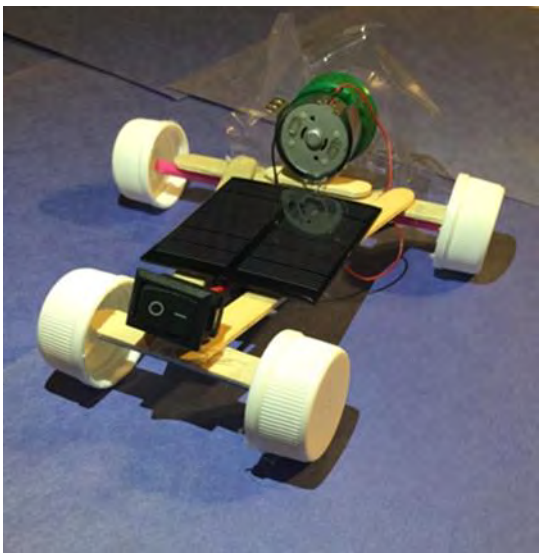

Figure 4: Mini Solar Car

Student and teacher workshops were held during the fall, spring, and summer semester. These sessions were co-hosted and held with the NASA MUREP Aerospace Academy (MAA). Feedback is gathered from surveys completed by their network of teachers from different school districts in the El Paso area. During the Summer 2017 in which the pre-made modules were implemented, a total number of 187 students participated in 1 day workshops. The new educational modules were integrated last summer. A total number of 58 students participated in the energy modules in Summer 2018. Throughout this past fall semester, a total of 252 students also experienced the new modules during student sessions and demonstrations. Feedback gathered from both students and teachers included that activities were more interactive, student population was more engaged, more exercise problems to be implemented into modules, and challenging modules to be developed for advanced students.

3 Summary

The Consortium for Integrating Energy System in Engineering and Science Education (CIESESE) was established to prepare the future generations in engineering and science in pursuing a career in the energy workforce. The UTEP CIESESE program works alongside the NASA MUREP Aerospace Academy (MAA) to maximize impact and increase dissemination in the community. As part of this project, both teacher and student workshops were developed. Pre-made modules that were developed in 2017 were too expensive for teachers to adopt into their classroom curriculum. As a result, alternative experiments for broader teacher adoption were developed. These new modules are low-cost effective, easily attainable, and promote the usage of recycled materials. Materials used during summer and fall sessions are available on the CIESESE website http://engineering.utep.edu/ciesese.

The Effect of Surface Roughness on LCH_4 Convection Through Traditionally and Additively Manufactured Rocket Engine Cooling Channels

L. Hernandez[1], R. Palacios[1], D. Ortega[1], J. Adams[1], L. Bugarin[1], M. M. Rahman[1], A. Choudhuri[1]*
[1] Mechanical Engineering, The University of Texas at El Paso, El Paso, TX 79968, USA;

Keywords*: Boiling, convection, regenerative cooling, engine*

ABSTRACT

This work experimentally characterizes the effect of surface roughness on liquid methane (LCH4) boiling heat transfer performance of traditionally and additively manufactured rocket engine cooling channels. The high heat flux methane boiling tests were conducted using a system designed and developed to investigate the steady state heat transfer of cryogenic propellants at the NASA Micro Center for Space Exploration and Technology Research at the University of Texas at El Paso. For this specific study, total five samples were tested; four made of Inconel 625 and one made of copper. Square channels with a cross-section of 3.2 mm x 3.2 mm and various roughness values were fabricated using conventional milling and advanced 3D printing technologies.

1 Introduction

In this study there are five different test channels. All of these channels possess a square-cross section of 3.2 mm x 3.2 mm. The copper test section that will be used for comparison is made of copper C12800 with a surface finish of 0.8 μm. Three Inconel 625 test sections were traditionally manufactured and have roughened channels with surface finishes of 0.8, 3.2, and 6.4 μm. The final test section was also made of Inconel 625, although this section was additively manufactured by using the selective laser melting (SLM) process. This last test channel has a surface roughness of 12.5 μm. The purpose of the selected test sections is to study the effects of surface roughness on cooling effectiveness.

To conduct such experiments, the cSETR has developed and designed a high heat flux test facility (HHFTF), where all the test section cooling channels are heated using a conduction-based thermal concentrator. Once the desired temperature is achieved, liquid cryogenic propellant is flown through a single cooling channel. This allows for the simulation of one-dimensional asymmetric heat flow, which is experienced by the hot wall of a cooling channel in a regenerative cooled rocket engine. This allows to characterize the heat transfer characteristics of any liquid cryogenic propellant. This permits to the design of a regenerative cooled rocket engine

2 Experimental Set Up

a. High Heat Flux Facility

The high heat flux test facility is a conduction based thermal concentrator system that transfers heat onto a fluid by supplying a constant heat flux to a test section resembling a cooling channel. A unique characteristic of the high heat flux test facility is that it can asymmetrically heat the cooling channel from one side. Achieving a better simulated environment for the engine's regenerative cooling system by providing a hot-wall and a cold-wall side. In this test facility, the heat supplied by the copper heating block simulates the heat generated by the combustion of propellants developed inside a rocket engine. Fluid conditions are monitored through the duration of the test through the use of temperature and pressure instrumentation placed around the cooling channel sample.

The components that make up the HHFTF include an assembled 316L stainless steel test stand, a heating block made of C12200 copper with 17 fissures on its sides to accommodate cartridge heaters, a thin (0.2") aluminum wafer sandwiched in between the heating block and cooling channel, a cradle made of 6061-Al, and test sections. Grooves were machined on top of the heating block and on the bottom of the test sections in order to accommodate thermocouples for real time temperature measurements across the wafer. Please note that the channels interface with the wafer and there is no direct contact with the thermal block. Figure 1 below shows the high heat flux

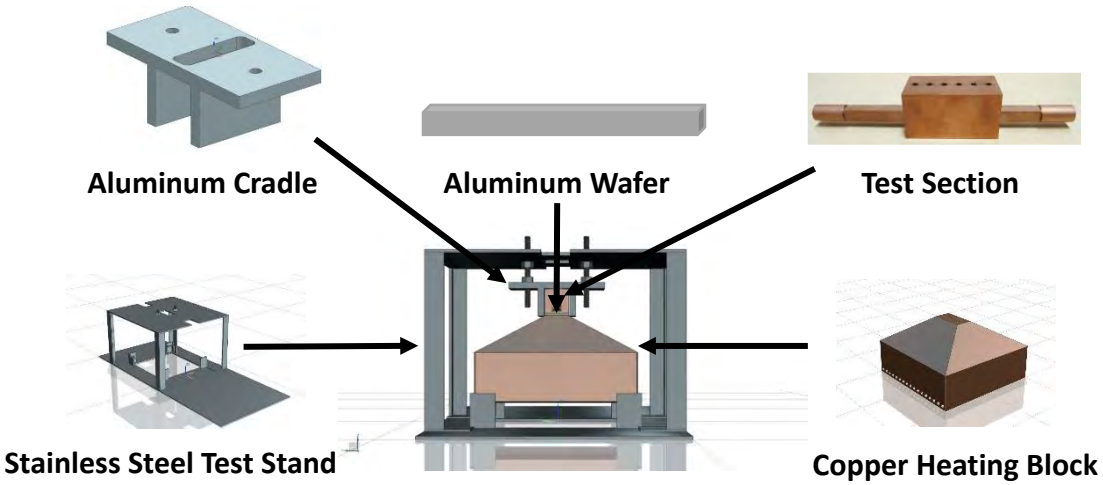

Figure 1: High Heat Flux Test Facility Assembly

b. Methane Condensing Unit

The high heat flux test facility is incorporated with a methane condensing subsystem known as the methane condensing unit (MCU) to achieve steady-state liquid methane (LCH_4) data. Figure 2 shows the methane condensing unit. This is a 13-liter condensing system used to liquefy gaseous methane (GCH_4) and provide the experiment with liquid methane. In order to liquify GCH_4 several fluids were utilized such as liquid nitrogen (LN_2), and gaseous helium.

Figure 2: Methane Condensing Unit

c. Cooling Channels

Considering that typical cooling channels inside a regenerative cooled engine may vary in cross-sectional geometry throughout the engine's contour, the HHFTF was developed such that different test section cooling channels can be simply substituted for testing without greatly affecting the experimental set up. The test section consists of a calculated entry length, a heated section and an exit length. The entry length was designed to allow the fluid to become fully turbulent before entering the heated section. Once the fluid enters the heated section, the temperature profile of the fluid is recorded. This is done by utilizing six axially placed type-E thermocouples on the test section. Note that these thermocouples are not in direct contact with the fluid, therefore there is no fluid disruption. Additionally, there exists a very small wall thickness (1.27mm) separating the tip of the thermocouples from the fluid. Figure 3 illustrates the schematic of the test section design and thermocouple positions.

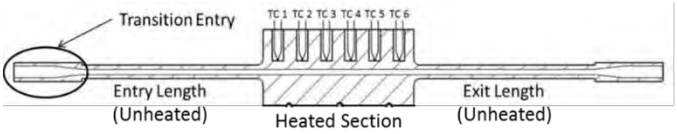

Figure 3: Test section schematic.

3 Theorical Approach

The key parameter considered in this study is the rate of heat transfer to the fluid. The total rate of heat transfer was calculated by using the basic heat transfer equation. This equation is based on the specific heat of the fluid C_p, mass flow rate $\dot{m}$, and the difference of temperature from the inlet to the outlet ΔT, as shown on Eq. (1) [7]. Heat flux, q'', was obtained by using the test section channel wetted wall surface area A_w, and utilizing the rate of heat transfer obtained in Eq. (1) this is described in Eq. (2):

$$Q = \dot{m} C_p (T_{out} - T_{in}) \tag{1}$$

$$q'' = \frac{Q}{A_w} \tag{2}$$

The mass flow rate of the fluid was recorded from the flow meter throughout the test duration. For this to be possible the needle valve located downstream of the channel needs to be at the appropriate position. Once the flow reaches a steady point by deviating only by ±0.0002 kg/s, it is deemed appropriate for flow measurements. The convection coefficient h was then calculated using Eq. (3) by using the resultant heat flux from Eq. (2), the average wall temperature T_w, and the average bulk temperature $T_b = ½(T_{in}+T_{out})$:

$$h = \frac{q''}{(T_w - T_b)} \tag{3}$$

The measured results were used to develop a correlation between Nusselt and Reynolds numbers. Nusselt number, $Nu_{D,}$ is defined as the ratio of the convection coefficient to the fluid conduction coefficient k at the specified hydraulic diameter of the testing channel $D_{hyd,}$ as shown in Eq. (4). Reynolds number is defined by Eq. (5) using the fluid density ρ, fluid viscosity μ, hydraulic diameter of the test channel D_{hyd}, and bulk velocity υ obtained from the mass flow rate, pressure, and coolant channel cross-sectional area:

$$Nu_D = \frac{h}{k} D_{hyd} \tag{4}$$

$$Re = \frac{\rho \upsilon D_{hyd}}{\mu} \tag{5}$$

Please note that: all state properties ρ, μ, C_p, and k, were calculated using REFPROP [8] at the average fluid pressure P_{av}, where $P_{av} = ½(P_{in}+P_{out})$, and T_b.

4 Future Work and Conclusion

The Center for Space Exploration and Technology Research (cSETR) is currently focusing on the implementation of additively manufactured test articles. The overall purpose of this test was to compare the performance of the typically manufactured channels versus the additively manufactured test channel. This was achieved by testing samples with different roughness. Testing on these channels is currently underway. Please not that data is still pending. Next efforts will consist on data filtering and comparison for each examined test article. Note that these samples have been previously tested with liquid nitrogen (LN_2). Once the testing campaign is completed, a comparison between these two campaigns will be made to see if a correlation between the effects of surface roughness and the cryogenic used exists. Currently the cSETR is developing a new generation of cooling channels to be additively manufactured with Inconel 625 and copper alloys. Once those test articles are completed, they will undergo testing for validation.

5 References

[1] Trejo, A., Garcia, C., and Choudhuri, A., "An Experimental Investigation of the Heat Transfer Characteristics of Liquid Methane," *48th AIAA/ASME/SAE/ASEE Joint Propulsion Conference and Exhibit,* AIAA Paper 2012-4121, 2012.

[2] Glickstein, M. R. and Whitesides, R. H. 1967. Forced-Convection Nucleate and Film Boiling of Several Aliphatic Hydrocarbons, ASME-AIChE Heat Transfer Conference and Exhibit, Seattle, WA.

[3] Trejo, A., Garcia, C., and Choudhuri, A., "An Experimental Investigation on the Steady State Heat Transfer Characteristics of Liquid Methane," *49th AIAA/ASME/SAE/ASEE Joint Propulsion Conference and Exhibit,* AIAA Paper 2013-4145, 2013.

[4] Trejo, A., Trujillo, A., Galvan, M., and Choudhuri, A., "Experimental Investigation of Methane Convection and Boiling in Rocket Engine Cooling Channels," *50th AIAA/ASME/SAE/ASEE Joint Propulsion Conference and Exhibit,* AIAA Paper 2014-8722, 2014.

[5] Trejo, A., Garcia, C., and Choudhuri, A., "Experimental Investigation of Transient Forced Convection of Liquid Methane in a Channel at High Heat Flux Conditions," *Experimental Heat Transfer,* Vol. 29, No. 1, 2016, pp. 97-112.

[6] Irvine S.A., and Burns R.M. 2005. Preliminary Heat Transfer Characteristics of RP-2 Fuel as Tested in the High Heat Flux Facility. Air Force Research Laboratory, AFRL-PR-ED-TP-2005-545, Edwards AFB, CA.

[7] Cengel, Y.A. 2007. Heat and Mass Transfer. 3rd ed., McGraw-Hill, p. 459.

[8] Lemmon, E. W. Huber, M. L. McLinden, M. O. 2013. NIST Standard Reference Database 23: Reference Fluid Thermodynamic and Transport Properties-REFPROP, Version 9.1, National Institute of Standards and Technology, Standard Reference Data Program, Gaithersburg.

THERMAL AND STRUCTURAL ANALYSIS OF A CYLINDRICAL HIGH PRESSURE OXY-COAL COMBUSTOR

Md Mohieminul Islam Khan[1], Mehrin Chowdhuri. Ana Rios[1], Ahsan Choudhuri *,
[1]Mechanical Engineering, Center for Space Exploration and Technology, El Paso, TX 79968, USA;
* Corresponding author (ahsan@utep.edu)

Keywords*: structural analysis, combustion, oxy-fuel*

ABSTRACT

Oxy-coal combustion refers to burning coal in presence of pure oxygen instead of air. This type of combustion facilitates carbon capture by producing sequestration ready carbon dioxide, and running the combustion in a high-pressure environment increases the available heat to be extracted by power generation cycle. Due to all the advantages, high pressure oxy-coal combustion has emerged as an interesting method to study for power generation. This study focuses on analyzing the mechanical design of the vessel where the combustion will take place. The vessel will be designed for 1 MW firing input operating at 10 bar pressure. Several analytical calculations were done to ensure the safety of the vessel. Introduction
Coal combustion is a technology that has been used to produce energy for a long time. Currently, 30% [1-2] of the total energy production of electricity in the United States is derived from coal alone. The benefits of oxy-coal combustion are that higher temperatures theoretically allow for higher achievable efficiencies, and the exhaust products n theoretically will not contain NO_x pollutants. Therefore, without the presence of nitride oxides, up to 100% of the carbon dioxide produced can be captured at the post-combustion stage [3,4,5] .The combustor will be operated at a pressure of 10 bar inside a cylindrical pressure vessel while oxy-water-coal slurry based combustion occurs within the vessel. Due to the high operating pressure and high temperatur generated from oxygen-based flame within the combustor, deformation of the chamber can occur and need to be prevented.
. A mechanical analysis must be performed to analyze and determine the temperature at which point the combustor would start to plastically deform. Additionally, design decisions could be made based on this information on the temperature (with an appropriate safety factor) at which the cooling system should aim to reach at the combustor wall to ensure the continuity of the vessel service.

1. Design Methodology

1.1. Material Selection

In order to find the material of the combustor, yield strength of different materials with temperature were compared to each other. The search was constricted to steel because this kind of material is widely available, inexpensive and easy to manufacture comparing to other materials. The research group had an already built combustor with a methane burner made with Stainless Steel 410 previously used [6] at 232 kW and 16 bar where the wall reached at 325^{o}C. This inherited combustor

is studied to find out if that can be retrofitted for the new project with different operating condition. The methane burner will act as a pilot burner. In Figure 1, steel of 300-series and carbon steel were compared to Stainless Steel 410. The difference in yield strengths between SS 410 and other materials is clearly visible. So, it was clear that SS 410 is the material with the highest temperature endurance than the other options. For this reason, it was decided that SS 410 would be the material that would be used for the combustor body, flanges (to avoid any mismatch referring to thermal expansion) and front and end caps.

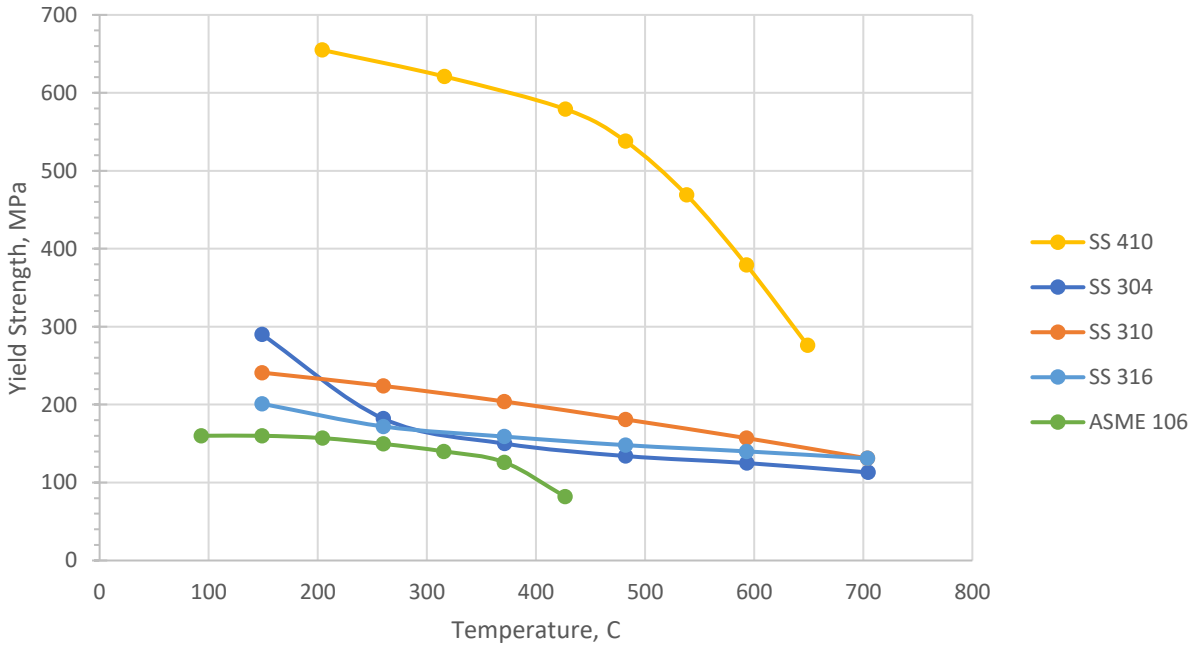

Figure 1: Yield Strength vs Temperature for different Steel

1.2. Thick wall Pressure vessel

Since the high-pressure combustor is a cylindrical vessel that will be operated at a pressure of maximum 10 bar, it is analyzed using the thick-walled pressure vessel model. It was assumed that the pressure inside the combustor is uniform and positive while on the outside it is atmospheric pressure. The formula for thick walled hoop stress is,

$$\sigma_h = \frac{r_i^2 P_i - r_o^2 P_o}{(r_o^2 - r_i^2)} + \frac{(P_i - P_o) r_i^2 r_o^2}{(r_o^2 - r_i^2) r_i^2} \quad [1]$$

Where, r_o is the outer diameter, r_i is the inner diameter, P_o is the outer pressure and P_i is the inside pressure.

The vessel will have a very high temperature on the inside and atmospheric temperature on the outside. This high temperature difference will cause a thermal stress on the combustor body The thermal stress was calculated using the following equation :

$$\sigma = \frac{E \alpha q t}{2(1-\vartheta)k} \quad [2]$$

Where, E is Young's Modulus, α is the coefficient of thermal expansion, q is the heat flux, t is the thickness, υ is Poisson's ratio of the material and the k is the thermal conductivity. The formula for heat flux is,

$$q = \frac{k\,(T_{wg} - T_{wair})}{t} \qquad [3]$$

Where, T_{wg} is the temperature of the wall from the hot gas side and T_{wair} is the temperature of the wall from the air side. By substituting [3] into [2], the resulting thermal stress equation becomes:

$$\sigma_t = \frac{E\alpha\,(T_{wg} - T_{wair})}{2(1-\vartheta)} \qquad [4]$$

Change in the total thermal stresses varied with the thickness and radii of SS 410 was calculated. Figure 2 represents the total stresses at 325°C, the limiting temperature in which the pilot burner test was operated. At this temperature the Yield Strength of the steel is around 630 MPa. The objective is to select a thickness and radius that have a safety factor of 1.4.

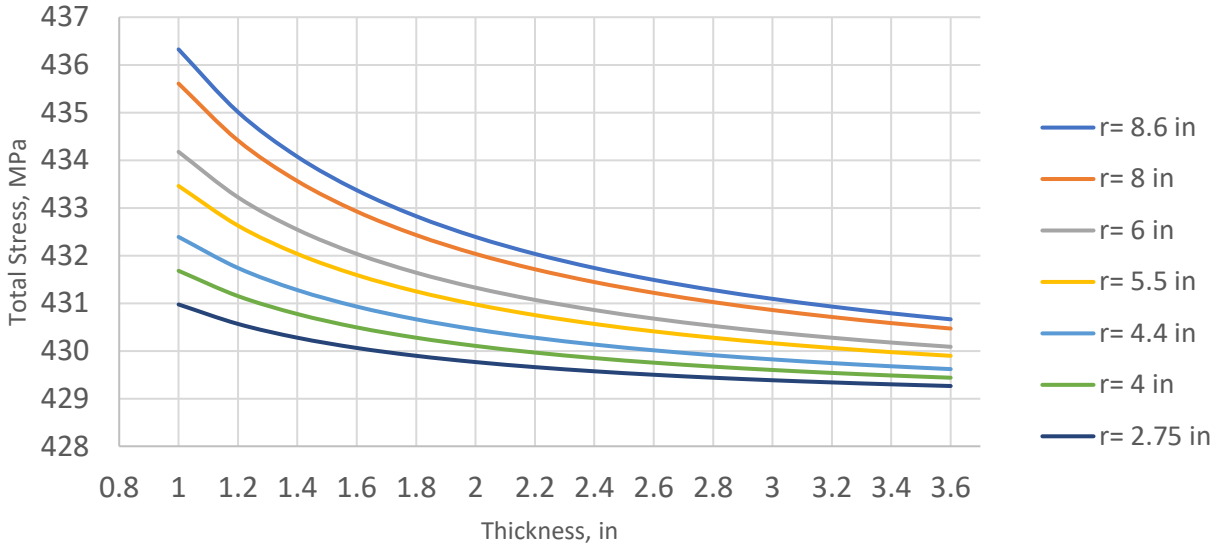

Figure 2: Total Stress at 325°C vs Thickness, for several Radii

All of the conditions shown above satisfy the safety factor criteria . Since the radius and the thickness of the inherited combustor also satisfied the requirement it was decided to keep that one to run the present project. That combustor has a radius of 5.5 inch and thickness of 3.5 inch. This decision was also supported by Figure 3 which showed that stress with increasing temperature doesn't vary much if the thickness is varied. Selecting the thickness of the previously used combustor can also provide the option of lowering the safety factor for higher temperature operation and slowing down the heat transfer from the wall chamber to the outside wall which was attractive to the investigation.

.

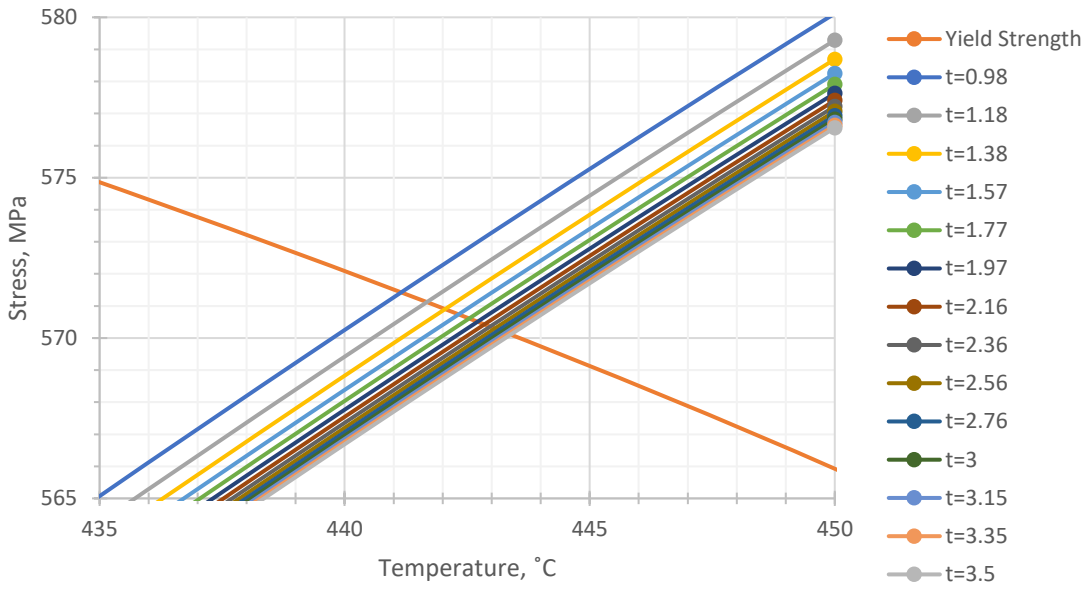

Figure 3: Total Stress and Yield Stress vs Temperature at D=11 in at different thickness(in)

1.3. Flange and Weld Selection

In order to find the suitable flange for the combustor body analytical calculations were made. The stresses on the flanges were analyzed and based on that the pressure rating was chosen for the suitable flange class. The equation for the operating forces on the flange is,

$$F_{operating} = \left(P * A_{flange} + Weight\right) + P * G_{eff} + GF_s \qquad [5]$$

Where, P is the operating pressure, A_{flange} is the area of the flange, G_{eff} is the gasket effective area and GF_s is the gasket sealing force. High temperature-high pressure commercially available metallic gasket with graphite filler was selected for the flanges. Stainless Steel bolt with a tensile strength of 70,000 psi or 483 MPa was selected. The highest force the flanges will have to carry is found to be 1570 kN and the required bolt area is 5 in^2. To meet the requirements 410 SS 300 class flange is selected. Flange of the same material as the combustor body was chosen to minimize the thermal mismatch. . Also, for 410 SS working pressure at 400^{o}C is 28.4 bar. And for 300 class, total bolt area is 36 in^2.

In order to attach the combustor cylinder with the flange welding will have to be done. The height and material of the weld should be chosen carefully so that it can withstand the stress due to the operating pressure and weight of the whole combustor. Since in this case the combustor cylinder and the flange are two metal body whose central axis are perpendicular to each other transverse fillet joint will the best choice for that.

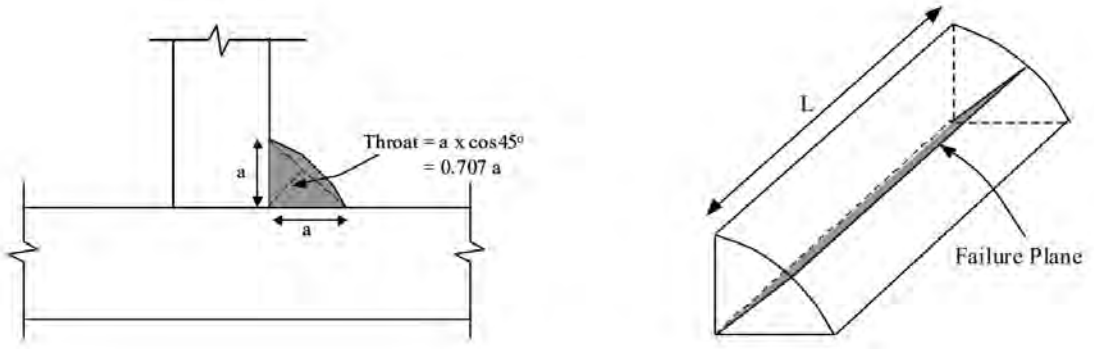

Figure 4:Cross section of a transverse fillet weld

Total allowable stress on the weld is,

$$Allowable\ stress = \phi R_{\mathrm{n}} = 0.75 * f_w * 0.707a * L \qquad [6]$$

Where,
$f_{\mathrm{w}} = Ultimate\ Shear\ Strength = 0.6 * Tensile\ Strength$
And the operating conditions are,
Operating pressure = 10 bar
Mass = 2.5 ton = 2268 kg
Weight = 2268 kg* 9.8 m/s^2 = 716 kN
Operating stress = Weight+ Operating pressure = 393 MPa
Material for the weld was chosen to be 410 ss. Material for both the metal body and weld were same to minimize thermal mismatch. Weld of 410 SS has a tensile strength of 80,000 psi or 552 MPa. Now according to the equation stated above for a weld height of 0.05 in (a=0.05 in) allowable stress is 546 MPa which far above 393 MPa. So, considering the total operating stress and material strength it can be concluded that 0.05 in weld height should be enough to put between the flanges and the combustor body.

2. Conclusion

The study was done to do a structural analysis on the mechanical design of the pressure vessel to be used as a high-pressure, high-temperature combustor. SS 410 was chosen as the combustor material since it met all the physical requirements. Also, the inherited pressure vessel of SS 410 from the previous project added the advantage of reducing cost. Flange, gasket, weld and other additional body parts were chosen carefully so that they also can withstand the extreme operating conditions with a safety factor. According to the stress analysis the design of the combustor should be effective under the extreme operating condition for the project. As a future work, a transient FEA might be done on the whole combustor computationally integrating both thermal and mechanical stresses to check how the mechanical properties change with increasing temperature over time.

References

1 *US, E. (2016). Electric power monthly with data for november 2015.*

2 Hristov, A. N., Harper, M., Meinen, R., Day, R., Lopes, J., Ott, T., ... & Randles, C. A. (2017)., “Discrepancies and uncertainties in bottom-up gridded inventories of livestock

methane emissions for the contiguous United States.," *Environmental science & technology, 51(23), 13668-13677.*

[3] Zhang, N., & Lior, N., "Two novel oxy-fuel power cycles integrated with natural gas reforming and CO2 capture," *Energy*, vol. Vol. 33, 2008, pp. 340–351.

[4] Buhre, B. J. P., Elliott, L., Sheng, C. D., Gupta, R. P., & Wall, T. F., "Oxy-fuel combustion technology for coal-fired power generation," *Progress in Energy and Combustion Science*, vol. 31, 2005, pp. 283–307.

[5] Hong, J., Chaudhry, G., Brisson, J. G., Field, R., Gazzino, M., and Ghoniem, A. F., "Analysis of oxy-fuel combustion power cycle utilizing a pressurized coal combustor," *Energy*, vol. 34, 2009, pp. 1332–1340.

[6] Love, N. D., Chowdhury, A. S. M. A., Aboud, J., and Rios, A., "DESIGN AND EXPERIMENTAL DEMONSTRATION OF A HIGH PRESSURE OXY-METHANE COMBUSTOR," 2018, pp. 2–5.

Thermal and Mechanical Energy Harvesting Using Piezoelectric Ceramics

Luis A Chavez[1], Victor F. Elicerio[1,2], Jaime E. Regis[1], Hoejin Kim[1], Carlos A. Garcia Rosales[3], Norman D. Love[1], Yirong Lin[1]

[1]Department of Mechanical Engineering, The University of Texas at El Paso, El Paso, TX 79968, USA

[2]W.M. Keck Center for 3D Innovation, The University of Texas at El Paso, El Paso, TX 79968, USA

[3]Department of Electrical and Computer Engineering, The University of Texas at El Paso, El Paso, TX 79968, USA

Abstract

The field of energy harvesting has drawn an increased amount of interest due to the rapid development of wireless sensors and self-powered devices. Currently, there is limited information regarding the impact of coupling both thermal and mechanical excitations in a single material and its energy harvesting capabilities. This paper demonstrates the use of Lead Zirconate Titanate (PZT) as a coupled thermal and mechanical energy harvesting device. PZT ceramic was subject to different thermal and mechanical loading conditions. The sample consistently generated the least power when only subject to mechanical cycling, averaging a power output of less than 200 nW. An increase in power output was observed under mechanical cycling and higher temperatures. A peak power of 500 nW was seen under thermal cycling, as well as under coupled thermal-mechanical cycling. This study demonstrated the feasibility to harvest different waste energies from a single device.

1. Introduction

Recently, demands for both efficient and environmentally benign power generation have increased in the fossil energy industry, generating extensive research interest for viable solutions such as energy harvesting systems in the form of wind turbines and solar power [1]. By burning 1.2 billion tons of coal per year globally, the current state of global energy generation points to coal becoming the world's top source of energy by 2017, making substantial increases in CO_2 emissions a topic of concern [2]. This energy is attainable through various mediums including body heat, solar energy, vibration energy [3-6]. Energy harvesting can also be performed at a smaller scale by harnessing energy that would normally be lost in the form of waste heat or vibrations that are generated as a byproduct of electrical power generation. The two most widely used methods to harvest waste thermal energy are through the thermoelectric and pyroelectric effects [7, 8]. Thermoelectric materials operate using the principles of the Seebeck effect and convert the heat flow to electrical power when subject to a temperature gradient [9]. ~~Thermoelectric energy conversion is an irreversible thermodynamic process and therefore is not as efficient as energy conversion through the pyroelectric effect [9].~~ The pyroelectric effect occurs when temperature fluctuates through a material, resulting in electrical displacements, inducing charge separation, therefore forming an electrical current [10]. The charge flow generated can best be described with Eq. (1).

$$i_p = \frac{dQ}{dt} = Ap\frac{dT}{dt} \quad (1)$$

where Q denotes the generated charge, p denotes the pyroelectric effect, A denotes the cross-sectional area on the electrode, and dT/dt denotes the rate of change of temperature with respect to time. Several efforts to harvest thermal energy utilizing the pyroelectric effect have been performed successfully in recent years [10-12]~~. Much like thermal energy harvesting, mechanical energy harvesting is a growing topic of interest in the realm of self-sufficient wireless energy sources~~. Piezoelectric materials are the most viable solution due to their high energy densities and are easily incorporated into systems subjected to dynamic energy [13]. The piezoelectric principle is best described as a material's ability to generate an electrical charge in response to an applied mechanical stress. Equations (2) and (3) describe the standard piezoelectric constitutive law in strain charge form,

$$S=s^E*T+d^t*E \quad (2)$$

$$D=d*T+\varepsilon^T*E \quad (3)$$

where S denotes material strain, T denotes material stress, D denotes charge density displacement, E denotes electric field, d denotes the matrix containing the piezoelectric coefficients of the material, and t stands for the transpose of the matrix. Efforts using different materials including polyvinylidene difluoride (PVDF), Lead Zirconate Titanate (PZT), $BaTiO_3$, and ZnO with different configurations including the use of bulk materials, as well as composites, nanowires, and nanofins [16, 17]. Although the aforementioned case studies describe instances where energy was successfully harvested from a variety of sources, harvesting energy from thermal and mechanical ubiquitous sources simultaneously is an area of interest that yields great potential. Both mechanical and thermal energy harvesting have shown independent success, however, it is important to realize that all pyroelectric materials are also piezoelectric, meaning that in addition to charge generation from temperature change, electrical power can also be generated through the application of mechanical energy [18]. ~~Therefore, it is possible to simultaneously harvest thermal and mechanical energy from the same material. In a recent combined energy harvesting study, photovoltaic, thermoelectric, and piezoelectric energies were simultaneously harvested through a single inductor and energy conversion efficiency boosts as high as 83% were achieved [19]. Similarly, in a case study set towards achieving both energy harvesting and structural health monitoring from the same source, a PZT patch generates voltage and power up to 4.753 μJ when subjected to harmonic excitations [20].~~

In this paper, the ability to harvest thermal and mechanical energy either separately or simultaneously from a commercial PZT 5H ceramic plate under a variety of applications of loading conditions and thermal cycles was demonstrated. A custom designed load frame fixture was used. The energy output from the sample was quantified through a varying electrical resistance due to the current. Various electrical resistances were used in order to determine the load that would generate peak power for each specific loading condition.

2. Methods

2.1 Sample. The sample used was a PZT-5A square plate with dimensions of 50 mm by 50 mm and a thickness of 1 mm. This ceramic wafer was electroded by the manufacturer and was supplied by Piezo Systems, Inc. Physical properties of the sample used are listed in Table 1.

Table 1. Relevant material properties of the sample tested.

Sample properties	
Name	Lead-Zirconate Titanate
Area (mm^2)	2500
Thickness (mm)	1.0
Piezoelectric Coefficient [g_{33}] (V-m/N)	25 x 10^{-3}
Curie Temperature (°C)	350
Density (g/cm^3)	7.8
Heat Capacity (J/K·mol)	89
Capacitance (F)	4.040 x 10^{-8}
Resistance (Ω)	1.826 x 10^5

2.2 Testing setup. Sample was tested using a custom designed load frame fixtures which were mounted to an INSTRON 8801 load frame and used to transfer compression-compression mechanical loads to the sample. Figure 1 shows a representation of the custom fixtures used. In order to characterize the response due to mechanical, thermal and combined loadings, five testing methods were utilized. These testing methods are described in Table 2.

Table 2. Testing methods used to characterize the power output of the PZT plate.

Test	Initial Mechanical Conditions	Initial Thermal Conditions	Mechanical Cycling load	Thermal Cycling Load
Pure Mechanical	2500 N Compression	Room Temperature	1000 N Amplitude at 0.05 Hz	No Thermal Cycling
Pure Thermal	2500 N Compression	Room Temperature	No Cycling Load Applied	Temperature cycled at 50 to 60 °C
Mechanical at 50	2500 N Compression	50 °C	1000 N Amplitude at 0.05 Hz	Constant Temperature
Mechanical at 60	2500 N Compression	60 °C	1000 N Amplitude at 0.05 Hz	Constant Temperature
Combined	2500 N Compression	Room Temperature	1000 N Amplitude at 0.05 Hz	Temperature cycled at 50 to 60 °C

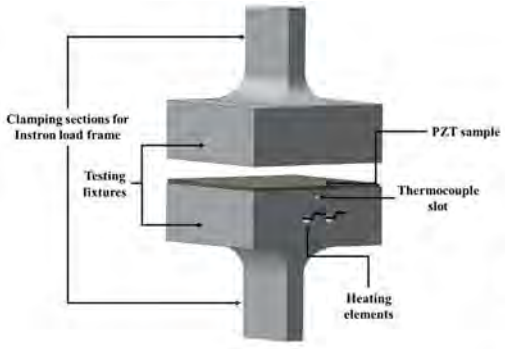

Figure 1. CAD assembly of the custom built testing fixtures.

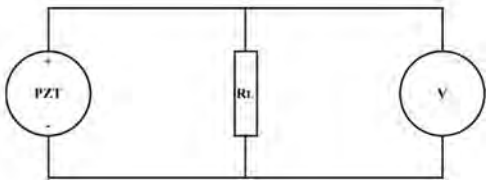

Figure 2. Schematic of circuit used to measure voltage across resistive load.

2.3 Output measurements. The electrical power outputted by the sample under these different loads was characterized using a Keithley 2100 digital multimeter and a varying electrical resistance. Voltage generated across the varying resistance due to the current created by the sample was measured and recorded to determine the electrical power that the sample was capable to output. Power generated by the sample was calculated using Eq. (4) [21],

$$P = V^2/R \tag{4}$$

where P is power, V is the measured voltage, and R is the applied resistance.

~~A schematic of the measurement mechanism is found in Figure 2. R_L is the applied electrical load, V is the multimeter device used to measure the voltage generated. R_L was varied throughout the tests to determine the optimum load that led to the most power. In addition, the PZT wafer was directly connected to the multimeter when characterizing the open circuit voltage output of the sample.~~

3. Results and Discussion

Voltage output due to mechanical loading was characterized. This was done by measuring the open circuit voltage generated on the sample under pure mechanical loads, refer to Table 2. Figure 3 shows the voltage output (blue dashed) plotted with the corresponding load (red solid). A peak to peak voltage output of 15V under a peak to peak mechanical load of 2000N was obtained.

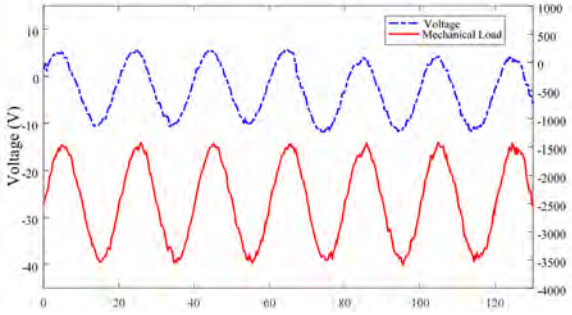

Figure 3. Voltage response of the sample under pure mechanical load.

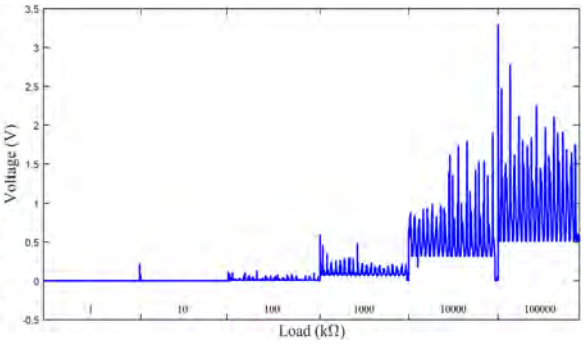

Figure 4. Rectified voltage of the sample across different resistors under pure mechanical loads.

Despite Figure 3 clearly showing that the voltage generated by the sample closely follows the stress applied, this does not give a good insight to the peak power generation capabilities of the sample. As a result, voltage measurements were carried out across different resistors to determine the optimum load to achieve peak power under the different loadings tested. In order to be able to harvest the most energy possible, negative voltages needed to be converted to positive values before passing them through the resistive load. This was done using a simple full bridge rectifying circuit. The voltage output of the sample under a pure mechanical

test was recorded using a wide range of resistors. An increase in the voltage was observed as the resistive load was increased. The voltage output of the sample during this test is shown in Figure 4.

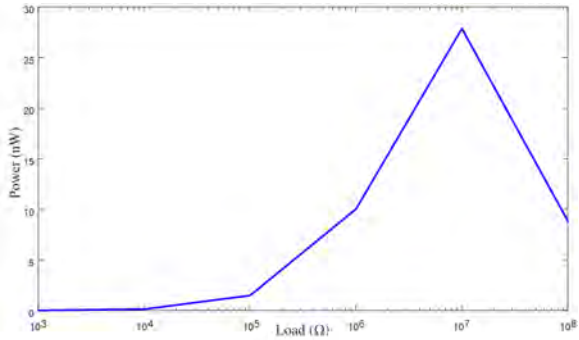

Figure 5. Power output under pure mechanical loads using different electrical resistors.

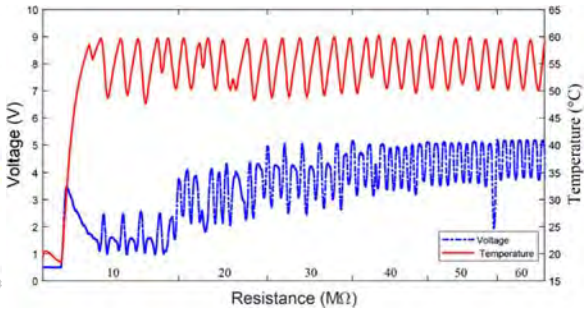

Figure 6. Voltage response of the sample under pure thermal load.

Using the voltage generated by the sample under pure mechanical load across the different resistors, the power output was calculated. The power output across this varying resistance is shown in Figure 5. It was observed that although voltage increased as a function of electrical resistance, a peak in power was present at a resistance 10 MΩ. It was determined that the optimal resistance to obtain the maximum power out of the sample was between 1 MΩ and 100 MΩ. The electrical load in the 1 MΩ to 100 MΩ was then varied in smaller steps to further refine the testing range. Based on the results observed, a testing range of 10 MΩ to 60 MΩ was selected. The rectified voltage response across different resistors due to thermal stresses in the sample are shown in Figure 6. The sample was thermally cycled between 50 °C and 60 °C at different electrical loads. The voltage across each resistor was measured during five thermal cycles and then the electrical resistance was increased. The initial electrical resistance was 10 MΩ and was incremented by 10 MΩ until a 60 MΩ resistance was achieved. The same rectifying and changing load procedure was used for all the testing methods utilized. Power was calculated from the applied resistance and the measured voltage.

Power generated by the sample across different resistive loads is shown in Figure 8. First, it can be seen that the sample generates the least power under pure mechanical load. Next, it was observed that the next lowest power was yielded when the sample was subject to mechanical stress at 50 °C. This was followed by the mechanical load at 60 °C. Finally, peak power under pure thermal and combined loads was found to be practically the same. However, power under pure thermal loads generally outperformed the power generated due to combined loads. A summary of the highest and lowest power outputs observed under the different testing conditions is shown in Table 3.

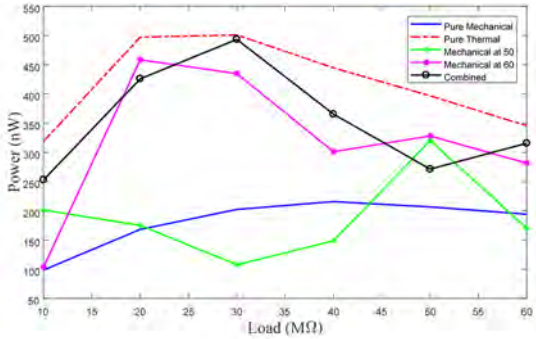

Figure 7. Power output of the sample under different testing conditions at varying electrical loads.

Table 3. Summary of power outputs observed under the different testing methods.

Test	Peak power (nW)	Load at peak power (MΩ)	Lowest power (nW)	Load at lowest power (MΩ)
Pure Mechanical	216	40	98.6	10
Pure Thermal	501	30	319	10
Mechanical at 50	320	50	108	30

Mechanical at 60	458	20	103	10
Combined	494	30	253	10

Using the sample dimensions and peak power outputs obtained, power density calculations were performed. The highest power density observed was generated under pure thermal loads, with a value of 200.4 nW/cm^3. This power density was closely followed by that obtained under combined loadings at of 197.6 nW/cm^3. Next mechanical at 60 °C and mechanical °C yielded power densities of 183.2 nW/cm^3, and 128 nW/cm^3 respectively. Finally, the lowest power density was observed under pure mechanical loads, at 86.4 nW/cm^3.

4. Conclusion

Energy was successfully harvested from a piezoelectric material by applying either thermal or mechanical loads on the sample as well as combined loads. An increase of at least 48% in the peak power generated by the sample was observed when thermal loads were introduced. Further, a peak power density increase of 132% was observed when comparing pure mechanical to pure thermal loads. A small drop of 1.4% in power output was observed when mechanical and thermal loads were combined in comparison to pure thermal loads. This is believed to be caused by the internal counter strain due to the loads applied being out of phase with each other. The appearance of a second power peak due to the different frequencies of the loads applied was observed. An increasing trend in the power generated as temperature increased was observed, with increments of 48% and 112% at 50 °C and 60 °C under mechanical loads was observed. This increase in power output is due to the sample being more compliant at higher temperatures, facilitating a higher mechanical strain under the same force. It is demonstrated that simultaneous mechanical and thermal energy harvesting from the same material is feasible. Pure thermal loading resulted in the highest energy harvesting density and combined energy harvesting showed two distinct peak energy density due to frequency mismatch between mechanical and thermal loadings.

Acknowledgments

This research is funded by Department of Energy (DOE) under Grant No. DE-FE0027502, and National Science Foundation (NSF) under NSF-PREM Grant No. DMR-1205302. Their financial support is greatly appreciated.

References

[1] R. R. Romanosky and S. M. Maley, "Harsh environment sensor development for advanced energy systems," Proceedings of SPIE, pp. 1-9, 2013.

[2] "Coal's share of global energy mix to continue rising, with coal closing in on oil as world's top energy source," 17 December 2012. [Online]. Available: https://www.iea.org/newsroom/news/2012/december/share-of-coal-in-energy-mix-to-keep-rising-nearing-oil-as-top-source-by-2017.html.

[3] H. Kim, Y. Tadesse, S. Priya, "Piezoelectric energy harvesting", Energy Harvesting Technologies, pp. 3-39, 2009.[4] V. Leonov, "Thermoelectric Energy Harvesting of Human Body Heat for Wearable Sensors," IEEE Sensors Jounal, pp. 2284-2291, 2013.

[5] J. Fang, H. Niu, H. Wang, X. Wang and T. Lin, "Enhanced mechanical energy harvesting using needleless electrospun poly(vinylidene fluoride) nanofibre webs," Energy & Environmental Science, pp. 2196-2202, 2013.

[6] C. Alippi and C. Galperti, "An Adaptive System for Optimal Solar Energy Harvesting in Wireless Sensor Network Nodes," IEEE Transactions on Circuits and Systems, pp. 1742-1750, 2008.

[7] N. S. Hudak and G. G. Amatucci, "Small-scale energy harvesting through thermoelectric, vibration, and radiofrequency power conversion," Journal of Applied Physics, p. 101301, 2008.

[8] M. Vaish, M. Sharma, R. Vaish and V. S. Chauhan, "Harvesting thermal energy (via radiation) using pyroelectric materials (PZT-5H): An experimental study," Ferroelectrics Letters Section, pp. 35-51, 2017.

[9] G. Sebald, S. Pruvost and D. Guyomar, "Energy harvesting based on Ericsson pyroelectric cycles in a relaxor ferroelectric ceramic," Smart Materials and Structures, p. 015012, 2007.

[10] H. Karim, M. R. H. Sarker, S. Shahriar, M. A. I. Shuvo, D. Delfin, D. Hodges, T.-L. Tseng, D. Roberson, N. Love and Y. Lin, "Feasability study of thermal energy harvesting using lead free pyroelectrics," Smart Materials and Structures, pp. 1-8, 2016.

[11] A. Cuadras, M. Gasulla and V. Ferrari, "Thermal energy harvesting through pyroelectricity," Sensors and Actuators A: Physical, pp. 132-139, 2010.

[12] L. A. Chavez, F. O. Zayas-Jimenez, B. R. Wilburn, L. C. Delfin, H. Kim, N. Love, Y. Lin, "Characterization of thermal energy harvesting using pyroelectric ceramics at elevated temperatures," *Energy Harvesting and Systems*, *5*(1-2), 3-10, 2018

[13] Y. Liao and H. A. Sodano, "Model of a single mode energy harvester and properties for optimal power generation," Smart Materials and Structures, pp. 1-15, 2008.
[16] H.-B. Fang, J.-Q. Liu, Z.-Y. Xu, L. Dong, L. Wang, D. Chen, B.-C. Cai and Y. Liu, "Fabrication and performance of MEMS-based piezoelectric power generator for vibration energy harvesting," Microelectronics Journal, pp. 1280-1284, 2006.
[17] C. Sun, J. Shi and X. Wang, "Fundamental study of mechanical energy harvesting using piezoelectric nanostructures," Journal of Applied Physics, p. 034309, 2010.
[18] R. W. Whatmore, "Pyroelectric devices and materials," Reports on Progress in Physics, pp. 1335-1386, 1986.
~~[19] S. Bandyopadhyay and A. P. Chandrakasan, "Platform Architecture for Solar, Thermal, and Vibration Energy Combining With MPPT and Single Inductor," IEEE of Solid-State Circuits, pp. 2199-2215, 2012.~~
~~[20] N. Kaur and S. Bhalla, "Combined Energy Harvesting and Structural Health Monitoring Potential of Embedded Piezo-Concrete Vibration Sensors," Journal of Energy Engineering, pp. 1-18, 2015.~~
[21] Y. C. Shu and I. C. Lien, "Analysis of power output for piezoelectric energy harvesting systems," Smart materials and structures, vol. 15, no. 6, p. 1499, 2006.
[22] J. Granstrom, J. Feenstra, H. A. Sodano and K. Farinholt, "Energy harvesting from a backpack instrumented with piezoelectric shoulder straps," Smart Materials and Structures, vol. 16, no. 5, p. 1810, 2007.

THERMAL CHARACTERIZATION OF ABS/CARBON FIBER AND ABS/GLASS FIBER COMPOSITES USED IN LARGE AREA ADDITIVE MANUFACTURING

F. Rodriguez[12]* K. Billah[12] X. Jimenez[12], R. Wicker[12] D. Espalin[12]
[1] Mechanical Engineering, The University of Texas at El Paso, El Paso, TX 79968, USA;
[2]W. M. Keck Center for 3D Innovation, El Paso, TX 79968, USA
* Corresponding author (farodriguezlorenzana@miners.utep.edu)

Keywords*: ABS, TGA, thermal decomposition, DSC, glass transition temperature*

ABSTRACT

Large area pellet extrusion additive manufacturing is an emerging technology created to increase the extrusion rates and printing speeds of thermoplastic 3D printers. This allows introducing all the advantages of AM in a large scale setting at a reduced cost if compared to fused deposition technologies. Because large scale systems use pellet feedstock (like the one used in injection molding) instead of filament, a vast number of materials are readily available for use. A method of determining printing parameters needs to be defined as to reduce the time that it takes for a printer to produce parts with new material. Thermal characterization by thermogravimetric analysis and differential scanning calorimetry allows the user to comprehend the molecular interaction from the polymeric compounds to develop best printing parameters. Therefore, thermal characterization can be used to determine the behavior that acrylonitrile butadiene styrene (ABS) has inside the different temperature's zones located on a Big Area Additive Manufacturing (BAAM) Cincinnati's machine single screw extruder. In addition, it allows an understanding of how the temperature profile influences the thermal properties of thermoplastic composites.

1 Introduction

In past years, additive manufacturing (AM) has been of great interest as the result of the development of new technologies and materials. Consequently, the different potential candidates' technologies must be evaluated in terms of user needs. Large area additive manufacturing offers faster printing rates and enables to create 3D printed prototypes aimed to accommodate more substantial projects. One of the machines developed using this technology is the Big Area Additive Manufacturing (BAAM), with a feedstock cost of ($2-$10 kg/hr.) and material deposition capability up to (50 kg/hr.) and it provides the advantage of building structures approximate 10 larger than commercial systems. (Duty et al., 2017). In comparison, fused deposition modeling (FDM) is another additive manufacturing technique known for using filament feedstocks instead of pelletized feedstocks. FDM has the potential for minimal material wastage and material change. ABS, polycarbonate (PC), polylactide (PLA), polyamide (PA) are some filament feedstocks available for FDM. (Ning, Cong, Qiu, Wei, & Wang, 2015). A typical commercially available machine is a standalone system. The build

chamber in such a system measures 254 × 254 × 254 mm. The system costs around $100,000, deposits approximately 380 mm of material a second, produces layer thicknesses of 50–762 mm and has an accuracy of ± 127 m. (Pham & Gault, 1998).

The BAAM system can print both thermoplastics and reinforced thermoplastics, which allows improving the mechanical and thermal properties of the material. Thermogravimetric analysis (TGA) and differential scanning calorimetry (DSC) is convenient to interpret the thermoplastic behavior if they are exposed to controlled temperatures and to inert/reactive atmospheres. The thermogravimetric analysis provides the decomposition onset temperature, percentage weight loss and residual mass. These are some of the advantages to compare the thermoplastic evolution with respect to a temperature profile. Differential scanning calorimetry studies conducted on an inert or reactive atmosphere enable to find the midpoint temperature glass transition of thermoplastic or report the peak integration if any reaction is observed. Glass is generally referred as a degree of freedom in the system caused by a change in temperature or pressure. For instance, the degree of freedom is reduced at low temperatures or high pressures. This fluctuation is difficult to identify in ordinary timescale measurements. Hence, the glass transition is the change of the moderate degree of freedom to a less or more abrupt degree of freedom. (Sivarajan et al., 2017). The purpose of thermal characterization by thermogravimetric analysis and differential scanning calorimetry will contribute to understanding the printing parameters on a BAAM machine and their effect into the molecular structure of the ABS.

As the materials in 3D printing process experience a series of thermal events such as pelletizing, extrusion at high temperature, sudden cooling, and heating, etc., temperature-dependent thermophysical properties are also expected to change. The goal of this research is to investigate the process induced effects on the materials as well as to determine the effect of filler materials in thermal stability and decomposition throughout the thermogravimetric analysis and differential scanning calorimetry analysis. This research could be later implemented in studies for fused deposition modeling with high-temperature materials.

2 Experimental

2.1. Thermogravimetric Analysis

The thermogravimetric analysis was conducted on a TGA 55 Discovery Series (TA Instruments, United States of America) in accordance with ASTM- E2550 – 17 (ASTM E2550 - 07, 2007). The samples were not grinded nor received prior heat treatment before the experiments. The pellets were accommodated into the samples pans and cut homogenously in terms of weight. (ASTM E2550 - 07, 2007). recommends a mass specimen range between 1 mg to 10 mg. The initial masses for all the samples were recorded. Three replicate experiments were performed for each of the materials. A 50 µL platinum-HT sample pan was used as the material container. In terms of testing parameters, the thermoplastic samples were thermally decomposed in Nitrogen. Nitrogen as an inert atmosphere allowed to avoid unwanted material reactions if compared with Air. (Noah et al., 2016) The nitrogen flow rate was steadily purged with a balance flow of 40 mL/min and a sample flow of 60 mL/min for all the thermal analysis. The experimental procedure consisted of a heating rate of 10 °C/min within a controlled

temperature from room temperature to 800°C. The results were processed with the Trios software v.4.4.0 from TA Instruments where the decomposition onset temperatures, steps

degradations, mass changes within mass the compositions steps, and the residual mass were reported. Mean values and standard deviation were examined as well. Table.1. lists the results for a thermogravimetric analysis and differential thermogravimetric analysis.

2.2. Differential scanning calorimetry

The differential scanning calorimetry analysis was performed with a DSC 250 Discovery Series (TA Instruments, United States of America) in accordance with ASTM E1356 – 08. (ASTM Standard E1356-08, 2008). It is necessary to clarify that the samples weights departed from the recommendation made in ASTM E1356 – 08. The capacity if the containers that this machine uses (DSC 250), is smaller than what is recommended in the standard. Consequently, the reported weight sample measurements were below the 5 to 20 mg range. T-zero series aluminum samples pans and lids were selected to encapsulate the samples. This process was conducted using a DSC sample encapsulation press with a T-zero hermetic upper and lower die. The encapsulations had a cylindrical geometry. The experimental procedure for all the samples consisted of completing two replicate experiments for the target temperatures. A target temperature of 220 °C for ABS 20 wt.% CF and ABS 20 wt.% GF was studied. This temperature was chosen based on the thermogravimetric analysis for each independent material. As volatiles could contaminate the equipment, a temperature under the decomposition onset temperature was used. The experiments were initialized once a temperature of 25 °C was reached by the DSC instrument. Then, the samples were heated at a rate of 10 °C/min. Lastly, the temperature was equilibrated to the target temperatures and proceeded to cool down the specimens with a scanning rate at 20 °C/min to 25 °C. An inert ultra-high purity nitrogen atmosphere was selected to purge the equipment with a recommended base purge flow of 300 mL/min and 50 mL/min volumetric flow rate for the cell purge. The extrapolated onset temperature, the midpoint temperatures, the heat capacities, and peak integration enthalpies were reported from the Trios software v.4.4.0.

3 Results

3.1. Thermogravimetric Analysis

Thermogravimetric analysis and differential thermal analysis for ABS 20 wt.% CF reflected one step degradation. This implicated a 74.51 % average weight loss and an average temperature peak at 414.58 °C. The average decomposition onset temperature (T_{dot}), referring to a 1 % weight loss of the total sample mass was recorded at 258.53 °C. Thermal degradation for ABS 20 wt.% GF showed one degradation step with a 75.45 % average weight loss, a temperature peak of 412.69 °C and T_{dot} of 260.24 °C.

Table.1. The decomposition onset temperatures attributed to 1 % weight loss under a nitrogen atmosphere for three replicate experiments. The mean and standard deviation results are listed as well. Weight residual masses were obtained at 750 °C where fixed mass losses were identified.

Material	$T_{decomposition}$ (°C)	Mean Value (T_{decom})	Standard Deviation (T_{decom})	$W\%_{loss}$	T_{peak} (°C)	Residual (mg)
Electrafil J-1200/CF/20 3DP	S1: 253.50 S2: 260.49 S3: 261.61	258.53°C	4.394	S1: 73.81 S2: 74.76 S3: 74.97	S1: 414.58 S2: 416.16 S3: 416.49	S1: .727 S2: .756 S3: .744
TES 11412-HiFill J-1200/20 3DP	S1: 255.75 S2: 264.32 S3: 260.66	260.24°C	4.300	S1: 75.89 S2: 75.37 S3: 75.10	S1: 413.09 S2: 412.38 S3: 412.60	S1: .780 S2: .924 S3: .889

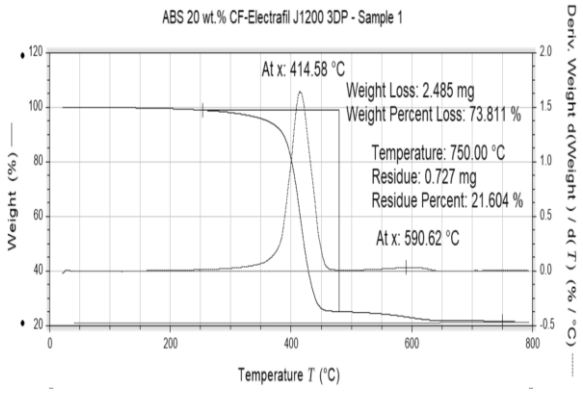

Fig.1. Thermogravimetric analysis and differential thermal analysis for ABS 20wt. % carbon fiber under a control temperature program with a nitrogen atmosphere.

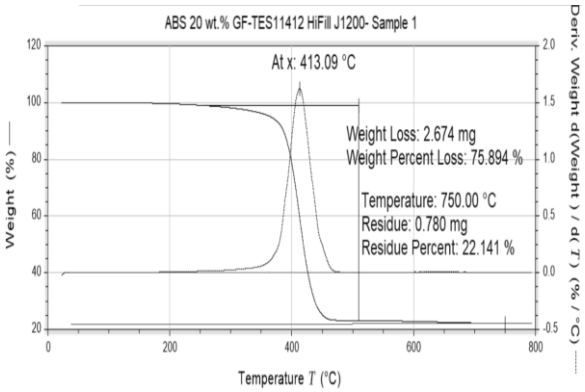

Fig.2. Thermogravimetric analysis and differential thermal analysis for ABS 20 wt. % glass fibers under a control temperature program with a nitrogen atmosphere.

3.1. Differential scanning calorimetry.

Differential scanning calorimetry (DSC) under a nitrogen atmosphere for ABS 20 wt.% CF exhibited an average midpoint temperature glass transition (T_m) of 105.45 ℃ and an average extrapolated onset temperature of 102.06 ℃. However, an average endothermic peak temperature under cooling scanning rates was observed at 139.04 ℃. Similarly, the midpoint temperature (T_m) for ABS 20 wt.% GF was examined at 104.61 ℃, extrapolated onset temperature of 102.27 ℃, and an average endothermic peak observed at 138.28 ℃.

Table.2. The midpoint temperature and extrapolated onset temperatures under a nitrogen atmosphere for ABS 20 wt. % CF and ABS 20 wt. % GF from differential scanning calorimetry

Material	Tm (°C)	Mean Value Tm (°C)	Standard Deviation (Tm)	T_f (°C)
Electrafil J-1200/CF/20 3DP	S1: 106.61 S2: 106.62 S3: 103.12	105.45 °C	2.01	S1: 103.45 S2: 102.73 S3: 100.00
TES 11412-HiFill J-1200/20 3DP	S1: 103.97 S2: 105.34 S3: 104.52	104.655°C	.6894	S1: 101.14 S2: 103.75 S2: 101.93

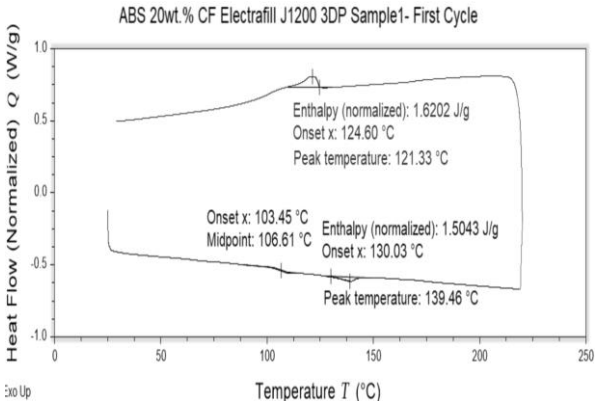

Fig.5. Differential scanning calorimetry curves for ABS 20 wt. % CF under a control temperature program with a nitrogen atmosphere.

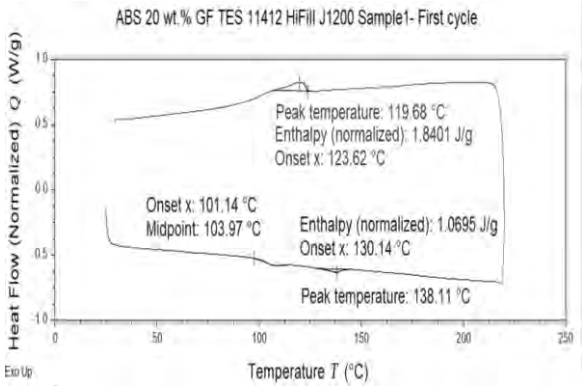

Fig.6. Differential scanning calorimetry curves for ABS 20 wt. % GF under a control temperature program with a nitrogen atmosphere.

4 Conclusion

ABS 20 wt.% CF and ABS 20 wt.% GF were both examined by thermogravimetric analysis and differential scanning calorimetry. The thermal degradation of both materials on a nitrogen atmosphere exhibited one step transition. It was shown a slight improvement for ABS 20 wt.% CF with a 74.51 % weight loss. The decomposition onset temperature was enhanced for ABS 20 wt.% GF with 260.24 °C. Differential scanning calorimetry showed an improvement with a midpoint temperature glass transition for ABS 20 wt.% CF at 105.45 °C. Thermal characterization by thermogravimetric analysis and differential scanning calorimetry can be beneficial to determine the temperatures ranges where material is extrudable without degrading and compromising its structural integrity. (Ajinjeru et al., 2018). It allows to extend the knowledge beyond the mechanical properties of the material and combining the thermal characterization to produce more reliable 3D printed objects.

References

[1]Ajinjeru, C., Kishore, V., Liu, P., Lindahl, J., Hassen, A. A., Kunc, V., … Duty, C. (2018). Determination of melt processing conditions for high-performance amorphous thermoplastics for large format additive manufacturing. *Additive Manufacturing*, *21*(May 2017), 125–132. https://doi.org/10.1016/j.addma.2018.03.004

[2]ASTM E2550 - 07. (2007). Standard Test Method for Thermal Stability by Thermogravimetry. *ASTM International*, *i*, 1–5. https://doi.org/10.1520/E2550-07

[3]ASTM Standard E1356-08. (2008). Standard Test Method for Assignment of the Glass Transition Temperatures by Differential Scanning Calorimetry. *ASTM International*, *22*(Reapproved 2014), 1–4. https://doi.org/10.1520/E1356-08R14.2

[4]Duty, C. E., Kunc, V., Compton, B., Post, B., Erdman, D., Smith, R., … Love, L. (2017). Structure and mechanical behavior of Big Area Additive Manufacturing (BAAM) materials. *Rapid Prototyping Journal*, *23*(1), 181–189. https://doi.org/10.1108/RPJ-12-2015-0183

[5]Ning, F., Cong, W., Qiu, J., Wei, J., & Wang, S. (2015). Additive manufacturing of carbon fiber reinforced thermoplastic composites using fused deposition modeling. *Composites Part B: Engineering*, *80*, 369–378. https://doi.org/10.1016/j.compositesb.2015.06.013

[6]Noah, P. M. A., Ohandja, L. M. A., Medjo, R. E., Chabira, S., Ebanda, F. B., & Ondoua, P. A. (2016). Study of thermal properties of mixed (PP/EPR)/ABS with five model compatibilizers. *Journal of Engineering (United States)*, *2016*(January). https://doi.org/10.1155/2016/8539694

[7]Pham, D. T., & Gault, R. S. (1998). A comparison of rapid prototyping technologies, *38*, 1257–1287.

[8]Sivarajan, S., Reading, F., Range, T. T., Using, S., Perturbations, O., Time, R., & Transitions, S. G. (2017). Glass Transition ☆, (June), 1–11. https://doi.org/10.1016/B978-0-12-803581-8.03155-6

THERMOMECHANICAL PROPERTIES OF LARGE AREA 3D PRINTED PARTS

E. Meraz Trejo[1]*, X. Jimenez[1], F. Rodriguez Lorenzana[1], D. Espalin[1], R. Wicker[1]
[1] W.M. Keck Center for 3D Innovation, The University of Texas at El Paso, El Paso, TX 79968, USA;
* Corresponding author (emeraztrej@miners.utep.edu)

Keywords: *Big Area Additive Manfuacturing (BAAM), 3D-printing, infrared imaging, compressive properties, large area*

ABSTRACT

In large area pellet extrusion additive manufacturing, the temperature of the substrate just prior to the deposition of a new subsequent layer has an effect on the overall structure of the part. Warping and cracking occur if the substrate temperature is below a specific threshold, and deformation and deposition adhesion failure occur if the substrate temperature is above a certain threshold just prior to deposition of a new layer. Currently, Big Area Additive Manufacturing (BAAM) machine users mitigate this problem by trial and error, which is costly and may result in mechanical property, monetary and time inefficiencies. Through thermal imaging, the range of temperatures present during the printing of a carbon fiber reinforced acrylonitrile butadiene styrene (ABS-CF) single-bead wall via the BAAM machine was identified – more specifically the temperature range at which deformation occurs. Moreover, compression tests were performed to understand the compressive behavior behind this deformation at temperatures seen in a conventional printing environment. It was concluded that if the substrate is above a temperature of 200 °C, deformation will occur in a newly added layer – attributed to the experimentally obtained low compressive strength of ABS-CF at temperatures above 200 °C. A newly deposited layer will deform the underlying top layer of the substrate in such a way that the next deposited layer will be deposited to thin air, causing a subsequent cascade of deformation in the printed part.

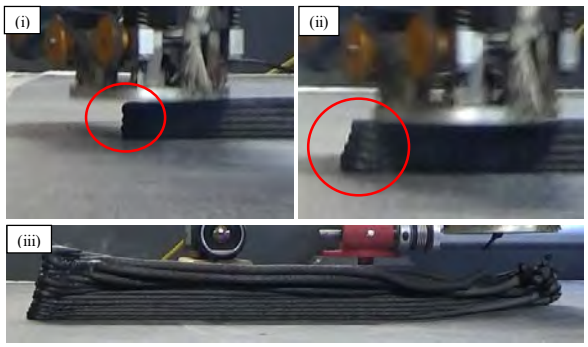

Fig. 1. The plastic deformation of the substrate in the printing direction just after deposition of layer 05. The first (i) frame shows layer 05 being deposited, and the second (ii) frame shows the substrate right after the deposition of layer 05. Notice the comparison between the substrate inside the circles in frames (i) and (ii). The third frame (iii) shows the finalized print, notice the failure in the top layers.

Fig. 2. A single-bead wall printed with an added standby time between layer depositions such that the temperature of the substrate cooled down to approximately 197 °C prior to the deposition of a new layer. Notice the misaligned start of print, and how the deposition is corrected along the direction of deposition.

Fig. 3. A single bead wall print with an added standby time between layer depositions such that the temperature of the substrate cooled down to approximately 220 °C prior to the deposition of a new layer. The initial failure occurred at the start of deposition of layer 7.

Table 1. The printing temperature settings in the BAAM thermoplastic extruder machine.

Material	Melt	Barrel 1	Barrel 2	Barrel 3	Barrel 4	Tip 1	Tip 2
ABS-20CF	225 °C	200 °C	215 °C	240 °C	240 °C	230 °C	225 °C

Table 2. The average compressive load and compressive stress to reach strain levels of 15, 30 and 60 percent at every temperature level. Notice the decline trend in load as the temperature increases and how the compressive stress levels remain constant at temperatures of 210 °C and above.

Temperature [°C]	**Compressive Load [N] at ε = 15%**	**Compressive Stress [MPa] at ε = 15%**	**Compressive Load [N] at ε = 30%**	**Compressive Stress [MPa] at ε = 30%**	**Compressive Load [N] at ε = 60%**	**Compressive Stress [MPa] at ε = 60%**
90	453.61	4.45	3017.89	29.61	6121.43	60.06
110	28.81	0.28	257.88	2.52	1678.57	16.43
130	9.08	0.09	42.11	0.42	193.95	1.91
150	3.20	0.03	15.16	0.15	59.82	0.59
170	0.71	0.01	4.73	0.05	24.76	0.24
190	1.04	0.01	3.23	0.03	16.81	0.16
210	0.86	0.01	1.86	0.02	8.07	0.08
230	0.88	0.01	1.99	0.02	7.63	0.07
250	0.89	0.01	2.09	0.02	7.53	0.07

1. Introduction

The introduction of Big Area Additive Manufacturing (BAAM) to the 3-D printing industry brought a wide range of new advantages to a field already full of innovation. However, while BAAM has a larger print envelope and a faster printing speed - as compared to conventional desktop material extrusion systems – it still has some considerable design and physical limitations [1]. A particular challenge that BAAM is facing today is the nearly erratic relationship between print quality and temperature distribution and history. Temperature control is important to ensure robust adhesion between layers, dimensional accuracy, and an overall successful print [1, 5].

Recent works conducted by Compton *et al*. have demonstrated a strong correlation between print temperature and print quality [2]. In-situ infrared temperature analysis during printing of a thin-wall section concluded that the temperature of the top layer just prior to the deposition of a new layer has a significant impact on the structural integrity of a part. As a guideline, the top layer has to be at least above the glass transition temperature of the material to avoid warping and cracking defects in a printed part. Additionally, with the interest of predicting the temperatures to avoid these defects, a one-dimensional temperature model was developed to predict the temperature evolution in a printed thin wall as a function of layer time – the time before a new subsequent layer is deposited. Compton *et al.* (2017) found that the layer temperature should be at Tg or higher for a newly deposited bead to correctly adhere. In the other hand, Roschli *et al.* (2019) described problems with printing small parts or small features within a large part if the temperature of the previously deposited layer is too high. At those temperatures, the material is mechanically unstable and is not able to support the weight of a new layer. Problems regarding a lower temperature threshold of the substrate have been addressed, but no efforts have specifically addressed the failure present when the substrate temperature is above a certain threshold. Recent efforts have mentioned this issue, but no experimental work has been performed to determine a high threshold temperature [1,5,6]. Currently, BAAM users modify print parameters based on empirical data and user experience.

The purpose of this paper is to evaluate the relationship between high temperatures and mechanical properties that lead to the structural failure of a printed part. This paper will analyze the failure mechanisms present during the continuous print of a single-bead, thin-wall section vis-à-vis recorded temperatures with an IR camera. In addition, the compressive mechanical properties of 20% by weight carbon fiber reinforced acrylonitrile butadiene styrene (ABS) – a common BAAM printing material – will be investigated at varying temperatures present during a conventional print. These compressive stress-strain curves, in conjunction with the thermal imaging analysis, will provide an insight to the behavior of BAAM printed parts to ensure a successful print.

2 Methods

2.1 Material

The material used for the experimental and analytical purposes of this paper was carbon reinforced (20% by weight) acrylonitrile butadiene styrene (Techmer Electrafil J-1200/CF/20 3DP, Techmer PM, Clinton, TN, US), henceforth referred to as ABS-20CF. The material was

dried for a period of 4 hours at 90 °*C* prior to printing. The several geometries performed for this paper – later described in detail - were printed using a BAAM-CI 100 (Cincinnati Inc., Harrison, OH, US) large scale thermoplastic extruder machine located at the University of Texas at El Paso (UTEP). The machine deposited the material at a rate of 100 mm/s over a heated bed set to 110 °C using a 7.62 mm (0.3") nozzle. The printing temperature settings are shown in Table 1 above, depicting the temperatures along the extruder barrel.

2.2 Single-layer Wall Print in situ Temperature Monitoring

A single bead wall of ABS-20CF was printed with the BAAM-CI thermoplastic extruder machine. The slicer for the machine is not able to produce G-code for this geometry, so, a G-code file was modified to achieve this geometry. The wall was 500 mm (19.685 in) in length, 11.81 mm (.465 in) in width (a single bead width), and 62.23 mm (2.45 in) in height (14 layers). A total of fourteen layers were printed, but the last two failed to adhere to the substrate. Data was collected with a FLIR D695 infrared camera, and processed with the FLIR ThermaCAM Researcher Pro 2.10 software (FLIR Systems, Wilsonville, OR, USA). In addition to this, two more videos of the print were recorded with the purpose of visual analysis, one from the front of the wall, located across from the IR camera, and another from the side, perpendicular to the direction of print.

2.3 Stress Deformation

As previously mentioned, when printing with the BAAM machine, high temperatures present in the substrate at the time of deposition lead to unwanted deformation of the part. In order to simulate real life printing conditions, a single layer, single bead wall was printed. From this print, test specimens were obtained and used for compression testing under temperatures seen during a conventional BAAM print [1]. The purpose of this single bead print is to evaluate the deformation of a single layer of material as a consequence of the added weight of subsequent layer, at varying temperatures.

The tests were performed per the standard ASTM D695-15: Standard Test Method for Compressive Properties of Plastics [7]. The compression tests were performed using an Instron 5866 electromechanical testing machine used in conjunction with an Instron 3119-600 temperature-controlled chamber (Instron, Norwood, MA, USA). The specimens were compressed per the ASTM D695-15 standard at a rate of 1.3 mm/min in the z-direction, until a strain level of 60% was achieved. A total of forty-five compression tests were performed under temperatures of 90, 110, 130, 150, 170, 190, 210, 230 and 250 C – five specimens tested at every temperature. It is important to notice that due to the current BAAM printing capabilities, a sample that adhered to the standard and showed fidelity to the BAAM printing conditions analyzed in this paper was not able to obtain, i.e. a piece with the recommended dimensions wouldn't accurately represent the scenario this work tries to replicate due to defects in the print that come from the multiple layer stacking. Therefore, in order to perform this compression testing, the test specimens were cut from a single bead, with average dimensions of 9.48 mm (0.37 in) by 10.87 mm (0.43 in) by 4.33 mm (0.17 in).

2.4 Final Print

Following the compression testing and results analysis, two more single-bead wall prints was performed using the same printing parameters previously described, except for a

newly introduced standby time between layer-depositions to control the temperature of the substrate just prior to deposition to be just below 200 °C in one print. The other print did not have any standby time; substrate temperatures were above 210 °C in this print. In order to obtain the waiting time between layer depositions, the 1-D thermal model developed by Compton et al. was modified by evaluating if the layer temperature was under a desired threshold before deposition. If this was not achieved, the layer time was adjusted accordingly [2]. The temperature of the substrate during the final print was monitored with an FLIR D695 IR camera; processed with the ThermaCAM Researcher Pro 2.10 software.

3 Results and Discussion

3.1 Single-Bead Wall In Situ Temperature Analysis

The print experienced adhesion failure after the deposition of layer 9 – the underlying layer deformed in the direction of the camera. As a consequence of this deformation, the subsequent layers, while adhering to the substrate, do not conform to the desired geometry. The deformation escalates in such a manner that the final layers do not adhere to the substrate – as they are deposited into thin air - and fall to the print bed. The temperature of the substrate remains above 210 °C after deposition of layer 3, and above 230 °C after the deposition of layer 4. Although collapse and compressive failure is seen in layer 08 and subsequent layers, plastic deformation can be seen after the deposition of layer 4. This failure is attributed to compressive deformation caused by the load applied from the extruded material as well as the tamper mechanism.

3.2 Compression Testing

Every compression curve obtained from testing followed a similar shape. However, the compression curves for the tests conducted at 90, 110, 130 and 150 °C all have an initial loading section, a linear elastic region, a plateau, and a final load bearing region, albeit at different displacement and loading conditions. The compressive behavior where the plateau is present is analogous to the compression behavior of foam and porous materials and attributed to the porosity of the printed part [3, 4, 7]. In the compression curves, an inverse relationship was found between the temperature of the specimen and the load withstood prior to deformation. Additionally, it is noticed that the tests conducted at a temperature of 170 °C and above, do not possess a plateau region. The average loads at which a strain levels of 15, 30, and 60 percent was reached for every temperature can be seen in Table 2 above.

The most significant observation is that at temperatures of 210 °C, 230 °C, and 250 °C, the compressive behavior is virtually the same at every strain level, as can be noticed in Table 2 above. Any temperature above 250 °C would be higher than the conventional printing range for ABS [1, 2, 3, 5].

3.3 Final Print

Twenty layers were printed on the single-bead wall printed where the temperature was controlled to be below 200 °C just prior to deposition of a new layer. The average temperature of the substrate prior to deposition of a new layer was 197 °C. No significant deformation was observed, except at the start of the print, as can be observed in Figure 2 above. This deformation at the start of the print attributed to the variability of a layer deposition, which in turn is due to leftover material at the nozzle exit, positioning error, and the tamper mechanism.

The single-bead wall where the temperature was above 210 °C had an average substrate temperature of 220 °C just prior to deposition. Twenty layers were printed in this part, but failure was observed during the initial deposition of layer 7. The deformation of layer 7 caused the subsequent layers to be poorly deposited, as can be seen in Figure 3 above. In both of these prints, deformation is seen at the start of the print, attributed to previously mentioned conditions. The difference between them is that in the part that did not fail, the substrate had enough compressive strength to resist deformation caused by the extruder depositing a new layer, despite initial misalignments in the print. In the failed part, the substrate deformed according to the initial misalignment of the print, causing a "zig-zag" effect in subsequent stacked layers, thus causing poor dimensional accuracy and leading to the final layers being deposited into thin air or not having enough surface contact area – which is essential for proper adhesion [8].

3 Conclusion

As discussed, the temperature of the substrate prior to the deposition of a subsequent layer has a significant impact in the overall structural stability of an ABS-20CF BAAM printed part. Efforts by Compton et al. concluded that the substrate should be above the Tg of a material to avoid warping and crack defects in a part [2]. In this paper, it is concluded that if the substrate temperature is above 200 °C, the compressive strength of the material is lower than the load exerted by the extruder depositing a new layer. If there is misalignment at the start of the print, the substrate will conform to this misalignment and deform accordingly such that subsequent layers will be deposited on an already deformed part. Future research includes evaluating the adhesion strength between deposited layers at the recommended range of temperatures in this paper, as well as the effect of varying geometry on the structural integrity of a part.

References

[1] A. Roschli, K.T. Gaul, A.M. Boulger, B.K. Post, P.C. Chesser, L.J. Love, F. Blue, M. Borish "Designing for Big Area Additive Manufacturing". *Additive Manufacturing,* Vol. 25, pp. 275-285, 2019.

[2] B.G. Compton, B.K. Post, C.E. Duty, L.J. Love, V. Kunc "Thermal analysis of additive manufacturing of large-scale thermoplastic polymer composites". *Additive Manufacturing,* Vol. 17, pp. 77-86, 2017.

[3] C.E. Duty, V. Kunc, B.G. Compton, B. Post, D. Erdman, R. Smith, R. Lind, P. Lloyd, L.J. Love "Structure and mechanical behavior of Big Area Additive Manufacturing (BAAM) materials". *Rapid Prototyping Journal,* Vol. 23, No. 1, pp. 181-189, 2017

[4] M.S. Rajput, M. Burman, J. Koll, S. Hallstrom "Compression of structural foam materials – Experimental and numerical assessment of test procedure and specimen size effects". *Journal of Sandwich Structures & Materials,* Vol. 0, pp. 1-19, 2017

[5] C. Ajinjeru, V. Kishore, X. Chen, J, Lindahl, Z. Sudbury, A. A. Hassen, V. Kunc, B. Post, L.J. Love, C. Duty "The influence of rheology on melt processing conditions of amorphous thermoplastics for Big Area Additive Manufacturing (BAAM)". Solid Freeform Fabrication 2016: Proceedings of the 27th Annual International Solid Freeform Fabrication Symposium – An Additive Manufacturing Conference, Austin, TX, 2016

[6] I. Gibson, D. Rosen, B. Stucker "*Additive Manufacturing Technologies – 3D Printing, Rapid Prototyping, and Direct Digital Manufacturing".* 2nd Edition. Springer. 2015.

[7] ASTM Standard D695, 2015, "Standard Test Method for Compressive Properties of Rigid Plastics," ASTM International, West Conschohocken, PA, 2015.

[8] Li. L "*Analysis and Fabrication of FDM Prototypes with Locally Controlled Properties".* University of Calgary. 2002.

THERMOPHYSICAL ANALYSIS OF MATERIAL EXTRUSION 3D PRINTING MATERIALS

Kazi Md Masum Billah[1, 2]*, Ryan Wicker[1, 2] David Espalin[1,2]
[1] Department of Mechanical Engineering, The University of Texas at El Paso, TX 79968, USA
[2]W. M. Keck Center for 3D Innovation, El Paso, TX 79968, USA
* Corresponding author (kbillah@miners.utep.edu)

Keywords*: Thermogravimetry, differential scanning calorimetry, material extrusion AM*

ABSTRACT

Material extrusion 3D printing is capable of extruding polymer materials with a variety of thermophysical properties. Thermal properties play an essential role to develop the printing process parameters such as extrusion temperature, pressure, environment temperature, deposition rate between others. In the case of a newly developed extrusion system, trial and error of the printing process are common to optimize the overall performance. While printing at relatively high temperature helps to achieve a superior bond strength by avoiding clogging in the nozzle, materials could be negatively affected at those processing conditions. This research studied the thermophysical properties of low-cost materials such as PLA and ABS to determine the temperature-depended strain effect on the polymer chain. Results of thermogravimetry and differential scanning calorimetry showed that the printing process slightly affects PLA properties while having no effect on ABS.

1. Introduction

Material extrusion additive manufacturing (MEAM) is the method of melting and dispensing thermoplastic materials in a layer by layer fashion directly from CAD data. The three critical thermal events that occur with the material in this extrusion-based AM are melting, deposition, and fusion[1]. Melting is required to control the rheology of the deposited material that ultimately helps to adhere to the previously deposited layer. Selective deposition of the material in MEAM is temperature dependent, and while relatively high temperature helps to deposit the material without nozzle clogging, an extremely high temperature can damage the material. Those excessive deposition temperatures can cause degradation and poor thermophysical and mechanical properties. After the deposition of the extruded material on top of a new layer, the temperature-dependent fusion process begins by developing a neck area between rasters. Authors in [2] demonstrated the overall mechanism of the neck growth process at elevated temperature by plastic sintering experiment. The key finding was that the neck growth is a temperature dependent property. Understanding neck growth requires knowledge of the thermophysical properties at a specified temperature to identify the polymer chain diffusion mechanism. Determining the thermal properties of thermoplastic materials at different temperatures is important to develop process parameters and design specification for MEAM machines. Thermal properties such as the glass transition, melting, heat deflection, and decomposition temperature can be used to predict the behavior of the material in different temperature and processing conditions. In MEAM, the printing process begins by producing filament from pellets, then that filament is used for printing. The next step is to apply surface finishing techniques and post-processing (in some cases). It is evident that before printing,

each material undergoes thermal processing. Authors in [3][4] showed the effect that processing conditions have on PLA and ABS materials during MEAM. This research paper focuses on PLA and ABS since they are the most common materials in MEAM due to the low cost and relatively easier processing window. The goal of this research paper is to identify the different thermophysical properties of materials before and after the printing process. It is anticipated that comparing those values could give an insight into the effect that processing of thermoplastic-based polymer has at different temperatures.

2. Experiment

Thermogravimetric and differential scanning calorimetry analysis were carried out to investigate the thermophysical properties of 3D printing materials.

2.1 Materials

In MEAM, the two most common materials are Poly-Lactic-Acid (PLA) and Acrylic-Butadiene-Styrene (ABS). The reason for choosing these two materials are the low cost, relatively low processing temperature, and low printing temperature. 3 mm in diameter PLA filament was obtained from SunTop (Los Angeles, CA US). The glass transition temperature reported by the manufacturer was 62°C. ABS filament with 1.75 mm diameter was obtained from Stratasys (Eden Prairie, MN US). The glass transition temperature according to the manufacturer was 108°.

2.2 Thermogravimetric Analysis

Thermogravimetric analysis (TGA) of PLA and ABS was done using a Q550 TGA from TA Instruments (New Castle, DE, US). The goal was to determine the decomposition temperature of the materials. 2.18mg of PLA and 3.2 mg of ABS was collected from 3D printed parts. According to the ASTM E2550−17 standard [5], the heating rate chosen was 10°C/min and the sample was heated to 800°C. The sample purge in the TGA was 40ml/min

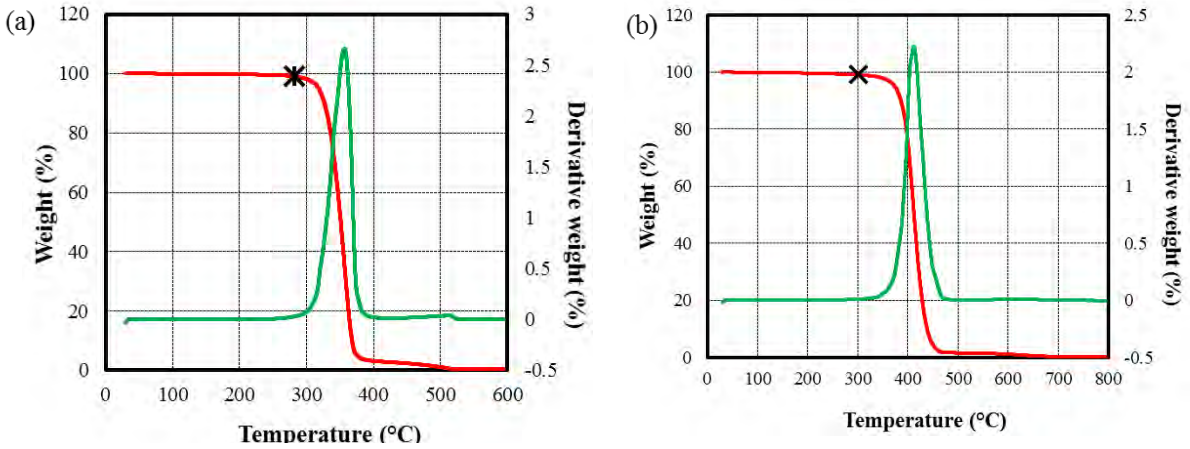

Figure 1. Thermogravimetric analysis of (a) PLA and (b) ABS materials. The cross mark on the red curve in each material is representing the 1% decomposition onset

(compressed air), and balance purge was 60 ml/min (ultra-high purity gas nitrogen).

2.3 Differential Scanning Calorimetry

Differential scanning calorimetry (DSC) experiments were performed in a DSC 250 from TA Instruments. (City, state US). Using ASTM D3418-15 standard, the samples were heated from 40°C to 200°C at a scanning rate of 10° C/min [6]. During the cooling phase, the scanning rate was 10°C/min from 200°C to 40°C. After the first run of heating and cooling, the second run was performed with a similar scanning rate. The goal was to determine the effect of process-induced changes in the thermophysical properties of the materials. DSC tests were conducted under a nitrogen atmosphere in order to diminish oxidation using a purge rate of 50ml/min.

3. Results

3.1 Thermogravimetric analysis

The thermogravimetric analysis of PLA and ABS is shown in Figure 1. The degradation onset temperature (DOT) was chosen based on a 1% loss of weight. For PLA, the DOT was 272°C as shown by a cross mark in Figure 1 (a). The 100% weight loss was found at 478°C. The dynamic TGA graph represents the peak of the temperature at which all the materials burn out. For ABS, the DOT was found to be 300°C which indicates that the thermal stability of ABS is higher than for PLA. The 100% weight loss was found at 500°C. Although the decomposition of the butadiene component in ABS materials occurs first, the sign of the degradation was not prominent in the TGA graph. The derivative weight loss of the ABS shows the total burn out temperature was 412°C. The maximum temperature used in the DSC analysis was chosen based on the DOT, as higher temperatures create volatiles which contaminates the instrument.

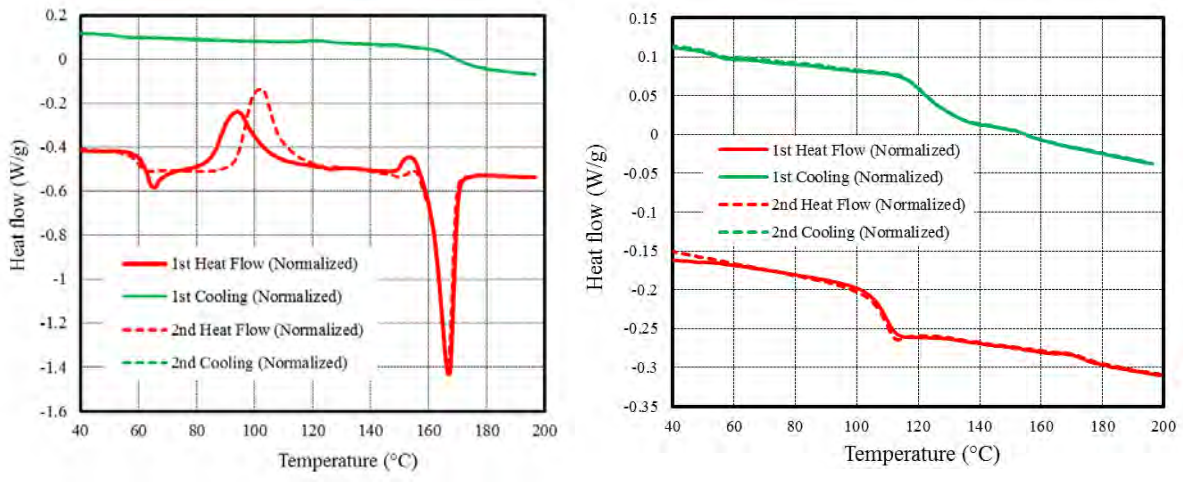

Figure 2. DSC curve of (a) PLA and (b) ABS. In both of the graphs, solid lines are representing the 1st heating and cooling while the dotted lines are represnting the 2nd heating and cooling

3.1 Differential scanning calorimetry

DSC tests were carried out by heating and cooling in two steps to determine the thermophysical properties of PLA and ABS material. In the first step heating, the PLA has a phase transition at 54°C which corresponds to the glass transition temperature. The endothermic peak observed at 168°C correspond to the melting process. During the cooling stage, no transitions were found. In the second heating, PLA showed a slight change in the glass transition temperature and the melting point. The shifting of the graph occurred due to the transition of the alpha phase during the first heating step. As the material went through a phase change during the first step heating, the exothermic peaks were shifted. This behavior was attributed to the process-induced thermal strain relief. For ABS, heating, and cooling in both steps followed a similar path. Although the melting point did not create a sharp point in the TGA graph due to the amorphous structure of the ABS, the glass transition temperature was 108°C. Note that, the processing temperatures of ABS did not affect the thermophysical properties like it was observed with PLA. Since both materials were tested after printing at relatively high temperatures, it was anticipated that the material crystallinity would transform while there were no notable changes found in second heating and cooling. Therefore, these materials do not change their structural properties; thus the respective thermophysical properties remain the same.

4. Conclusion

TGA and DSC tests were conducted to determine the thermophysical properties of commonly used materials. TGA tests result were used to determine the DOT which provided the temperature limit for the thermal stability of materials. By using the DOT, DSC test temperatures were determined. While PLA showed a slight difference in glass transition and phase transformation temperature between the two heating steps, ABS did not show any changes. Thermal events during the 3D printing of thermoplastic materials can cause a process induced strain effect, although the results in this paper only partially confirmed this hypothesis.

References

[1] ASTM, “F2792-12a - Standard Terminology for Additive Manufacturing Technologies,” Rapid Manuf. Assoc., pp. 10–12, 2013.

[2] C. Bellehumeur, L. Li, Q. Sun, and P. Gu, “Modeling of bond formation between polymer filaments in the fused deposition modeling process,” J. Manuf. Process., vol. 6, no. 2, pp. 170–178, 2004.

[3] F. S. Senatov, K. V. Niaza, M. Y. Zadorozhnyy, A. V. Maksimkin, S. D. Kaloshkin, and Y. Z. Estrin, “Mechanical properties and shape memory effect of 3D-printed PLA-based porous scaffolds,” J. Mech. Behav. Biomed. Mater., vol. 57, pp. 139–148, 2016.

[4] A. J. Bonon, M. Weck, E. A. Bonfante, and P. G. Coelho, “Physicochemical characterization of three fiber-reinforced epoxide-based composites for dental applications,” Mater. Sci. Eng. C, vol. 69, pp. 905–913, 2016.

[5] ASTM E2550 − 11, "Standard Test Method for Thermal Stability by Thermogravimetry,” ASTM Stand., vol. E37-01, pp. 1–5, 2014.

[6] ASTM D 3418, “Standard Test Method for Transition Temperatures and Enthalpies of Fusion and Crystallization of Polymers by Differential Scanning Calorimetry,” ASTM Stand., vol. 08, pp. 1–7, 2012.

TRAJECTORY GENERATION FROM CAD FOR AERIAL INSPECTION OF STRUCTURAL COMPONENTS IN GPS DENIED ENVIRONMENTS

A. G. Ortega[1*], R. Valenzuela Najera[1], A. Flores-Abad[1], M. McGee[1], A. Choudhuri[1]
[1] Mechanical Engineering, University of Texas at El Paso, El Paso, TX 79968, USA;
* Corresponding author (agortega@miners.utep.edu)

Keywords*: UAV, Autonomous, GPS-Denied Environment, CAD, Inspection*

ABSTRACT

Robotic technologies for inspection purposes have grown in interest. Such technologies are encouraged to reduce the risk human operators are involved in and to reduce costs due to downtime of equipment. High interest is placed on powerplant components where their correct operation is paramount. This work involves the use of a trajectory generation method from a Computer Aided Design (CAD) Model for Autonomous Unmanned Aerial Vehicles (UAV's) in GPS denied environments. This method also has various applications in the environmental and defense sectors.

1 Introduction

Power plants are critical components in the energy sector and their proper maintenance and operation are of vital importance. To do so, the industry must constantly inspect the critical components such as the boiler systems in coal-fired power plants. Usually human operators must personally inspect the structures placing them in a very hazardous environment. That is the reason why the robotics community has made advancements in recent years to prevent injury to the operators thus saving time and money. Different robotics technology has been used to inspect these structures. Examples of inspection include robots that climb cables and multiple UAV systems [1][2].

Autonomous UAV navigation has gained interest recently due to advancement in the hardware of such systems. For GPS-denied environments, most of the research is based on hardware such as sensors and cameras used as the primary location system. Using two cameras, Nikolic et al. [3], demonstrated a successful approach for UAV navigation inside a coal-fired power plant boiler. Their research tackled the particulate deflection problem successfully but requires mounting of two external cameras to the UAV thus limiting the minimum payload requirement of the drone. The system relies heavily on the sensing capabilities of the hardware to avoid contact with the structure.

Shan et al. [4] propose a system that compares the current image obtained by the UAV's camera to the Google Maps database to obtain the current position of the UAV. Although their system employs an extensive database to use virtually anywhere in the world, it faces the problem that the database is not updated constantly so it may encounter inconsistencies. Another problem with the approach for our purposes is the fact that aerial images do not contain much information in the third dimension of the structures. Structure elements such as overhangs are not visible and therefore limit the application of the system for inspection purposes.

In the area of defense, great advancements have been made with Nano Air Vehicles (NAV) as explained by Zhang et al. [5], where they developed a Nano-scale quadrotor helicopter weighing less than 50 grams. Such research is supported by agencies such as the Defense Advanced Research Projects Agency (DARPA) for its great potential in the field. Their system uses on-board vision to calculate its current location. This poses a challenge since repetitive structure features can easily confuse system. To eliminate this problem, they used Parallel Tracking and Mapping (PTAM) algorithm but it requires an initialization procedure to generate the required initial map.
The system explained in this article tackles all those issues through the use of a CAD model of the structures in question. Since the trajectory is pre-programmed into the system, additional hardware is only based upon the type of inspection/mission the UAV will tackle. Close contact sensing can then be applied only as a fail-safe mechanism to prevent crashes due to structures not accounted for in the CAD model. Since a 3D model of the structure is present, the UAV can be accurately placed in all three dimensions not just latitude and longitude. Also because of the latest hardware size advancements, the system can be decreased to a Nano-scale since the positioning of the UAV is mostly based in the software. This would provide a means to conduct inspection in a wide array of locations with very low signal acquisition such as indoors and disaster zones. The areas of implementation include the energy, environmental, and defense sectors. Vehicles with this capability have the potential to minimize human interaction in hazardous environments and significantly reduce the time and cost requirements for such inspections. This system provides an alternative to expensive location equipment by utilizing CAD models of the inspection structures which are for the most part readily available.

2 Methodology

This system uses a CAD model to project a trajectory through the use of a MATLAB algorithm. The algorithm utilizes the slicer concept taken from the Additive Manufacturing field. Just like in AM, the CAD model must first be converted into a StereoLithography (STL) file which contains only the surface information of a model. The information is derived into a triangular mesh that defines the surface geometry of the model. The STL file also contains the normal vector information for each triangle in the mesh. Once the STL file has been created, it is then arranged into matrices within MATLAB for its further manipulation where it is first “sliced” and then the data acquired is calculated to become a trajectory. In AM, the idea of the slicer irises from the need of defining the layer thickness for the AM technology being employed. For inspection purposes, the layer thickness is not defined from material and extruder needs but from hardware parameters like camera view angle and overlap percentage needed to map the camera feed. Keeping this in mind, the system can be easily calibrated to different values by changing a few lines of code. Once the data of the slices is acquired, it is then processed to become a trajectory that the UAV can follow.

2.1 CAD Model

Because of the advantages that CAD software offers, it has now become a fundamental part of the design process in almost every field. A great amount of resources are destined by companies into the CAD models and that translates to models that are extremely accurate to the

manufactured components. This makes the CAD a perfect starting point for the trajectory generation needed for the UAV to complete its mission.
For this research, a simple CAD model was created following literature and online resources since access to power plant components is limited and so is the access to their CAD models. Even though the model lacks detail, it is perfect for testing the algorithm and troubleshooting the code. Since a slicer method in our algorithm is employed, if more detail was provided in the CAD, it would only add more points of intersection per slice, producing an even better trajectory. It is important to note that CAD models exist in almost every engineering discipline including civil engineering meaning that our system is still a viable option of inspection not only on mechanical components but also structures in general. Once the CAD is available, it is converted to an STL that will then be transferred to MATLAB.

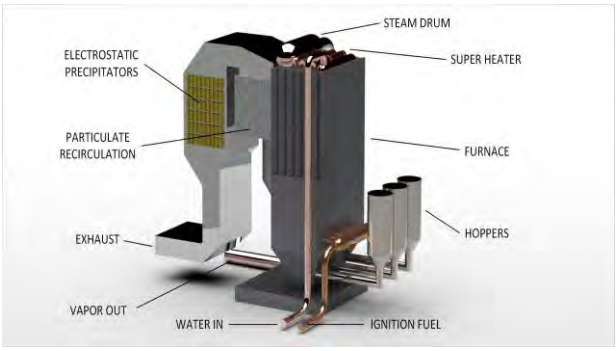

Fig.1. CAD Model of Coal-Fired Powerplant.

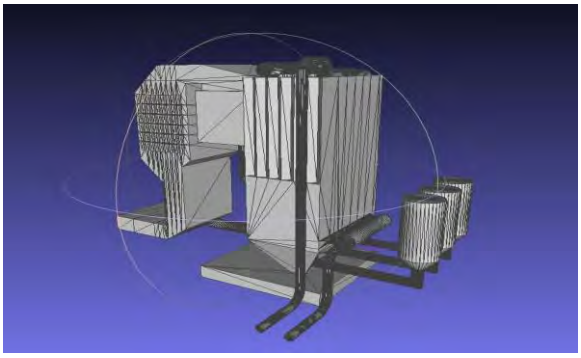

Fig 2. STL File of CAD Model

2.2 Slicer Algorithm

Since the STL file provides a triangular mesh defining the surface of the model, all that is needed to do is create an imaginary x-y plane at a set height in the z direction and calculate the intersection points between this plane/slice and the triangular mesh. Only the triangles that intersect that particular slice are considered. The triangles that intersect the slice may do so at one or two points. These points are important since they will define the outline of the body. If the slice intersects at exactly one or two corners of the triangle, then the x and y values of those points are taken as outline, but if the slicer intersect the triangle at any other location, an extra calculation is required to obtain the x and y coordinates. In order to identify those points the linear interpolation equation is used.

$$x = \frac{x_2 - x_1}{z_2 - z_1} * (z - z_1) + x_1 \quad (1)$$

In this equation, the known values include the slice height (z), and the point coordinates (x_1, x_2, z_1,and z_2). This equation must be used to find both the x and y coordinates by substituting the y-coordinates for all the x-coordinates in the equation. This will yield the x and y-coordinate of the intersection point between the slice and a single side of the triangle. The process can then be repeated to find the other intersection point. Both points would share the z coordinate with the slice. This part of the process repeats the last step to all the triangles in that

slice and then to all the slices that make up the model. This data is stored as a matrix containing all the data points in their corresponding x, y, and z-coordinates.

2.3 Trajectory from Slicer Data

The data points obtained in the slicer are arranged in a single matrix. This matrix includes multiple repeated points that are eliminated in the sorting process that takes place to generate a trajectory. At this point, the number of points has significantly decreased, meaning that a CAD with extreme detail poses no issues for the algorithm and that this data is small enough to transfer to the UAV memory. The next step is to introduce a wall offset, which is a set distance we need from the wall to prevent collision and to be at the correct distance for image acquisition. This is achieved by expanding the outline with the center of the outline as a reference point.

After that, the data must be sorted to generate the desired trajectory. If only a single outline is present, then the trajectory for that slice is simple as the data only needs to be sorted using the repeated values. If the data includes multiple outlines, the process to obtain the trajectory is more complex. In this step, multiple approaches have been studied but the one that shows the most potential is to separate the multiple outlines into separate matrices and analyze if the data points intersect or not. Results for this approach have not been achieved but the approach shows greats potential to allow the UAV to reach areas of interest with the trajectory.

After the data has been correctly sorted, it can be called a trajectory. The trajectory obtained in this work is extremely similar to G-Code which is often used in other robotic systems like Additive Manufacturing (AM) and Computer Numerical Control (CNC) machines.

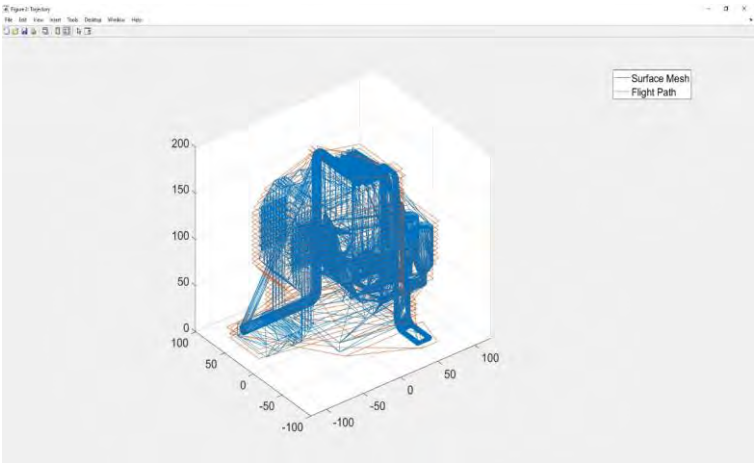

Fig 3. STL File of CAD Model

2.4 Yaw Generation for Attitude Control

The system uses a quadcopter as the UAV. This type of aircraft was chosen for its stability and compact size. Another advantage of using a quadcopter is the ability to maneuver without a difference in roll and pitch. For that reason, the only degree of freedom that requires calculation based on the trajectory points is the yaw. Since we are interested in inspection, the attitude of

the UAV is important. The system is equipped with infrared cameras that can be used both for data acquisition and for obstacle detection.
The yaw was obtained by calculating the normal vectors of the trajectory by using the following formula.

$$\vec{n} = \left(\frac{-\Delta x}{|\vec{n}|}, \frac{\Delta y}{|\vec{n}|}\right) \quad (2)$$

This formula contains the differences of the x and y-coordinates of two points which would give the vector notation of the line connecting the two points. The equation also incorporates a ratio by the magnitude of that vector to convert the vector to a unit vector instead. Lastly a sign change is applied to the x-coordinate to rotate the vector by 90 degrees making it a unit vector normal to the existing line. The sign change could be applied to either the x or the y coordinate since the vector does not need to have a specific direction for the yaw calculation. The calculation is repeated for every point in the trajectory. Finally, the yaw is calculated by finding the angle difference between each consecutive normal vector and is either added or subtracted from the previous yaw.

Conclusion

This method presents a means to inspect structures by using an existing CAD model with a UAV system that does not require GPS to complete its mission. A trajectory is successfully achieved from the STL file of the CAD model. Doing inspections using robotic technology allows workers to not be involved in hazardous environments while saving time and money thus being more efficient. Also, this system can be complemented with most of the existing developments for collision avoidance making it suitable for almost any mission thinkable ranging from energy to defense applications.

References

[1] Kim, Ho & Cho, Kyeong ho & Liu, F & Choi, Hyouk. (2011). Development of cable climbing robotic system for inspection of suspension bridge. 1422-1423.
[2] Rakha, Tarek & Gorodetsky, Alice. (2018). Review of Unmanned Aerial System (UAS) applications in the built environment: Towards automated building inspection procedures using drones. *Automation in Construction*. 93. 252-264.
[3] J. Nikolic, M. Burri, J. Rehder, S. Leutenegger, C. Huerzeler and R. Siegwart, "A UAV system for inspection of industrial facilities," *2013 IEEE Aerospace Conference*, Big Sky, MT, 2013, pp. 1-8.
[4] M. Shan, F. Wang, F. Lin, Z. Gao, Y. Z. Tang and B. M. Chen, "Google map aided visual navigation for UAVs in GPS-denied environment," *2015 IEEE International Conference on Robotics and Biomimetics (ROBIO)*, Zhuhai, 2015, pp. 114-119.
[5] X. Zhang, B. Xian, B. Zhao and Y. Zhang, "Autonomous Flight Control of a Nano Quadrotor Helicopter in a GPS-Denied Environment Using On-Board Vision," *in IEEE Transactions on Industrial Electronics*, vol. 62, no. 10, pp. 6392-6403, Oct. 2015.

TUNING OF MECHANICAL AND ELECTRICAL PROPERTIES OF 3D PRINTED CNT-PHOTOPOLYMER NANOCOMPOSITES THROUGH IN-SITU DISPERSION

J. E. Regis[1], L. A. Chavez[1], L. C. Delfin Manriquez[1], Y. Lin PhD. [1]*
[1] Department of Engineering, University of Texas at El Paso, El Paso, TX 79968, USA;
* Yirong Lin PhD. (ylin3@utep.edu)

Keywords*: 3D Printing, Photopolymer. Electrical, Mechanical, Nanocomposites*

ABSTRACT

This study presents the fabrication and mechanical characterization of functionalized Multi-Walled Carbon Nanotubes (CNT_F) reinforced photopolymer nanocomposites. CNT was used for its high electrical conductivity as well as its mechanical robustness. The fabrication of composites of this nature through additive manufacturing is a concept that has not been thoroughly explored. In this study, parametric studies were held to find settings that would allow the fabrication of functionalized CNT through stereolithography (SLA). In addition, the mechanical properties of functionalized composites under tensile stress were tested. An improvement of 77.4% and 64.0% in the Youngs modulus was observed over pristine resin from both random and aligned CNT_F, while an improvement of 20.1% in the UTS was observed when aligning the CNT_F. Demonstrating the tuning capabilities of this fabrication method.

1 Intoduction

Carbon nanotubes (CNTs) have attracted a great amount of attention from the scientific and engineering community since they were first synthesized over two decades ago. This interest has been due to their exceptional thermal, electrical, and mechanical properties, and therefore potential applications. Despite the amazing properties shown in individual form, these properties are not exhibited when used in bulk [1]. As a result, a great amount of work has been dedicated to the use of CNTs as reinforcements or fillers in different composite systems. CNT composites have been mostly fabricated using a polymer matrix to improve electrical and mechanical properties [2]. CNT-polymer composites have been mainly produced using traditional techniques such as solution processing [3], melt processing [4], in situ polymerization processing [5], among others. However, a very limited amount of research has been dedicated to the use of additive manufacturing techniques. Efforts to produce CNT polymers nanocomposites through additive manufacturing commonly use a low percentage of CNT due to the tendency of these to agglomerate and therefore become a point of failure for the composite instead of a reinforcement [6]. Therefore, methods to inhibit the agglomeration of CNTs in polymer solutions need to be implemented. One of the reported techniques to avoid the agglomeration of CNT-polymer composites is the application of an electric field to the CNT-polymer solution [7]. This technique is reported to not only disperse the CNT, but to also give the ability to control the alignment of these nanoparticles. This project presents the in situ dispersion of CNT through an electric field during the manufacture of CNT-photopolymer nanocomposites to tune its electrical and mechanical properties.

2 Methods

2.1 Preparation of Resin

Multi-Walled carbon nanotubes functionalized with nitric acid (CNT_F) was mixed with Tethon's Genesis Development Resin to prepare the solution for 3D printing. 1.0 weight percent (wt%) of CNT_F was added into a centrifugal tube and was shaken until visible, even dispersion was acquired. The tube was then vortexed for 15 minutes before being dumped into the 3D printer's resin tank.

2.2 Printing

A Formlabs Form 1 digital light processing (DLP) 3D printer was used for the fabrication of *Type V* ASTM standard dog bones. Formlabs uses its own software, PreForm, to prepare convert STL files into machine readable code. The printing parameters used in the PreForm software were those used for Castable resin uses the longest exposure time of the available parameters. The highest layer resolution of 25 µm was also used. Dog bones were printed in sets of five with 5 mm of space in-between them. The total print time for every set was 2 h 45 min.

2.3 Alignment of Carbon Nanotubes

For alignment of CNT_F in the Genesis resin, two electrodes with the length of the 3D printer's build plate were placed at both ends of the resin tank as illustrated in *Fig.1*. An electric field was applied generated by an Agilent 33210A Function/ Arbitrary Waveform Generator amplified from 1 to 6000 by an Acopian P030HP2 high voltage regulator. Dog bone samples were printed and aligned using various electric fields including 300 V/cm at 10kHz with the dog bones being aligned in parallel to the electric field.

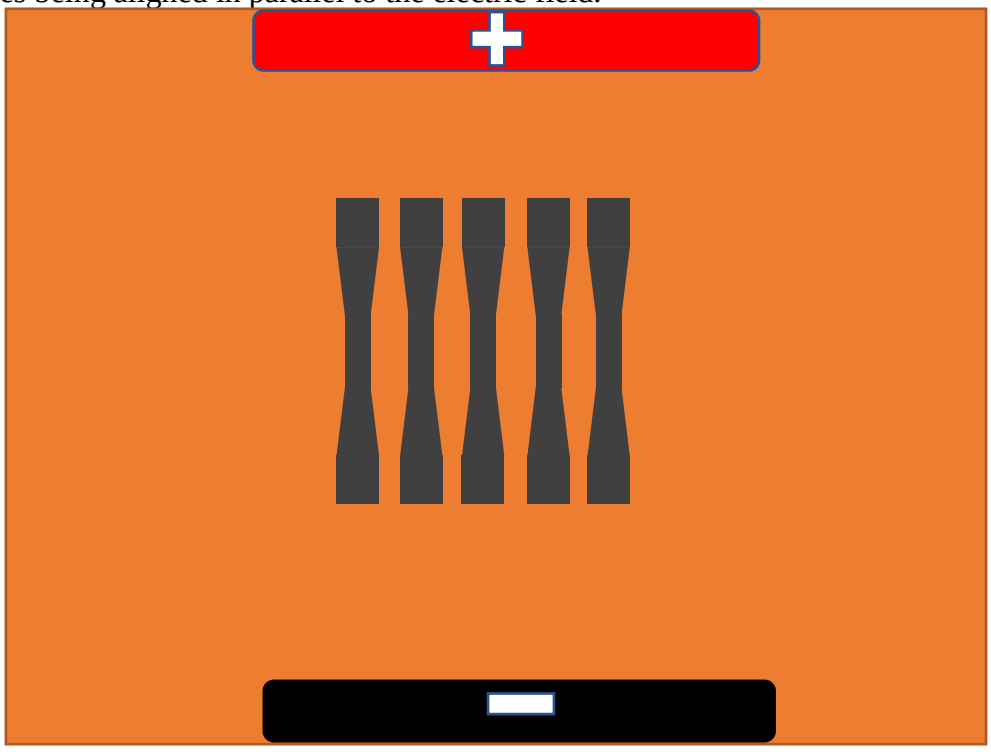

Fig. 1. Schematic of alignment setup for printing of dog bone samples

3 Results

Fig. 2 shows the results for tensile test of dog bone samples printed from pure Genesis resin, CNT_F with Genesis resin, and CNT_F with Genesis resin aligned in parallel. Tensile testing was done at a strain rate of 1 mm/min and was left running until the samples broke. As it can be observed from *Fig. 2* and *Table 1* both CNT_F and CNT_F aligned in parallel displayed a higher Young's Modulus than pure Genesis resin. CNT_F showed a 77.4% increase while aligned CNT_F showed a 64.0% increase in Young's Modulus from pure Genesis resin. While CNT_F showed a decrease in ultimate tensile stress of 15.6%, aligned CNT_F increased by 20.1%. Both CNT_F samples saw a decrease in strain at break meaning the samples became more brittle; however, when comparing the strain at break between CNT_F and aligned CNT_F, the aligned dog bones showed an increase in strain at break.

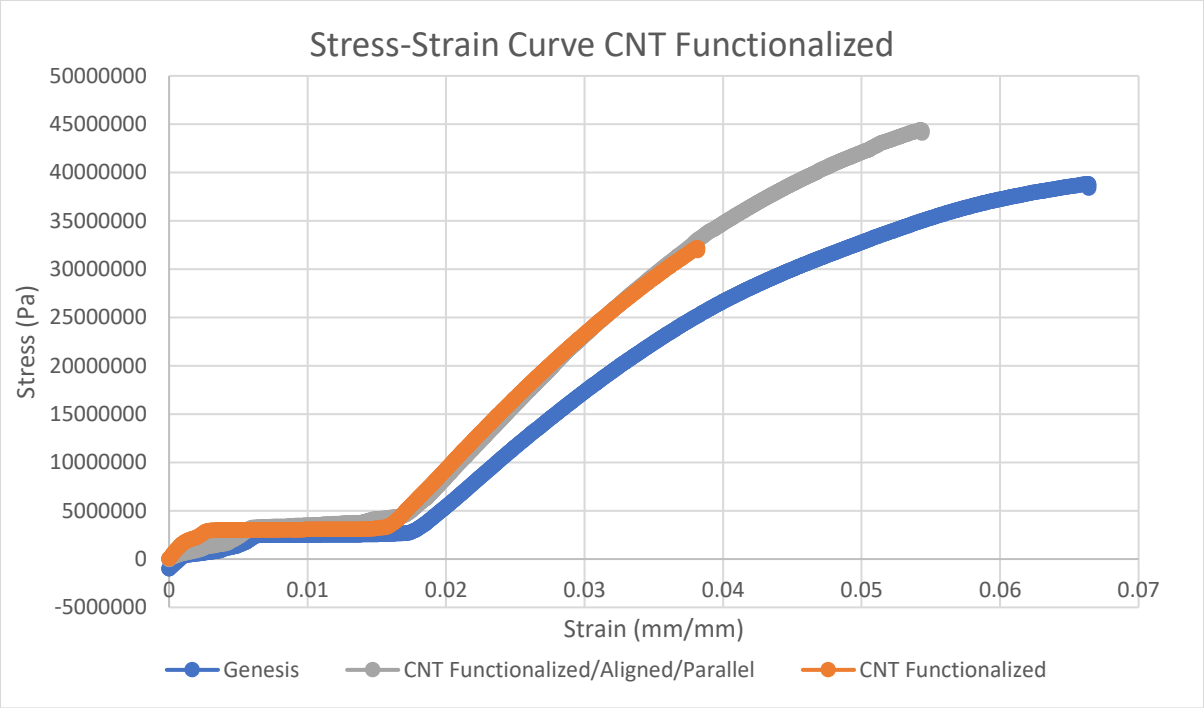

Figure 2. Results of tensile test for Genesis, Functionalized CNT, and Functionalized CNT aligned in parallel

Table 1. Numerical results for tensile test

Sample	AverageYoung's Modulus (Pa)	Average UTS(Pa)	Average Strain at Break (mm/mm)
Genesis	695358634.4	35703413.72	0.064025459
CNT No Alignment	1233346037	30150921.45	0.038206772
CNT Parallel Alignment	1140557471	42882823.75	0.05027622

The three different types of samples also displayed different points of fracture as shown in *Fig. 3*. While most pure Genesis samples broke in the center, CNT_F and aligned CNT_F samples broke above the central point with CNT_F samples breaking higher above the central point than aligned CNT_F.

Figure 3. Dog bone samples from left to right Genesis, CNT Functionalized, CNT Functionalized Aligned

4 Conclusion

In conclusion, it was possible to observe the changes in mechanical properties in Genesis resin with the addition of functionalized Multi-Walled Carbon Nanotubes (CNT_F). As it was hypothesized, alignment of CNT_F produced a composite with more favorable mechanical properties than pure Genesis. By increasing the dispersion of aligned CNT_F, it was possible to retain the increase in Young's modulus from pure Genesis resin of CNT_F while increasing the ultimate tensile stress.

References

[1] Khan, W., Sharma, R., & Saini, P. (2016). Carbon nanotube-based polymer composites: synthesis, properties and applications. In Carbon Nanotubes-Current Progress of their Polymer Composites. InTech.

[2] Coleman, J. N., Khan, U., Blau, W. J., & Gun'ko, Y. K. (2006). Small but strong: a review of the mechanical properties of carbon nanotube–polymer composites. Carbon, 44(9), 1624-1652.

[3] Dufresne, A., Paillet, M., Putaux, J. L., Canet, R., Carmona, F., Delhaes, P., & Cui, S. (2002). Processing and characterization of carbon nanotube/poly (styrene-co-butyl acrylate) nanocomposites. Journal of materials science, 37(18), 3915-3923.

[4] Tang, W., Santare, M. H., & Advani, S. G. (2003). Melt processing and mechanical property characterization of multi-walled carbon nanotube/high density polyethylene (MWNT/HDPE) composite films. Carbon, 41(14), 2779-2785.

[5] Zhao, C., Hu, G., Justice, R., Schaefer, D. W., Zhang, S., Yang, M., & Han, C. C. (2005). Synthesis and characterization of multi-walled carbon nanotubes reinforced polyamide 6 via in situ polymerization. Polymer, 46(14), 5125-5132.

[6] Zhang, Y., Li, H., Yang, X., Zhang, T., Zhu, K., Si, W., ... & Sun, H. (2016). Additive manufacturing of carbon nanotube‐photopolymer composite radar absorbing materials. Polymer Composites.

[7] Oliva-Avilés, A. I., Avilés, F., Sosa, V., Oliva, A. I., & Gamboa, F. (2012). Dynamics of carbon nanotube alignment by electric fields. Nanotechnology, 23(46), 465710.

Hosted by:

In conjunction with the office of Congresswoman Veronica Escobar

THANK YOU TO OUR SPONSORS!

Center for Space Exploration and Technology Research
500 W. University Avenue
Engineering Bldg., Suite M305
El Paso, TX 79968-0521
Phone 915.747.8252 | Fax 915.747.5549
cSETR@utep.edu | SETS@utep.edu
http://engineering.utep.edu/sets